Quantification of Regional Cardiac Function: Clinically-Motivated Algorithm Development and Application to Cardiac Magnetic Resonance and Computed Tomography



Davis Marc Vigneault

Keble College

University of Oxford

A thesis submitted for the degree of

Doctor of Philosophy

Trinity 2017

For Breezy

Acknowledgements

I would like to begin by thanking my two mentors, Alison Noble at Oxford and David Bluemke at the National Institutes of Health. Your depth of knowledge, uncompromising integrity, and unwavering dedication to the advancement of human knowledge has been inspiring, to say the least.

To the collaborators who have lent me their time and their expertise–Anneline te Riele at Johns Hopkins University, Carolyn Ho at Brigham and Women's Hospital, Ron Beyers and Tom Denney at Auburn Medical Center, and Amir Pourmorteza at the National Institutes of Health, among many others–your patience and selflessness has made this work possible, and I sincerely thank each of you.

Thanks to the NIH Intramural Research Program for giving scientists and engineers like myself the resources to investigate some of the most pressing issues of our time; to everyone behind the NIH-Oxford Scholars Program for making a crazy dream come true; and to Jim Schwob and Naomi Rosenberg at Tufts University School of Medicine for giving me the space to embark on this adventure in the first place.

To the countless developers, scientists, and mathematicians in the open source community who have donated so many hours of their lives to implementing the infrastructure on which this work has been built, thank you–while I cannot repay my debt to you, I will continue to donate what hours I can find to the next generation of computational scientists, and to promote open science and open source software wherever I can.

Thanks also to my peers in the Noble lab–Chris Bridge, Ruobing Huang, Weidi Xie, Ana Namburete, Mike Tee, and Richard Stebbing–for your kindness, your humour, and your biting intelligence. I look forward to our many reunions across the globe in the coming decades, and in the meantime I will miss you all dearly.

And finally, thank you to my best good friend Henry, my mother Nancy, and my wife Brianna Beehler, from whom I have been untethered in time and space these four years. It was a good ride, but I'll be home soon.

Abstract

Techniques described to date for the reproducible and noninvasive quantification of regional cardiac function have been largely relegated to research settings due to time-consuming and cumbersome image acquisition and analysis. In this thesis, feature tracking algorithms are developed for 2-D+Time cardiac magnetic resonance (CMR) and 3-D+Time cardiac computed tomography (CCT) image sequences that are easily acquired clinically, while emphasising reproducibility and automation in their design.

First, a commercially-implemented CMR feature tracking algorithm for the analysis of steady state free precession (SSFP) cine series is evaluated in patients with hypertrophic cardiomyopathy (HCM) and arrhythmogenic right ventricular cardiomyopathy (ARVC), which primarily affect the left ventricle (LV) and right ventricle (RV), respectively, and functional impairment compared with control populations is found in both cases. The limitations of this implementation are then used to guide development of an automated algorithm for the same purpose, making use of fully convolutional neural networks (CNN) for segmentation and spline registration across all frames simultaneously for tracking. This study is performed in the subjects with HCM, and functional impairment is again identified in disease subjects. Finally, as myocardial contraction is inherently a 3-D phenomenon, a technique is developed for quantification of regional function from 3-D+Time functional CCT studies using simultaneous registration of automatically generated Loop subdivision surface models for tracking. This study is performed in canine mongrels, and compared with the current state of the art technique for CCT functional analysis.

This work demonstrates the feasibility of automated, reproducible cardiac functional analysis from CMR and CCT image sequences. While work remains to be done in extending the principles demonstrated and modular components described to fully automated whole-heart analysis, it is hoped that this thesis will accelerate the clinical adoption of regional functional analysis.

Contents

List of Figures **ix**

List of Tables **xi**

List of Abbreviations **xii**

Mathematical Notation **xiv**

1 Background and Motivation **1**

1.1 Contributions . . . 1
1.2 Clinical Motivation . . . 2
1.3 Clinical Coordinate Systems . . . 3
1.4 Quantitative Metrics of Cardiac Function . . . 4
1.4.1 Strain . . . 5
1.4.2 Strain Rate . . . 8
1.4.3 Coordinate System . . . 9
1.4.4 Rotation, Twist, and Torsion . . . 10
1.4.5 SQUEEZ . . . 11
1.5 Image Acquisition . . . 12
1.5.1 Cardiac Magnetic Resonance (CMR) . . . 12
1.5.1.1 Tissue Tagging: SPAMM, CSPAMM, and MICSR . 12
1.5.1.2 Harmonic Phase (HARP) Imaging . . . 15
1.5.1.3 Strain ENCoded (SENC) Imaging . . . 18
1.5.1.4 Displacement and Velocity Encoding . . . 20
1.5.1.5 Feature Tracking CMR . . . 21
1.5.2 Echocardiography . . . 23
1.5.2.1 Speckle Tracking . . . 23
1.5.2.2 Tissue Doppler Imaging (TDI) . . . 24
1.5.3 Cardiac Computed Tomography (CCT) . . . 25
1.5.3.1 Feature Tracking CCT . . . 25
1.5.3.2 Deformable Image Registration . . . 25
1.5.3.3 Coherent Point Drift (CPD) . . . 26
1.5.4 Comparison . . . 27

1.6 Conclusions 29
1.7 Acknowledgements 29

2 Clinical Studies in Regional Cardiac Function 31
2.1 Motivation 31
2.2 Hypertrophic Cardiomyopathy (HCM) 33
2.2.1 Contributions 33
2.2.2 Background 33
2.2.3 Materials and Methods 35
2.2.3.1 Patient Population 35
2.2.3.2 CMR Acquisition 36
2.2.3.3 Image Analysis 36
2.2.3.4 Statistical Analysis 37
2.2.4 Results 39
2.2.4.1 Patient Characteristics 39
2.2.4.2 Circumferential Strain and cTSD 39
2.2.4.3 Correlation of cTSD with Functional Parameters . 42
2.2.4.4 Multivariate Analysis 44
2.2.4.5 Genetics 45
2.2.4.6 Reproducibility 46
2.2.4.7 Myocardial Strain by CMR Tagging 47
2.2.5 Conclusions 48
2.3 Arrhythmogenic Right Ventricular Cardiomyopathy (ARVC) 50
2.3.1 Contributions 50
2.3.2 Background 51
2.3.3 Materials and Methods 51
2.3.3.1 Patient Population 51
2.3.3.2 CMR Acquisition 52
2.3.3.3 Image Analysis 52
2.3.3.4 Statistical Analysis 55
2.3.4 Results 56
2.3.4.1 Baseline Characteristics 56
2.3.4.2 Global (Average) Strain Analysis 56
2.3.4.3 Regional Strain Analysis 58
2.3.4.4 Strain vs Qualitative Radiologist Interpretation . . 60
2.3.4.5 Strain Reproducibility 61
2.3.5 Conclusions 63
2.4 Conclusions 65

3 MRI: Uniform Quadratic Basis Spline Registration 67
3.1 Contributions . . . 67
3.2 Introduction . . . 68
3.3 Methods . . . 69
3.3.1 Segmentation . . . 70
3.3.2 Quadratic Bézier Curve Registration . . . 72
3.3.2.1 Quadratic Bézier Curve Representation . . . 72
3.3.2.2 Formulating the Optimisation . . . 73
3.4 Experiments . . . 75
3.4.1 Data Preparation . . . 75
3.4.2 Segmentation . . . 76
3.4.3 SA Tracking . . . 76
3.4.4 Regional Function . . . 77
3.5 Results . . . 77
3.5.1 Segmentation . . . 77
3.5.2 Network Visualisation . . . 80
3.5.2.1 Maximizing Filter Response . . . 80
3.5.2.2 Minimizing Information Loss . . . 86
3.5.3 Functional Parameters . . . 87
3.6 Conclusions . . . 91

4 CT: Loop Subdivision Surface Registration 97
4.1 Contributions . . . 97
4.2 Background . . . 98
4.3 Methods . . . 101
4.3.1 Boundary Candidate Selection . . . 101
4.3.2 Mesh Model Generation . . . 102
4.3.3 Registration . . . 104
4.3.3.1 Subdivision Surface Evaluation . . . 105
4.3.3.2 Optimisation . . . 109
4.3.3.3 Multiresolution Approach . . . 112
4.3.4 Cardiac Function . . . 112
4.3.5 Statistics . . . 113
4.4 Implementation Details . . . 113
4.5 Experiments . . . 114
4.5.1 Canine Infarct Model . . . 114
4.5.2 Image Acquisition . . . 114
4.5.3 Validation . . . 114
4.6 Results . . . 115
4.7 Conclusions . . . 116

5 Conclusions and Future Directions **122**
5.1 Summary and Advancements in Knowledge 122
5.2 Limitations and Future Directions 126
5.3 Implications for Specialised Image Sequences 127
5.3.1 Contributions 127
5.3.2 Cine Watermark Imaging 127

Appendices

A Wall Thickness vs cTSD in HCM **133**
A.1 Motivation 133
A.2 Proof 134
A.3 Results 135

B Mesh Decimation **137**

C Loop Subdivision Surfaces **140**
C.1 Barycentric B-Spline Basis Functions 141
C.2 Loop Subdivision Matrices 141
C.2.1 Subdivision Matrix S 141
C.2.2 Extended Subdivision Matrix, A 142
C.2.3 Bigger Subdivision Matrix, $\bar{A}$ 143
C.2.4 Picking Matrix, Pk 143
C.3 Eigenstructure of A 144
C.3.1 Eigenstructure of S 145
C.3.2 Eigenstructure of A 146
C.3.3 Evaluating a Subdivision Patch at the Origin 148

D Quartic Triangle Bezier Surfaces **149**
D.1 Barycentric Bezier Basis Functions 149
D.2 Converting from a B-Spline Surface to a Bezier Surface 149

References **153**

List of Figures

1.1 Cardiac Coordinate System 4
1.2 Clinical Cardiac Planes 5
1.3 American Heart Association (AHA) 17-Segment LV Segmentation . 6
1.4 Spatial Modulation of Magnetization (SPAMM) 14
1.5 SPAMM, CSPAMM, and MICSR 16
1.6 Harmonic Phase Imaging (HARP) 17

2.1 cTSD versus Midwall Circumferential Strain 35
2.2 Feature Tracking Tracings in HCM 38
2.3 Segmental cTSD in HCM 42
2.4 Correlation of cTSD with functional parameters 44
2.5 Stratification of cTSD by Genetic Assignment 46
2.6 Reproducibility of cTSD 47
2.7 Right Ventricular Feature Tracking in a Healthy Subject 54
2.8 Right Ventricular Feature Tracking in Overt ARVC 54
2.9 Right Ventricular Segmentation 55
2.10 Regional cTSD in ARVC 59
2.11 Diagnostic Performance of Subtricuspid Strain in ARVC 61
2.12 Reproducibility of Feature Tracking RV Strain in ARVC 62

3.1 Schematic of Traditional Feature Tracking Methods 68
3.2 Architecture of the Baseline Segmentation Network 70
3.3 Simple vs Dilated Convolution (DC) Kernels 71
3.4 Preparation of Image Data for CNN Segmentation 75
3.5 Histograms of Segmentation Metrics for Network A 78
3.6 Representative Segmentation Results in a Healthy Subject 81
3.7 Representative Segmentation Results in Overt HCM 82
3.8 Selected Failure Cases from CNN Segmentation 83
3.9 Maximum Prediction from a SA Mask (Multi-View Network) 85
3.10 Maximum Prediction from a SA Mask (Single-View Network) . . . 85
3.11 Information Loss given a SA Image (Multi-View Network) 87
3.12 Information Loss given a SA Image (Single-View Network) 88

3.13 Multiresolution Spline Registration 89
3.14 Segmentation and Tracking Results 90
3.15 Representative Strain Curves in a Healthy Control Subject 93
3.16 Representative Strain Curves in a Patient with Overt HCM 94

4.1 Boundary Candidate Selection 102
4.2 Subdivision Mesh Model Generation 103
4.3 Improvement of Mesh Quality with Gaussian Noise 104
4.4 Numbering Vertices in a Loop Subdivision Patch 106
4.5 Geometric Loop Subdivision 107
4.6 Residual Error at Each Registration Stage 116
4.7 Calculation of SQUEEZ from Registered Subdivision Surfaces . . . 117
4.8 Average Peak SQUEEZ 118
4.9 Global SQUEEZ Curves: Subdivision vs CPD Methods 119
4.10 Peak Global SQUEEZ: Subdivision vs CPD Methods 119
4.11 Peak Segmental SQUEEZ: Subdivison vs CPD Methods 120

5.1 Representative Cine Watermarking Images 128
5.2 Cine Watermarking CNN Architecture 129
5.3 Simulated Cine Watermarking Images 130
5.4 Predicted Displacement Fields in Simulated Cine Watermark Images 131

A.1 Measured vs Predicted cTSD 136

B.1 Distribution of Triangle Areas 138
B.2 Distribution of Triangle Aspect Ratios 138
B.3 Distribution of Valencies 139

List of Tables

2.1 Baseline Characteristics of the HCM Study Population 40
2.2 Functional Imaging Characteristics of the HCM Study Population . 41
2.3 Univariate Analysis of Segmental cTSD in HCM 43
2.4 Multivariate Analysis of cTSD in HCM 45
2.5 Imaging Characteristics for the ARVC Study Population 56
2.6 Clinical Characteristics of the ARVC Study Population 57
2.7 Global Strain Values by ARVC Diagnostic Group 57
2.8 Regional Strain Values by ARVC Diagnostic Group 58
2.9 Multivariate Analysis of Subtricuspid Strain in ARVC 60

3.1 CNN Architecture Variants Considered 71
3.2 Network Performance Compared with Ground Truth 79
3.3 Global LV Strain in Overt HCM vs Control Subjects 89
3.4 Segmental LV Circumferential Strain in Overt HCM vs Control Subjects 92

4.1 Hyperparameters of the Loop Subdivision Surface Optimization . . 113

List of Abbreviations

2C . . . . . Two-Chamber View (i.e., Vertical Long Axis View)

4C . . . . . Four-Chamber View (i.e., Horizontal Long Axis View)

AHA . . . . . American Heart Association

ANOVA . . . . ANalysis Of VAriance

ARVC . . . . . Arrhythmogenic Right Ventricular Cardiomyopathy

BMI . . . . . Body Mass Index

BNP . . . . . Brain Natriuretic Peptide

BP . . . . . Blood Pressure

BSA . . . . . Body Surface Area

CMR . . . . . Cardiac Magnetic Resonance

CNN . . . . . Convolutional Neural Network

CO . . . . . Cardiac Output

CPD . . . . . Coherent Point Drift

CSPAMM . . Complementary SPAtial Modulation of Magnetization

cTSD . . . . . circumferential Transmural Strain Difference

DC . . . . . Dilated Convolution

DENSE . . . . Displacement ENcoding with Stimulated Echoes

ED . . . . . End Diastole, End Diastolic

EDV . . . . . End Diastolic Volume

EF . . . . . Ejection Fraction

ES . . . . . End Systole, End Systolic

ESV . . . . . End Systolic Volume

FFT . . . . . Fast Fourier Transform

FNR . . . . . False Negative Rate

FPR . . . . . False Positive Rate

FT . . . . . Feature Tracking
GRE . . . . . GRadient Echo
HARP . . . . . HARmonic Phase
HCM . . . . . Hypertrophic CardioMyopathy
HR . . . . . Heart Rate
ICC . . . . . Intraclass Correlation Coeficient
IoU . . . . . Intersection over Union
IQR . . . . . InterQuartile Range
LA . . . . . Left Atrium, Left Atrial
LV . . . . . Left Ventricle, Left Ventricular
LVH . . . . . Left Ventricular Hypertrophy
MICSR . . . . Magnitude Image CSPAMM Reconstruction
MTT . . . . . Multimodality Tissue Tracking
MWT . . . . . Maximal Wall Thickness
n**-D** . . . . . n-Dimensional, $n \in \{2, 3\}$
RA . . . . . Right Atrium, Right Atrial
RF . . . . . RadioFrequency
RV . . . . . Right Ventricle, Right Ventricular
SA . . . . . Short Axis View
SENC . . . . . Strain ENCoding
SGD . . . . . Stochastic Gradient Descent
SI . . . . . Shape Index
SPAMM . . . SPAtial Modulation of Magnetization
SQUEEZ . . . Stretch QUantifier for Endocardial Engraved Zones
SSFP . . . . . Steady State Free Precession
STN . . . . . Spatial Transformer Network
SV . . . . . Stroke Volume
TDI . . . . . Tissue Doppler Imaging
TEE . . . . . Trans-Esophageal Echocardiography
TFC . . . . . Task Force Criteria
TTE . . . . . Trans-Thoracic Echocardiography
WT . . . . . Wall Thickness

Mathematical Notation

$\mathbb{R}$	Real
$\mathbb{C}$	Complex
$\mathbb{N}$	Natural numbers, $0, 1, 2, ...$
$\mathbb{Z}$	Integers
atan2	Four Quadrant Arctangent Operator
arg	Shorthand for Four Quadrant Arctangent Operator
tanh	Hyperbolic Tangent Operator
sgn	Sign Operator
$\mathcal{F}$, $\mathcal{F}^{-1}$	Forward, Inverse Fourier Operators
$\mathcal{W}$	Wrapping Operator
$\Re$, $\Im$	Operators Returning Real, Imaginary Components
ε, ϵ	Lagrangian, Eulerian Strain Components
E_L, E_E	Lagrangian, Eulerian Strain Tensors
γ	Gyromagnetic Ratio
σ	Standard Deviation
t, t_0	Current, Initial Time
n	Spatial Dimension
$Y \in \mathbb{N}^{n \times k}$, $\mathbf{y}_i$	Matrix of k Indices, Column of i of Y
$X \in \mathbb{R}^{n \times k}$, $\mathbf{x}$	Matrix of k Material Positions, Column of X
$U \in \mathbb{R}^{n \times k}$, $\mathbf{u}$	Matrix of k Displacements
r, s	Parametric Coordinates
I	Identity Matrix
$F \in \mathbb{R}^{n \times n}$	Deformation Gradient Tensor

Unless explicitly stated or obvious from context, the above mathematical notation and conventions will be adhered to. Note that a superposed dot indicates a temporal derivative (i.e., $\dot{U}$ indicates a matrix of velocity vectors).

1 Background and Motivation

Contents

1.1 Contributions 1
1.2 Clinical Motivation 2
1.3 Clinical Coordinate Systems 3
1.4 Quantitative Metrics of Cardiac Function 4
1.4.1 Strain 5
1.4.2 Strain Rate 8
1.4.3 Coordinate System 9
1.4.4 Rotation, Twist, and Torsion 10
1.4.5 SQUEEZ 11
1.5 Image Acquisition 12
1.5.1 Cardiac Magnetic Resonance (CMR) 12
1.5.2 Echocardiography 23
1.5.3 Cardiac Computed Tomography (CCT) 25
1.5.4 Comparison 27
1.6 Conclusions 29
1.7 Acknowledgements 29

1.1 Contributions

[1] Mimount Bourfiss, Davis M Vigneault, Mounes Aliyari Ghasebeh, Brittney Murray, Cynthia A James, Crystal Tichnell, Firdaus A. Mohamed Hoesein, Stefan L Zimmerman, Ihab R Kamel, Hugh Calkins, Harikrishna Tandri, Birgitta K Velthuis, David A Bluemke and Anneline S J M te Riele. 'Feature tracking CMR reveals abnormal strain in preclinical arrhythmogenic right ventricular dysplasia/ cardiomyopathy: a

multisoftware feasibility and clinical implementation study'. In: *Journal of Cardiovascular Magnetic Resonance* 19.1 (Dec. 2017), p. 66.

[2] Michael W. Tee, Samuel Won, Fabio S. Raman, Colin Yi, Davis M. Vigneault, Cynthia Davies-Venn, Songtao Liu, Albert C. Lardo, João A. C. Lima, J. Alison Noble, Craig A. Emter and David A. Bluemke. 'Regional Strain Analysis with Multidetector CT in a Swine Cardiomyopathy Model: Relationship to Cardiac MR Tagging and Myocardial Fibrosis'. In: *Radiology* 277.1 (Oct. 2015), pp. 88–94.

1.2 Clinical Motivation

Cardiovascular diseases are the most common cause of death both in industrialised countries and globally, accounting for 160,000 annual deaths (275 age-standardised deaths per 100,000 population) in the United Kingdom [1], 600,000 annual deaths (167 age-standardised deaths per 100,000 population) in the United States [2], and 17.5 million annual deaths worldwide [3]. For this reason, quantitative assessment of cardiac function–which may be broadly defined as the magnitude and pattern of myocardial contraction–is a central goal in cardiology. Clinically, ejection fraction (EF), defined in terms of end systolic and diastolic volumes (ESV, EDV),

$$EF = \frac{EDV - ESV}{EDV}, \tag{1.1}$$

is widely measured and reported clinically. While EF is a *global* metric of cardiac function, most heart disease is *regional* in nature. Coronary heart disease, which is inherently regional, is the most common form of heart disease both in the United Kingdom and the United States (70,000 and 365,000 annual deaths, respectively [1, 2]). Patients with less common diseases such as genetic cardiomyopathies, and myocarditis may also present with regional dysfunction. Additionally, EF may be preserved in certain global diseases of the heart, such as diastolic heart failure. EF is generally a poor biomarker of disease in these cases, especially early in their disease course, and has been a poor predictor of cardiovascular events in large population studies [4–7].

In order to better characterise disease, it is necessary to quantify local myocardial contraction patterns [8], which are poorly assessed by qualitative observation [9]. Left

ventricular (LV) contraction is typically described in terms of a cylindrical coordinate system centred on the long axis of the heart (Fig. 1.1). To a first approximation, contraction of the LV causes shortening in the longitudinal and circumferential directions, and thickening in the radial direction. However, this contraction is not uniform. Simple geometric considerations dictate that the endocardium experiences greater circumferential shortening than the epicardium, a hypothesis which was verified by sonomicrometry in canine studies [10, 11] and later by cardiac magnetic resonance (CMR) in humans [12]. Moreover, due to the helical, depth-dependent orientation of myocardial fibres [13], the subepicardial fibres course clockwise from base to apex; the midwall fibres course circumferentially; and subendocardial fibres course anticlockwise from base to apex when viewed from apex to base. The consequences of this structure are twofold. First, the LV tends to rotate clockwise and anticlockwise during contraction at the base and apex, respectively, resulting in a "wringing" motion. Second, this wringing motion opposes the transmural gradient in circumferential strain, causing contraction to be more uniform across the wall of the heart than would be expected from a simple cylindrical model.

1.3 Clinical Coordinate Systems

In order to observe cardiac function in a uniform way, 2-D cine (video) sequences are acquired in one of a handful of standard clinical planes (Fig. 1.2). The short axis (SA) plane is perpendicular to the longitudinal axis of the heart; the horizontal long axis (4C) plane is parallel to the longitudinal axis and bisects both the right ventricle (RV) and LV; and the vertical long axis (2C) plane is rotated $\pi/2$ radians from the 4C view around the longitudinal axis, such that it bisects the LV only.

In reporting qualitative and quantitative measures of LV contraction, it is typical to divide the LV according to the 17-segment American Heart Association (AHA) model [14], giving researchers and clinicians a unified paradigm for reporting (Fig. 1.3). Results from some relevant subset (the cardiac apex, segment 17, is often excluded, for example) of these segments are frequently reported as a polar projection, where the most apical segments are in the centre of the plot and the most

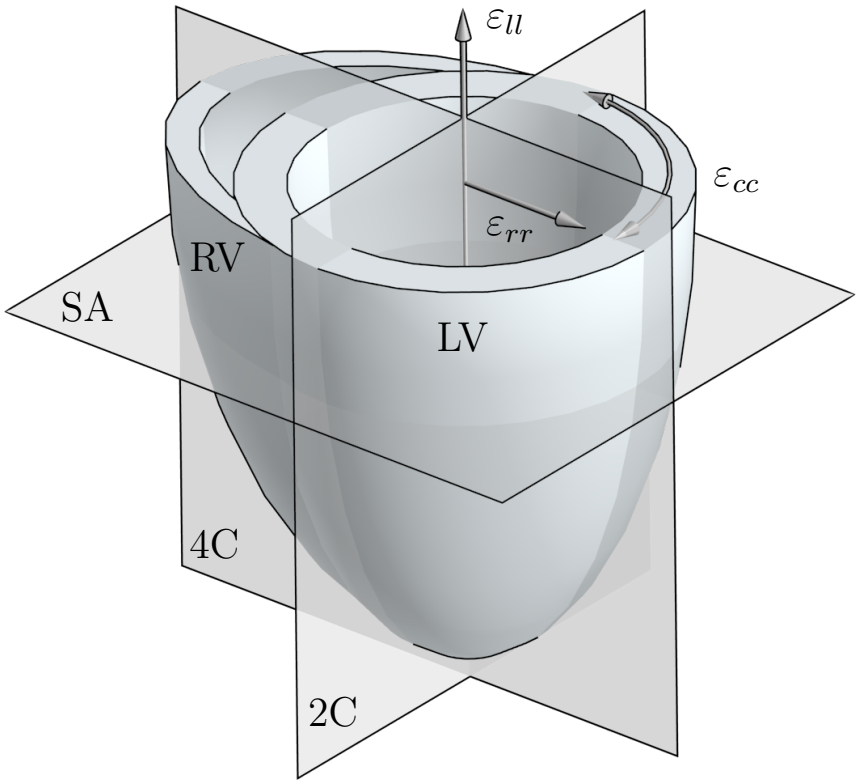


Figure 1.1: Cardiac Coordinate System. Clinically, a cylindrical coordinate system centered on the left ventricle is used to simplify reporting of regional functional parameters. LV: Left Ventricle; RV: Right Ventricle; SA: Short Axis; 4C: Four Chamber; 2C: Two Chamber; ε_{ll}: Longitudinal Strain; ε_{rr}: Radial Strain; ε_{cc}: Circumferential Strain.

basal segments in the periphery. Although significant normal biological variability exists in cardiac vasculature, it is known approximately which AHA segments are perfused by which major arteries in the most common anatomical variants. Note also that not all quantitative metrics apply to all AHA segments; for example, because the apex of the heart by definition does not include the endocardium, inherently endocardial measurements such as SQUEEZ (§1.4.5) are not applicable.

1.4 Quantitative Metrics of Cardiac Function

In order to quantitatively characterise the complex pattern of myocardial contraction, various metrics have been developed. For brevity, this discussion is restricted to those

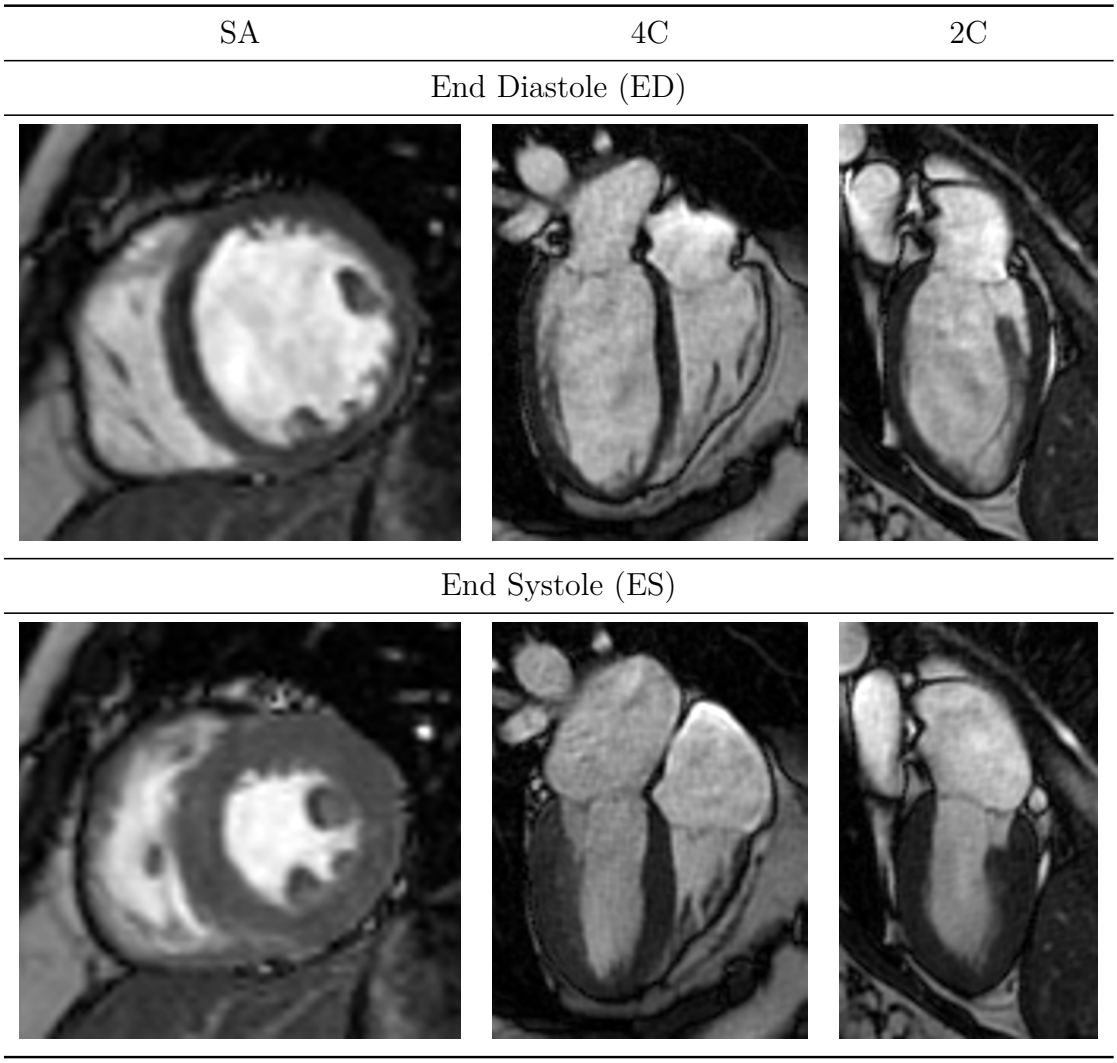
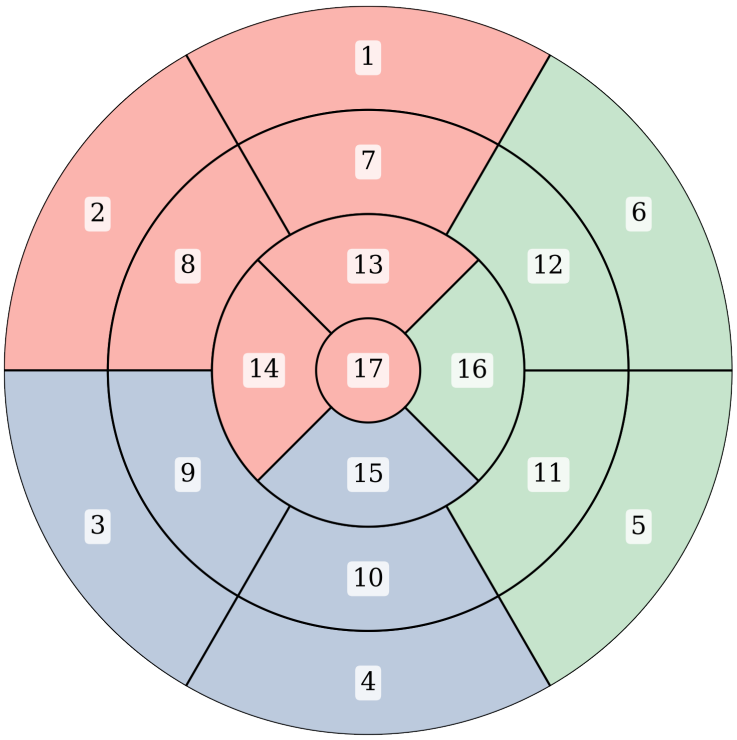


Figure 1.2: Clinical Cardiac Planes. Example clinical planes (SA: Short Axis; 4C: Horizontal Long Axis; 2C: Vertical Long Axis) from a healthy, 38-year-old female are shown at end systole (ES) and end diastole (ED).

metrics which are either widely used in the literature or directly pertinent to this work, in particular: strain and strain rate (Section 1.4.1); rotation, twist, and torsion (Section 1.4.4); and stretch quantifier for endocardial engraved zones (Section 1.4.5).

1.4.1 Strain

Cardiac strain has been widely used in the cardiology literature as a surrogate for regional function. The mathematics applied to cardiac modelling correspond to *finite strain theory* in the mechanical engineering literature (as opposed to



AHA	Slice	Segment
1	B	Ant
2	B	AntSep
3	B	InfSep
4	B	Inf
5	B	InfLat
6	B	AntLat
7	M	Ant
8	M	AntSep
9	M	InfSep
10	M	Inf
11	M	InfLat
12	M	AntLat
13	A	Ant
14	A	Sep
15	A	Inf
16	A	Lat
17	P	Apex

Figure 1.3: American Heart Association (AHA) 17-Segment LV Segmentation. Segments are displayed as a polar plot of the LV, where the outer segments correspond to the base of the heart and the inner segments to the apex. Red segments are perfused by the left anterior descending artery; blue segments by the right coronary artery; and green segments by the left circumflex. B: Base; M: Midslice; A: Apex; P: Peak; Ant: Anterior; AntSep: Anteroseptal; InfSep: Inferoseptal; Inf: Inferior; InfLat: Inferolateral; AntLat: Anterolateral.

infinitesimal strain theory and large-displacement strain theory, both of which rely upon small deformation assumptions which are violated in cardiac mechanics). Along a single dimension, strain is defined in terms of length as a function of time $l(t)$ such that strain is positive, negative, and zero for expansion, contraction, and stasis respectively. Although many definitions of strain have been proposed (and are used) in mechanical engineering, only two are commonly used in cardiology: Lagrangian and Eulerian strain. These definitions differ in whether they take the perspective of the *tissue* or the *space*. Lagrangian strain takes the point of view of a material (tissue) point, and is normalised to the length at ED, $l(t_0)$,

$$\varepsilon(t) = \frac{l(t) - l(t_0)}{l(t_0)}. \tag{1.2}$$

Eulerian strain, by contrast, takes the point of view of a spatial coordinate, and is normalised to the length at time t,

$$\epsilon\left(t\right) = \frac{l\left(t\right) - l\left(t_0\right)}{l\left(t\right)}. \tag{1.3}$$

For very small strains, $\varepsilon(t) \approx \epsilon(t)$, but this assumption does not hold given the large deformations observed in cardiac mechanics.

In n dimensions, the deformation of a point is described in terms of n^2 individual strains $\varepsilon_{i,j}$, comprising n "normal" or "direct" strains ($\varepsilon_{i,j} \mid i = j$) and $n^2 - n$ "shear" strains ($\varepsilon_{i,j} \mid i \neq j$). A normal strain describes the change in length parallel to a given axis, similar to the 1-D case. A shear strain, in contrast, describes the change in angle between a given pair of axes. For a 3-D Cartesian coordinate system, the Lagrangian strain tensor E_L is defined as

$$E_L = \begin{bmatrix} \varepsilon_{x,x} & \varepsilon_{x,y} & \varepsilon_{x,z} \\ \varepsilon_{y,x} & \varepsilon_{y,y} & \varepsilon_{y,z} \\ \varepsilon_{z,x} & \varepsilon_{z,y} & \varepsilon_{z,z} \end{bmatrix}, \tag{1.4}$$

noting that the dependence on time has been omitted for clarity. The corresponding Eulerian strain tensor E_E is defined analogously. Note also that E_L and E_E are symmetric, i.e., $\varepsilon_{i,j} = \varepsilon_{j,i}$ and $\epsilon_{i,j} = \epsilon_{j,i}$.

In some cases, it is possible to calculate the relevant components of this tensor directly by observing the change in length of a segment or the change in angle between a pair of segments. Frequently, however, it is necessary to calculate pixelwise strain tensors from a displacement $\mathbf{u}(t) = \mathbf{x}(t) - \mathbf{x}(t_0)$, where $\mathbf{x}(t)$ and $\mathbf{x}(t_0) \in \mathbb{R}^n$ describe a material point's position in its current and reference configurations, respectively. For a particular displacement $\mathbf{u}(t)$ at time t, the Lagrangian (material) displacement gradient tensor is defined as the matrix of partial derivatives with respect to the reference configuration $\mathbf{x}(t_0)$,

$$\nabla_{t_0}\mathbf{u}(t) = \begin{bmatrix} \dfrac{\partial u_x(t)}{\partial x_x(t_0)} & \dfrac{\partial u_y(t)}{\partial x_x(t_0)} & \dfrac{\partial u_z(t)}{\partial x_x(t_0)} \\ \dfrac{\partial u_x(t)}{\partial x_y(t_0)} & \dfrac{\partial u_y(t)}{\partial x_y(t_0)} & \dfrac{\partial u_z(t)}{\partial x_y(t_0)} \\ \dfrac{\partial u_x(t)}{\partial x_z(t_0)} & \dfrac{\partial u_y(t)}{\partial x_z(t_0)} & \dfrac{\partial u_z(t)}{\partial x_z(t_0)} \end{bmatrix}. \tag{1.5}$$

Note also that x_i and u_i represent the i^{th} components of $\mathbf{x}$ and $\mathbf{u}$, respectively. The deformation gradient tensor F may be defined in terms of Equation 1.5,

$$\begin{aligned} F &= \nabla_{t_0}\mathbf{x}(t) \\ &= \nabla_{t_0}\left(\mathbf{u}(t) + \mathbf{x}(t_0)\right) \\ &= \nabla_{t_0}\mathbf{u}(t) + I. \end{aligned} \tag{1.6}$$

The Lagrangian strain tensor E_L may now be written in terms of the right Cauchy-Green deformation tensor $F^\top F$,

$$E_L = \frac{1}{2}\left(F^\top F - I\right) \tag{1.7}$$

and the Eulerian strain tensor E_E may be written in terms of the Piola tensor $(FF^\top)^{-1}$,

$$E_E = \frac{1}{2}\left(I - (FF^\top)^{-1}\right). \tag{1.8}$$

1.4.2 Strain Rate

Given a Lagrangian strain tensor $E_L(t)$, it is straightforward to calculate strain rate as the derivative with respect to time,

$$\dot{E}_L(t) = \frac{dE_L}{dt}, \tag{1.9}$$

noting that the Eulerian strain rate tensor $\dot{E}_E$ is defined similarly. However, it is also common in medical imaging to measure a velocity field $\dot{U}(t) = dU(t)/dt$ from the perspective of spatial coordinates. For a particular velocity $\dot{\mathbf{u}}(y_i, t)$ (a column of $\dot{U}$), the Eulerian (spatial) velocity gradient tensor is defined as the matrix of partial derivatives with respect to the current configuration $X(t)$,

$$\nabla_t\dot{\mathbf{u}}(t) = \begin{bmatrix} \dfrac{\partial\dot{u}_x(t)}{\partial x_x(t)} & \dfrac{\partial\dot{u}_y(t)}{\partial x_x(t)} & \dfrac{\partial\dot{u}_z(t)}{\partial x_x(t)} \\ \dfrac{\partial\dot{u}_x(t)}{\partial x_y(t)} & \dfrac{\partial\dot{u}_y(t)}{\partial x_y(t)} & \dfrac{\partial\dot{u}_z(t)}{\partial x_y(t)} \\ \dfrac{\partial\dot{u}_x(t)}{\partial x_z(t)} & \dfrac{\partial\dot{u}_y(t)}{\partial x_z(t)} & \dfrac{\partial\dot{u}_z(t)}{\partial x_z(t)} \end{bmatrix}. \tag{1.10}$$

It is possible to decompose $\nabla_t \dot{\mathbf{u}}(t)$ into symmetric and asymmetric components,

$$\nabla_t \dot{\mathbf{u}}(t) = \overbrace{\frac{\nabla_t \dot{\mathbf{u}}(t) + \nabla_t \dot{\mathbf{u}}(t)^\top}{2}}^{\text{symmetric, } \dot{E}_E} + \overbrace{\frac{\nabla_t \dot{\mathbf{u}}(t) - \nabla_t \dot{\mathbf{u}}(t)^\top}{2}}^{\text{asymmetric, } W}, \tag{1.11}$$

where the symmetric component $\dot{E}_E$ is the Eulerian strain rate tensor (known in the mechanics literature as the rate of deformation tensor, often denoted D) and the asymmetric component W is the spin tensor.

1.4.3 Coordinate System

Given that images are generally reconstructed on a rectilinear grid, it has been natural to formulate the initial discussion of strain in Cartesian coordinates. However, it is unclear how to interpret Cartesian strain relative to cardiac anatomy. The most common approach is to transform the strain tensor onto a cylindrical coordinate system (longitudinal, radial, and circumferential) where the longitudinal direction coincides with the axis of the chamber of interest (Fig. 1.1). The appropriate transformation $\{x, y, z\} \rightarrow \{l, r, c\}$ is written in terms of the longitudinal, radial, and circumferential unit vectors $\hat{l}$, $\hat{r}$, and $\hat{c}$ in the original Cartesian coordinate system,

$$E' = \begin{bmatrix} \hat{l} & \hat{c} & \hat{r} \end{bmatrix}^\top E \begin{bmatrix} \hat{l} & \hat{c} & \hat{r} \end{bmatrix}. \tag{1.12}$$

In the healthy LV, circumferential and longitudinal strain become more negative during systole, reaching a peak (most negative) at end systole, and then recovering towards zero. Radial strain, on the other hand, becomes more positive during systole, reaching a peak (most positive) at end systole, and likewise recovering towards zero. Consequently, strain rate curves have two peaks (systolic and diastolic). Peak systolic and diastolic strain rate occur during mid-systole and early diastole, and have the same sign and opposite sign of their corresponding peak strain, respectively (i.e., in order to reach a positive peak strain and return to zero, strain rate must first be positive and then negative; to reach a negative strain and then return to zero, strain rate must first be negative and then positive). While information can be gleaned from other strain and strain rate curve descriptors (e.g., time-to-peak strain, and the

standard deviation among segmental time-to-peak strain, has shown some utility in characterizing arrhythmia [15]), it is common to report only the peak values. This is due in part to the fact that peak values are relatively straightforward to interpret, peak strain, peak systolic strain rate, and peak diastolic strain rate corresponding to maximum contraction, maximum rate of contraction, and maximum rate of relaxation, respectively. Additionally, reporting peak segmental circumferential, radial, and longitudinal strain and systolic and diastolic strain rate quickly becomes burdensome to report and interpret. Reporting strain and strain rate curves in full would exacerbate this problem without providing clear benefit.

Rather than converting to a cylindrical coordinate system, it is possible to rotate the strain tensor matrix E such that all shear strains are equal to zero, in which case the normal strains are known as "principal strains". The magnitudes and directions of these principal strains are the eigenvalue, eigenvector pairs resulting from the eigendecomposition of the tensor $E = V_E \Lambda_E V_E^{-1}$, where V_E and Λ_E are the matrix of columnwise eigenvectors and the diagonal matrix of eigenvalues, respectively.

In the healthy LV, the first principal strain is positive, and oriented approximately in the radial direction, while the two remaining principal strains are negative, and oriented in the longitudinal and circumferential directions [16].

1.4.4 Rotation, Twist, and Torsion

Due to the orientation of myocardial fibres, the LV contracts in a wringing motion around the longitudinal axis of the heart, rather than contracting exclusively along the three axes of the cylindrical coordinate system (Section 1.2). Although this motion may be described in terms of shear strains, other more convenient metrics are more often used. To this end, myocardial rotation, twist, and torsion are introduced.

Rotation ρ is defined for a particular point as the angle in the circumferential-radial plane traversed around the longitudinal axis with reference to an initial position at t_0. Here, anticlockwise rotation when viewed along the longitudinal axis from apex to base is defined as positive. Twist τ is defined as the difference in rotation between the cardiac apex and cardiac base,

$$\tau = \rho_A - \rho_B. \tag{1.13}$$

Torsion $\hat{\tau}$ has been defined variously in the literature as the circumferential-longitudinal skew component $\varepsilon_{c,l}$ of the strain tensor E, as a synonym to twist, and as twist normalised to the distance $L_{A,B}$ between base and apex in the longitudinal direction. In this work, the last definition of torsion is used,

$$\hat{\tau} = \frac{\tau}{L_{A,B}} = \frac{\rho_A - \rho_B}{L_{A,B}}. \tag{1.14}$$

Due to the greater mass of and torque exerted by the epicardial fibres, the gross systolic rotation of the myocardium is negative (clockwise) at the base and positive (anticlockwise) at the apex (when viewed along the longitudinal axis from apex to base). Twist and torsion are consequently positive.

1.4.5 SQUEEZ

Stretch QUantifier for Endocardial Engraved Zones (SQUEEZ), represented in this work as $Q(t)$, has been proposed more recently [17] as the square root of the ratio between the area $A(t)$ of an element at time t and $A(t_0)$ at a reference time t_0,

$$Q(t) = \sqrt{\frac{A(t)}{A(t_0)}}. \tag{1.15}$$

This is a unitless and directionless quantity which is useful for quantifying contraction on a 2-D manifold. In cardiac computed tomography (CCT), extraction of the endocardial surface (as a 2-D manifold) is relatively straightforward due to high contrast between the bloodpool and myocardium. For this reason, SQUEEZ has been useful in quantifying endocardial contraction in the circumferential-longitudinal plane from CCT [17, 18].

1.5 Image Acquisition

The gold-standard for quantification of cardiac dimensions [19, 20] and function [10, 11, 21] has long been sonomicrometry, in which piezoelectric crystals are sutured to the epicardium and endocardium, or implanted into the myocardial wall, and their relative distance measured in a method analogous to sonar. While this technique was successfully exploited in early biomechanical studies of the canine heart, the invasiveness of the procedure precludes its practical or ethical use in humans. Imaging techniques using CMR, echocardiography, and CCT have since been developed. Both CMR [22] and echocardiographic [23] techniques have been directly validated against sonomicrometry.

1.5.1 Cardiac Magnetic Resonance (CMR)

CMR images obtained with variants of the balanced Steady State Free Precession (SSFP) pulse sequence [24] are widely used in clinical practice due to their high signal-to-noise ratio, as well as T_2^*/T_1 weighted image contrast, which produces high blood-tissue contrast [25]. Although SSFP images provide strong edge features between the myocardium and the blood pool, the homogeneity of the myocardium itself results in a lack of trackable midwall features. In order to counteract this limitation, a wide variety of bespoke pulse sequences have been developed with the goal of either introducing trackable features, or providing contrast which is mathematically related to myocardial motion.

1.5.1.1 Tissue Tagging: SPAMM, CSPAMM, and MICSR

The SPAtial Modulation of Magnetisation (SPAMM) prepulse sequence causes a spatially periodic modulation in tissue signal within the plane of the image [26]. Visually, this results in “stripes” or “tags” in the image plane, which deform along with the underlying tissue deformation (Fig. 1.4). In its simplest form (termed “1-1 SPAMM”), the sequence consists of two radiofrequency (RF) pulses of equal flip angle, separated by a single gradient pulse perpendicular to the desired tag line direction. The first RF pulse tips the magnetisation into the transverse plane, such

that all tissue has the same phase throughout the image. Following application of the gradient pulse, the phase increases linearly across the image; at this point, the longitudinal magnetisation remains uniform. Finally, the second RF pulse tips the magnetisation again into the transverse plane, resulting in sinusoidal variation in the longitudinal magnetisation across the image. If two such image sequences are acquired with orthogonal tag lines (or, alternatively, if two sets of orthogonal tag lines are superimposed in a single image sequence, [27]), then 2-D in-plane motion may be characterised by tracking the tag deformation (noting that through-plane motion is not accounted for).

Typically the prepulse is applied at ED and allowed to deform over the cardiac cycle. Longitudinal magnetisation is recovered with the T1 time of the myocardium (approximately 950ms and 1050ms at 1.5T and 3T, respectively; [28]), resulting in significant tag fading by end diastole. Shortly after SPAMM was introduced, an extension (termed Complementary SPAMM, or CSPAMM) was described [29] in which two sets of parallel tag lines are acquired, where the tags of the second are offset by π relative to the first. This may be achieved by inverting any of the four RF pulses (typically the last). By subtracting a shifted SPAMM image $f_{s,\pi}(x,t)$ from its unshifted complement $f_{s,0}(x,t)$, a zero-mean image CSPAMM image $f_c(c,t)$ with doubled peak-to-peak amplitude and substantially reduced tag fading is achieved (emphasising that $f_c(x,t)$, $f_{s,0}(x,t)$, and $f_{s,\pi}(x,t)$ are complex),

$$f_c(x,t) = f_{s,\pi}(x,t) - f_{s,0}(x,t). \tag{1.16}$$

A further improvement to Equation 1.16 has since been proposed [30], termed the Magnitude Image CSPAMM Reconstruction (MICSR). An MICSR image $f_m(x,t)$ provides enhanced tag persistence and optimum tag contrast during late systole, requires only the magnitudes of $f_{s,0}$ and $f_{s,\pi}$ (which are more readily available, as commercial SPAMM protocols do not typically save the phase component by default), and results in a sinusoidal tag pattern even when the flip angle exceeds $\pi/4$,

$$f_m(x,t) = |f_{s,\pi}(x,t)|^2 - |f_{s,0}(x,t)|^2. \tag{1.17}$$

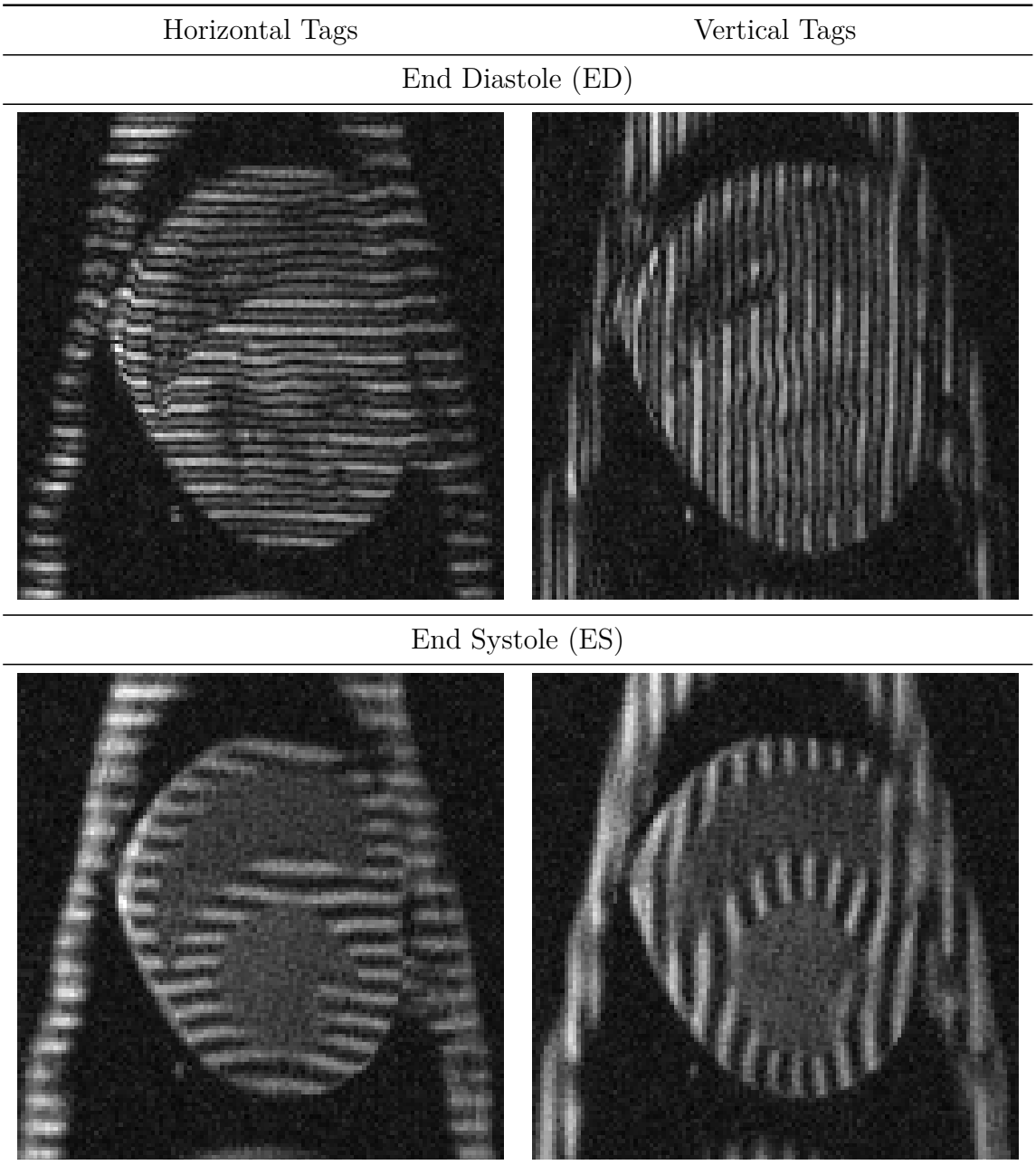


Figure 1.4: Spatial Modulation of Magnetization (SPAMM). Horizontal and vertical tags (left, right) are shown at ED and ES (top, bottom). Note that the ES images appear to be modulated by a simple sinusoid, whereas in the ES images, the magnetization appears to bounce upwards in what one might expect to be the trough. This occurs when the SPAMM flip angle exceeds $\pi/4$, causing the magnetization to flip past the transferse plane. High flip angles are generally preferred in order to counteract tag fading, but cause unwanted harmonics in the Fourier domain if the transform is performed on the magnitude image alone.

The resulting image is of zero-mean and has a sinusoidal profile. The authors additionally describe a so-called "trinary image" visualisation $f_t(x,t)$, which makes use of a modified sgn operator, sĝn,

$$\hat{\text{sgn}}\left(f_m(x,t)\right) = \begin{cases} +1: & f_m(x,t) \geq \alpha \\ f_m(x,t)/\alpha: & |f_m(x,t)| < \alpha \\ -1: & f_m(x,t) \leq \alpha \end{cases}, \tag{1.18}$$

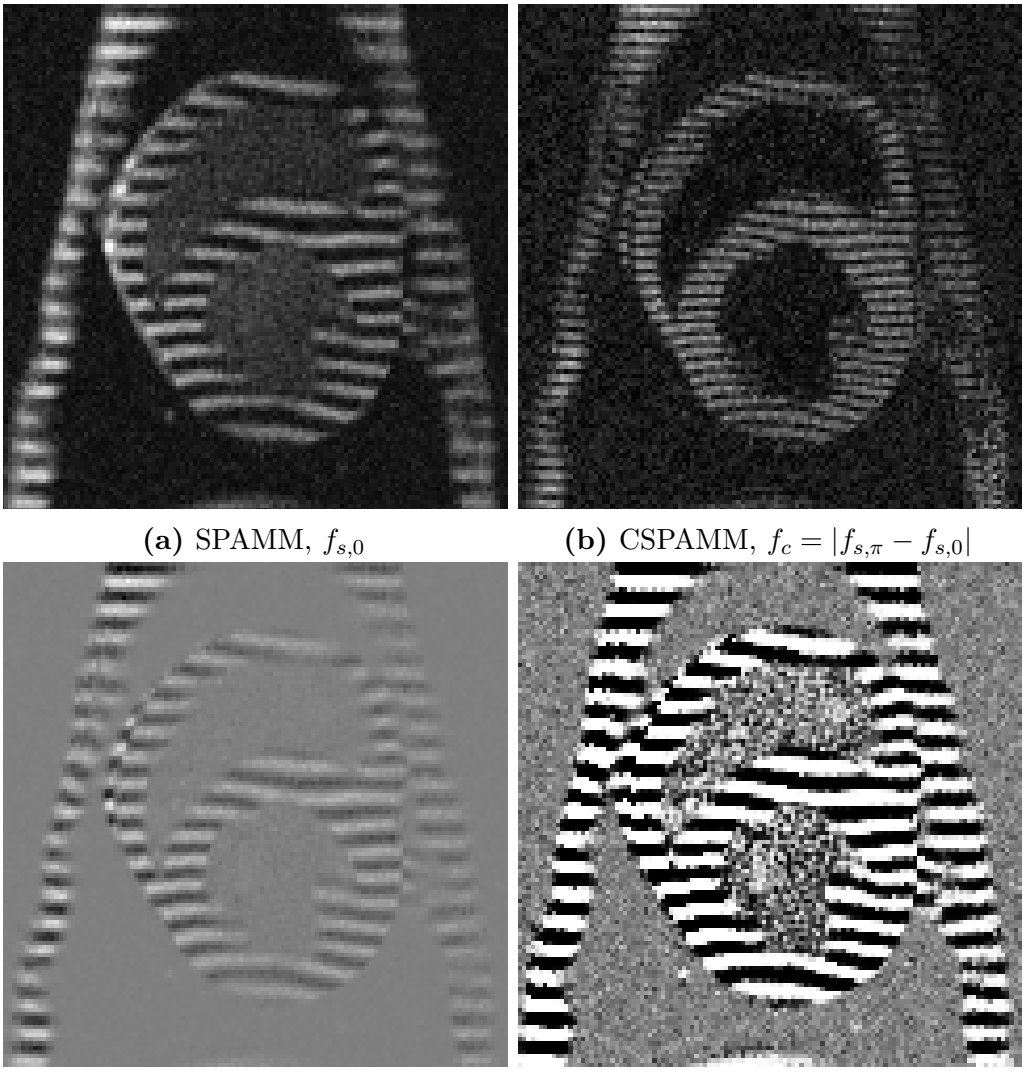
where $0 < \alpha \ll 1$. The constant α is chosen empirically to be small enough to yield crisp tags, but large enough to envelop the background noise. Though not stated in the original paper, it is worth noting that a similar effect may be achieved more succinctly using the hyperbolic tangent, $f_t(x,y) = \tanh\left(k f_m(x,y)\right)$, where $k \gg 1$, with the additional benefit over sĝn of being differentiable everywhere.

Importantly, the methods described above can all be extended to volumetric image acquisition at the expense of increased scan time [31], though this requires clinically impractical breath holds. Representative SPAMM, CSPAMM, MICSR, and trinary images are shown in Figs. 1.4 and 1.5.

1.5.1.2 Harmonic Phase (HARP) Imaging

While the methods described above provide visually striking features which reflect myocardial deformation, it was not obvious how to automatically transform these features into metrics of contraction before the introduction of HARmonic Phase (HARP) analysis of tagged CMR [32–34]. 1-1 SPAMM tagging produces a pair of harmonic peaks in frequency space, obtained with a 2-D fast Fourier transform (FFT). Isolating one of these two peaks (or a single principal harmonic in a composite SPAMM pattern) using an elliptical mask blurred with a Gaussian kernel and performing an inverse 2-D FFT results is a complex image, $f_h(x,t)$, the argument $\arg(f_h(x,t))$ of which is known as a HARP image (Fig. 1.6). Here, $\arg(\cdot) = \text{atan2}(\Re(\cdot), \Im(\cdot))$ and $\Re$ and $\Im$ are operators which extract the real and imaginary components, respectively.

Harmonic phase is a "material property" of the myocardium [33], and remains constant with deformation for a given tissue point, allowing for the recovery of



(a) SPAMM, $f_{s,0}$ **(b)** CSPAMM, $f_c = |f_{s,\pi} - f_{s,0}|$

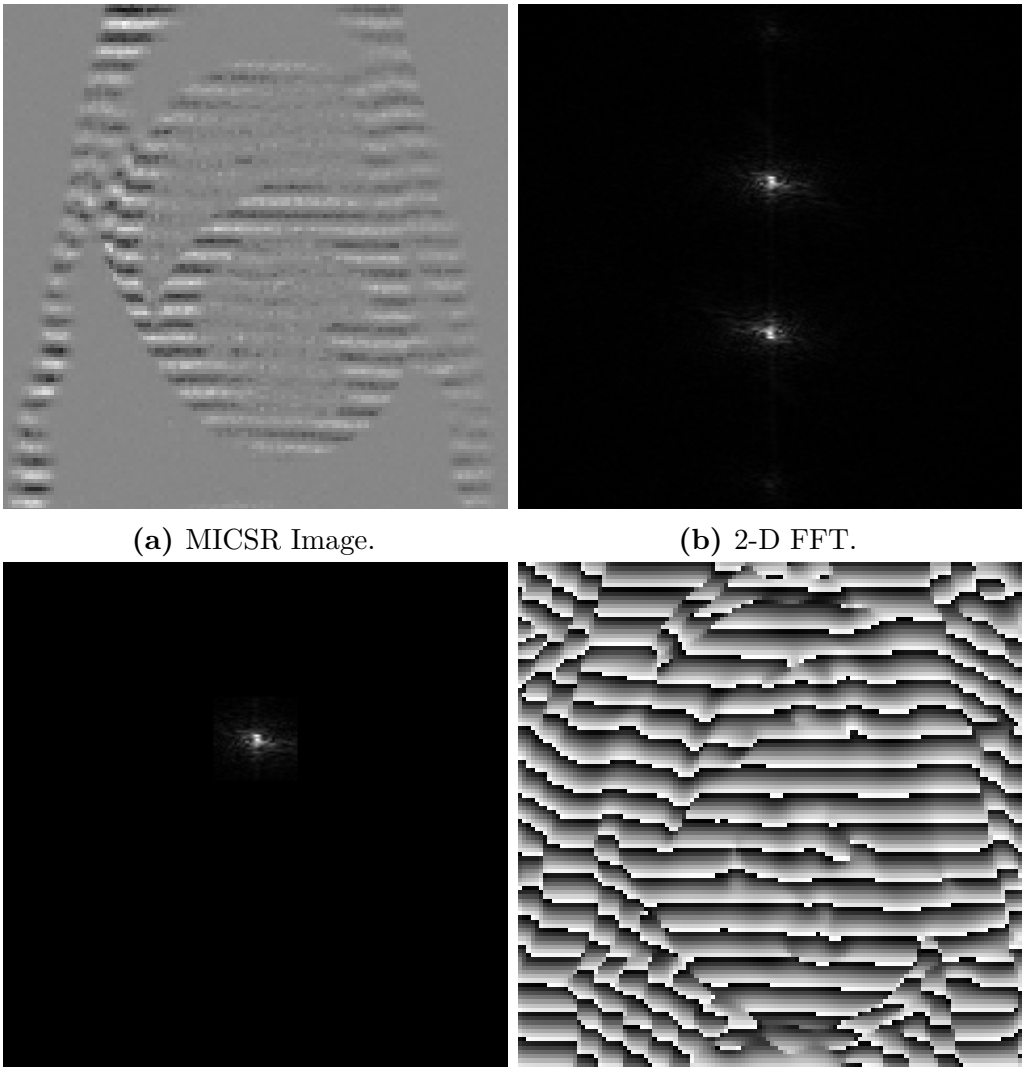
(c) MICSR, $f_m = |f_{s,\pi}|^2 - |f_{s,0}|^2$ **(d)** Trinary, $f_t = \tanh(25 f_m)$

Figure 1.5: SPAMM, CSPAMM, and MICSR. The dependence on x and t has been omitted for clarity.

the Eulerian strain tensor from a single HARP image, and the Lagrangian strain tensor from a pair of HARP images.

For an n-D image, $\mathbf{y} \in \mathbb{N}^n$ is the vector of pixel indices, $\mathbf{x}_0 \in \mathbb{R}^n$ is the image origin, $H \in \mathbb{R}^{n \times n}$ is the (orthogonal) direction matrix of the image, and $W \in \mathbb{R}^{n \times n}$ is the tag direction matrix. The physical coordinates $\mathbf{x}(y)$ for a particular pixel index are given by

$$\mathbf{x}(y) = H\mathbf{y} + \mathbf{x}_0. \tag{1.19}$$



(a) MICSR Image. **(b)** 2-D FFT.

(c) Isolated Harmonic. **(d)** HARP Image.

Figure 1.6: Harmonic Phase Imaging (HARP). Calculation of a HARP image from an MICSR image in a canine heart. Note that the MICSR image $f_m(x,t)$ is preferable over its trinary image $f_t(x,t)$ for HARP analysis, as the the former affords greater isolation of the principal harmonic.

The HARP image $\hat{\phi}(\mathbf{x},t) = \arg(f_h(\mathbf{x},t))$ is the principal value of an ideal, unwrapped phase image $\phi(\mathbf{x},t)$,

$$\hat{\phi}(\mathbf{x},t) = \mathcal{W}(\phi(\mathbf{x},t)), \tag{1.20}$$

where $\mathcal{W}$ is the wrapping operator,

$$\mathcal{W}(\cdot) = \mathrm{mod}(\cdot + \pi, 2\pi) - \pi. \tag{1.21}$$

In the Eulerian formulation [34], a particular strain component ϵ in the direction of the unit vector $\mathbf{e}$ is given by

$$\epsilon(\mathbf{y}, t, \mathbf{e}) = \left\| \left[\nabla_y \phi(\mathbf{x}, t) \right]^{-1} W^\top H \mathbf{e} \right\| - 1, \tag{1.22}$$

where

$$\nabla_y \phi = \begin{cases} \nabla_y \hat{\phi}, & \left\| \nabla_y \hat{\phi} \right\| \leq \left\| \nabla_y \mathcal{W}(\hat{\phi} + \pi) \right\| \\ \nabla_y \mathcal{W}(\hat{\phi} + \pi) & \text{otherwise.} \end{cases} \tag{1.23}$$

Note that dependence of ϕ and $\hat{\phi}$ on $\mathbf{x}$ and t has been omitted for clarity.

In the Lagrangian formulation [33], on the other hand, correspondences are established between material points in successive frames based on the assumption that the harmonic phase of a material point remains constant between frames. This is a substantially more difficult problem than in the Eulerian case, which [33] addresses using Newton-Raphson iteration.

Exploiting the fact that only the principal harmonic is necessary to reconstruct a HARP image, the Fast-HARP pulse sequence was developed which shifts the acquisition window and acquires a small, 32×32 matrix in k-space [35]. The resulting matrix is padded to restore symmetry in k-space before being transformed into the spatial domain. Although the resulting pulse sequence is substantially faster than traditional SPAMM tagging, it has not been implemented commercially and is not used clinically to the author's knowledge.

1.5.1.3 Strain ENCoded (SENC) Imaging

While HARP analysis of SPAMM images allows the measurement of *in-plane* strain components, strain encoded (SENC) imaging allows measurement of *through-plane* strain components [36]. In HARP and related techniques, 1-1 SPAMM images are acquired such that the tag surfaces (planes of constant magnetisation) are *perpendicular* to the plane of the image. In SENC imaging, by contrast, two 1-1

SPAMM images with varying phase shifts are acquired such that the tag surfaces are *parallel* to the image plane. The tag period is chosen to be several times smaller than the slice thickness, such that multiple tag periods contribute to a single pixel. The initial tag frequency vector $\mathbf{w}$ is defined such that the magnitude can be calculated directly from the gyromagnetic ratio γ and the tagging gradient $G(t)$,

$$|w| = \gamma \int G(t)dt, \tag{1.24}$$

and the orientation is perpendicular to the image plane (which is initially aligned with the tagging plane). Because the magnetisation deforms along with the tissue, the frequency and orientation of the tag frequency vector $\mathbf{w}$ clearly reflect myocardial contraction. Moreover, the initial and final states of this vector are all that is needed in order to calculate Eulerian strain. $\mathbf{w}$ is decomposed into through-plane and in-plane components ($\mathbf{w}_\perp$ and $\mathbf{w}_\parallel$),

$$\mathbf{w} = \mathbf{w}_\perp + \mathbf{w}_\parallel. \tag{1.25}$$

It can be further shown that Eulerian strain perpendicular to the plane of the image is given by

$$\epsilon(t) = \frac{\|w(t_0)\|}{\sqrt{\|w_\perp(t)\|^2 + \left\|w_\parallel(t)\right\|^2}} - 1. \tag{1.26}$$

In [36], two central insights make it possible to estimate the necessary components. First, as the vector $\mathbf{w}$ tilts, a spatial phase gradient is introduced in the image plane, which is mathematically related to the in-plane component $\mathbf{w}_\perp$. Second, by choosing a tag period much smaller than the slice thickness, the brightness of a particular voxel is equal to the integral of a cosine, which may be rewritten as the Fourier transform of the slice profile evaluated at a particular frequency. This frequency is selected by applying a second through-plane gradient during the refocusing lobe of the acquisition. By selecting this frequency to be near to the position of the spectral peak corresponding to the strain-modulated tag frequency, the image contrast is dominated by that spectral peak. The spectral shift $\mathbf{w}_\parallel$

may then be estimated by acquiring multiple images varying a second through-plane gradient. Having measured these components, it is possible to reconstruct an image whose contrast is proportional to the underlying strain in the direction perpendicular to the plane of the tag lines.

Selective excitation, limited field of view, interleaved acquisition, and spiral acquisition were later used to decrease the acquisition time in a sequence called Fast-SENC [37].

1.5.1.4 Displacement and Velocity Encoding

Thus far the focus has been on modulating myocardial magnetisation at a reference point (typically ED) and recovering strain as a function of deviation from that reference. However, it is also possible to construct so-called "phase contrast" techniques, in which either tissue velocity or tissue displacement are encoded into the phase (i.e., the measured phase is directly proportional to one of these two quantities). Note that the information encoded in phase contrast velocity and displacement encoding can theoretically be recovered from one another via integration (to an additive constant) and differentiation, respectively.

In phase contrast velocity imaging, which has been described both for 2-D [38] and for 3-D [39] sequences, a velocity sensitising gradient is applied in the readout direction i, which brings about a phase shift ϕ_i. Assuming approximately constant tissue velocity, ϕ_i is proportional to the component of the velocity in the readout direction, $\phi_i = v_i k_i$, where k_i is a function of the readout gradient $G(t)$ and the echo time TE,

$$k_i = \int_0^{TE} 2\pi G(t) t dt. \tag{1.27}$$

A velocity field is constructed by composing two acquisitions with perpendicular, in-plane gradients. The Eulerian strain rate tensor may then be recovered from the acquired velocity field using Equations 1.10 and 1.11.

The goal of Displacement ENcoding with Stimulated Echoes (DENSE) [40] is conceptually similar to phase contrast velocity imaging, except that tissue *displacements* are encoded rather than velocity, with the ultimate goal of recovering the *strain* tensor rather than the *strain rate* tensor. Initially, the magnetisation is position-encoded using 1-1 SPAMM. The phase is then allowed to disperse according to displacement, the magnetisation is tipped into the transverse plane with a third radiofrequency pulse, and the phase dispersion due to the SPAMM gradient is rewound with a second gradient lobe. In the resulting image, the final phase shift is proportional to the displacement of the tissue in the direction of the gradient, such that the displacement may be recovered using the so-called displacement sensitivity constant (which may be calculated from the magnitude of the gradient lobe). This procedure must be repeated for each displacement component (which need not lie in the image plane). The component displacements are then composed into the displacement field $\mathbf{u}(t)$, from which Lagrangian and Eulerian strain may be calculated as in Equations 1.5, 1.7, and 1.8. Limitations in temporal resolution, signal-to-noise, and low displacement sensitivity have also been addressed [41].

1.5.1.5 Feature Tracking CMR

Unfortunately, the techniques for quantifying regional function from CMR are subject to a number of limitations which have hindered clinical adoption. First, each requires highly specialised image acquisition and analysis procedures, which are difficult to implement robustly in the clinical workflow. Second, with conventional tagged CMR, only mid-myocardial LV strain is assessed; strain is not accurately measured at endo- and epicardial borders of the LV or RV. In order to counteract these limitations, efforts have recently focused on feature tracking CMR, which, by contrast to conventional tagging, is applied to routinely acquired balanced SSFP images, may be ideal for calculating strain at the cardiac borders, and is not necessarily limited to the LV. At least four commercial implementations exist, all of which require manual contouring of at least one cardiac frame (typically

end diastole and systole), followed by automatic propagation of these contours throughout the cardiac cycle.

In the Multimodality Tissue Tracking (MTT) algorithm (Toshiba Medical Systems Corporation, Tokyo, Japan) [42], endocardial and epicardial contours for the cardiac chamber of interest are drawn manually in a semiautomated fashion. Each point along the ED contour is used to define a 10×10 mm neighbourhood, which is matched to a neighbourhood of the subsequent frame within a search window by minimising the sum of squared differences between the pixel intensities.

In the TomTec Diogenes Software (Tomtec Imaging Systems, Munich, Germany) [43], an arbitrary frame is first contoured. A fixed number of points along the contour are sampled, and a line orthogonal to the contour is constructed passing through each point. Cross correlation is used to determine the motion of the wall perpendicular to the contour in each frame. Following border tracking, optical flow is used to capture more general 2-D motion. These steps are repeated at increasingly fine resolutions.

Medis (Leiden, the Netherlands) and Circle CVI (Calgary, Alberta, Canada) have also recently released feature tracking implementations, but to the author's knowledge the details of these algorithms have not been published in the literature.

RV longitudinal strain measured by MTT, TomTec, Medis, and Circle CVI was recently compared in a population of subjects with arrhythmogenic right ventricular cardiomyopathy (ARVC) [44].[1] All four software packages showed reduced global and regional strain in overt ARVC compared with healthy control subjects. Additionally, Medis showed reduced regional RV longitudinal strain in preclinical ARVC compared with healthy control subjects. Unfortunately, the authors also noted sporadic failure of RV wall tracking, as well as poor correlation of absolute strain values between software packages. Overall, this suggests that SSFP feature tracking may have a roll in the quantitative evaluation of both advanced and early RV dysfunction, though improvements in automation and reproducibility are necessary.

[1] This work was done in collaboration with the author, and includes MTT strain analysis presented in Chapter §2.

1.5.2 Echocardiography

There is substantially less flexibility in echocardiographic acquisitions compared with CMR, where bespoke pulse sequences may be designed specifically for the purpose of quantifying cardiac function. However, the high spatial and temporal resolution of echocardiography, combined with the dense, trackable, intramyocardial features inherent to the technique have nonetheless yielded promising techniques.

1.5.2.1 Speckle Tracking

The contrast and texture of echocardiography images are dominated by an imaging artefact known as "speckle". It is important to note that speckle is not noise in the sense of being random, as speckle patterns are a repeatable function of the transducer (configured with a constant set of parameters), the anatomical structure being imaged, and the geometric relationship between the two [45]. While speckle can be detrimental in some image processing applications, it provides useful, trackable features which have been successfully exploited in strain imaging. Speckle tracking techniques are broadly categorised into block-matching, optical flow, and elastic image registration algorithms.

In block-matching algorithms, displacements may be estimated by centring a window on a material point of interest, sliding that window over a neighbourhood surrounding that pixel, finding the position which minimises (or maximises) an evaluation metric, such as sum of squared differences, sum of absolute differences, and normalised cross correlation. The most conceptually simple application is to track the spatial B-mode intensity image (B-Mode block-matching). However, the same algorithm may be applied equally well to the radiofrequency data itself (radiofrequency block-matching) [46].

A naive implementation of this technique is computationally intensive, especially for large windows and 3-D images, as it involves a large number of redundant computations. However, by precomputing the integral image [47], it is possible to express the sum over a window as a constant-time operation (four lookups for a 2-D image, eight for a 3-D image, 2^n lookups for an n-D image). This highly

efficient block matching implementation has been successfully applied to both 2-D and 3-D ultrasound images [48].

It is also possible to successfully apply many of the optical flow algorithms developed in the computer vision literature to echocardiography [49]. A significant benefit of this approach is that, whereas in block matching algorithms deformation field smoothness must typically be applied as a postprocessing step, in optical flow it is possible to build a smoothness regularizer directly into the motion model itself [46].

Like optical flow, elastic image registration is a very flexible class of registration algorithms. Importantly, these techniques generally allow smoothness and tissue incompressibility penalties to be added to the global cost function, which allows principled physical modelling of the data.

1.5.2.2 Tissue Doppler Imaging (TDI)

The Doppler effect is a phenomenon whereby a sound with frequency f_0 and travelling through a medium with speed c appears to have a shifted frequency f at a receiver, where the frequency shift is related to the relative velocity of the source v_s and receiver v_r,

$$f = \left(1 + \frac{v_r - v_s}{c}\right) f_0. \tag{1.28}$$

This phenomenon may be used to measure an object's velocity. In the context of echocardiography, it was first used to measure blood flow velocity (Doppler Ultrasound). Due to the low velocity of myocardium relative to blood flow, the Doppler shift generated by myocardial motion is much lower and is intentionally filtered out in this application. However, it was later found that the low Doppler shifts produced by the myocardium may be analysed to recover myocardial motion (Tissue Doppler echocardiography, also known as Tissue Doppler Imaging or TDI and Tissue Velocity Imaging, [50]). Because this technique measures velocity at material points, the velocity field can be used either to directly calculate the Lagrangian strain rate tensor, or integrated to obtain a material displacement field which can be used to calculate the Lagrangian strain tensor [15].

1.5.3 Cardiac Computed Tomography (CCT)

Recent technological advances in CCT image acquisition have brought about a precipitous decrease in radiation dose, such that high spatial-resolution, volumetric, functional images of the heart can now be acquired in as little as a single cardiac cycle [7]. This has resulted in a surge of interest in quantifying regional function from CCT.

1.5.3.1 Feature Tracking CCT

The most straightforward attempts have been in the direct application of feature tracking methods developed in the context of echocardiography to 2-D cine series resliced from 3-D+Time CCT studies. The multimodality tissue tracking (MTT) algorithm [42], for example, uses a block matching approach to track the endocardial and epicardial borders. This technique has shown impairment in myocardial function in both animal [51] and human [52] studies. Unfortunately, due to the sparsity of myocardial features in CCT images, tracking relies heavily on the endocardial and epicardial borders and is plagued by the "aperture problem". The aperture problem refers to the inability to infer motion parallel to an edge, leading to ambiguity in motion quantification. Perhaps as a result, correlation with disease has been largely limited to radial strain. Moreover, this technique discards much of the rich volumetric information present in CCT images.

1.5.3.2 Deformable Image Registration

Attempts have also been made to quantify function using deformable image registration. In one implementation, a finite element model of the LV was constructed at the ED frame and then deformed throughout the cardiac cycle using displacement fields obtained from deformable image registration [53]. This approach has the benefit of making full use of the volumetric CCT data. Historically, deformable, volumetric registration has been very computationally intensive, adding to already long image reconstruction times for CCT. More recently, efficient methods making use of discrete optimisation have been proposed, which may alleviate these concerns [54].

1.5.3.3 Coherent Point Drift (CPD)

An alternative metric and approach has been proposed in [17], who employed the coherent point drift (CPD) method [55] to register a bespoke template mesh representing the LV endocardium at ED to each subsequent frame. In CPD, the "moving" point set is represented as a Gaussian Mixture Model (GMM). Using Expectation Maximisation (EM), the GMM is deformed so as to maximise the probability of the "fixed" point set having been sampled from it. "Coherent" motion is enforced by constraining the motion of the GMM centroids relative to one another. CPD can be used for non-rigid registration, and does not prescribe any specific transformation model. Having performed the registration, [17] calculated for each face the square root of the ratio between the face's area and the area of the corresponding face at ED. This metric, which they termed Stretch QUantifier for Endocardial Engraved Zones (SQUEEZ, §1.4.5), is closely related to area strain and may be interpreted as a surrogate for cardiac contraction (< 1) or expansion (> 1). SQUEEZ is well suited to volumetric CCT data due to its ability to capture the endocardial trabeculation which SQUEEZ relies upon. SQUEEZ by CPD is was subsequently shown to correlate with strain obtained by tagged CMR [18]. The authors in [17] utilise "shape index" (SI), a scale-independent shape measure [56], which they hypothesise will remain constant throughout the cardiac cycle for a given material point:

$$SI = \frac{2}{\pi}\text{atan}\frac{k_1 + k_2}{k_1 - k_2} : k_1 \geq k_2. \tag{1.29}$$

Here, k_1 and k_2 are the principal curvatures at a point of interest. In order to encourage each point in the ED mesh to warp into the same anatomical position in the remaining frames, a penalty for warping a point in the template mesh into a point with dissimilar SI in the target mesh was incorporated into the CPD registration. Notably, penalising SI discrepancies may be interpreted as a means of *implicitly* sharing information between frames.

1.5.4 Comparison

The noninvasive quantification of regional cardiac function from medical images is an important clinical problem which has inspired four decades of concerted effort from the research community. Each technique has its own strengths and drawbacks, which must be accounted for in assessing readiness for clinical adoption, as well as areas of interest for future research.

In general, hardware availability is not a significant limitation, as CMR, 2-D and 3-D echocardiography, and CCT have been widely deployed in the clinic. In terms of specific CMR protocols, however, only SSFP and SPAMM pulse sequences have been implemented by all major manufacturers. Assuming that the appropriate hardware and protocol are available, typical contraindications and considerations for these modalities must be adhered to as always. Due to radiation exposure, CCT is absolutely contraindicated in pregnancy, and should be avoided in children and in cases where repeated scanning is required. Allergies to contrast agents must also be considered. Severe claustrophobia may preclude the use of either CMR or CCT, and mechanical noise can also limit the use of CMR in children. CMR has traditionally been contraindicated in patients with implantable defibrillators, though experience suggests that scanning can be done safely in some circumstances [57]. Barring gross chest wall abnormalities and patient compliance, there are no contraindications for transthoracic echocardiography (TTE); transesophageal echocardiography (TEE) is an uncomfortable and invasive procedure, but has few contraindications outside of esophageal disease.

The complexity and duration of each procedure is also worth considering. TTE may be performed at the bedside, requires no contrast, and can generally be performed in roughly 30min, though image quality is operator-dependent and hampered by limited acoustic window. A whole-heart 3-D+Time functional study may be obtained in as little as a single heart beat, though a timed contrast bolus is required, and image reconstruction can be time-consuming. CMR acquisitions are generally the most time-consuming. As an example, SSFP and grid-tagged SPAMM

acquisitions typically require one 15s breath-hold for each of 12 SA and 3 LA slices, and line-tagged and CSPAMM acquisitions require duplicate scans.[2]

At a fundamental level, the ability to reliably measure and localize cardiac functional parameters is limited by the spatial and temporal resolution of the data. In terms of spatial resolution, CMR performs least well, with typical in-plane image resolutions of between 1 and 2mm, compared with submillimeter resolutions in both echocardiography and CCT. Temporal resolution is highest in echocardiography ($10 - 25$ms), lowest in CCT ($83 - 175$ms), and intermediate in CMR ($25 - 50$ms), though improvements in the temporal resolution of CCT are expected as gantry rotation times fall [7].

While all techniques discussed are applicable to the LV, extension to other cardiac chambers is variable. Though some limited success has been had in assessing the RV using tissue tagging [58], SENC [37], and DENSE [59], these techniques are best suited to the LV midwall and are not applicable to the atria. Early work in SSFP feature tracking has shown promise in the RV [60–62] and both atria [63, 64], though further validation is required. Of the techniques discussed, speckle tracking echocardiography has been applied most successfully outside the LV (RV: [65–67]; LA: [68–70]; RA: [71–73]). To the author's knowledge, regional functional analysis of CCT images has not been described outside the LV, though there is no reason to believe that this is a fundamental limitation given imaging is appropriately timed with the contrast bolus. It is also worth noting that, while SSFP CMR and CCT images have strong endocardial and epicardial edge and surface features, respectively, features *within* the LV myocardium are largely absent, precluding direct LV midwall analysis.

Clinical adoption is also limited by the commercial availability of analysis software. Echocardiography has taken the lead in this regard, with software for speckle-tracking and TDI being provided on commercial scanners. Commercial software is also available for HARP analysis of tagged CMR images, and for feature

[2]Note that scan time is not necessarily additive (i.e., two line-tag acquisitions do not necessarily require twice the scan time of a single grid-tag acquisition), as scan lines in the phase-encoding direction can be reduced in the former without discarding information orthogonal to the tag lines.

tracking analysis of SSFP CMR images. The author is unaware of commercial software available for the specific purpose of functional CCT analysis.

1.6 Conclusions

In this thesis, feature tracking algorithms are developed for 2-D+Time cardiac magnetic resonance (CMR) and 3-D+Time cardiac computed tomography (CCT) image sequences that are easily acquired clinically, while emphasising reproducibility and automation in their design. In §2, a commercially-implemented CMR feature tracking algorithm for the analysis of steady state free precession (SSFP) cine series is evaluated in patients with hypertrophic cardiomyopathy (HCM) and arrhythmogenic right ventricular cardiomyopathy (ARVC), which primarily affect the left ventricle (LV) and right ventricle (RV), respectively. In §3, the limitations of this implementation are then used to guide development of an automated algorithm for the same purpose, making use of fully convolutional neural networks (CNN) for segmentation and spline registration across all frame simultaneously for tracking. Finally, as myocardial contraction is inherently a 3-D phenomenon, a technique is developed in §4 for quantification of regional function from 3-D+Time functional CCT studies using simultaneous registration of automatically generated subdivision surface models for tracking.

1.7 Acknowledgements

The author would like to acknowledge the following collaborator contributions, which are also footnoted in the text. In §2.2, James Jensen replicated strain measurements for the purpose of interobserver reproducibility. In §2.3, Drs. David Bluemke and Stefan Zimmerman performed qualitative readings; Dr. Mariana Selwaness replicated strain measurements for the purpose of interobserver reproducibility; and Dr. Anneline te Riele advised on statistical analysis. In §3, Weidi Xie aided in the design of the neural network segmentation architecture and visualisation experiments. In §4, Dr. Amir Pourmorteza performed the coherent point drift analysis used to

validate the subdivision mesh registration technique. In §5, Dr. Ronald Beyers designed the cine watermarking image reconstruction technique.

2

Clinical Studies in Regional Cardiac Function

Contents

2.1 Motivation 31
2.2 Hypertrophic Cardiomyopathy (HCM) 33
2.2.1 Contributions 33
2.2.2 Background 33
2.2.3 Materials and Methods 35
2.2.4 Results 39
2.2.5 Conclusions 48
2.3 Arrhythmogenic Right Ventricular Cardiomyopathy (ARVC) 50
2.3.1 Contributions 50
2.3.2 Background 51
2.3.3 Materials and Methods 51
2.3.4 Results 56
2.3.5 Conclusions 63
2.4 Conclusions 65

2.1 Motivation

In Chapter §1, currently available methods for quantifying regional function from cardiac magnetic resonance (CMR, §1.5.1), echocardiography (§1.5.2), and cardiac computed tomography (CCT, §1.5.3) were reviewed. In particular, it was noted

that there has recently been increased interest in CMR feature tracking due to its potential application to routinely acquired images, though these methods have not been thoroughly validated or adopted for routine clinical use. Moreover, it was suggested that, as cardiac borders and trabeculation are the primary structures exploited in feature tracking CMR, this technique may have particular utility for measuring cardiac strain at cardiac borders of the left and right ventricles (LV, RV). The purpose of this chapter is to investigate the strengths and weaknesses of a state-of-the-art commercial implementation of feature tracking CMR in measuring LV strain measured at the cardiac borders, and in measuring RV strain measured at the endocardium.

Steady State Free Precession (SSFP) image sequences were available from two well-characterised populations of subjects with the two most common genetic cardiomyopathies: hypertrophic cardiomyopathy (HCM) and arrhythmogenic right ventricular cardiomyopathy (ARVC). While the presentations of both HCM and ARVC are variable, they are regional diseases, primarily affecting the septum of the LV and the subtricuspid region of the RV, respectively. The regional expression of HCM and ARVC and the careful characterisation of patients in the available cohorts make them ideal for investigating feature tracking CMR.

Although the investigations into the two populations were carried out separately, the study designs were broadly similar. Both HCM and ARVC populations contained three subsets of patients in roughly equal proportion: patients with clinical disease confirmed by genetics (referred to as "overt" HCM and ARVC in this work), mutation carriers who fail to meet clinical criteria for disease (referred to as "preclinical" HCM and ARVC in this work), and healthy control subjects. In both studies, feature tracking was performed using the Multimodality Tissue Tracking (MTT) software (Toshiba Medical Systems, Tokyo, Japan), which is described in §1.5.1.5. The remainder of this chapter details the studies carried out in HCM (§2.2) and ARVC (§2.3).

2.2 Hypertrophic Cardiomyopathy (HCM)

2.2.1 Contributions

[1] Davis M. Vigneault, Eunice Yang, C. Linda Chu, Carolyn Y. Ho and David A. Bluemke. 'Left Ventricular Strain Gradient Is Abnormal in Hypertrophic Cardiomyopathy: Assessment by CMR Feature Tracking'. In: *RSNA*. Chicago, IL, 2014.

[2] Davis M. Vigneault, Eunice Yang, Patrick J. Jensen, Michael W. Tee, Hoshang Farhad, Linda Chu, J. Alison Noble, Sharlene M. Day, Steven D. Colan, Mark W. Russell, Jeffrey Towbin, Mark V. Sherrid, Charles E. Canter, Ling Shi, Carolyn Y. Ho and David A. Bluemke. 'Left Ventricular Strain is Abnormal in Preclinical Hypertrophic Cardiomyopathy: Assessment by CMR Feature Tracking'. In: *Radiology [In Preparation]* (2017).

2.2.2 Background

HCM is the most common genetic cardiomyopathy, affecting up to 1 in 500 individuals. The clinical course of HCM is variable: most patients have normal longevity and manageable symptoms, but some may suffer from refractory heart failure or potentially lethal arrhythmias. Though inheritance of known HCM mutations is autosomal dominant, phenotypic expression of overt left ventricular hypertrophy (LVH) is often delayed until adulthood and penetrance may be incomplete. Overt HCM is diagnosed using conventional echocardiographic or CMR imaging by a maximal LV wall thickness > 15 mm in adults and a z-score > 2 in children, in the absence of other etiologies for wall thickening [74], although modified criteria are typically used for at-risk relatives [75]. The current understanding of the progression from preclinical (phenotype negative) to overt (phenotype positive) HCM is incomplete. Prior echocardiographic strain studies suggest functional abnormalities in individuals who carry HCM sarcomere mutations but who do not have overt HCM (defined as preclinical HCM) [76, 77]. However, routine identification of imaging features that detect early expression of HCM remains an open question.

As discussed in §1.2, circumferential strain is known to become more negative (i.e., circumferential shortening becomes greater) from epicardium to endocardium in normal patients [8, 78]. However, this difference is smaller than expected from purely geometric considerations, owing to an ordered transmural gradient in myocardial

fibre angle which tends to increase circumferential shortening at the epicardium and decrease circumferential shortening at the endocardium [8]. Due to the greater mass of and torque exerted by the epicardial fibres relative to the endocardial fibres, cardiac torsion grossly follows the former.

Abnormally high torsion has been observed in patients with overt HCM [79–81] and in preclinical mutation carriers with normal wall thickness [82]. Though a definitive mechanism has not been elucidated, prior studies speculate that abnormally high torsion may be explained by a combination of subendocardial dysfunction (owing to impaired perfusion and myofibril disarray) and decreased subendocardial torque (owing to hypertrophy and a consequently shorter lever arm) [82]. If subendocardial dysfunction is indeed the mechanism for increased torsion in HCM, it is reasonable to suspect that circumferential shortening at the endocardium may also be increased, given that normal subendocardial function tends to decrease circumferential shortening at the endocardium.

With conventional tagged CMR, strain is not accurately measured at endo- and epicardial borders and only mid-myocardial strain is routinely assessed. Thus, transmural abnormalities in myocardial strain have not been previously investigated, in favour of measuring midwall strain. Newer methods using CMR feature tracking may be ideal for calculating strain differences at the endocardial and epicardial borders of the heart (Fig. 2.1). Transmural differences in circumferential strain are diluted by taking the mean of epicardial and endocardial strain (analogous to midwall strain); therefore, circumferential strain differences may not have been apparent on prior studies of midwall strain in HCM.

The purpose of the study was to evaluate myocardial strain and circumferential Transmural Strain Difference (cTSD), a novel functional parameter defined as the difference between epicardial and endocardial circumferential strain (cTSD = $\varepsilon_{cc}^{epi} - \varepsilon_{cc}^{endo}$) as a marker of disease in overt and preclinical HCM in comparison to other markers of disease status. Strain results using CMR feature tracking were also compared to those obtained from CMR tissue tagging.

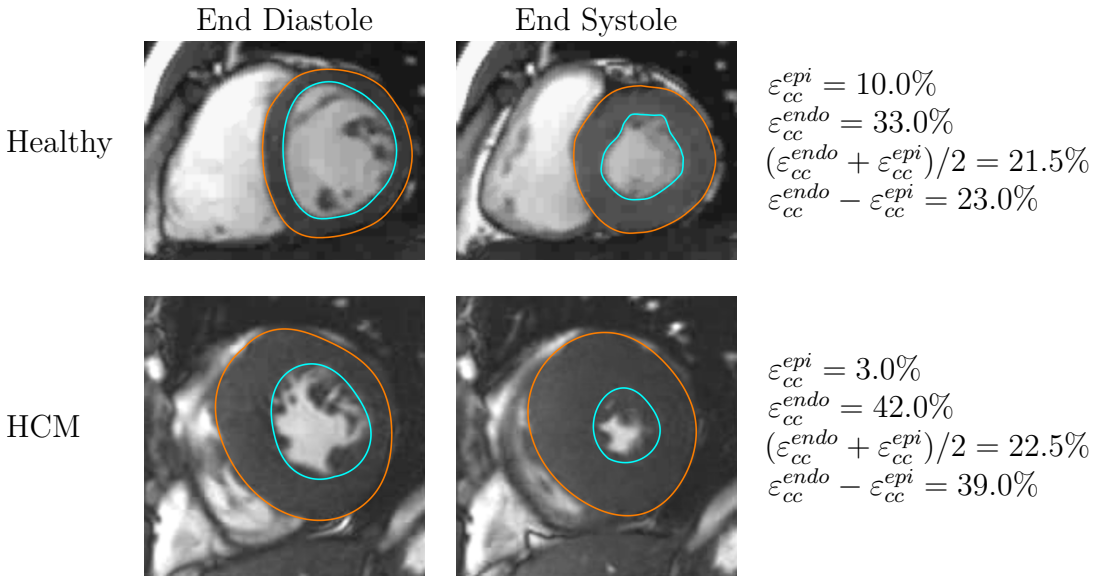


Figure 2.1: cTSD versus Midwall Circumferential Strain. This figure illustrates the concept of cTSD in healthy (top) and hypertrophied (bottom) myocardium. Note that in the hypertrophied myocardium, epicardial shortening is lower and endocardial shortening is higher relative to the healthy scan. This divergence is diluted by taking the mean (analogous to midwall strain) but is enhanced by taking the difference (cTSD). LVH: Left Ventricular Hypertrophy; ε_{cc}^{epi}: Epicardial circumferential strain; ε_{cc}^{endo}: Endocardial circumferential strain.

2.2.3 Materials and Methods

2.2.3.1 Patient Population

The images analysed in this work were acquired as part of the HCMNet study [83], a multicenter, observational, cross-sectional study of patients with a clinical diagnosis of HCM and their family members. Subjects either carried pathogenic or likely pathogenic sarcomere mutations, or were confirmed to be mutation-negative healthy relatives and served in the control population. LVH was defined as maximal wall thickness (MWT) $\geq$ 12 mm for adults or z-score $\geq$ 2 for children based on echocardiographic core laboratory measurement of LV wall thickness. Based on genetic and imaging studies, patients were categorised as either overt HCM [mutation+/LVH+], preclinical HCM [mutation+/LVH–], or genotype negative healthy control subjects [mutation–/LVH–].

2.2.3.2 CMR Acquisition

CMR was performed with a standardised protocol at 10 centres from 9 April, 2009 to 30 January, 2012. Nine centres used 1.5-T magnets, and one centre used a 3-T magnet (Espree or Avanto, Siemens Medical Systems, Erlangen, Germany; Intera, Philips Medical Systems, Best, the Netherlands; Signa, GE Medical Systems, Waukesha, WI). Short axis (SA), horizontal long axis (4C), and vertical long axis (2C) cine series were acquired using an SSFP sequence with representative TR/TE values of 2.2/1.1 msec at 1.5T, flip angle 60 degrees. SA cine images consisted of 10 to 12 slices covering from 1 cm above the mitral valve plane to the apex with 8 mm thickness, 2mm gap between slices. Tagged CMR was obtained using a gradient echo SPAtial Modulation of Magnetisation (SPAMM) sequence with typical parameters TR/TE 34/2.5, flip angle 12 degrees, 10 mm slice thickness, 5 mm gap between slices, tag spacing 7 mm. Preliminary studies demonstrated poor feature tracking in longitudinal views; therefore, longitudinal strain was not investigated despite prior studies in echocardiography showing decreased longitudinal strain in this population [77].

2.2.3.3 Image Analysis

Strain from feature tracking analysis of mid-ventricular SA SSFP cines was performed by the author using MTT (Version 6.1.4826, Toshiba Medical Systems Corporation, Tokyo, Japan) [42]. Endocardial and epicardial LV contours were drawn in a semiautomated fashion, and the ventricle was segmented into six segments according to the American Heart Association (AHA) model by setting the anterior and inferior right ventricular insertion points (Fig. 2.2). Tracking occurred through a block matching algorithm, as described in §1.5.1.5. The most prominent features on CMR images are located on the epicardial and endocardial surface, and there is a known gradient of strain between these layers of myocardium. Therefore, circumferential Transmural Strain Difference (cTSD) between epicardial and endocardial strain (ε_{cc}) was also defined, where more positive cTSD indicates greater transmural dysfunction. LV mass, LV and LA volumes, and functional parameters

were determined with CIM software (The University of Auckland, New Zealand). Mid-ventricular circumferential strain was obtained from tagged CMR images using HARmonic Phase (HARP) analysis (Diagnosoft, v4.61, Durham, NC).

2.2.3.4 Statistical Analysis

Continuous and discrete data are presented as mean ($\pm$ SD) and n (%), respectively. In univariate analysis, means were compared by Student's t-test (paired or unpaired as appropriate) following ANalysis Of VAriance (ANOVA) when more than two groups were being compared. Categorical data were compared using Pearson's χ^2 test. Continuous variables were compared using Pearson's correlation. For single comparisons, $p < 0.05$ was considered significant. For n comparisons, $p < 0.05/n$ was considered significant (Bonferroni correction). Multivariate analysis to predict diagnosis (control vs preclinical and control vs overt HCM separately) was performed using binary logistic regression. In each case, an initial (fully adjusted) model was constructed controlling for demographics (age, sex) and relevant cardiac parameters (cTSD, septal wall thickness, LV mass index, septal E-Wave velocity, and log-transformed brain natriuretic peptide, BNP). A refined (minimally adjusted) model was constructed through stepwise backward selection by successively removing the least significant parameter until all predictors were significantly related to the outcome. Cardiac volumes were indexed to body surface area (BSA). Intra- and inter-observer reproducibility was evaluated visually by Bland-Altman analysis;[1] correlation and bias were assessed by intraclass correlation coefficient (ICC) and Student's t-test, respectively. ICC ≥ 0.75 was considered excellent, < 0.75 and ≥ 0.40 moderate, and < 0.40 poor. All statistical analysis was performed using R (v3.1.0).

[1]The author would like to acknowledge James Jensen for replicating strain measurements for the purpose of assessing interobserver reproducibility.

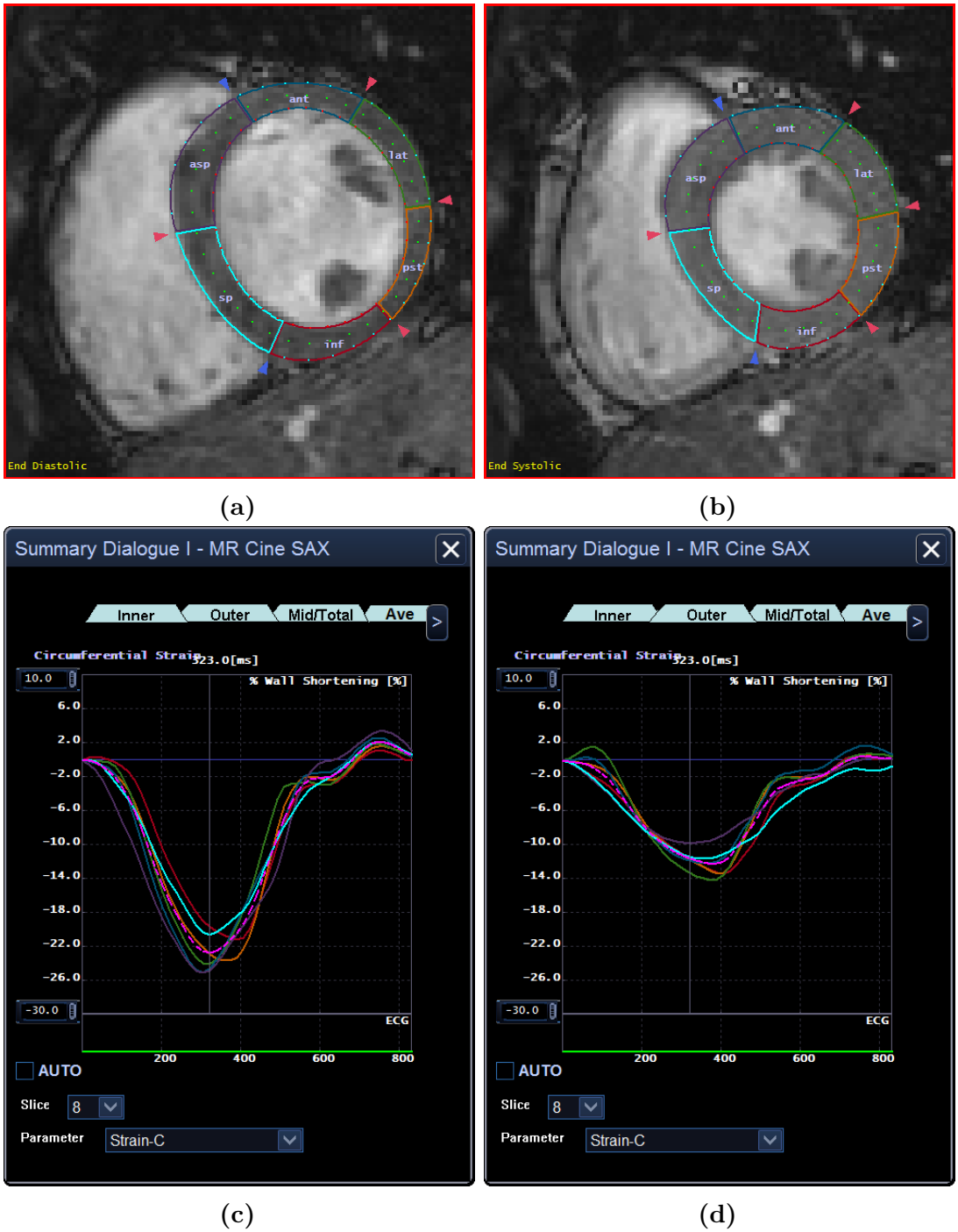


Figure 2.2: Feature Tracking Tracings in HCM. Endocardial and epicardial contours and segmentation at end diastole (a) and end systole (b), with corresponding segmental and global circumferential strain curves at the endocardial (c) and epicardial (d) borders. Images are from a short axis midslice in a 24-year-old Caucasian male with a family history of HCM but a negative genetic screen and no clinical disease. Note that peak endocardial ε_{cc} is substantially more negative than peak epicardial ε_{cc}.

2.2.4 Results

2.2.4.1 Patient Characteristics

The study cohort consisted of 99 subjects: 23 control subjects (23.2%), 34 preclinical HCM patients (34.3%), and 42 overt HCM patients (42.4%). In terms of patient demographics (Table 2.1), the average age was 25.0 ± 11.0 years, 44 (44.4%) were women, and 8 (8.1%) were non-Caucasian. Compared with control subjects, patients with overt HCM were older (21.6 ± 7.1 vs 29.9 ± 13.0 years, $p < 0.01$), and more commonly male (34.8 vs 69.0%). Patients with preclinical HCM were similar to control subjects. In terms of functional imaging characteristics (Table 2.2), patients with overt HCM had higher wall thicknesses ($p < 0.001$), higher ejection fraction (EF, 66.2 ± 9.1 vs 59.3 ± 4.4%, $p < 0.001$), higher LV mass index (88.5 ± 24.6 vs 62.6 ± 13.1 g/m^2), lower indexed ES volume (26.1 ± 9.7 vs 31.5 ± 6.8 mL/m^2, $p = 0.011$), higher indexed LA ED volume (47.3 ± 17.5 vs 32.3 ± 8.7 mL/m^2), more negative septal E' z-score (-1.4 ± 1.4 vs 0.0 ± 0.6, $p < 0.01$), and lower E Wave velocities ($p < 0.01$) relative to control subjects. Patients with preclinical HCM had lower indexed ES volume (26.4 ± 6.7 vs 31.5 ± 6.8 mL, $p < 0.01$) and higher EF (63.2 ± 6.6 vs 59.3 ± 4.2%, $p < 0.01$) relative to control subjects, but were otherwise similar.

2.2.4.2 Circumferential Strain and cTSD

Of the 99 mid-ventricular SA series analysed, 7 (7.1%) were excluded due to poor image quality (4) or poor tracking (3). By CMR feature tracking, mean endocardial ε_{cc} in control subjects was similar to that of preclinical HCM patients (-24.9 ± 4.3 vs -27.5 ± 4.9%, $p =$ NS); likewise, mean epicardial ε_{cc} in control subjects was similar to that of preclinical HCM patients (-11.8 ± 2.0 vs -11.1 ± 2.6%). Endocardial ε_{cc} was significantly greater in overt HCM patients compared to control subjects (-30.1 ± 5.4 vs -24.9 ± 4.3%, $p < 0.0001$) and epicardial ε_{cc} was significantly less in overt HCM patients compared to control subjects (-9.4 ± 3.6 vs -11.8 ± 2.0%, $p < 0.01$). The circumferential Transmural Strain Difference (cTSD) was greater in the overt HCM group compared to control subjects (21.8 ± 6.8 vs 13.6 ± 3.6%, $p < 0.0001$), reflecting myocardial dysfunction in overt HCM (Table 2.3). cTSD was also greater in the

Variable	Control $n = 23$	Preclinical HCM $n = 34$	Overt HCM $n = 42$	p			
				ANOVA	C vs P	P vs O	C vs O
Age (yrs)	21.6 ± 7.2	21.4 ± 8.2	29.9 ± 13.0	< 0.001	NS	< 0.001	< 0.01
Female (n, (%))	15 (65.2)	16 (47.1)	13 (31.0)	0.027	NS	NS	0.016
Non-Caucasian (n)	3 (13.0)	0 (0.0)	5 (11.9)	NS	NS	NS	NS
BMI (kg/m^2)	25.1 ± 4.8	23.6 ± 4.2	26.0 ± 5.3	NS	NS	0.035	NS
BSA (m^2)	1.8 ± 0.3	1.7 ± 0.3	1.9 ± 0.3	0.016	NS	< 0.01	NS
HR (bpm)	71.1 ± 9.3	73.6 ± 10.9	65.7 ± 12.4	< 0.01	NS	< 0.01	0.05
Systolic BP (mmHg)	115.0 ± 12.5	113.8 ± 12.5	118.5 ± 14.7	NS	NS	NS	NS
Diastolic BP (mmHg)	67.4 ± 7.5	68.4 ± 9.1	68.8 ± 10.3	NS	NS	NS	NS
BNP (pg/mL)	28.2 ± 25.0	44.1 ± 37.0	360.7 ± 560.0	< 0.001	NS	< 0.001	< 0.001
Troponin (ng/mL)	4.5 ± 11.4	6.0 ± 14.9	10.7 ± 14.7	NS	NS	NS	NS
Gene: MYH7 (n)	NA	14 (41.2)	8 (19.0)	NA	NA	NS	NA
Gene: MYBPC3 (n)	NA	16 (47.1)	28 (66.7)	NA	NA	NS	NA
Gene: Other (n)	NA	4 (11.8)	6 (14.3)	NA	NA	NS	NA

Table 2.1: Baseline Characteristics of the HCM Study Population. HCM: Hypertrophic Cardiomyopathy; BMI: Body Mass Index; BSA: Body Surface Area; HR: Heart Rate; BP: Blood Pressure; BNP: Brain Natriuretic Peptide; ANOVA: Analysis of Variance; C: Control; P: Preclinical; O: Overt; NS: Not Significant; NA: Not Applicable.

Variable	Control	Preclinical	Overt	p	C vs P	P vs O	C vs O
EF (%)	59.3 ± 4.2	63.2 ± 6.6	66.2 ± 9.1	<0.01	<0.01	NS	<0.001
SV (mL)	83.0 ± 21.7	77.1 ± 18.3	97.7 ± 28.4	<0.01	NS	<0.001	0.024
CO (L)	5.9 ± 1.5	5.6 ± 1.1	6.3 ± 1.7	NS	NS	0.029	NS
LV Mass (g)	113.7 ± 32.2	107.3 ± 35.3	175.4 ± 66.3	<0.0001	NS	<0.0001	<0.0001
LV Mass / BSA (g/m^2)	62.6 ± 13.1	61.7 ± 13.7	88.5 ± 24.6	<0.0001	NS	<0.0001	<0.0001
ED Volume (mL)	140.2 ± 35.9	122.0 ± 26.5	149.2 ± 45.0	<0.01	0.044	<0.01	NS
ED Volume / BSA (mL/m^2)	77.3 ± 14.1	71.5 ± 11.9	76.4 ± 16.1	NS	NS	NS	NS
ES Volume (mL)	57.2 ± 16.2	44.9 ± 13.5	51.6 ± 24.4	NS	<0.01	NS	NS
ES Volume / BSA (mL/m^2)	31.5 ± 6.8	26.4 ± 6.7	26.1 ± 9.7	0.027	<0.01	NS	0.011
LA ED Volume (mL)	59.7 ± 20.3	54.7 ± 26.6	94.2 ± 43.3	<0.0001	NS	<0.0001	<0.001
LA ED Volume / BSA (mL/m^2)	32.3 ± 8.7	32.1 ± 12.6	47.3 ± 17.5	<0.001	NS	<0.001	<0.001
LA ES Volume (mL)	18.6 ± 7.9	19.2 ± 10.8	41.3 ± 29.5	<0.0001	NS	<0.001	<0.001
LA ES Volume / BSA (mL/m^2)	10.1 ± 3.6	11.1 ± 5.3	20.6 ± 12.5	<0.0001	NS	<0.001	<0.0001
LA EF (%)	0.7 ± 0.1	0.7 ± 0.1	0.6 ± 0.1	<0.001	NS	0.011	<0.001
Maximal Wall Thickness (mm)	9.5 ± 1.4	9.8 ± 2.2	16.1 ± 5.3	<0.0001	NS	<0.0001	<0.0001
Septal Wall Thickness (mm)	7.5 ± 1.3	7.6 ± 1.4	12.2 ± 4.7	<0.0001	NS	<0.0001	<0.0001
Lateral Wall Thickness (mm)	7.0 ± 1.4	7.3 ± 1.8	8.5 ± 2.1	<0.01	NS	<0.01	<0.001
Septal:Lateral Wall Thickness (mm)	1.1 ± 0.2	1.1 ± 0.2	1.4 ± 0.4	<0.0001	NS	<0.0001	<0.0001
Lateral E' (z-score)	-0.9 ± 0.8	-0.6 ± 0.8	-1.6 ± 1.4	<0.01	NS	0.011	NS
Septal E' (z-score)	0.0 ± 0.6	-0.3 ± 1.1	-1.4 ± 1.4	<0.001	NS	0.011	<0.01
Lateral E Wave Velocity (cm/s)	16.1 ± 2.9	17.1 ± 2.1	13.5 ± 4.3	<0.0001	NS	<0.0001	<0.01
Septal E Wave Velocity (cm/s)	13.9 ± 2.0	13.0 ± 2.2	9.8 ± 3.0	<0.0001	NS	<0.0001	<0.0001
Anterior E Wave Velocity (cm/s)	16.4 ± 4.0	16.4 ± 2.9	11.7 ± 4.3	<0.0001	NS	<0.0001	<0.0001
Inferior E Wave Velocity (cm/s)	16.6 ± 2.6	15.3 ± 2.3	11.3 ± 3.4	<0.0001	NS	<0.0001	<0.0001

Table 2.2: Functional Imaging Characteristics of the HCM Study Population. Bolded values represent p statistics that remain significant after Bonferroni correction. EF = Ejection Fraction; SV = Stroke Volume; CO = Cardiac Output; LV = Left Ventricle; BSA = Body Surface Area; ED = End Diastole; ES = End Systole; WT = Wall Thickness; LA = Left Atrium; C: Control; P: Preclinical; O: Overt; NS: Not Significant; NA: Not Applicable.

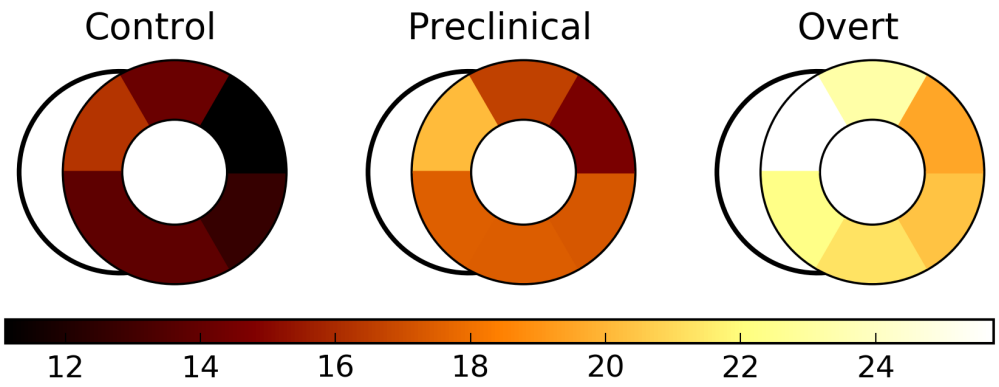


Figure 2.3: Segmental cTSD in HCM. Segmental cTSD is more negative in patients with preclinical and overt HCM compared to control. Segmental cTSD values are presented for control, preclinical HCM, and overt HCM groups. Differences between control subjects and overt HCM were significant in all segments. Differences between control subjects and preclinical HCM were significant in the inferoseptal and lateral segments.

preclinical subjects compared control subjects (17.1 ± 4.0 vs $13.6 \pm 3.6\%$, $p < 0.01$). The median cTSD for control subjects was 13.1%; the majority (26/32, 81.3%) of patients with preclinical HCM had greater cTSD values than control subjects. Since HCM often exhibits regional variation, each of the six mid-ventricular AHA segments was compared between control, preclinical, and overt groups. cTSD (Fig. 2.3) was significantly greater in patients with overt HCM compared to control subjects (all segments, $p < 0.0001$). cTSD was greater in patients with preclinical HCM compared to control subjects in the lateral and septal segments ($p < 0.01$).

2.2.4.3 Correlation of cTSD with Functional Parameters

cTSD was then correlated with cardiac functional parameters (Fig. 2.4). Considering all study subjects, segmental cTSD was correlated with increased wall thickness (1.0% per millimetre, $r = 0.42$, $p < 0.0001$). Global cTSD was correlated with increased LV mass index (0.11% per gram/m^2 increase in LV mass index, $r = 0.38$, $p < 0.001$) and log-transformed BNP (1.8% per ln(pg/mL), $r = 0.40$, $p < 0.0001$), and was inversely correlated with increased septal E wave velocity (-0.83%/z-score, $r = -0.41$, $p < 0.0001$). After excluding the overt HCM group, significance was lost for all parameters, suggesting that alterations in function identified by cTSD

Variable	Control	Preclinical	Overt	ANOVA	C vs P	P vs O	C vs O
Anterior	14.1 ± 3.1	16.7 ± 5.4	23.2 ± 7.7	<0.0001	0.033	<0.001	<0.0001
Anteroseptal	16.3 ± 5.4	20.2 ± 5.0	25.7 ± 8.5	<0.0001	0.011	<0.01	<0.0001
Inferoseptal	13.9 ± 4.2	17.4 ± 5.2	22.6 ± 8.3	<0.0001	<0.01	<0.01	<0.0001
Inferior	13.8 ± 5.0	17.4 ± 6.5	21.5 ± 7.6	<0.001	0.029	0.019	<0.0001
Inferolateral	12.7 ± 3.8	17.3 ± 5.8	20.7 ± 7.8	<0.0001	<0.01	0.036	<0.0001
Anterolateral	11.1 ± 3.4	14.5 ± 4.6	19.7 ± 7.5	<0.0001	<0.01	<0.001	<0.0001
Average	13.6 ± 3.6	17.1 ± 4.0	21.8 ± 6.8	<0.0001	<0.01	<0.001	<0.0001

Table 2.3: Univariate Analysis of Segmental cTSD in HCM. Segmental differences in circumferential transmural strain difference (cTSD, %) were noted between control subjects and patients with preclinical HCM. ANOVA: Analysis of Variance; C: Control; P: Preclinical; O: Overt.

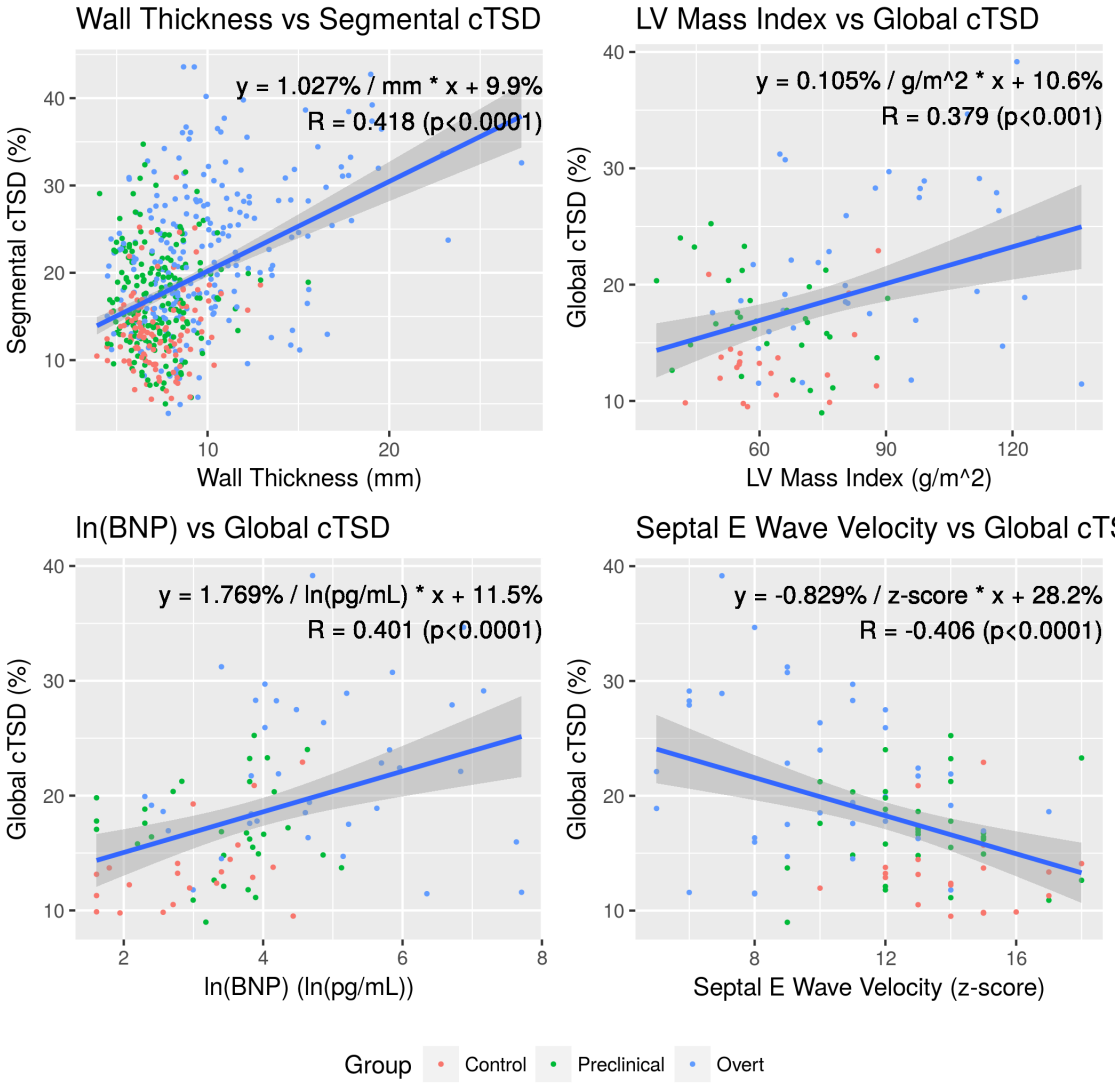


Figure 2.4: Correlation of cTSD with functional parameters. Globally, cTSD correlates moderately LV mass index, ln(BNP), and septal E wave velocity; segmentally, cTSD correlates moderately with wall thickness. Equations of linear regression lines and Pearson's R coefficients are indicated. Gray regions surrounding regression lines indicate 95% confidence intervals.

were driven by the presence of a sarcomere mutation rather than LV mass and wall thickness in the preclinical HCM subjects.

2.2.4.4 Multivariate Analysis

Two separate analyses were performed: one predicting overt HCM diagnosis and the other predicting preclinical HCM diagnosis (Table 2.4). In terms of predicting overt disease, in the initial (fully adjusted) model, average cTSD was a significant

Variable	Ia	Ib	IIa	IIb
Average cTSD (%)	$0.304^{\dagger}$	$0.344^{\ddagger}$	0.209^{*}	$0.249^{\ddagger}$
Septal E-Wave Velocity (%/z-score)	-0.484	$-0.528^{\ddagger}$	-0.200	–
Septal Wall Thickness (%/mm)	0.050	–	-0.337	–
LV Mass Index (%/g/m^2)	0.036	–	-0.046	–
Age (%/yr)	0.007	–	-0.043	–
Female (%)	-0.627	–	$-2.698^{\dagger}$	–
ln(BNP) (%/ln(pg/mL))	0.060	–	0.550	–

Table 2.4: Multivariate Analysis of cTSD in HCM. Fully adjusted (Models Ia and IIa) and refined (Models Ib and IIb) binary logistic regression models predicting overt (Ia and Ib) and preclinical (IIa and IIb) disease status. β values for predictors are related to the log odds of preclinical and overt disease status. LV: Left Ventricle; BNP: Brain Natriuretic Peptide; cTSD: circumferential Transmural Strain Difference; *: $p < 0.1$; †: $p < 0.05$; ‡ : $p < 0.01$.

predictor ($p = 0.038$), with an increase in cTSD of 0.30% bringing about a unit increase in log odds of overt disease status. In the final (minimally adjusted) model, average cTSD and septal E-wave velocity were both significant predictors, with a 0.34% increase in cTSD and a 0.53 cm/s decrease in E-wave velocity bringing about a unit increase in log odds of overt disease status, respectively ($p < 0.01$). In terms of predicting preclinical disease, in the initial model, female sex was a significant predictor ($p = 0.04$) of disease status, decreasing the log odds of preclinical disease status by 2.70. Average cTSD was of borderline significance ($p = 0.053$), with a 0.20% increase in cTSD bringing about a unit increase in log odds of preclinical disease status. In the final model, average cTSD alone was a significant predictor of disease status ($p < 0.01$), with a 0.24% increase in cTSD bringing about a unit increase in log odds of preclinical disease status.

2.2.4.5 Genetics

The relationship between cTSD and genetic assignment was additionally evaluated (Fig. 2.5). Compared with gene negative patients, cTSD was significantly higher in patients with the MYH7 mutation (13.6 vs 20.1%, $p < 0.0001$) and with the MYBPC3 mutation (13.6 vs 19.2%, $p < 0.0001$), and had borderline significance in patients with other mutations (13.6 vs 20.7%, $p = 0.017$). cTSD was

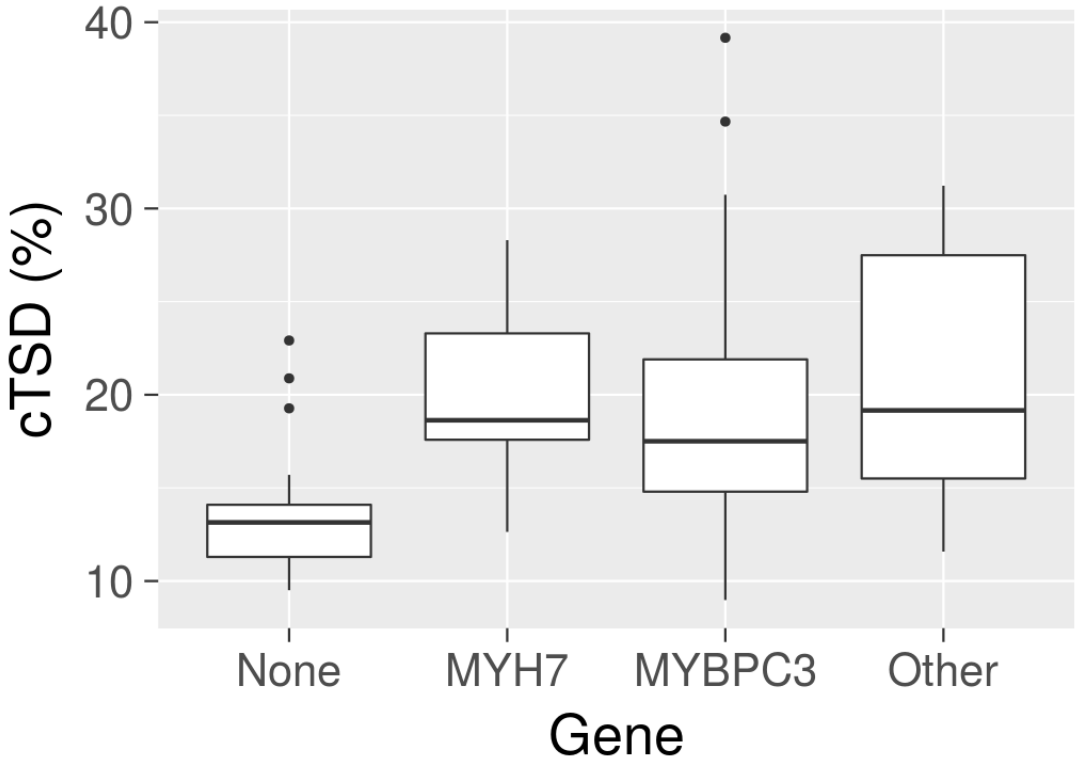


Figure 2.5: Stratification of cTSD by Genetic Assignment. Compared with gene negative patients, cTSD was significantly higher in patients with the MYH7 mutation (13.6 vs 20.1%, $p < 0.0001$) and with the MYBPC3 mutation (13.6 vs 19.2%, $p < 0.0001$), and had borderline significance in patients with other mutations (13.6 vs 20.7%, $p = 0.017$). cTSD was not significantly different in pairwise comparisons between patients with MYH7, MYBPC3, and other mutations.

not significantly different in pairwise comparisons between patients with MYH7, MYBPC3, and other mutations.

2.2.4.6 Reproducibility

Thirty-three (33) randomly selected cases were reanalysed for intra- and inter-observer reproducibility of segmental strain measurements. As judged by the thresholds specified in §2.2.3.4, reproducibility of cTSD was excellent within observers (ICC = 0.783, $p < 0.0001$) and moderate between observers (ICC = 0.670, $p < 0.0001$). No bias was noted either by Student's t-test (p = NS) or visually by Bland-Altman analysis (Fig. 2.6) in either intra- or inter-observer measurements.

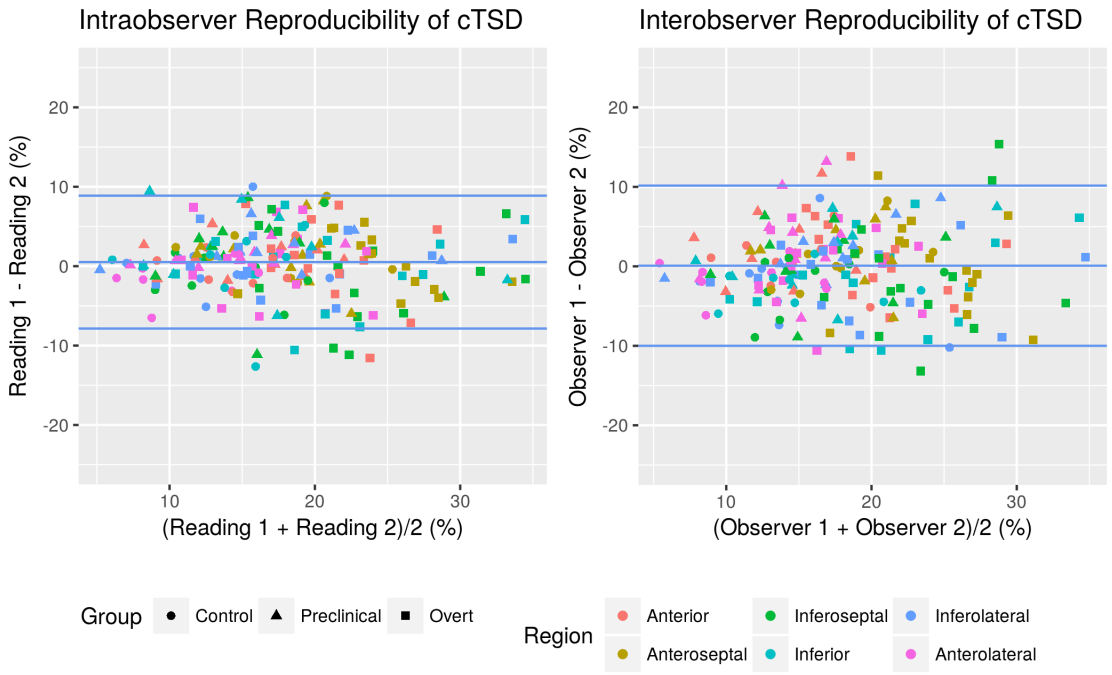


Figure 2.6: Reproducibility of cTSD. cTSD is reproducible both within and between observers by visual inspection of Bland-Altman plots. In each plot, the x-axis represents mean strain (%) and the y-axis represents strain difference (%, Reading 1 - Reading 2 and Observer 1 - Observer 2, respectively). Horizontal lines represent mean differences ±2 standard deviations.

2.2.4.7 Myocardial Strain by CMR Tagging

Mid-myocardial strain and cTSD was calculated using HARP analysis of tagged CMR in the subset of patients with adequate tagging. Analysable tagged CMR (defined as the availability of one midventricular grid tagged sequence or both horizontal and vertical line tagged sequences without gross registration errors, absent gross motion artifacts) was available for 65 (66%) of subjects. Using tagged sequences, no differences were seen in midwall mean circumferential strain between control subjects ($-20.9 \pm 2.0\%$), patients with preclinical HCM ($-20.7 \pm 2.7\%$), and patients with overt HCM ($-20.7 \pm 2.7\%$) (p = NS). Based on CMR tagging, cTSD values in overt HCM, preclinical HCM and control subjects were $13.2 \pm 3.3\%$, $10.1 \pm 2.6\%$, and $9.0 \pm 1.9\%$ respectively (overt vs control, $p < 0.0001$; preclinical vs control, p = NS).

2.2.5 Conclusions

Identifying early phenotypic markers for preclinical HCM is valuable in characterising early disease expression and the initial phenotypic manifestations of sarcomere mutations. The impact of sarcomere mutations on myocardial function in preclinical and overt HCM has not been robustly described in the literature [83]. CMR feature tracking is particularly well suited to assessing strain at the endocardial and epicardial myocardial surfaces. A more pronounced difference was observed in strain across the myocardium, between the epicardial and endocardial surfaces (cTSD), in overt HCM patients compared to control subjects, an indicator of myocardial dysfunction compared with control subjects. Of particular interest, cTSD was also abnormal in preclinical HCM compared to control subjects, indicating that divergence of the endocardial and epicardial circumferential strain values may be an early manifestation of the underlying sarcomere mutation. These contractile abnormalities were not detected by conventional CMR tagging in the preclinical group as tagging is poorly suited to measuring strain/motion at the myocardial surfaces.

Using CMR, subtle patterns in the trabeculation of the LV have been noted in HCM carriers to a lesser degree than overt HCM subjects [84, 85]. The concept that genetic abnormalities in HCM result in early/occult functional abnormalities is well grounded. Several echocardiographic studies have observed that LV diastolic function is reduced in sarcomere mutation carriers with normal LV wall thickness compared to control subjects [76, 86] although these results have been heterogeneous, likely related to genetic variation [87].

Regarding systolic function, echocardiographic studies have shown preserved LV strain in preclinical HCM [77, 88]. However, Yiu, et al, [89] evaluated 46 overt HCM and 47 preclinical HCM patients with 25 control subjects with echocardiographic speckle tracking. They found regional changes (anteroseptal segments) with reduced longitudinal systolic strain (i.e., less negative) in preclinical HCM by speckle tracking analysis compared to control subjects. CMR tagging is the standard of reference for measurement of myocardial strain. With CMR tagging, there was no difference in midwall circumferential strain between overt HCM, preclinical HCM,

and control groups. The result presented here supports their conclusions with quite independent methodology, indicating the presence of systolic abnormalities in preclinical HCM carriers.

That endocardial strain should be more negative than epicardial strain follows geometrically given the incompressibility of myocardium [8]. Moreover, it is clear that this difference should be larger in the context of wall thickening, given that the same change in area is associated with a proportionally larger change in circumference at smaller radii. It should be emphasised, however, that geometric considerations are insufficient in explaining these findings, given that the preclinical group had normal wall thicknesses. A detailed analysis of the relationship between geometry and cTSD in this cohort reaffirms this conclusion, and is given in Appendix §A. cTSD remained a significant predictor of disease designation in multivariate analysis.

In terms of cTSD, results from conventional CMR tagging showed trends similar to that identified by CMR feature tracking, but mid-myocardial circumferential strain in subjects with preclinical HCM was not significantly different from control subjects. Tagging was inadequately powered due to the small number of analysable tagging images (66% tagging vs 93% feature tracking), highlighting the difficulty of reliably acquiring tagged CMR in a multicenter trial. Additionally, due to interference with the blood pool, HARP contours must be drawn interior to the true endocardium and epicardium, dampening the measured strain difference between them, which could also contribute to the lack of significant differences. This highlights a second limitation of tagging: the inability to assess structures other than the midwall of the LV. Preliminary studies have additionally shown that feature tracking may be helpful in other chambers, such as in the quantitative assessment of the right ventricle in arrhythmogenic right ventricular cardiomyopathy (ARVC) [61, 62].

The overall population in this study included 99 subjects; the cohort was well characterised, but small, suggesting that the results should be investigated in a larger population. The patients in this study were young, limiting the range of disease represented. Not all patients with preclinical HCM ultimately express clinical disease, and in these patients abnormalities in cardiac function are not expected. Moreover,

women and non-Caucasians were underrepresented in this study at 44.4% and 8.1%, respectively. The differences observed were small relative to biological variability, and therefore poorly suited to simple diagnostic thresholding. In terms of the MTT algorithm, LV papillary muscles frequently interfered with tracking, requiring frequent manual correction of LV endocardial contours. Moreover, preliminary studies in longitudinal LV strain analysis demonstrated poor performance, and were not investigated further. Finally, standard CMR SSFP images were used without further optimisation for feature tracking.

In conclusion, CMR feature tracking identified differences in a circumferential-strain-based metric between the overt HCM group and the preclinical HCM patients, as well as preclinical HCM patients compared to control subjects. Specifically, there was a measurable difference in circumferential strain between endocardium and epicardium in sarcomere mutation carriers that becomes more pronounced in subjects with overt HCM. CMR feature tracking may be a favourable alternative to tagged CMR since routine CMR sequences can be more feasibly acquired and analysed. The feature tracking approach allows additional insight into subtle abnormalities in myocardial mechanics that appear to be an early manifestation of sarcomere mutations. Prospective studies are necessary to see whether prognostic value may be attributed to early aberrations in circumferential strain.

2.3 Arrhythmogenic Right Ventricular Cardiomyopathy (ARVC)

2.3.1 Contributions

[1] Davis M Vigneault, Anneline S.J.M. te Riele, Cynthia A. James, Stefan L. Zimmerman, Hugh Calkins, Harikrishna Tandri and David A. Bluemke. 'Right Ventricular Strain Abnormalities in Arrhythmogenic Right Ventricular Cardiomyopathy: Analysis of CMR by Feature Tracking'. In: *RSNA*. Chicago, IL, 2014.

[2] Davis M. Vigneault, Anneline S.J.M. te Riele, Cynthia A. James, Stefan L. Zimmerman, Hugh Calkins, Harikrishna Tandri and David A. Bluemke. 'Abnormal Right Ventricular Strain by Cardiac Magnetic Resonance in Preclinical Arrhythmogenic Right Ventricular Cardiomyopathy'. In: *AHA*. Chicago, IL, 2014.

[3] Davis M. Vigneault, Anneline S.J.M. te Riele, Cynthia A. James, Stefan L. Zimmerman, Mariana Selwaness, Brittney Murray, Crystal Tichnell, Michael Tee, J. Alison Noble, Hugh Calkins, Harikrishna Tandri and David A. Bluemke. 'Right ventricular strain by MR quantitatively identifies regional dysfunction in patients with arrhythmogenic right ventricular cardiomyopathy'. In: *Journal of Magnetic Resonance Imaging* 43 (2016), pp. 1132–1139.

2.3.2 Background

ARVC is an inherited cardiomyopathy with disease frequently presenting with regional dysfunction and enlargement of the RV [90]. Affected patients typically present during the second to fifth decades of life, most commonly with palpitations, syncope, or sudden cardiac death [91–93]. Diagnosis is made based on the Task Force Criteria (TFC) [94], which involves assessment for major and minor criteria in six categories, including imaging assessment, to detect RV global and regional dysfunction, as well as RV enlargement. To date, regional function by CMR in ARVC is only analysed qualitatively (visually); this can lead to variability between readers and false positive diagnoses [95, 96].

For the RV, identification of regional disease by CMR is problematic since quantitative tools to determine regional function are not generally available. Tagged CMR provides quantitative assessment of LV strain, but has not generally proven to be useful in measuring RV strain due to the thinness of the myocardial wall [58]. Because CMR feature tracking relies upon trabeculation and myocardial edges rather than features within the wall itself, it was hypothesised that this technique may be useful for quantifying cardiac function in the RV. The purpose of this study was to determine the feasibility and reproducibility of RV myocardial strain analysis of cine CMR images in ARVC patients via CMR feature tracking in comparison to control subjects.

2.3.3 Materials and Methods

2.3.3.1 Patient Population

The images analysed in this work were acquired as part of a prospective study of 110 individuals who were evaluated for ARVC at a large, urban, tertiary medical

centre. Patients were selected from a preexisting database based on availability of genetic and CMR data. All selected patients had undergone comprehensive clinical evaluation including CMR to determine the presence or absence of diagnostic TFC for ARVC [94]. Cases included 79 ARVC-associated desmosomal mutation carriers who were divided in two groups: overt ARVC (those fulfilling diagnostic criteria for ARVC, $n = 39$), and preclinical ARVC (those not fulfilling diagnostic criteria for ARVC, $n = 40$). All overt patients were diagnosed with ARVC independently of CMR, so that the diagnostic TFC provide an independent standard of reference. As a control group, 31 individuals were included who were either mutation-negative family members of mutation-positive ARVC patients ($n = 9$), or subjects without ARVC upon comprehensive clinical evaluation ($n = 22$) and had been referred for preemptive evaluation or to rule out ARVC.

2.3.3.2 CMR Acquisition

Cine images in the horizontal long axis (4C), axial, and short axis (SA) planes were acquired at 1.5 Tesla (Avanto, Siemens Medical Imaging, Erlangen, Germany) using a balanced SSFP sequence (TR/TE/FA 2.4/1.2/50-75 degrees, matrix 256-192, field of view 30-36 cm, temporal resolution ≤ 40 msec, slice thickness 6-8 mm).

Since little is known about quantitative strain in the RV in ARVC, the analysis was approached in a stepwise manner: a) global strain (average of all segments) to determine which CMR cine view distinguished overt and control groups; b) segmental (local) strain in various views to determine if differences between groups were primarily driven by regional abnormalities; c) qualitative reads by radiologists in comparison to quantitative strain measurements to determine if there is any advantage of quantitative strain analysis.

2.3.3.3 Image Analysis

Quantitative Analysis: Global Functional Metrics For global metrics, RV and LV EF, end systolic volume (ESV), and end diastolic volume (EDV) were measured with CVI42 (Circle Cardiovascular Imaging; Client Version 248, Server

Version 258; Calgary, Alberta, Canada). RV ESV and EDV were indexed to body surface area (BSA) using the Dubois formula:

$$BSA = \mathrm{Mass_{kg}}^{0.425} \times \mathrm{Height_{cm}}^{0.725} \times 0.007184. \tag{2.1}$$

Quantitative Analysis: Regional Functional Measurements For regional analysis, peak longitudinal (4C and axial) and circumferential (SA) strain were measured using MTT (Version 6.0.4725, Toshiba Medical Systems Corporation, Tokyo, Japan) [42]. On SA views, the most basal slice without right atrium through-plane motion during systole was analysed. This position was chosen to optimise detection of abnormalities both at the inferior RV base and anteriorly at the RV outflow tract. On long axis (4C and axial) views, the most central slice in which the valve plane was visible throughout the cardiac cycle was analysed. Endocardial and epicardial contours were drawn in a semiautomated fashion from the apical insertion point to the mitral valve plane in the 4C and axial views and from the anterior to the inferior RV insertion points in the circumferential view. Tracking occurred through a block matching algorithm, as described in §1.5.1.5; representative contours for a control subject and a patient with overt ARVC are shown in Figs. 2.7 and 2.8, respectively. The quality of tracking was visually verified and manually adjusted if necessary. Of the 330 possible CMR series, 55 (16.7%) were excluded due to poor image quality (poor electrocardiogram gating due to arrhythmia, patient motion).

The segmentation of the RV for various views is illustrated in Fig. 2.9. In the 4C and axial views, the RV was segmented into subtricuspid, anterior wall, and apical regions; in the SA view, the RV was segmented into outflow tract, free wall, angle, and inferior regions. Image quality was inadequate for feature tracking in 19 (6.9%) regions in the 4C view, 24 (9.1%) in the axial view, and 14 (3.7%) in the SA view. By convention for strain, segmental shortening is negative; segments that show greater local contraction have more negative strain.

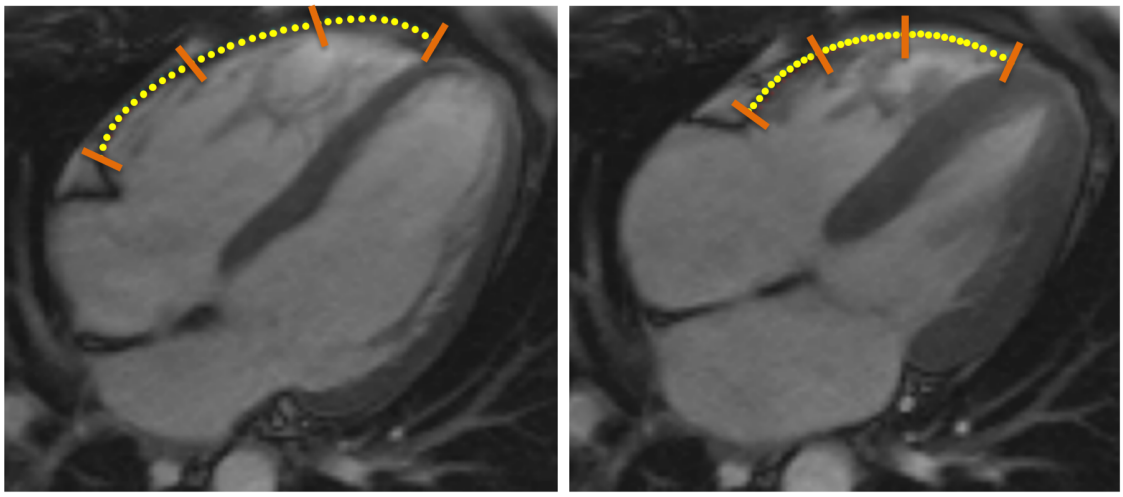


Figure 2.7: Right Ventricular Feature Tracking in a Healthy Subject. Right ventricular feature tracking of cine steady state free precession (SSFP) images in the horizontal long axis (4C) view of a 44 y/o female control subject. Contours were drawn in a semiautomated manner at end-diastole (left) and propagated throughout the cardiac cycle. The position of the propagated contours at end-systole (right) are also shown. Multimodality Tissue Tracking (MTT) points have been overlain with yellow circles to be more easily visualized; orange bars indicate demarcation between segments.

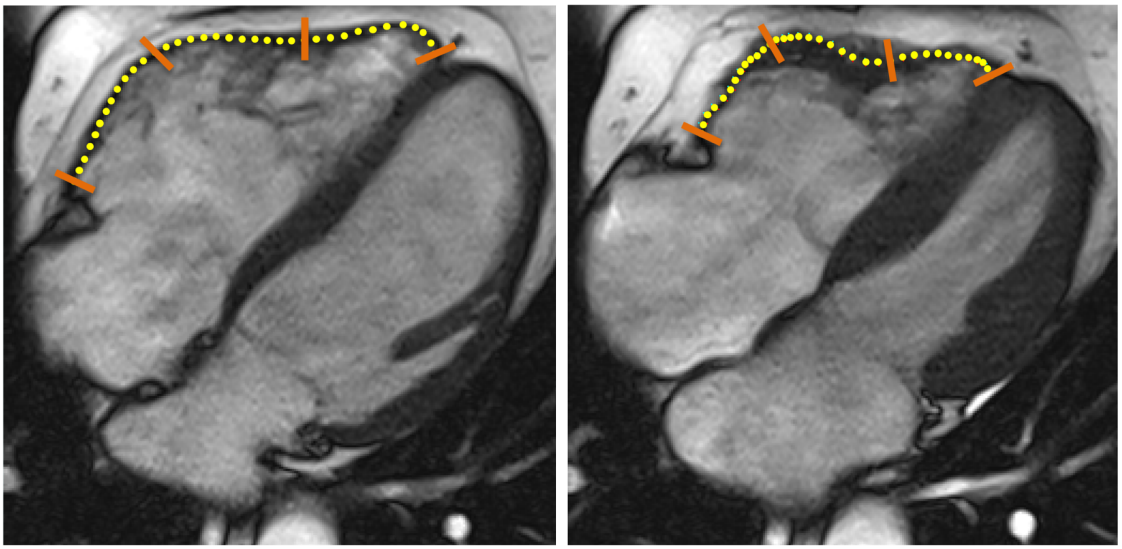


Figure 2.8: Right Ventricular Feature Tracking in Overt ARVC. Right ventricular feature tracking of cine steady state free precession (SSFP) images in the horizontal long axis (4C) view of a 55 y/o male patient with overt ARVC. Contours were drawn in a semiautomated manner at end-diastole (left) and propagated throughout the cardiac cycle. The position of the propagated contours at end-systole (right) are also shown. Multimodality Tissue Tracking (MTT) points have been overlain with yellow circles to be more easily visualized; orange bars indicate demarcation between segments.

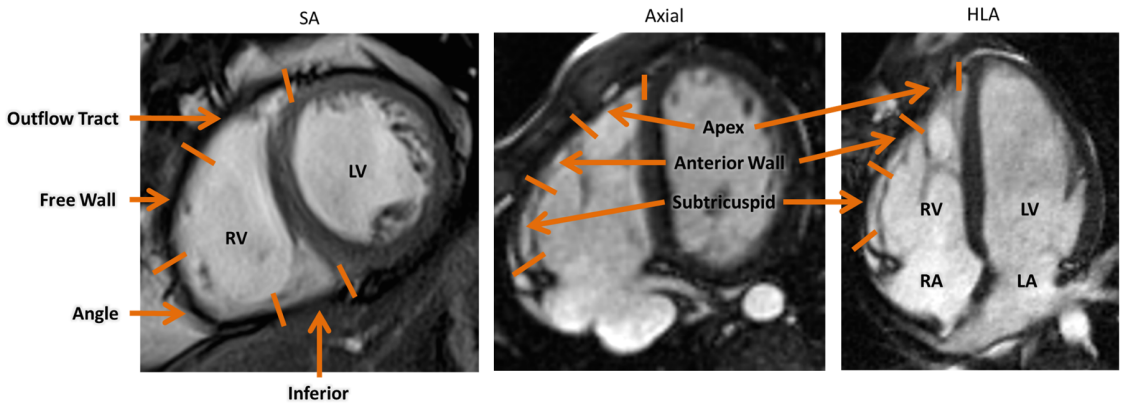


Figure 2.9: Right Ventricular Segmentation. Definition of regions for the RV in the SA (left), axial (center), and 4C (right) views. Abbreviations: SA: Short axis; 4C: Horizontal Long Axis; RV: Right Ventricle; LV: Left Ventricle; RA: Right Atrium; LA: Left Atrium.

Qualitative Readings Two radiologists[2] qualitatively assessed wall motion blinded to group assignment and demographic data. Wall motion on the 4C cine views was scored as 1 (normal, no abnormality), 2 (possible abnormality), or 3 (definite abnormality). After independent assessment, the readers conferred over the cases and decided upon a consensus read. Interobserver agreement was assessed using the Cohen's κ coefficient.

2.3.3.4 Statistical Analysis

Continuous and discrete data are presented as mean ($\pm$ SD) and n (%), respectively. For continuous data, comparisons to the control group were performed using Dunnett's test, which inherently accounts from multiple comparisons. Categorical data were compared using Pearson's χ^2 test. Univariate and multivariate cumulative odds logistic regression was used to determine predictors of clinical diagnosis based on regional strain and clinical risk factors.[3] Model selection was performed using stepwise backward selection based on Akaike's information criterion. Intra- and inter-observer reproducibility of strain measurements was evaluated visually by Bland-Altman analysis;[4] correlation was assessed by intraclass correlation coefficient

[2]Drs. David Bluemke and Stefan Zimmerman, with 15 and 5 years of experience in interpreting ARVC, respectively.

[3]The author would like to acknowledge Dr. Anneline te Riele for advising on multivariate statistical analysis.

[4]The author would like to acknowledge Dr. Mariana Selwaness for replicating strain measurements for the purpose of assessing interobserver reproducibility.

Variable	Overt ARVC $n = 39$	Preclinical ARVC $n = 40$	Control Subjects $n = 31$
Male	17 (44)	22 (55)	17 (55)
Age (yrs)	32.3 ± 13.5	31.3 ± 18.1	37.2 ± 14.9
RV EDV Index	$88.3 \pm 25.6^{\dagger}$	68.4 ± 14.4	69.7 ± 12.9
RV ESV Index	$47.4 \pm 24.9^{\dagger}$	31.1 ± 9.8	30.0 ± 8.6
RV EF	$48.3 \pm 11.7^{\dagger}$	54.9 ± 9.6	56.9 ± 9.7
LV EDV Index	77.4 ± 12.1	69.1 ± 12.9	73.5 ± 9.6
LV ESV Index	30.6 ± 9.5	25.2 ± 7.0	30.9 ± 15.1
LV EF	62.7 ± 6.3	63.2 ± 11.7	58.9 ± 13.3

Table 2.5: Imaging Characteristics for the ARVC Study Population. ARVC: Arrhythmogenic Right Ventricular Cardiomyopathy; LV: Left Ventricle; RV: Right Ventricle; EDV: End-Diastolic Volume; ESV: End-Systolic Volume; EF: Ejection Fraction; †: $p < 0.05$; ‡ : $p < 0.01$.

(ICC). For ICC, a value ≥ 0.75 was considered excellent, < 0.75 and ≥ 0.40 moderate, and < 0.40 poor. $p < 0.05$ was considered significant. All statistical analysis was performed using R (v3.1.0).

2.3.4 Results

2.3.4.1 Baseline Characteristics

CMR images from 110 subjects (39 overt ARVC [mutation+/phenotype+] (35.5%), 40 preclinical ARVC [mutation+/phenotype–] (36.3%), and 31 control subjects [mutation–/phenotype–] (28.2%)) were evaluated. Clinical characteristics of the study population are shown in Tables 2.5 and 2.6. The average age was 33.3 ± 15.8 years; 54 (49.1%) of patients were female. Age and gender were similar between the groups. As expected, RV EF was lower and RV EDV Index was greater in overt ARVC relative to control subjects; there were no significant differences in LV function or dimension between groups. Patients with preclinical ARVC were similar to control subjects for all global metrics.

2.3.4.2 Global (Average) Strain Analysis

As shown in Table 2.7, global strain magnitude was lower in overt ARVC compared to control subjects in all CMR views ($p < 0.0001$, $p = 0.017$, and $p < 0.01$ for 4C,

Variable	Overt ARVC	Preclinical ARVC
Repolarization criteria	36 (92)	4 (10)
T-wave inversion V1-3	33 (85)	0 (0)
T-wave inversion V1-2	3 (8)	4 (10)
T-wave inversion V1-4 w/ CRBBB	0 (0)	0 (0)
Depolarization criteria	22 (56)	13 (33)
Epsilon wave	2 (5)	0 (0)
Prolonged TAD	17 (44)	5 (13)
Late potentials	15/34 (44)	12/38 (32)
Arrhythmia criteria	25 (64)	2 (5)
LBBB superior axis VT	6 (15)	0 (0)
LBBB inferior axis VT	9 (23)	0 (0)
$>$ 500 PVCs/24 hrs	21/32 (66)	2/35 (6)
Structural criteria	23 (59)	0 (0)
Major	16 (41)	0 (0)
Minor	7 (18)	0 (0)
Median Number of TFC Criteria	6 (IQR $5-7$)	2 (IQR $2-3$)

Table 2.6: Clinical Characteristics of the ARVC Study Population. ARVC: Arrhythmogenic Right Ventricular Cardiomyopathy; CRBBB: Complete Right Bundle Branch Block; LBBB: Left Bundle Branch Block; PVC: Premature Ventricular Complex; TAD: Terminal Activation Duration; TFC: Task Force Criteria; VT: Ventricular Tachycardia; †: $p < 0.05$; ‡ : $p < 0.01$.

View	Overt ARVC	Preclinical ARVC	Control
Global 4C (ε_{ll})	-19.3 (± 6.2)‡	-26.2 (± 5.0)	-27.7 (± 5.5)
Global Axial (ε_{ll})	-23.3 (± 8.1)†	-28.6 (± 7.2)	-28.5 (± 5.2)
Global SA (ε_{cc})	-11.0 (± 5.6)‡	-16.3 (± 4.7)	-14.8 (± 3.2)

Table 2.7: Global Strain Values by ARVC Diagnostic Group. ARVC: Arrhythmogenic Right Ventricular Cardiomyopathy; 4C: Horizontal Long Axis; SA: Short Axis; †: $p < 0.05$; ‡ : $p < 0.01$.

axial, and SA views, respectively). However, the greatest strain differences between overt ARVC subjects and control subjects were in the 4C view (-19.3 vs -27.7%, $p < 0.0001$), corresponding to $30.3 = (27.7 - 19.3)/27.7 \times 100\%$ lower strain in overt subjects. Global strain was similar between control subjects and patients with preclinical ARVC. Global strain was not related to either gender or age ($p =$ NS).

View	Overt ARVC	Preclinical ARVC	Control
4C (ε_{ll}) View			
Subtricuspid	-24.4 (± 10.8)‡	-33.4 (± 10.9)	-36.9 (± 10.5)
Anterior wall	-17.7 (± 6.4)‡	-23.0 (± 6.1)	-22.8 (± 6.3)
Apex	-18.6 (± 8.8)‡	-23.3 (± 7.8)	-25.5 (± 9.6)
Axial (ε_{ll}) View			
Subtricuspid	-31.0 (± 13.2)	-38.2 (± 11.8)	-31.4 (± 13.7)
Anterior wall	-22.1 (± 13.1)	-24.1 (± 8.5)	-25.9 (± 5.9)
Apex	-22.4 (± 10.4)†	-29.0 (± 14.9)	-30.6 (± 12.7)
SA (ε_{cc}) View			
Outflow tract	-11.3 (± 6.8)	-15.3 (± 6.8)	-14.4 (± 6.4)
Free wall	-10.7 (± 4.2)‡	-16.7 (± 5.8)	-15.7 (± 3.0)
Angle	-11.6 (± 6.7)†	-17.0 (± 6.4)	-15.2 (± 3.9)
Inferior	-13.8 (± 7.9)	-20.4 (± 8.7)	-17.9 (± 5.5)

Table 2.8: Regional Strain Values by ARVC Diagnostic Group. ARVC: Arrhythmogenic Right Ventricular Cardiomyopathy; 4C: Horizontal Long Axis; SA: Short Axis; †: $p < 0.05$; ‡ : $p < 0.01$.

2.3.4.3 Regional Strain Analysis

Table 2.8 shows strain by region for the 4C, axial, and SA views. Overt ARVC and control groups were compared first, since regional strain was expected to be most different for those groups. In the 4C view, strain magnitude was lower in overt ARVC compared to control subjects for the subtricuspid ($p < 0.001$), anterior wall ($p < 0.01$), and apical ($p < 0.01$) regions. In the axial view, only the apical segment showed differences in strain for the overt vs the control subjects ($p = 0.04$). In the SA view, only the free wall ($p < 0.001$) and angle ($p = 0.045$) segments showed lower strain for the overt vs the control subjects. Thus, it was concluded that the 4C view was most likely to discriminate overt ARVC from control subjects. Using a cutoff of greater (more negative) than -31% as normal subtricuspid strain in the 4C view, overt ARVC patients were separated from control subjects with 75.0% sensitivity and 78.2% specificity.

For evaluation of the preclinical (mutation+/phenotype–) group, some patients with early disease may have subtle signs of ARVC such as regional wall motion abnormality while other patients may never develop a full ARVC phenotype. Thus,

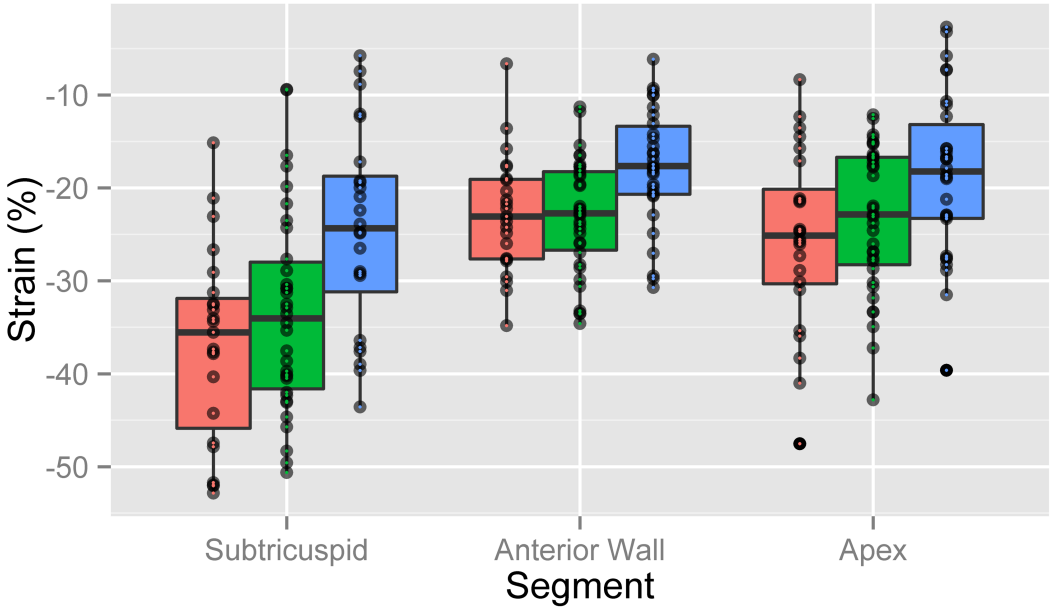


Figure 2.10: Regional cTSD in ARVC. Regional strain by group in the horizontal long axis view. Red, green, and blue boxplots correspond to control subjects, preclinical ARVC, and overt ARVC, respectively.

for a sufficiently large sample size, RV strain may be on average intermediate between control and overt ARVC subjects. Indeed, in the 4C view, regional strain in the preclinical group was intermediate between control and overt groups (Fig. 2.10). Using the -31% cutoff described above, 13/34 (38.2%) patients in the preclinical group showed reduced (less negative) subtricuspid strain. Preclinical patients with abnormal strain were more often male ($n = 10/13$ [77%] vs 10/21 [48%], $p = 0.092$) and older (30.5 ± 18.6 vs 27.5 ± 15.4 years, $p = 0.621$) than preclinical subjects with normal strain. Interestingly, compared to individuals with normal strain, subjects with abnormal strain were significantly more likely to have other minor clinical abnormalities in addition to their genetic predisposition ($n = 10/13$ [77%] vs $n = 7/21$ [33%], $p = 0.013$).

Multivariable analyses was performed to determine the independent predictive value of regional strain for presence or absence of disease. Abnormal 4C strain in the subtricuspid region (defined as less negative than -31% subtricuspid strain) was considered the predictor variable of interest in the multivariable analysis. As shown

	Univariate β (95% CI)	Multivariate β (95% CI)
Age (yr)	-0.01 $(-0.03, 0.01)$	–
Female	0.35 $(-0.34, 1.04)$	1.46 $(0.36, 2.55)^{\ddagger}$
Subtricuspid Strain $< \lvert -31\% \rvert$	1.67 $(0.77, 2.58)^{\ddagger}$	1.38 $(0.28, 2.47)^{\dagger}$
RV EF (%)	-0.10 $(-0.15, -0.06)^{\ddagger}$	-0.06 $(-0.12, 0.01)$
RV EDV Index (m^2/mL)	0.06 $(0.04, 0.09)^{\ddagger}$	0.06 $(0.02, 0.10)^{\dagger}$

Table 2.9: Multivariate Analysis of Subtricuspid Strain in ARVC. Multivariable analysis using cumulative logistic regression for the prediction of group assignment (control, preclinical ARVC, and overt ARVC) by abnormal subtricuspid strain and relevant clinical factors. RV: Right Ventricle; EF: Ejection Fraction; EDV: End Diastolic Volume; †: $p < 0.05$; ‡ : $p < 0.01$.

in Table 2.9, abnormal subtricuspid strain was an independent predictor of ARVC diagnosis ($\beta = 1.38$, $p = 0.014$) in multivariable analysis controlling for gender, RV EF and RV EDV index, while RV EF was not significant in the multivariable model.

2.3.4.4 Strain vs Qualitative Radiologist Interpretation

Cohen's κ coefficient for the two readers was 0.78, indicating moderate to good interobserver reproducibility. A consensus wall motion abnormality rating of 'Definitely Abnormal' was specific but not sensitive for overt ARVC (specificity 95.7% vs sensitivity 44.4%). A consensus wall motion abnormality rating of either 'Definitely Abnormal' or 'Possibly Abnormal' was moderately sensitive and specific for overt ARVC (sensitivity 55.6% vs specificity 63.8%).

The diagnostic accuracy of abnormal qualitative wall motion (defined by radiologists as 'Possibly' or 'Definitely' abnormal) was compared to abnormal subtricuspid strain (less negative than -31%) between overt ARVC and control subjects. As shown in Fig. 2.11, abnormal subtricuspid strain reduced the false positive rate (FPR) from 50% ($n = 15/30$) to 22% ($n = 5/23$), while simultaneously reducing the false negative rate (FNR) from 44% ($n = 16/36$) to 25% ($n = 6/24$). In addition, accuracy increased from 53% ($n = 35/66$) to 77% ($n = 36/47$) Fig. 2.11.

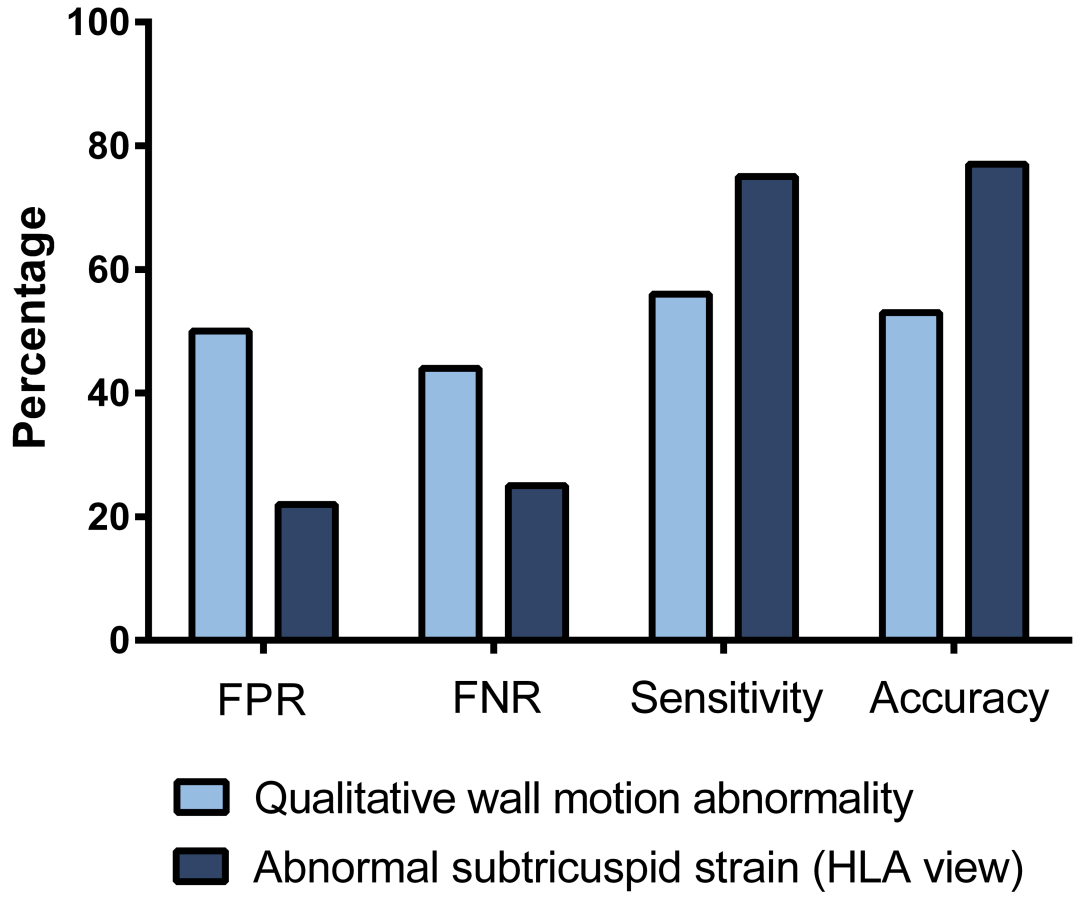


Figure 2.11: Diagnostic Performance of Subtricuspid Strain in ARVC. Diagnostic performance of abnormal strain (defined as more positive than −31% subtricuspid strain in the 4C view) compared to qualitative wall motion abnormality. Abbreviations: FPR: false positive rate; FNR: false negative rate, 4C: horizontal long axis.

2.3.4.5 Strain Reproducibility

Forty (40) randomly selected cases were reanalysed for intra- and inter-observer reproducibility. As judged by the thresholds specified in §2.3.3.4, intraobserver agreement was excellent in the 4C view (ICC = 0.81) and moderate in the axial (ICC = 0.66) and SA view (ICC = 0.70) (Fig. 2.12). Interobserver agreement was moderate in the 4C, axial, and SA views (ICC = 0.62, 0.60, and 0.61, respectively).

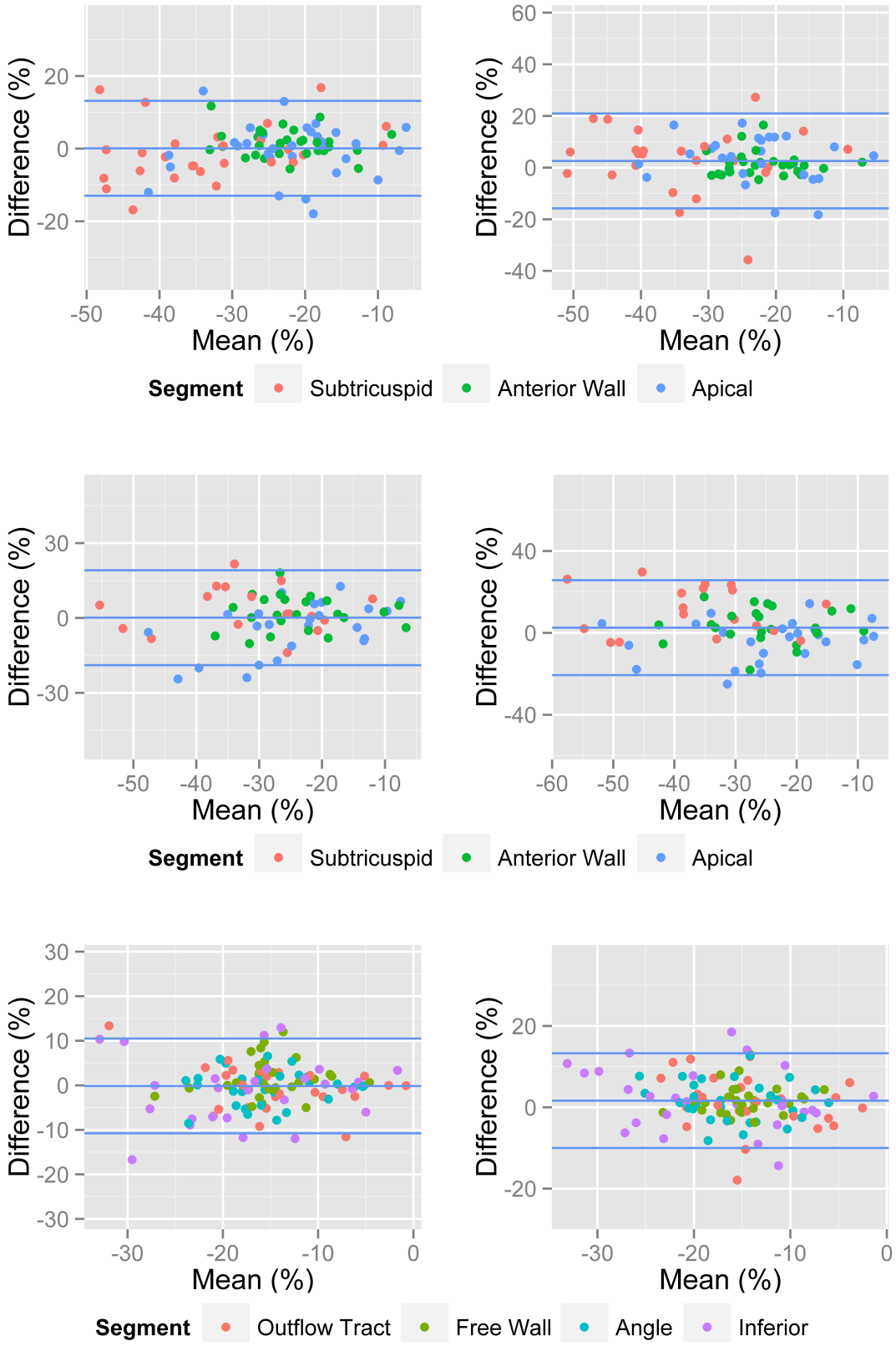


Figure 2.12: Reproducibility of Feature Tracking RV Strain in ARVC. Bland-Altman plots for intraobserver (left) and intraobserver (right) reproducibility in of strain measurements in the (a) horizontal long axis (top), (b) axial (middle), and (c) circumferential (bottom) views.

2.3.5 Conclusions

Qualitative determination of abnormal contraction patterns in the RV is currently a diagnostic problem for imaging physicians, due to the unusual shape and variations in contraction patterns of the RV. Using quantitative metrics, regional RV myocardial strain was assessed through CMR feature tracking in a cohort including control, preclinical, and overt ARVC subjects. Quantitative strain measurements were moderately reproducible within and between observers. Globally, strain magnitude was significantly lower in overt ARVC compared to control subjects in all CMR views. However, regional strain measured in the 4C view showed the greatest differences between control and overt ARVC subjects. Regionally, subtricuspid strain separated overt ARVC from control subjects with high sensitivity and specificity. Of note, abnormal strain had higher diagnostic accuracy with lower false positive and false negative diagnoses compared to qualitative wall motion assessment. These results suggest that CMR feature tracking may have clinical utility in ARVC evaluation.

In ARVC, a basic, yet unanswered question is the ideal plane of imaging. For feature tracking, the 4C view provided (a) the most reproducible measurements, (b) the greatest separation between overt and control, particularly in the subtricuspid region, and (c) a continuous downward trend in strain magnitude between control subjects, preclinical ARVC, and overt ARVC. The superior reproducibility and separation seen in 4C measurements may be due to less through-plane motion compared to axial and SA views.

Strain has previously been quantified in ARVC using speckle tracking echocardiography [97–100]. These studies have been limited by a combination of small numbers of patients and lack of regional analysis, genetic characterisation, and a preclinical ARVC group. Prior studies report global longitudinal RV strain of approximately -30% in control subjects, and varying study-to-study from -10 to -25% in overt ARVC. These values are in agreement with the results presented here. Impairment of regional function was primarily in the basal region of the RV, consistent with the finding that subtricuspid strain allowed for the greatest discrimination between control subjects and overt ARVC. These findings are also in

agreement with prior work showing that structural abnormalities most frequently localise to the subtricuspid region in ARVC. [61, 101] evaluated feature tracking of cine CMR in ARVC, including 20 patients with ARVC and 10 control subjects. In that study, the 4C view was not evaluated, so that long axis strain was evaluated only on axial views. Heermann et al [61] found that strain evaluated in the short axis views and ejection fraction provided the greatest difference between ARVC patients and normal subjects. Since the orientation of the heart within the chest cavity varies considerably between subjects, the angular variation between the true 4C long axis view and the axial view may be up to 35 degrees [102]. This variation may explain the result that the 4C view provided greater separation between ARVC patients and control subjects. In the multivariable model, regional subtricuspid strain was superior to global ejection fraction for prediction of the presence of disease, consistent with the concept of ARVC as a regional disease.

The present study suggests CMR feature tracking has the potential to improve the reliability of ARVC diagnosis and detection of regional wall motion abnormalities. Although CMR may be considered a standard of reference for ARVC, a long-standing limitation is the lack of quantitative metrics for regional wall motion abnormality of the RV [95, 103]. Although patients with overt ARVC have global changes in RV EF and volumes, preclinical ARVC patients who have known desmosomal mutations may have normal or only subtle RV motion abnormalities. Thus, a major focus of clinical effort is based on accurate phenotyping of this early ARVC group in order to accurately triage therapy. In this study, subjects with preclinical ARVC had strain abnormalities that were intermediate between control and overt subjects. Further studies are warranted to follow these patients over time to determine if they indeed represent a high-risk group who may progress to overt disease or have adverse cardiovascular events.

The results of this study should be interpreted in light of its strengths and limitations. Although ARVC is a relatively common reason for heart evaluation by CMR, the disease is quite rare and the sample size is therefore small. While this study is among the largest reported in the literature, a larger multicenter trial

may provide further insight. An important strength of this study is that clinical characterisation of study subjects was extensive and included genetic testing. In addition, ARVC diagnosis was made independently of CMR findings, so that the diagnostic TFC provide an independent standard of reference. While it would be interesting to correlate strain values by CMR feature tracking to those obtained by echocardiographic deformation imaging, reliable echocardiographic data was not available in part due to limitations of that technique for reliable identification of the RV. Finally, standard CMR SSFP images were utilised without further optimisation for feature tracking. It seems likely that improved temporal and/or spatial resolution of cine CMR may result in better feature tracking, possibly improving differences between patient groups and control subjects.

In conclusion, CMR feature tracking of the RV has the potential to provide reliable quantification of regional wall motion abnormalities in ARVC. The CMR approach identified abnormalities in ARVC most reliably in the 4C view. Compared to qualitative analysis, the approach provided incremental value in confirming the presence of wall motion abnormalities that were most commonly present in the subtricuspid region.

2.4 Conclusions

In this chapter, a commercial feature tracking CMR algorithm was used to assess LV function in a cohort of subjects with HCM, and RV function in a cohort of subjects with ARVC. In both cases, statistically significant differences in function were noted between healthy control subjects and patients with overt disease, suggesting that there may be clinical utility in this approach. Unfortunately, the technique remains subject to a number of limitations. First, tracking requires manual contouring at ED and ES, as well as frequent manual intervention to correct mistracked segments. This manual intervention is time-consuming, and contributes to only moderate reproducibility. Second, a significant number of series were excluded due either to poor image quality or poor tracking: 7.1% and 16.7% in the HCM and ARVC studies, respectively. That CMR feature tracking may be more difficult in longitudinal

views could possibly explain why initial attempts to quantify longitudinal strain in the HCM cohort were unsuccessful. Third, in the HCM study, compaction of the papillary muscles against the LV endocardium during contraction interfered with tracking, and required frequent manual correction. Finally, myocardial contraction is inherently a 3-D phenomenon, only part of which is captured by 2-D SSFP feature tracking. Subsequent chapters will focus on developing improved techniques to quantify cardiac motion which specifically address these limitations.

3

MRI: Uniform Quadratic Basis Spline Registration

Contents

3.1 Contributions 67
3.2 Introduction 68
3.3 Methods 69
3.3.1 Segmentation 70
3.3.2 Quadratic Bézier Curve Registration 72
3.4 Experiments 75
3.4.1 Data Preparation 75
3.4.2 Segmentation 76
3.4.3 SA Tracking 76
3.4.4 Regional Function 77
3.5 Results 77
3.5.1 Segmentation 77
3.5.2 Network Visualisation 80
3.5.3 Functional Parameters 87
3.6 Conclusions 91

3.1 Contributions

[1] Davis M. Vigneault, Weidi Xie, David A. Bluemke and J. Alison Noble. 'Feature Tracking Cardiac Magnetic Resonance via Deep Learning and Spline Optimization'. In: *FIMH*. Toronto, Canada: Springer, 2017.

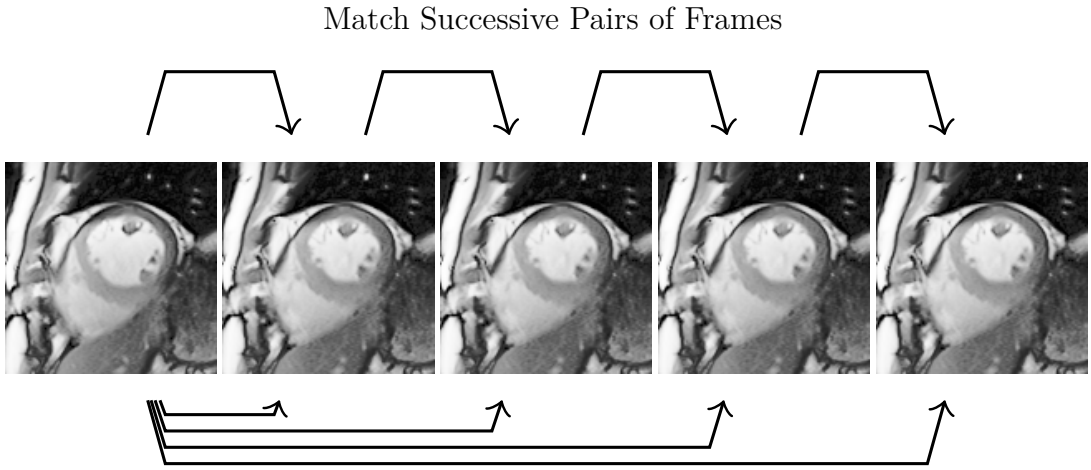


Figure 3.1: Schematic of Traditional Feature Tracking Methods. Each arrow represents a single pairwise registration between a fixed and moving image, and produces a displacement field. Through combinations of resampling, averaging, and regularization, these displacement fields are combined to form a final sequence of fields representing cardiac motion.

[2] Davis M Vigneault, Weidi Xie, Carolyn Ho, David A Bluemke and J Alison Noble. 'Omega-Net : Fully Automatic , Multi-View Cardiac MR Detection , Orientation , and Segmentation with Deep Neural Networks'. In: *Medical Image Analysis [In Preparation]* (2017).

3.2 Introduction

In Chapter §2, a commercial feature tracking (FT) algorithm was used to quantify regional left ventricular (LV) and right ventricular (RV) function from balanced Steady State Free Precession (SSFP) cardiac magnetic resonance (CMR) images. Strain by FT-CMR was found to be useful in both populations, identifying transmural strain variations in patients with both preclinical and overt hypertrophic cardiomyopathy (HCM), as well as RV subtricuspid dysfunction in patients with overt arrhythmogenic right ventricular cardiomyopathy (ARVC).

Despite these promising initial results, three important challenges remain. First, all current commercially available implementations (MTT, TomTec, CMR42, Medis) require manual contouring of one or more cine frames. Routine clinical use requires

full automation with excellent reproducibility. Second, LV papillary muscles frequently interfere with tracking, requiring manual correction of the contours §2.2.5. Third, feature tracking generally has been implemented by repeatedly applying methods designed to determine a displacement field between a *single pair* of images (e.g., optical flow, block matching, deformable registration), rather than an image *sequence*; either matching each frame to a single reference (typically end diastole, ED), or matching successive pairs (Fig 3.1). Each of these approaches has well-known potential drawbacks [53], which may be overcome by empirically optimising over all frames simultaneously [104].

In this chapter, a method is proposed for FT-CMR analysis which overcomes the first two of these challenges by using a deep learning approach in place of human contouring. Deep convolutional neural networks (CNNs) have been used to great effect in image classification [105, 106], and segmentation [107–109], including recently state-of-the-art performance in biomedical image analysis [110, 111]. CNN segmentation of short axis CMR has been applied to the LV blood-pool [112–114], the RV blood-pool [115], and both simultaneously [116, 117]. In this chapter, manual segmentation of the LV myocardium, LV blood-pool, and RV blood-pool is performed in three views: short axis (SA), horizontal long axis (4C), and vertical long axis (2C). Moreover, the segmentation is applied to a population of patients with HCM, as described in §2.2.3.1, which increases the complexity of the problem due to the highly variable appearance of the LV in these patients.

The last of these challenges is addressed by fitting quadratic basis splines to the segmentation data jointly, rather than frame by frame, adapting a technique presented in the context of cardiac ultrasound [104, 118]. In the proposed pipeline, *extraction* is performed using a CNN, *tracking* is performed with simultaneous spline optimisation, and cardiac strain is estimated from the registered basis splines.

3.3 Methods

Broadly, the automated analysis pipeline involves three steps: feature extraction (segmentation), feature tracking (spline fitting), and calculation of functional parameters

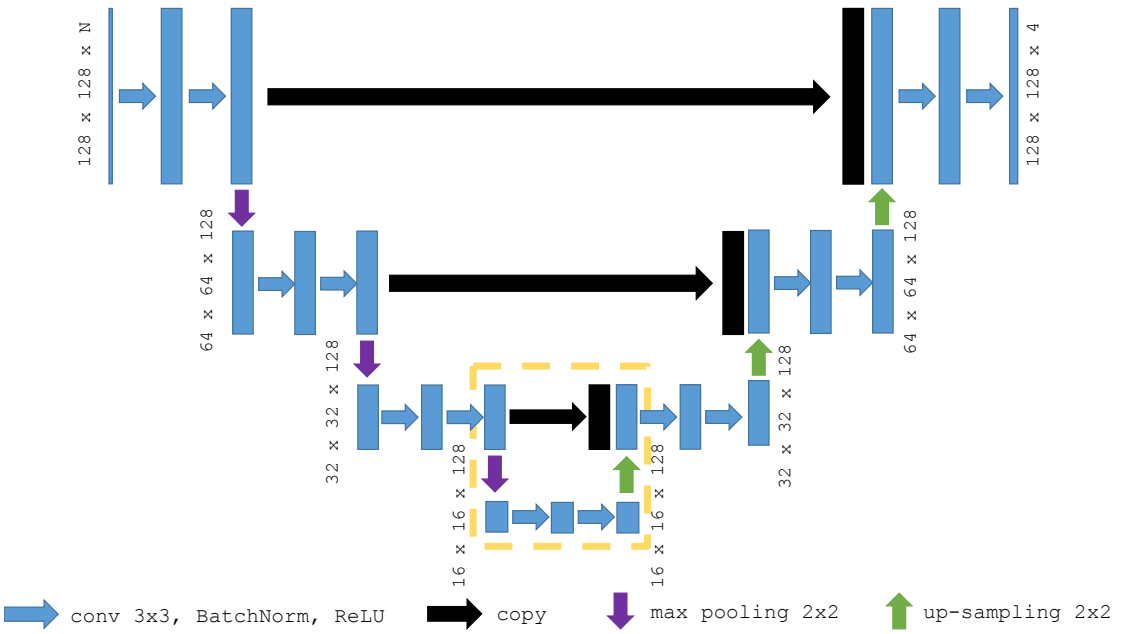


Figure 3.2: Architecture of the Baseline Segmentation Network. The input image is of size $128 \times 128 \times N$, where N is the number of channels (1 in networks A and B, 2 in networks C and D). Each blue and black box corresponds to a multilingual feature map (black indicates the result of a copy). The dimensions of the feature maps are indicated in the figure as first spatial dimension $\times$ second spatial dimension $\times$ channels. The number of channels in each feature map is fixed at 128. The dashed yellow box is replaced by dilated convolution in networks B and D.

(strain estimation). These steps are discussed in detail in the following sub-sections.

3.3.1 Segmentation

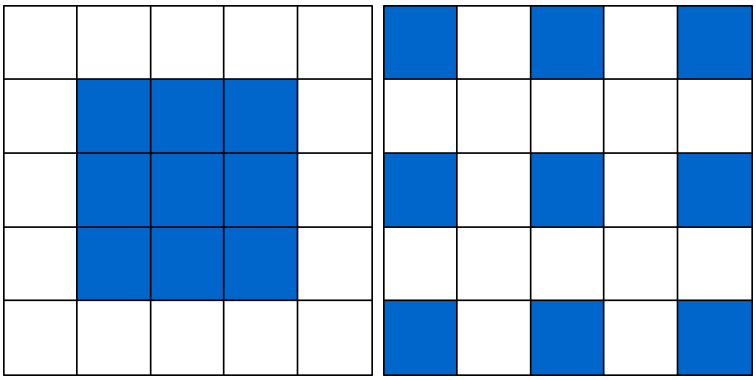
Following the work of [107, 110, 111], the segmentation architecture is designed as a fully convolutional network.[1] In order to obtain a segmentation map with the same spatial resolution as the input image, up-sampling operators are learned to compensate for the information loss due to the pooling operations in the downsampling path. This strategy enables the network to segment arbitrarily large images.

As shown in Fig. 3.2, the core U-Net architecture (which has performed well for biomedical image segmentation tasks, [110]) consists of a down-sampling path (left) followed by an up-sampling path (right) to restore the original spatial resolution. During the first several layers, the structure resembles the canonical classification

[1]The author would like to acknowledge Weidi Xie for his input in designing the network architectures.

Name	Variant	Input Size	Temporal Context
Network A	U-Net	$128 \times 128 \times 1$	None
Network B	DC	$128 \times 128 \times 1$	None
Network C	U-Net	$128 \times 128 \times 2$	ED Frame
Network D	DC	$128 \times 128 \times 2$	ED Frame

Table 3.1: CNN Architecture Variants Considered. ED: End Diastole; DC: Dilated Convolution.



(a) Simple Kernel **(b)** DC Kernel

Figure 3.3: Simple vs Dilated Convolution (DC) Kernels. (a) A simple 3×3 convolution kernel. (b) A 3×3 convolution kernel padded internally with zeros, resulting in a 5×5 DC kernel. Note that, relative to the simple convolution kernel, the receptive field is increased without increasing the number of parameters.

CNN [105, 106], as a 3×3 convolution, rectified linear unit (ReLU), and 2×2 max pooling are repeatedly applied to the input image and feature maps. In the second half of the architecture, the reduction in spatial resolution is "undone" by performing 2×2 up-sampling, ReLU activation, and 3×3 convolution, eventually mapping the intermediate feature representation back to the original resolution. To provide accurate boundary localisation, skip layers are used, where low-level feature representations from the down-sampling path are concatenated with feature maps from the up-sampling path. For all layers, 128 trainable kernels were applied. Batch normalisation [119], which has been shown to counteract gradient vanishing and to lead to better convergence, was performed between each pair of convolution and ReLU activation layers.

The architectures tested are summarised in Table 3.1. In addition to the core

architecture, the amount of temporal context was varied by either inputting the input image alone (Network A), or the input image and ED image together as a two-channel image (Network C). This was based on the intuition that the papillary muscles, which frequently interfere with LV segmentation, are least compacted at ED and may guide the segmentation of the input frame. Additionally, in Networks B and D, the final up-sampling/down-sampling pass was replaced by a dilated convolution (DC) [109], in which the convolution kernel is padded internally with zeros (Fig. 3.3) in order to expand the receptive field while maintaining a constant number of parameters. All architectures have ~ 3.1 million trainable parameters.

3.3.2 Quadratic Bézier Curve Registration

Following segmentation, contours defining the boundaries of the LV endocardium, LV epicardium, and RV endocardium were extracted through an exclusive or (`XOR`) operation with its binary morphological dilation. In this work, the pixels belonging to these contours are known as "boundary candidates". Unfortunately, these contours cannot be used directly to quantify cardiac function, because they lack anatomical correspondence between frames. It is the aim of the following subsections to define the closed, quadratic Bézier representation §3.3.2.1 and to describe an optimisation procedure for jointly registering a sequence of these curves to the boundary candidates §3.3.2.2.

3.3.2.1 Quadratic Bézier Curve Representation

A segment of a closed Bézier curve B of degree d parameterized by $s \in [0, 1]$ is a linear combination of $d + 1$ control points $x_i : 0 \leq i \leq d$,

$$B_d(s) = \sum_{i=0}^{d} b_{i,d}(s) x_i, \tag{3.1}$$

where $b_{i,d}(s)$ is the i^{th} Bernstein polynomial of degree d,

$$b_{i,d}(s) = \binom{d}{i} (1 - s)^{d-i} s^i, \tag{3.2}$$

and $\binom{d}{i}$, often read aloud as "d choose i", is the binomial coefficient,

$$\binom{d}{i} = \frac{d!}{i!(d-i)!}. \tag{3.3}$$

For $d = 2$, $B_2(s)$ expands to

$$B_2(s) = (1-s)^2 x_0 + 2s(1-s)x_1 + s^2 x_2, \tag{3.4}$$

which may be more conveniently expressed in terms of the monomial basis as

$$B_2(s) = \begin{bmatrix} x_0 & x_1 & x_2 \end{bmatrix} \begin{bmatrix} (1-s)^2 \\ 2s(1-s) \\ s^2 \end{bmatrix} = \begin{bmatrix} x_0 & x_1 & x_2 \end{bmatrix} \begin{bmatrix} 1 & -2 & 1 \\ 0 & 2 & -2 \\ 0 & 0 & 1 \end{bmatrix} \begin{bmatrix} 1 \\ s \\ s^2 \end{bmatrix}. \tag{3.5}$$

Importantly, the first and second derivatives of $B_2(s)$ with respect to s are trivial to compute.

3.3.2.2 Formulating the Optimisation

Levenberg-Marquardt least squares optimisation [120] was used to register a set of closed, quadratic Bézier curves to the boundary candidates. The parameters $\Delta X \in \mathbb{R}^{2\times(C\times K)}$ (where C is the number of control points in a single curve and K is the number of cardiac phases) of the optimisation are Cartesian displacements to the control points of all curve initialisations across all frames. A fixed number of points $\mathbf{u}_{f,j,s}$ were sampled across each curve. At each step in the optimisation, for each of these points, the nearest boundary candidate $\phi\left(\mathbf{u}_{f,j,s}\right)$ was calculated, where $\phi : \mathbb{R}^2 \to \mathbb{R}^2$. This was computed efficiently by representing the boundary candidate point set at each frame as a K_d tree. The Cartesian components of the distance between the points sampled from the curve and nearest boundary candidate were the residuals of E_{cf}, the first term of the cost function,

$$E_{cf} = \sum_{f,j,s} \| \mathbf{u}_{f,j,s} - \phi\left(\mathbf{u}_{f,j,s}\right) \|^2. \tag{3.6}$$

Additionally, two regularizers were included to enforce physical constraints of anatomical deformation: control point acceleration and spline curvature.

In the cost function, the control point acceleration regularizer allows information to be shared between frames. At a minimum, regularising against control point velocity as in [104] is necessary to maintain anatomical consistency (the assumption that, for fixed j and s, $\mathbf{u}_{f,j,s}$ corresponds to the same material point $\forall f$). By regularising against acceleration rather than velocity, the proposed method additionally encourages smooth, biologically plausible motion. The control point acceleration regularizer E_{ac} was defined as the Cartesian components of the second differences between corresponding vertices $\mathbf{x}_{f,c}$ in three adjacent frames, where $\mathbf{x}_{f,c}$ is the $(f \times C + c)^{\text{th}}$ column of X.

$$E_{ac} = \sum_{f,c} \left\| \begin{bmatrix} 1 & -2 & 1 \end{bmatrix} \begin{bmatrix} \mathbf{x}_{(f+2) \bmod K,c}^{\top} \\ \mathbf{x}_{(f+1) \bmod K,c}^{\top} \\ \mathbf{x}_{f,c}^{\top} \end{bmatrix} \right\|^2 \tag{3.7}$$

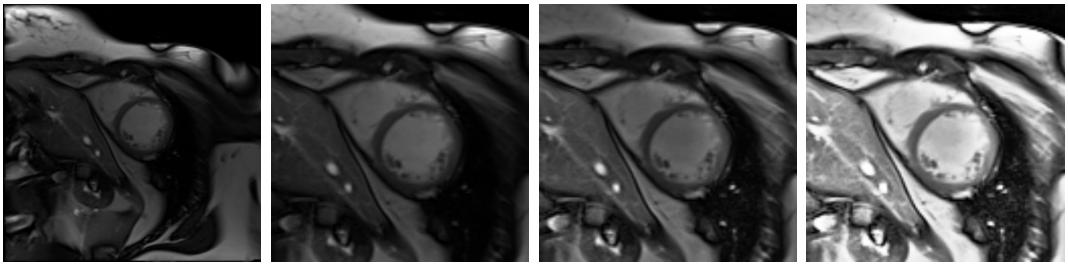
Curvature for segment j in frame f is the second derivative of $B_2(s)$ with respect to s.

$$E_{cv} = \sum_{f,c} \left\| \frac{d^2 B_2(s)}{ds^2} \right\|^2 \tag{3.8}$$

The overall optimisation problem may then be written in terms of Eqns. 3.6, 3.7, and 3.8 and corresponding scaling factors. Scaling factors $\rho_{cf} = 1.0$, $\rho_{ac} = 10.0$, and $\rho_{cv} = 0.1$ were set empirically to prevent any single term from dominating the optimisation.

$$E = \min \left(\rho_{cf} E_{cf} + \rho_{ac} E_{ac} + \rho_{cv} E_{cv} \right) \tag{3.9}$$

Two points relating to computational efficiency are worth noting. First, the Jacobians of Eqns. 3.6, 3.7, and 3.8 can all be calculated analytically. By providing explicit Jacobians, the need for numeric derivatives, which would slow computation precipitously, is avoided. Moreover, for a given set of correspondences between surface positions and boundary candidates, the Jacobians of all residuals are linear with respect to the Cartesian displacements of the control points and therefore trivial to calculate. Second, each individual residual depends upon a very small number of parameters. Specifically, each individual residual depends on exactly three



(a) **(b)** **(c)** **(d)**

Figure 3.4: Preparation of Image Data for CNN Segmentation. (a) Unproccessed input image. (b) Cropped image. (c) Background corrected image. The illumination field was estimated by thresholding the image below the 25^{th}percentile (with the replacement value being the previous 25^{th}percentile) and blurring the result with a 10×10 pixel gaussian kernel. Nonuniform illumination was corrected by dividing by cropped image by the estimated illumination field. (d) Histogram equalized image.

control points (six parameters). This sparsity is exploited during the optimisation to limit the number of components of the Jacobian which must be evaluated, further reducing computational cost.

Following the initial fit, the spline is subdivided and used to initialise a second optimisation, and this process is repeated one further time. This multiresolution approach avoids the sensitivity to initialisation which limits direct registration of the highly subdivided spline.

3.4 Experiments

3.4.1 Data Preparation

The data set consisted of 63 subjects described previously (§2.2.3.1), consisting of 42 patients with overt HCM and 21 healthy control subjects. Patients with preclinical HCM were not considered. Where available, three SA (basal, equatorial, and apical), one 4C, and one 2C SSFP cine series was obtained. Each volume was cropped to 128×128 pixels in the spatial dimensions, and varied from 20 to 50 frames in the time dimension. Nonuniform background illumination was corrected by dividing by an estimated illumination field, and background corrected images were histogram equalised (Fig. 3.4). Note that background illumination correction and histogram equalization are deterministic and require no user interaction.

3.4.2 Segmentation

The LV myocardium, LV blood-pool, and RV blood-pool were manually segmented in the SA, 4C, and 2C views (noting that the RV is not visible in the 2C view) using ITK-SNAP [121]. The papillary muscles of the LV and the trabeculation of the LV and RV were excluded from the myocardium. The subjects were partitioned into three folds of approximately equal size (4477, 4750, and 4625 images, respectively) such that the images from any one subject were present in one fold only. To perform cross validation, the four architectures employed (U-Net and DC with and without temporal information) were each trained on all three combinations of two folds and then tested on the remaining fold. The images were normalised to zero mean and unit standard deviation before being input into the CNN. The network weights were initialised with orthogonal weights [122], and were trained with standard stochastic gradient descent (SGD) with momentum (0.9) by optimising categorical cross-entropy. The learning rate was initialised to 0.001 and decayed by 0.1 every 16 epochs. To avoid over-fitting, considerable data augmentation (horizontal and vertical flipping, random translations and rotation) and a weight decay of 10^{-4} was used. Pixel accuracy and foreground intersection-over-union (IoU) were calculated imagewise between the prediction and manual segmentations. The model was implemented in the Python programming language using the Keras interface to Tensorflow [123], and trained on one NVIDIA Titan X graphics processing unit (GPU) with 12 GB of memory. For all network architectures, it took roughly 200 seconds to iterate over the entire training set (1 epoch). At test time, the network predicted segmentations at roughly 75 frames per second (real-time).

3.4.3 SA Tracking

Following segmentation, the LV endocardium, LV epicardium, and RV endocardium were tracked in all SA scans using the spline optimisation method. The tracking algorithm was implemented in the `C++` programming language using the Insight Toolkit (ITK) [124, 125] for reading, writing, and manipulating images and point

sets, and using the Ceres Solver [126], configured with OpenBLAS [127] for least squares optimisation. The three registration passes took $\sim 2.1s$ per cine sequence.

3.4.4 Regional Function

Following SA tracking, registered splines from the 63 subjects were used to calculate global strain. For each structure in each SA plane, global strain was compared between HCM and control subjects using the Student's t-test.

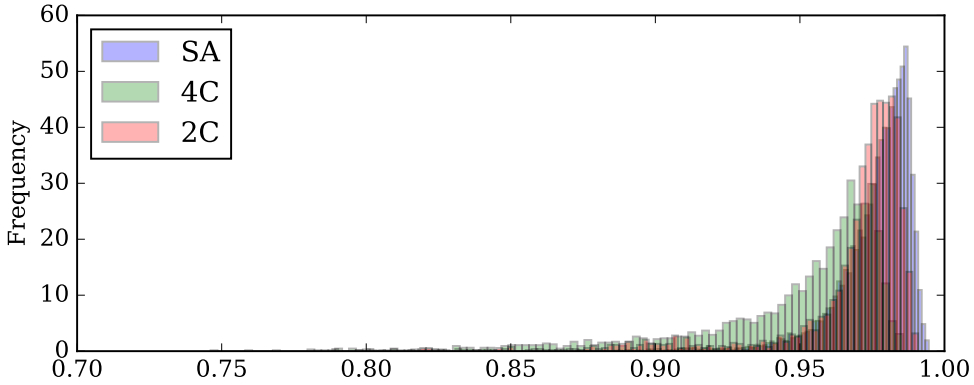
3.5 Results

3.5.1 Segmentation

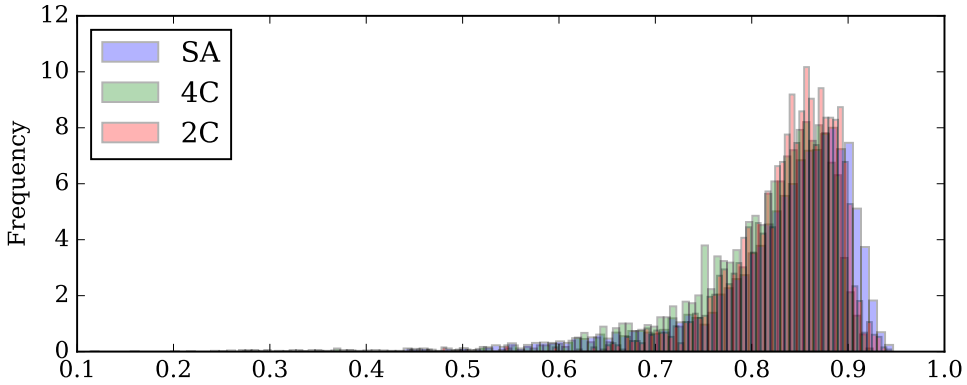
As accuracy is not necessarily the same across all clinical planes, the performance of the four networks relative to expert manual segmentation is reported for all views combined, and also for each clinical plane separately (Table 3.2). Accuracy metrics were calculated separately for each image, and the median and interquartile range (IQR) of all predictions is reported. Performance was similar across all networks. For all views combined, median pixel accuracy was $\sim 98\%$, and median intersection-over-union (IoU) across all foreground classes was $\sim 85\%$. For a binary image (one foreground class, one background class), IoU (also known as the Jaccard index) is defined for the ground truth and predicted images I_T and I_P as

$$IoU\left(I_T, I_P\right) = \frac{|I_T \cap I_P|}{|I_T \cup I_P|}. \tag{3.10}$$

To extend this concept to multiclass segmentation, IoU was calculated separately for each foreground class (LV bloodpool, RV bloodpool, and LV myocardium). A weighted sum of these three IoU values was then calculated, where the weights were given by the ratio between the relevant foreground class and the union of all foreground classes. When calculated separately for the SA, 4C, and 2C views, all networks again performed similarly in terms of both pixel accuracy and weighted foreground IoU. Small differences were noted between views, however, with both metrics being highest in the SA view and lowest in the 2C view. These differences



(a) Pixel Accuracy



(b) Weighted Foreground IoU

Figure 3.5: Histograms of Segmentation Metrics for Network A. Performance relative to expert manual segmentation was highest in the SA view and lowest in the 4C view, though the differences are small.

are also apparent in the image-wise accuracy distributions (Fig. 3.5). That the differences between views are more pronounced in terms of pixelwise accuracy than weighted foreground IoU follows from systematic differences in foreground-to-background ratio between views.

It should be noted that similar performance across networks does not necessarily mean that the four architecture variants have comparable representational capacity; more likely, it suggests that the complexity of the problem can be sufficiently represented by the simplest network (Network A: U-Net with no temporal context), and that increasing network complexity therefore does not yield improvements in segmentation performance. It is possible that, were the complexity of the problem to

Name	Description	View	Pixel Accuracy (%)	Weighted Foreground IoU
Network A	U-Net, No Context	All	97.6 [96.5, 98.3]	0.846 [0.798, 0.879]
		SA	98.0 [97.1, 98.5]	0.851 [0.801, 0.884]
		4C	96.1 [93.9, 97.1]	0.831 [0.778, 0.866]
		2C	97.6 [96.7, 98.1]	0.848 [0.810, 0.876]
Network B	DC, No Context	All	97.6 [96.5, 98.3]	0.846 [0.799, 0.879]
		SA	98.0 [97.2, 98.5]	0.851 [0.800, 0.885]
		4C	96.1 [94.3, 97.1]	0.833 [0.789, 0.865]
		2C	97.6 [96.7, 98.1]	0.847 [0.808, 0.876]
Network C	U-Net, Context	All	97.6 [96.6, 98.3]	0.848 [0.799, 0.879]
		SA	98.0 [97.2, 98.5]	0.853 [0.800, 0.885]
		4C	96.2 [94.1, 97.1]	0.833 [0.783, 0.867]
		2C	97.6 [96.8, 98.1]	0.846 [0.810, 0.873]
Network D	DC, Context	All	97.6 [96.5, 98.3]	0.846 [0.797, 0.880]
		SA	98.0 [97.1, 98.5]	0.852 [0.795, 0.885]
		4C	96.2 [94.0, 97.0]	0.830 [0.781, 0.862]
		2C	97.7 [96.9, 98.1]	0.849 [0.815, 0.878]

Table 3.2: Network Performance Compared with Ground Truth. Pixel accuracy and weighted foreground IoU of each network are calculated for all views combined and for each view separately. All four networks performed similarly in terms of both metrics. Network performance was highest in the SA view and lowest in the 4C view, though these differences are small.

be substantially increased (for example, by increasing both the number of foreground classes and the number of clinical views), performance differences between networks may emerge. For this reason, Network A was chosen for further analysis.

Representative segmentations produced by Network A in all views are shown for a control subject in Fig. 3.6 and for a patient with overt HCM in Fig. 3.7. Notably, the myocardial segmentation consistently excludes papillary muscles and myocardial trabeculation. Moreover, the network appears to reliably identify the atrioventricular valve plane in the long axis views, such that the RV and LV bloodpool segmentations correctly exclude the atria.

Occasional failure cases were observed, a selection of which are shown in Fig. 3.8. Fig. 3.8a shows a very apical segment at ES. Significant through-plane motion combined with relative infrequency of very apical segments in the dataset likely contributed to this failure. Fig. 3.8b shows an overt subject with extreme left atrial (LA) dilation, in which part of the LA is mistaken for the RA. In this ES frame, the LA is the largest chamber of the heart, and has approximately rotational symmetry with the RA along the septal plane. It is notable that the ventricles are segmented correctly, and that this segmentation is recovered in practice by selecting the largest connected component of each foreground class prior to tracking analysis. Finally, Fig. 3.8c shows a failure attributed to a combination of poor cardiac section and through-plane motion.

3.5.2 Network Visualisation

In order to gain insight into the features learnt by Network A, two methods to visualize the trained network were investigated.[2] In each case, an image is synthesized by solving an optimization problem involving the trained network.

3.5.2.1 Maximizing Filter Response

Intuitively, the objective of the first method is to increase the confidence of predicting a given (fixed) segmentation mask by perturbing an input image [128]. Given the

[2]The author would like to acknowledge Weidi Xie for his input in the network visualisation experiments.

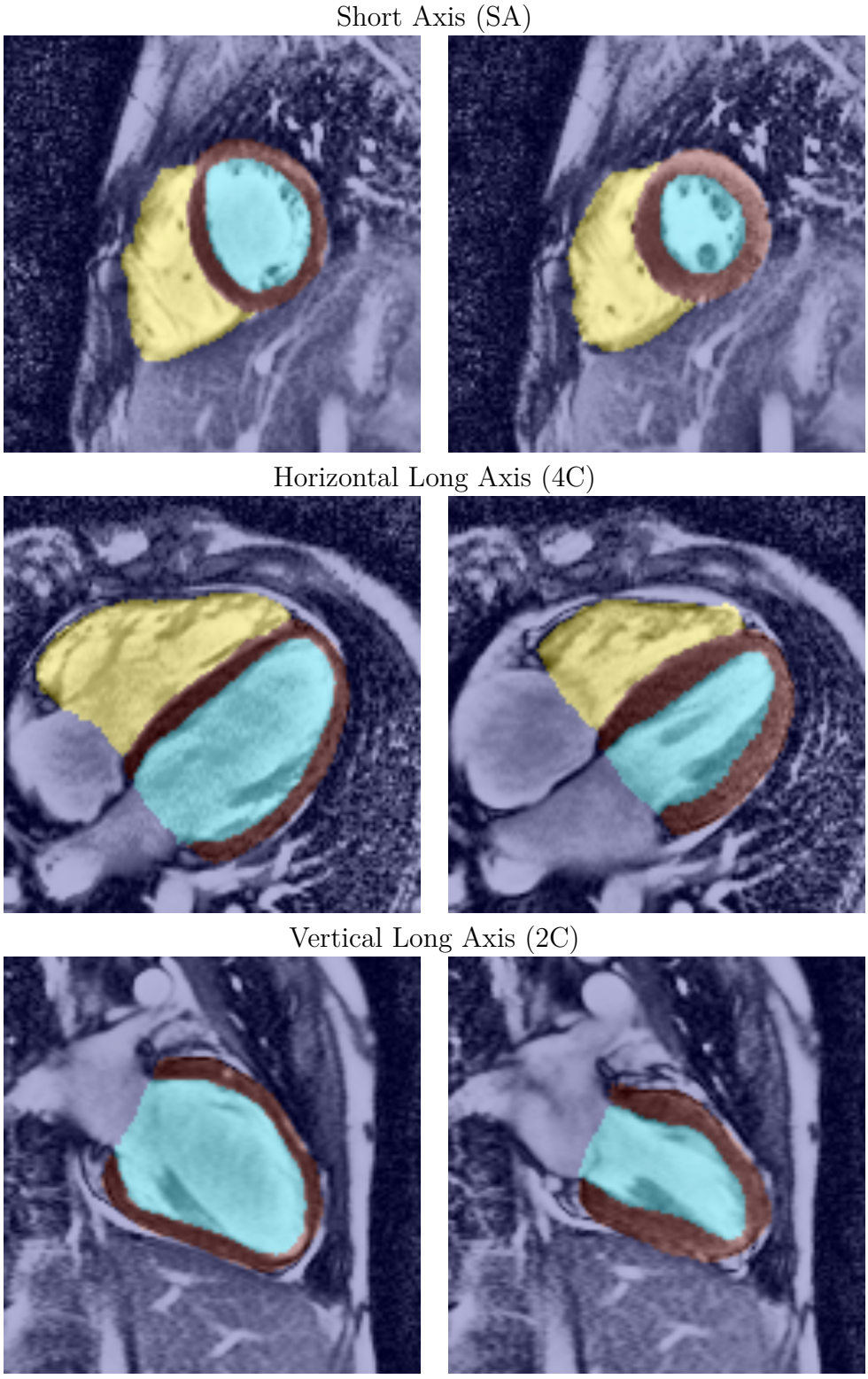


Figure 3.6: Representative Segmentation Results in a Healthy Subject. End diastolic (ED) and end systolic (ES) frames are shown in the left and right columns, respectively. Segmentation results were produced using Network A.

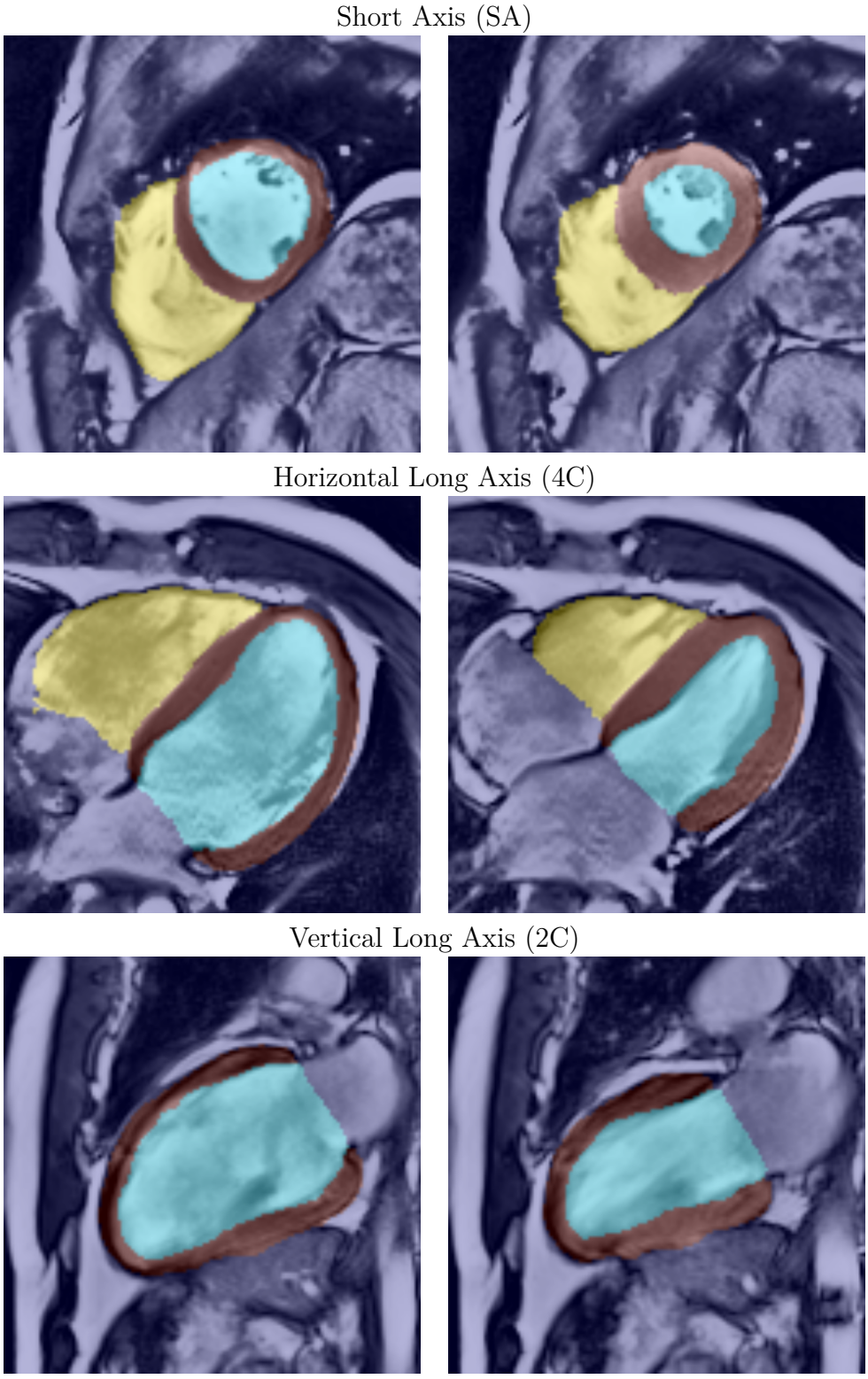
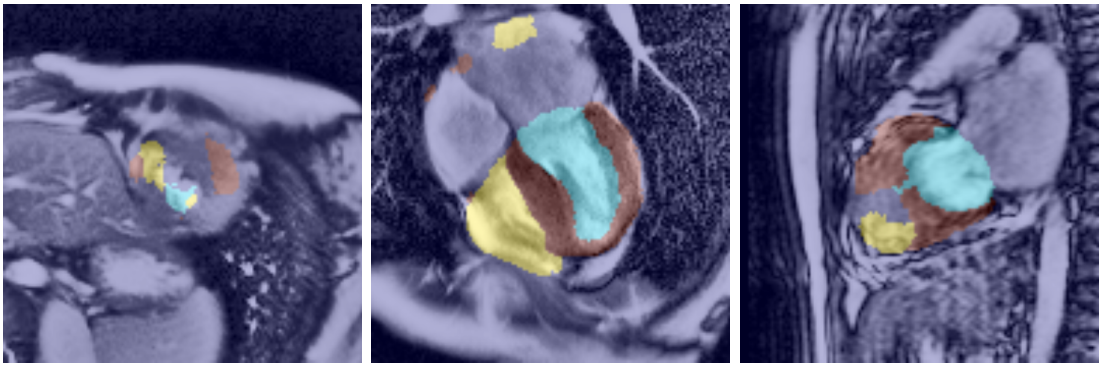


Figure 3.7: Representative Segmentation Results in Overt HCM. End diastolic (ED) and end systolic (ES) frames are shown in the left and right columns, respectively. Segmentation results were produced using Network A.



(a) SA **(b)** 4C **(c)** 2C

Figure 3.8: Selected Failure Cases from CNN Segmentation. See text for discussion.

space of all possible input images $I_x \in \mathbb{R}^{128\times128}$, the input image I_i is the particular position in I_x which maximises the predicted score $s_c(I_x)$ (the value immediately prior to the soft-max) of a single pixel in the segmentation mask. I_x is initialised with random noise and 300 iterations of gradient ascent are used to update I_x in such a way that the score $s_c(I_x)$ is maximized, while also L_2-regularising I_x,

$$I_i = \underset{I_x\in\mathbb{R}^{128\times128}}{\operatorname{argmax}} \left(s_c(I_x) - \rho\|I_x\|^2 \right), \tag{3.11}$$

where ρ is an empirical factor to scale the regulariser. This concept extends trivially from prediction of a single pixel $s_c(I_x)$ to a complete segmentation mask $S_c(I_x)$ (the mean of all pixels).

This technique was employed both with each foreground class individually, and with the mean of all foreground classes (Fig. 3.9). In the case of the LV and RV bloodpools alone, the region of interest is slightly illuminated, with a cloudy superimposed texture oriented in a radial orientation. In the case of the LV myocardium alone, a smooth ring structure is produced. When all classes are combined, both bloodpools are illuminated (though the RV endocardium in particular remains unclear) and the ring structure is somewhat better defined.

Overall, the feature map is cluttered and resistant clear to human interpretation. One hypothesis for this result is that the maximum predictions incorporate features from *all three clinical planes*. In order to investigate this hypothesis, Network A

was retrained on the *SA slices alone*, thus reducing the number of variables, and the same visualisation was calculated (Fig. 3.10). The analogous visualisations produced by this single-view network can more easily be explained. The LV bloodpool mask alone produces a pronounced papillary muscle template, repeated throughout the blood pool. The RV bloodpool alone similarly produces a repeated trabeculation template. The LV myocardium mask again produces a smooth ring structure, but now with endocardial trabeculation clearly visible. When all classes are combined, the trabeculation and papillary muscle templates persist, but are now localised, which one may hypothesise is due to the additional constraints posed by the orientation of the RV bloodpool relative to the LV bloodpool and myocardium.

More interestingly, the single-view visualisation demonstrates that the network learns contextual information in addition to the segmented structures. For instance, when maximising the input to predict RV bloodpool, the network also synthesises a surprisingly well-defined LV myocardium and bloodpool, which presumably serve as context information that increases the confidence of the prediction. Similar observations may be made for the other two foreground classes. This suggests that the network has learned to incorporate global information during prediction, rather than relying solely on local image features.

Given the striking difference in maximum predictions produced by Network A when trained on the three views together versus the SA views alone, with the latter being far more amenable to human interpretation, it is reasonable to hypothesise that the multi-view network's ability to internally represent any individual view is impaired relative to that of a single-view network. If this were the case, the single-view network would be expected to perform better. However, the single-view and combined-view networks in fact performed similarly (within $\sim 0.3\%$ pixel accuracy). This suggests that the "noisy" appearance of the maximum predictions produced by the multi-view network relative to the single-view network represents a loss of human interpretability, but not necessarily a loss of information.

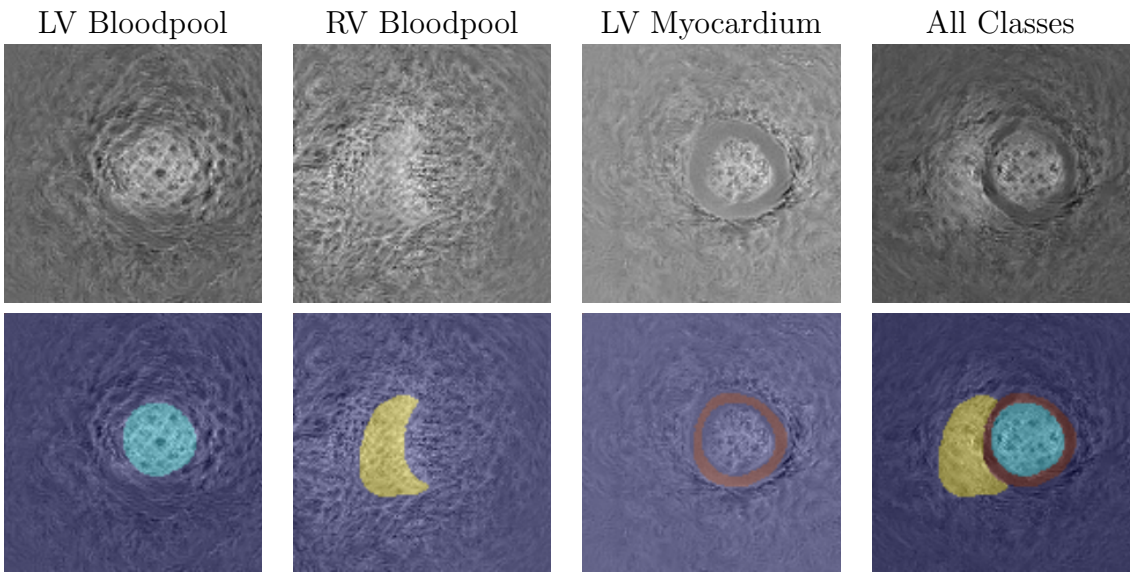


Figure 3.9: Maximum Prediction from a SA Mask (Multi-View Network). The synthesized feature maps maximizing the given feature map are shown with (bottom) and without (top) the mask overlay. See text for discussion.

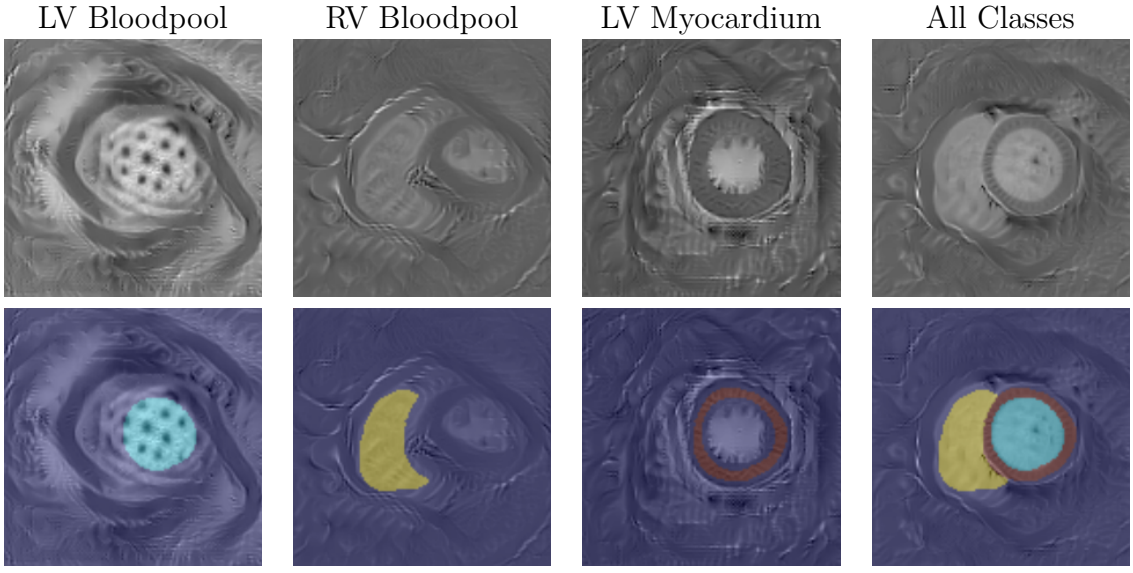


Figure 3.10: Maximum Prediction from a SA Mask (Single-View Network). The synthesized feature maps maximizing the given feature map are shown with (bottom) and without (top) the mask overlay. See text for discussion.

3.5.2.2 Minimizing Information Loss

The previous section visualised the information retained by the network after training, by synthesizing the input which maximally predicts a given ground truth segmentation. Here, conversely, the degree to which a given input image may be reconstructed by a feature representation at various network depths is visualised. The feature representation may be viewed as a form of data compression; therefore, the input approximation synthesised from this feature representation gives insight into which features are retained by the network, and which are discarded.

This visualisation is again formulated as an optimisation problem [129]. Given the space of all possible input images $I_x \in \mathbb{R}^{128\times128}$ and a fixed input image I_f, the synthesised input I_i is a specific position in I_x which minimises the loss between the feature representations $\phi(I_x)$ and $\phi(I_f)$, subject to L_2-regularisation of I_x,

$$I_i = \underset{I_x\in\mathbb{R}^{128\times128}}{\arg\min} \left(\|\phi(I_x) - \phi(I_f)\|^2 + \rho\|I_x\|^2 \right), \tag{3.12}$$

where ρ is an empirically-defined factor to scale the regulariser. The information loss is visualised at every other convolutional layer throughout the multi-view network (Fig. 3.11). As expected, fine detail is discarded throughout the downsampling path. It is noteworthy that some information is recovered through the upsampling path due to the skip connections. Although the image synthesised from the deepest layers (Fig. 3.11) bears little resemblance to the input image, careful inspection reveals circumferential "wrinkles" which neatly circumscribe the heart.

As before, the visualisation was also performed on the single-view network (Fig. 3.12). As in the multi-view case, fine detail lost in the downsampling path is regained to a large extent in the upsampling path. The image synthesised from the 9th convolutional layer bears somewhat greater resemblance to the input image, maintaining clearly each of the three foreground classes. Also of note is that the LV papillary muscles and RV trabeculations are faithfully reconstructed in the 15th convolutional layer.

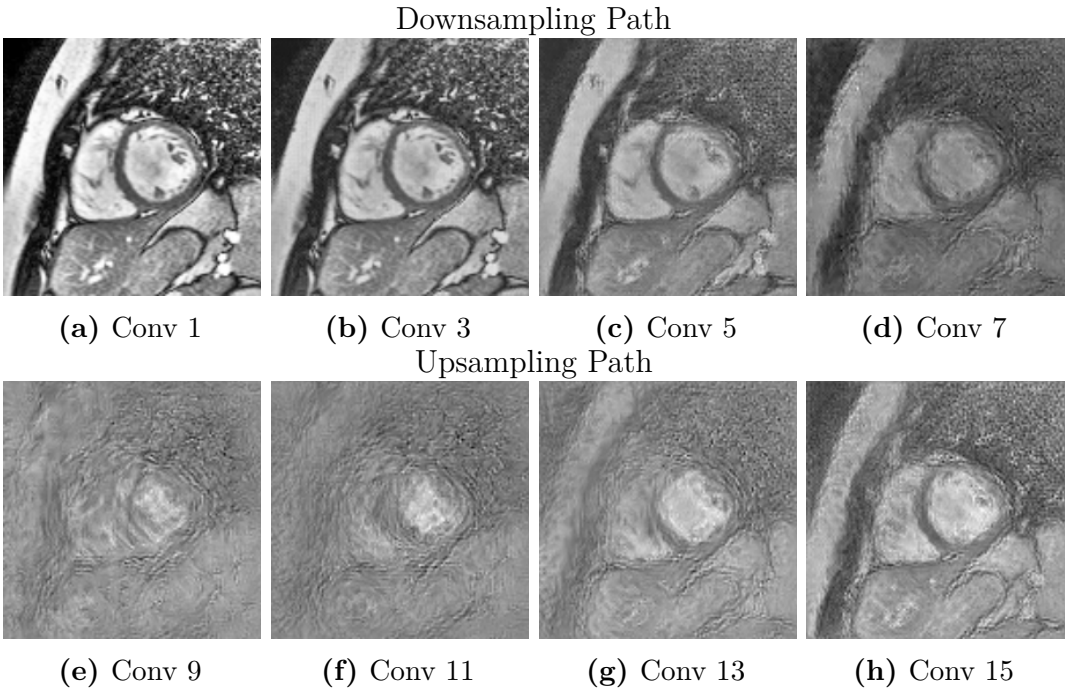


Figure 3.11: Information Loss given a SA Image (Multi-View Network).

Two competing interpretations of the data immediately suggest themselves. The first is that, as the single-view network appears to retain more information in the deepest network layers, the depth of the feature vector should be increased in the multi-view network so as to allow a more complete representation. The second is that the majority of the information being used in the segmentation task is passing through the skip connections, and that the deepest downsampling/upsampling level (convolutional layers 6 through 9) could be discarded without significant loss of accuracy. Investigation of this question is potentially interesting, and left for future work.

3.5.3 Functional Parameters

Tracking was performed in three passes (Fig. 3.13), where the output of one pass was subdivided and passed to the next pass. In each pass, the contours tighten towards the segmentation, allowing for acute structures such as the RV insertion points to be better described. Compared with registering a highly subdivided spline directly, this technique avoids local minima and affords faster convergence.

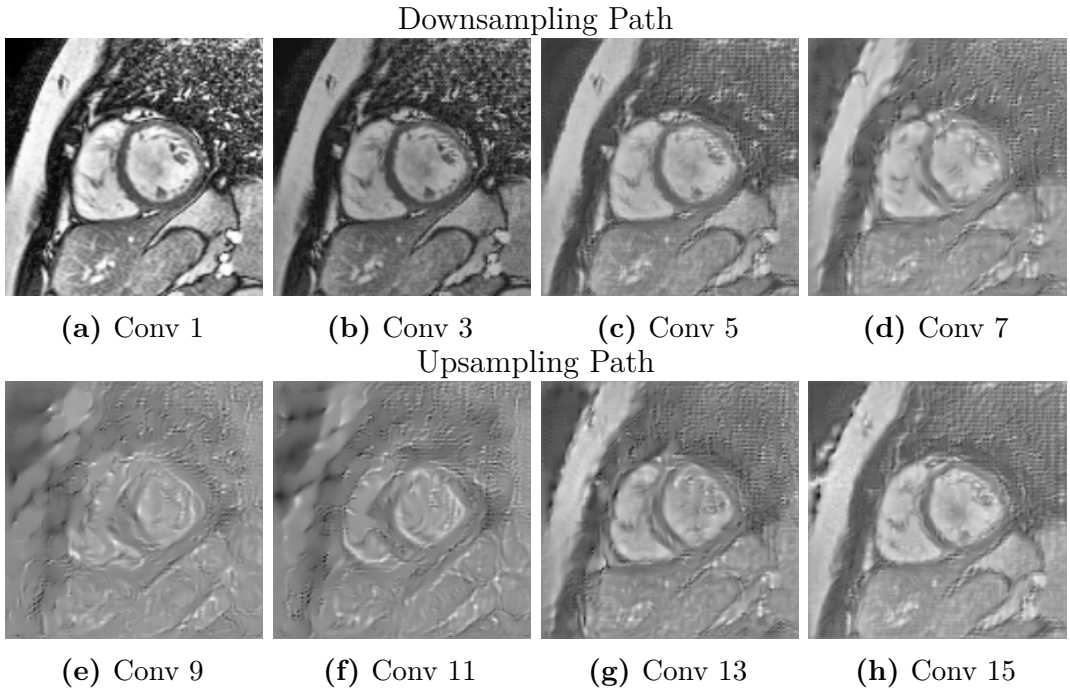


Figure 3.12: Information Loss given a SA Image (Single-View Network).

Representative tracking results are shown for control and overt subjects (Fig. 3.14). Tracking visually followed the contours of the segmentation closely.

As HCM is a pathology primarily of the LV, strain analysis was performed in the LV endocardium and epicardium in all three clinical planes.

In terms of global strain (Table 3.3), shortening was greater (circumferential and longitudinal strain was more negative) at the endocardium compared with the epicardium for each clinical plane within each patient group, as expected from prior studies [130] and from geometric considerations [8, 78]. Circumferential shortening at the basal epicardium was lower (i.e., strain was less negative) in patients with overt HCM compared with control subjects (-10.6 ± 3.5 vs $-13.2 \pm 3.1\%$, $p < 0.01$), while circumferential shortening at the midslice endocardium was higher (i.e., strain was more negative) in patients with overt HCM compared with control subjects (-28.7 ± 6.0 vs $-24.7 \pm 4.4\%$, $p < 0.05$). No other differences in global strain were observed.

In order to further investigate the circumferential differences noted in the global strain analysis, segmental strain analysis was additionally performed in the three SA views (Table 3.4). These results show that the difference in global

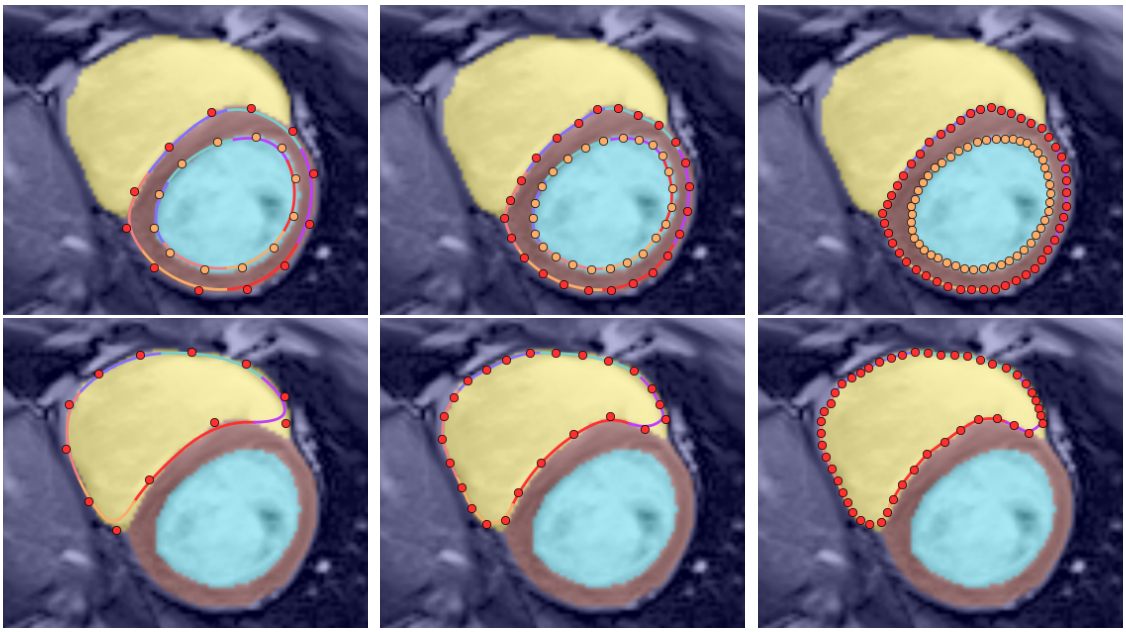


Figure 3.13: Multiresolution Spline Registration. Spline registration was conducted in successive passes (left to right), where the output of one was subdivided and used to initialise the next. LV and RV tracking results are shown above and below, respectively. Note especially regions of acute curvature, such as the insertion of the RV on the LV, which improves from left to right as the granularity of the spline increases.

Plane	Structure	Control (%)	Overt (%)	p
SA - Base	LV Endocardium	-28.0 ± 4.1	-28.6 ± 6.3	NS
	LV Epicardium	-13.2 ± 3.1	-10.6 ± 3.5	<0.01
SA - Midslice	LV Endocardium	-24.7 ± 4.4	-28.7 ± 6.0	<0.05
	LV Epicardium	-8.9 ± 2.7	-7.7 ± 3.2	NS
SA - Apex	LV Endocardium	-24.9 ± 7.8	-29.8 ± 13.6	NS
	LV Epicardium	-10.3 ± 3.5	-11.8 ± 13.7	NS
4C	LV Endocardium	-17.0 ± 3.8	-18.1 ± 5.2	NS
	LV Epicardium	-11.7 ± 3.9	-13.4 ± 4.2	NS
2C	LV Endocardium	-18.8 ± 3.7	-19.3 ± 6.9	NS
	LV Epicardium	-13.6 ± 2.5	-13.0 ± 3.9	NS

Table 3.3: Global LV Strain in Overt HCM vs Control Subjects. Global LV endocardial and epicardial strain is reported in patients with overt HCM compared with healthy control subjects in all three clinical planes, and in all three SA slices. Consistent with prior studies, circumferential endocardial strain is

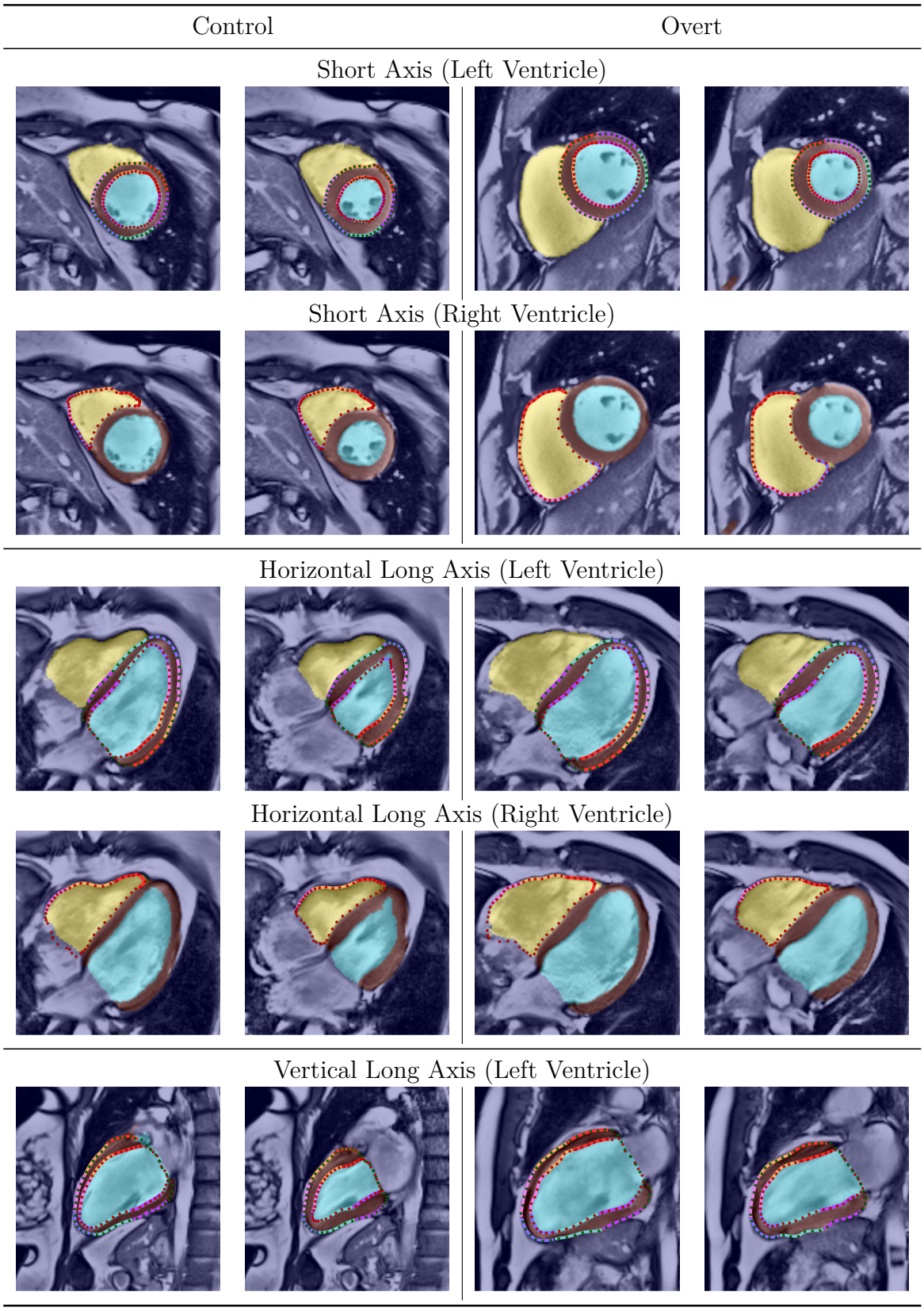


Figure 3.14: Segmentation and Tracking Results. Results are shown in a control subject and a patient with overt HCM. Contours are shown for the three clinical planes in the LV and RV, as applicable, both at ED (left) and ES (right).

epicardial circumferential strain in the basal slice between patients with overt HCM and control subjects was due primarily to the interior, anteroseptal, and inferior segments, whereas the difference between global endocardial circumferential strain in the midslice was primarily due to the septal and lateral segments. Additionally, segmental differences were apparent in the LV endocardium in the basal slice, and in the LV epicardium in the midslice, which were not observed in the global measurements, underscoring the value of regional functional analysis.

The result that endocardial and epicardial circumferential strain are more and less negative in subjects with overt HCM compared with control subjects is consistent with the results presented in §2.2.

Representative endocardial and epicardial strain curves are shown for the three clinical views in a healthy control subject (Fig. 3.15) and in a patient with overt HCM (Fig.3.16). In each subject, end systole is reached at approximately the same frame for both endocardial and epicardial strain, as expected.

3.6 Conclusions

Measuring cardiac function in a fully automated way from SSFP CMR has the potential to simplify quantification of regional cardiac function, and expedite clinical adoption of regional functional analysis. In this chapter, a method has been presented for fully automated cardiac segmentation, tracking, and estimation of cardiac strain. Segmentation results with and without temporal context in U-Net and DC architectures performed similarly, with a median pixel accuracy of $\sim 98\%$, and median IoU across all foreground classes of $\sim 85\%$. A feature tracking algorithm taking these segmentations as input and jointly optimising a set of quadratic splines over all frames simultaneously was also presented. This segmentation and tracking was applied to the LV endocardium, LV epicardium, and RV endocardium of healthy and disease subjects, and found statistically significant differences between control and overt HCM subjects consistent with previous studies [131].

The work is novel in four principal ways. First, in terms of application, the wide anatomical variability observed in subjects with overt HCM make segmentation

Slice	Structure	Segment	Control (%)	Overt (%)	p
Base	LV Endocardium	Anterior	-28.8 ± 4.9	-30.0 ± 6.8	NS
		Anteroseptal	-30.7 ± 4.7	-30.8 ± 8.7	NS
		Inferoseptal	-24.1 ± 7.1	-29.8 ± 8.3	<0.01
		Inferior	-32.1 ± 4.4	-29.0 ± 8.7	NS
		Inferolateral	-27.1 ± 6.3	-29.2 ± 7.6	NS
		Anterolateral	-28.5 ± 5.2	-28.1 ± 8.6	NS
	LV Epicardium	Anterior	-14.2 ± 3.3	-11.4 ± 4.2	<0.05
		Anteroseptal	-13.5 ± 3.6	-10.1 ± 4.2	<0.01
		Inferoseptal	-13.3 ± 4.0	-12.8 ± 5.7	NS
		Inferior	-14.1 ± 3.7	-10.0 ± 4.6	<0.001
		Inferolateral	-13.3 ± 4.2	-11.9 ± 4.1	NS
		Anterolateral	-14.0 ± 2.8	-11.6 ± 5.5	NS
Midslice	LV Endocardium	Anterior	-24.8 ± 4.7	-28.7 ± 8.4	NS
		Anteroseptal	-23.8 ± 4.5	-28.2 ± 6.9	<0.05
		Inferoseptal	-28.0 ± 6.1	-34.4 ± 9.3	<0.01
		Inferior	-24.3 ± 4.2	-26.4 ± 7.1	NS
		Inferolateral	-23.9 ± 5.2	-28.7 ± 8.9	<0.05
		Anterolateral	-26.7 ± 5.2	-31.3 ± 6.9	<0.05
	LV Epicardium	Anterior	-9.5 ± 3.4	-9.6 ± 3.9	NS
		Anteroseptal	-9.9 ± 3.0	-7.9 ± 2.6	<0.01
		Inferoseptal	-9.5 ± 3.4	-10.2 ± 4.9	NS
		Inferior	-9.1 ± 3.2	-7.7 ± 3.4	NS
		Inferolateral	-9.4 ± 3.2	-9.1 ± 4.2	NS
		Anterolateral	-9.6 ± 2.8	-8.1 ± 3.6	NS
Apex	LV Endocardium	Anterior	-25.7 ± 7.8	-30.8 ± 14.4	NS
		Septal	-26.4 ± 8.1	-30.8 ± 15.4	NS
		Inferior	-25.3 ± 8.3	-30.9 ± 14.0	NS
		Lateral	-24.9 ± 8.5	-30.1 ± 14.1	NS
	LV Epicardium	Anterior	-10.7 ± 4.4	-12.1 ± 13.2	NS
		Septal	-11.2 ± 4.3	-12.2 ± 15.5	NS
		Inferior	-11.8 ± 4.1	-12.5 ± 13.4	NS
		Lateral	-10.2 ± 4.0	-12.8 ± 14.8	NS

Table 3.4: Segmental LV Circumferential Strain in Overt HCM vs Control Subjects. Segmental circumferential strain results are shown for the LV endocardium and epicardium in all three SA slices.

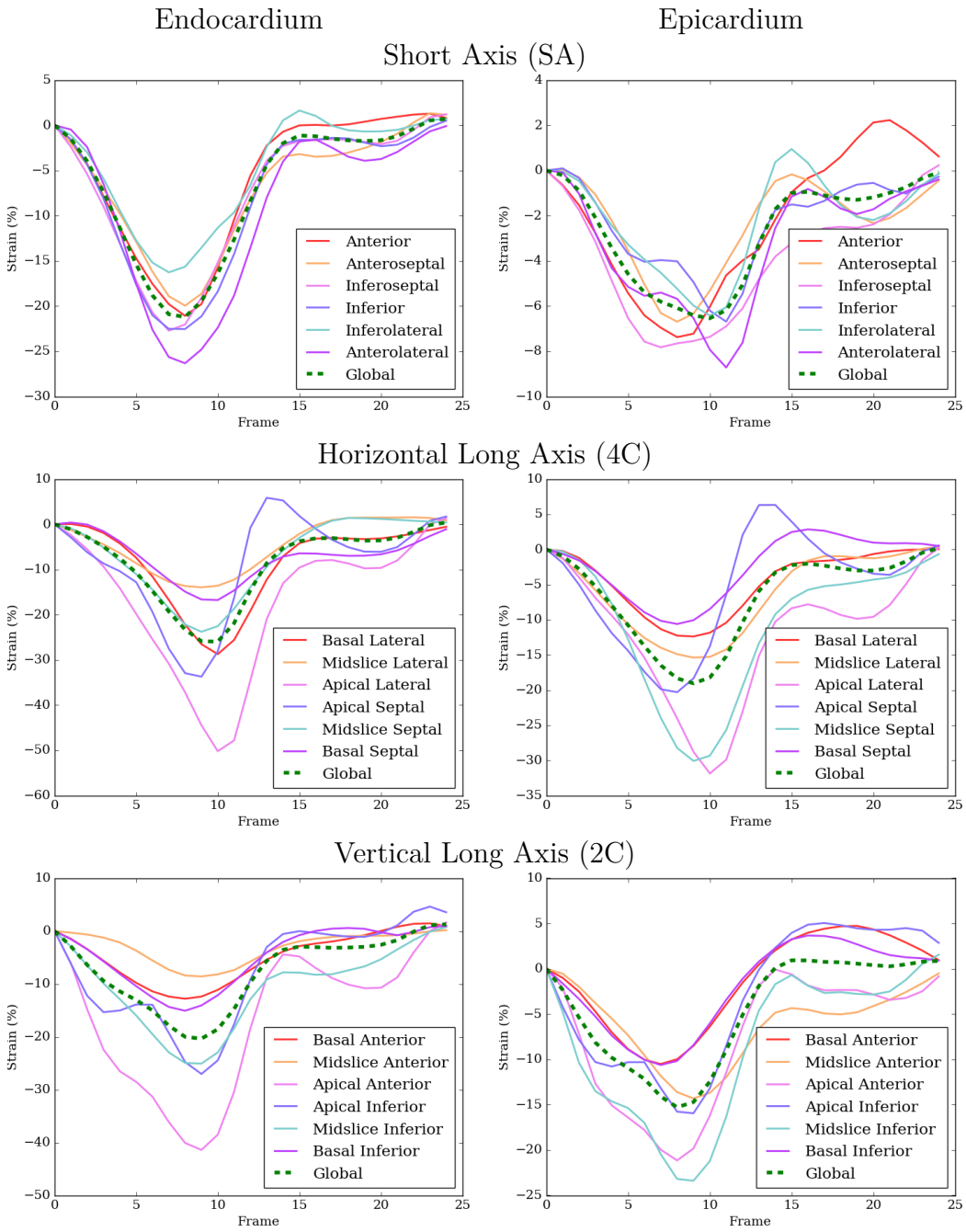


Figure 3.15: Representative Strain Curves in a Healthy Control Subject.

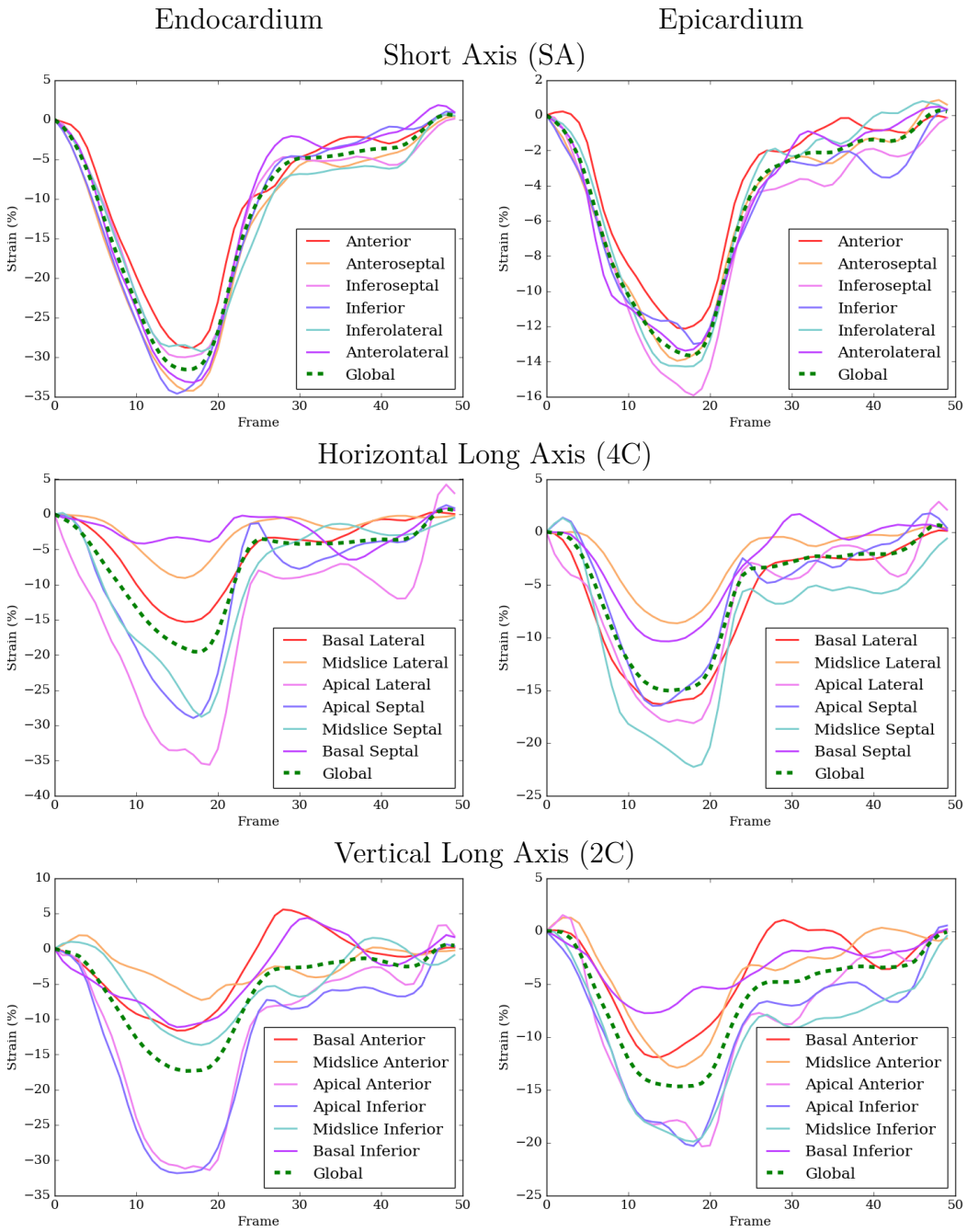


Figure 3.16: Representative Strain Curves in a Patient with Overt HCM.

a particularly difficult problem; this work is the first to demonstrate that CNN-based segmentation is effective in these subjects. In addition, dilated convolution and U-Net architectures have been directly compared to select an appropriate state-of-the-art architecture solution to this problem. Second, a persistent problem in FT-CMR is the interference of the papillary muscles in cardiac segmentation, as noted in §2.2; this work demonstrates that deep learning neatly solves this problem. Moreover, the author is unaware of deep learning segmentation being used for FT-CMR before. Third, the spline optimisation method presented avoids the errors inherent to the various pairwise sequential and reference frame formulations ubiquitous in the feature tracking literature to date. Lastly, the CNN network learned to segment three three foreground classes (LV bloodpool, RV bloodpool, and LV myocardium) in three cardiac planes (SA, 4C, and 2C), which is a more complex problem than addressed previously with CNNs in cardiac segmentation.

Although the dataset included three orthogonal cardiac planes and both healthy and disease subjects, the dataset is nonetheless subject to certain limitations. First, other cardiac planes used in clinical practice (such as the axial, three-chamber, and RV long axis views) should be added in future work. Second, the segmentation, tracking, and strain analysis for each 2-D+Time cine series was performed independently of one another. While it may be possible to register and collectively analyse multiple 2-D views, it may be simpler and more robust to directly analyse 3-D+Time SSFP sequences [132] or cardiac computed tomography (the latter being the subject of Chapter §4). Second, though the left and right atria are visible in this data set, they were not segmented. Atrial function is a largely unexplored aspect of cardiac function which should be considered as well. Finally, patients with preclinical HCM were not included, but would add additional variability and should be included in future work.

In terms of the network architecture, three immediate improvements suggest themselves. First, it may be possible to extend the network to predict the cardiac plane, providing meaningful prior information and guiding the network to a more optimal solution at training time, in addition to providing useful information for

cardiac analysis software at test time. Second, a spatial transformer network [133] prepended to the network could be used to rotate each view into a canonical orientation, simplifying the task of both the downstream network and the physician interpreting the images. Third, the presented architecture could be converted to a "stacked hourglass" architecture [134–137] with an intermediate loss following each upsampling stage, which has shown to increase accuracy over the U-Net alone.

Finally, because only edge features are tracked, the given method suffers from the so-called "aperture-problem" §1.5.3.1, such that anatomical correspondence may not be reliable. This may explain why significant differences in longitudinal strain were not observed between patients with overt HCM and healthy control subjects, though decreased strain has been reported in echocardiography studies [77]. In future work, features from the pretrained CNN will be incorporated into the spline optimisation to mitigate this effect. However, this may be a fundamental limitation of FT-CMR where trabeculation is minimal, such as when measuring LV endocardial strain in the basal slice.

4

CT: Loop Subdivision Surface Registration

Contents

4.1 Contributions 97
4.2 Background 98
4.3 Methods 101
4.3.1 Boundary Candidate Selection 101
4.3.2 Mesh Model Generation 102
4.3.3 Registration 104
4.3.4 Cardiac Function 112
4.3.5 Statistics 113
4.4 Implementation Details 113
4.5 Experiments 114
4.5.1 Canine Infarct Model 114
4.5.2 Image Acquisition 114
4.5.3 Validation 114
4.6 Results 115
4.7 Conclusions 116

4.1 Contributions

[1] Davis M Vigneault, Amir Pourmorteza, Marvin L Thomas, David A Bluemke and J Alison Noble. 'SiSSR : Simultaneous Subdivision Surface Registration for the Quantification of Cardiac Function from Computed Tomography'. In: *Medical Image Analysis [Under Review]* (2017).

[2] Davis M. Vigneault. 'Perturbing Mesh Vertices with Additive Gaussian Noise'. In: *Insight Journal* 80.1 (2016), pp. 1–8.

4.2 Background

Thus far, this work has been concerned with quantifying regional cardiac function from 2-D CMR cine series. While the 2-D techniques detailed in §2 and §3 provide useful clinical indicators and biological information, myocardial contraction is inherently a 3-D phenomenon. Attempts have been made to recover 3-D motion by correlating multiple 2-D image sequences [58], but these techniques are cumbersome and prone to registration error. Recently, it has become possible to acquire high spatial resolution, whole heart, 3-D+Time CCT studies at clinically viable radiation doses. Moreover, by administering intravenous contrast during image acquisition, high blood-pool-to-myocardium contrast may be achieved. Quantifying function from these images is the subject of the present chapter.

The objective of the proposed method is conceptually similar to [17] in that SQUEEZ is quantified from a series of registered meshes (§1.5.3.3). However, rather than registering meshes using coherent point drift (CPD), in this chapter a method which has been successfully used for cardiac modelling and segmentation in the context of 3-D echocardiography [104, 118] is adapted and extended to CCT. In [104], a subdivision surface is registered to an arbitrary point set obtained using an off-the-shelf edge detector. A notable advantage of this method is that the subdivision surfaces are registered *across all frames simultaneously*, contrasting with the conceptually simpler "frame-to-frame" and "reference-frame" formulations. In the frame-to-frame formulation, consecutive pairs of frames are registered, leading to propagation of error throughout the cardiac cycle. In the reference-frame formulation, each frame is registered to the end diastolic frame, leading to disjointed motion. By formulating the problem as a single, global optimisation, the method constructed by [104] avoids both drawbacks.

The specific mesh model used by [104] is a Loop subdivision surface. Loop subdivision is an approximating (as opposed to interpolating) procedure in which

a coarse triangle mesh is refined (either explicitly or implicitly) to a smooth underlying surface. Loop subdivision generalises quadratic triangle B-splines to triangle meshes with "extraordinary" ($N \neq 6$) valency, where quadratic triangle B-splines are themselves one possible generalisation of quadratic B-splines to a 2-D manifold in $\mathbb{R}^3$. Loop subdivision surfaces have properties which are highly desirable for cardiac mesh modelling.

Specifically, from an anatomical standpoint:

- Iterative subdivision converges to a limit surface with C^1 continuity, which is useful when representing an anatomical structure.
- Membrane and thin plate energies, which are physically-motivated measures of surface curvature, may be closely approximated for a given patch and used as regularizers to discourage excessive bending [138].
- The description is anatomically consistent; that is, a particular parametric position corresponds to the same anatomical location across all frames. This is a fundamental requirement of the present application, necessary to calculate any of the biomarkers of regional function enumerated above.

From a computational standpoint:

- Exact evaluation of a parametric position on the model surface requires at most one explicit subdivision [139].
- Surface positions and measures of surface curvature depend only on the one-ring surrounding a patch[1], meaning that the residuals of the optimisation depend only on a small number of parameters. This sparsity can be exploited during the optimisation in order to increase both computational and memory efficiency [126].

[1]In this context, the "one-ring" of a mesh face is defined as the collection of vertices which are at most one edge away from the vertices comprising the face itself.

- The models may be optimised jointly across all cardiac phases, circumventing the propagation of error inherent to "track-to-last" algorithms.
- Subdivision surfaces suggest a multiresolution approach, whereby the output of one registration pass is subdivided and used as the initialisation to a subsequent registration pass.

In this paper, the state-of-the-art method for Loop subdivision surface registration developed by [104] is extended in order to register a template subdivision surface representing the endocardium of the left ventricle to a 3-D+Time cardiac image sequence. The most notable differences between the method presented here and its predecessor are:

- The template mesh is constructed directly from the (segmented) image data, obviating the need for a bespoke mesh representing the structure of interest, and accounting for the wide anatomical variability between subjects.
- Two important changes are made to the cost function. First, by regularising with respect to the acceleration of the (coarse) mesh vertices rather than the velocity, a more plausible model of real cardiac motion is obtained. Second, (coarse) mesh faces with high aspect ratios are penalised, thereby explicitly discouraging solutions with low mesh quality.
- Subdivision surfaces naturally lend themselves to a multiscale approach, which may decrease computation time while directing the optimisation away from local minima. Therefore, an initial registration is performed, the result is explicitly subdivided, and the subdivided result is used to initialise a second pass.
- Although [104] notes anatomical correspondence between registered mesh frames as an advantage of the method, the author evaluates the method primarily as a segmentation algorithm, and stops short of calculating functional

parameters. Here SQUEEZ is calculated, and results are compared with the CPD approach [17].[2]

- The subdivision method was originally developed in the context of 3-D echocardiography. Here, 3-D+Time CCT is investigated, which has received relatively less attention and which will likely become increasingly common clinically in the near future.

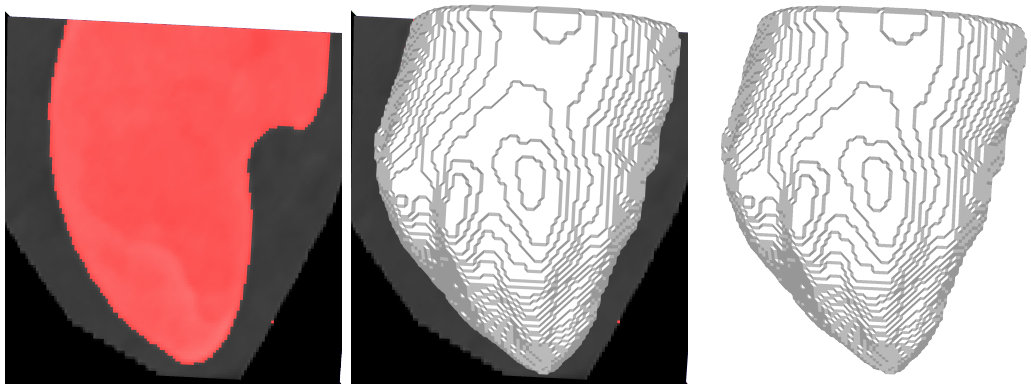
4.3 Methods

The method takes as its input a sequence of 3-D+Time contrast-enhanced CCT images, and produces as its output a sequence of registered, anatomically-consistent mesh models from which functional parameters may be calculated. Broadly, the pipeline involves selecting boundary candidates corresponding to the endocardium of the left ventricle (§4.3.1), generating a template mesh model from the boundary candidate data at end diastole (§4.3.2), registering the template mesh to the boundary candidates across all frames simultaneously (§4.3.3), and calculating functional parameters (§4.3.4).

4.3.1 Boundary Candidate Selection

Each input volume is binarized by selecting an upper and lower threshold for each subject based on the range of Hounsfield units which visually correspond to the intravenous contrast (Fig. 4.1). The blood pool of the left ventricle is then separated from other structures using standard morphological techniques (binary opening/closing, connected component selection, and hole filling), and the surface of the binary image (the "boundary candidate mesh") is extracted using marching cubes [140]. Where necessary, the right heart is pruned from the left ventricle before selecting the largest connected component. In order to aid comparison with the CPD method, the left ventricle is segmented from the left atrium, though this is not a requirement of the proposed pipeline. The result is a dense, triangular

[2]The author would like to acknowledge Dr. Amir Pourmorteza for performing the CPD analysis.



(a) (b) (c)

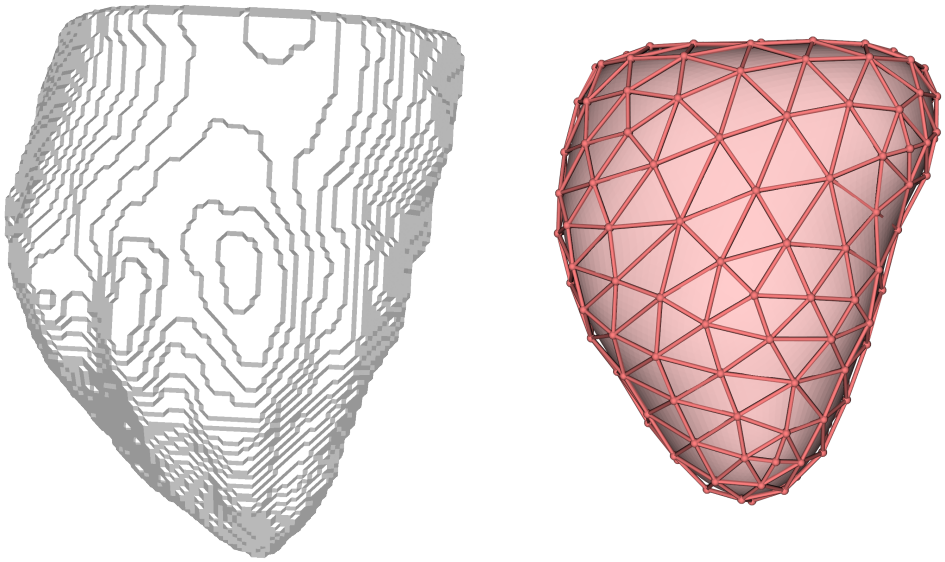
Figure 4.1: Boundary Candidate Selection. (a) Thresholding of the image to roughly select the bloodpool of the left heart (pink). (c) The resulting boundary candidate mesh. (b) The two overlain, demonstrating coincidence of the boundary candidate mesh with the endocardium.

boundary candidate mesh representing the endocardium of the left ventricle for each volume in the sequence.

4.3.2 Mesh Model Generation

The boundary candidate meshes produced in the previous step cannot be used directly to quantify cardiac function, because they lack anatomical correspondence between frames. Therefore, it is necessary to generate a single template mesh which can be registered to the boundary candidate meshes across all frames. The boundary candidate mesh at end diastole was selected as the starting point for generating the template mesh (Fig. 4.2). The end diastolic boundary candidate mesh is decimated to approximately 100 faces by iterative edge contraction, positioning new vertices so as to minimise quadric error relative to the prior iteration [141]. Quadric error is preferred over a simpler metric, such as squared edge length, due to the tendency of the former to preserve regions of high curvature (in the application, this was found to be helpful in preserving, in particular, the cardiac apex and atrial appendage).

The ability to generate the template mesh directly from the boundary candidates is possible because the boundary candidates are a mesh, as opposed to a point set as in [104]. This advantage justifies the choice to use marching cubes in the previous

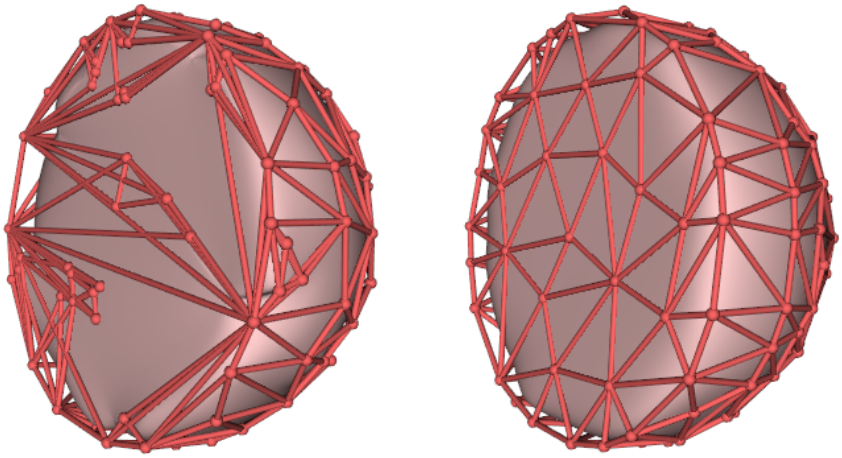


(a) (b)

Figure 4.2: Subdivision Mesh Model Generation. (a) The dense, triangular boundary candidate mesh, produced by the fast marching cubes algorithm for the end diastolic frame. (b) The initial model, generated through decimation of the boundary candidate mesh. The dark red wireframe represents the control points and their connections; the smooth, pink surface represents the underlying subdivision surface defined by the wireframe. Note the tendency of the surface to "contract" somewhat during decimation.

stage (§4.3.1). The decimation step is necessary because it dramatically reduces the number of vertices in the template mesh (a reduction of two orders of magnitude), each of which contributes three parameters to the first optimisation pass (§4.3.3). Note that the anatomical detail lost through the decimation procedure is largely recovered by treating the template mesh as a Loop subdivision surface, where each patch approximates a small subset of the boundary candidate mesh. Note also that by generating the template mesh directly from the boundary candidate data, the need to provide a bespoke template mesh, as required elsewhere [17, 104], is avoided.

As a practical note, it is common for the boundary candidate mesh to contain one or more regions which are perfectly flat, either due to manual pruning or to the region of interest extending beyond the bounds of the image. It was found that when decimating this mesh directly, the face count could be reduced by contracting edges in these flat regions with zero quadric error. The resulting mesh tended to score



(a) Without Gaussian Noise **(b)** With Gaussian Noise

Figure 4.3: Improvement of Mesh Quality with Gaussian Noise. Marching cubes was used to generate a fine mesh from a binary half-sphere. The mesh was decimated both directly (a) and after addition of a small amount of Gaussian noise (b). A dramatic improvement in mesh quality is visually apparent. A version of this figure appears in [142].

poorly in metrics of mesh quality, specifically the distribution of vertex valencies, triangle aspect ratios, and triangle areas (§B). These negative effects were largely circumvented by perturbing the vertices of the end diastolic boundary candidate mesh with a small amount of Gaussian noise prior to decimation (Fig. 4.3).

4.3.3 Registration

Having generated the template mesh and the boundary candidates, the former may be registered to the latter globally, across all frames simultaneously. The $3 \times C \times K$ parameters of the registration (where 3 is the dimensionality of the mesh, C is the number of control points in a single mesh, and K is the number of images in the sequence) are the Cartesian coordinates of the template mesh vertices. The primary residuals are the distances between three points (equally spaced in parametric coordinates) sampled *from the underlying surface* and the nearest boundary candidates (in terms of Euclidean distance). Additional regularizers encourage physically plausible motion and topology, and high mesh quality. The

details for evaluating an arbitrary position on a Loop subdivision surface, formulation of the cost function for the optimisation, and a multiresolution extension to the technique are presented next.

4.3.3.1 Subdivision Surface Evaluation

In order to calculate the primary residual of the cost function, it is necessary to evaluate an arbitrary position on the Loop subdivision surface. The details of Loop subdivision surface evaluation are provided elsewhere [104, 139]; in order to aid in understanding the cost function formulation (§4.3.3.2), the mathematics are briefly reviewed here.

A "patch" is the subset of the limit subdivision surface arising from a particular face in the initial, coarse mesh. A point $\mathbf{u}_{f,j,\mathbf{t}} \in \mathbb{R}^3$ on a subdivision surface is uniquely described by its frame index f, patch index j, and its parametric coordinates $\mathbf{t} = (s,t) \in \triangle = \{(s,t) : s,t \in [0,1], s+t \leq 1\}$. A patch is termed "ordinary" if the three vertices defining it each have valency $N = 6$. A patch is termed "extraordinary" if exactly one vertex has valency $N \neq 6$. Patches with more than one extraordinary vertex are disallowed[3]. This distinction is useful because ordinary and extraordinary patches require distinct procedures for evaluating surface positions. The "one-ring" of a patch is the set of the three vertices defining the central triangle, plus those vertices connected by exactly one edge. Any surface position in a patch may be evaluated given its one-ring. The vertices are numbered according to Fig. 4.4; adherence to this numbering system will be essential for consistency with the subdivision matrices defined by Loop and described here.

Let $X \in \mathbb{R}^{3\times(C\times K)}$ be the matrix of Cartesian coordinates comprising the subdivision surface control points across all frames, where C is the number of control points in a single mesh and K is the number of frames. $X_f \in \mathbb{R}^{3\times C}$ is the submatrix of X containing the control points in frame f, and $X_{f,j} \in \mathbb{R}^{3\times(N+6)}$

[3]The requirement that each patch has at most one extraordinary vertex does not impose any practical limitation, as it can be satisfied by subdividing the input mesh exactly once prior to surface point evaluation. This can be understood by recognising that subdivision of an extraordinary patch results in three ordinary patches, and one extraordinary patch with connectivity identical to its parent.

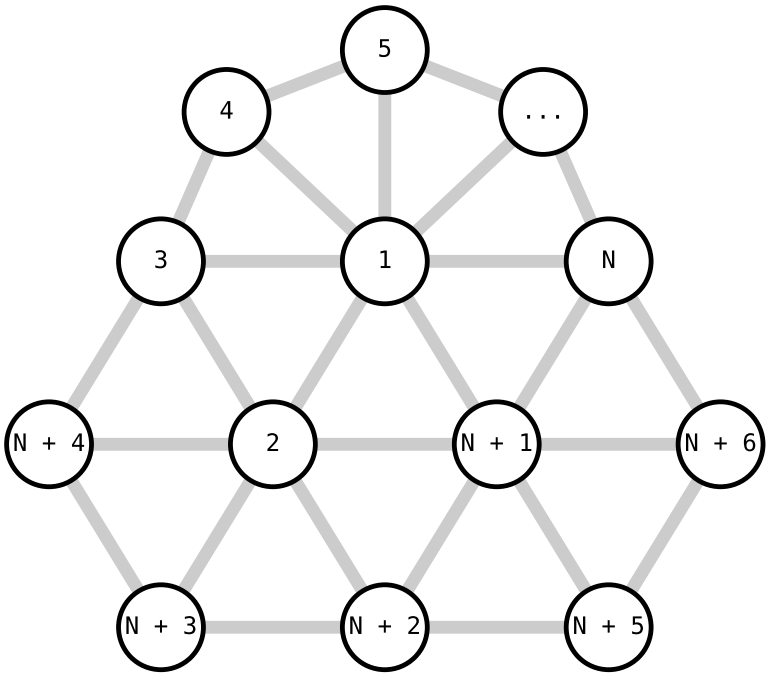
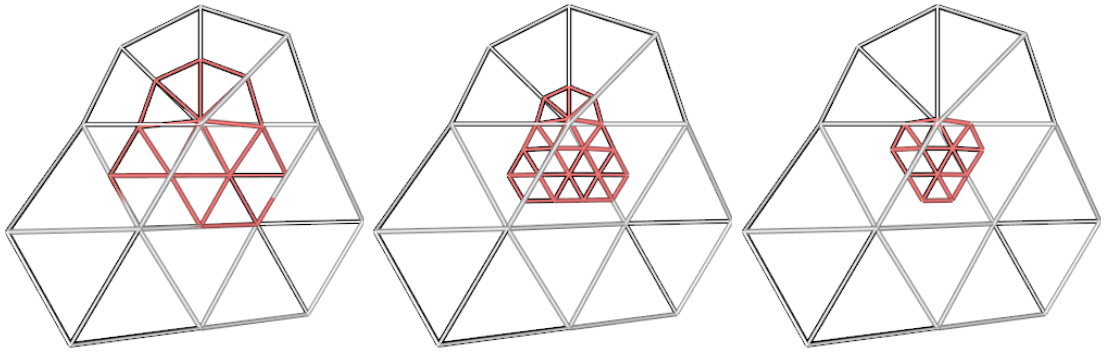


Figure 4.4: Numbering Vertices in a Loop Subdivision Patch. This particular ordering of patch vertices is tied to the construction of the subdivision matrix S, the bigger subdivision matrix A, and the extended subdivision matrix $\bar{A}$.

is the submatrix of X_f containing the control points comprising the one-ring of patch j. A function $\chi : \mathbf{t}, X_{f,j} \to \mathbb{R}^3$ is defined which gives the position of a surface point $\mathbf{u}_{f,j,\mathbf{t}}$ given the parametric coordinates and the one-ring matrix for a given frame and patch. For an ordinary patch, χ can be evaluated directly as a barycentric combination of the 12 relevant control points, where $\mathbf{b}(\mathbf{t}) \in \mathbb{R}^{12}$ is a vector of quartic polynomials (§C.1).

$$\chi(\mathbf{t}, X_{f,j}) = X_{f,j} \cdot \mathbf{b}(\mathbf{t}) = \mathbf{u}_{f,j,\mathbf{t}} \tag{4.1}$$

In the case of a patch with a single extraordinary vertex, a simple set of barycentric weights does not exist. However, geometric subdivision of an extraordinary patch results in four "child" patches: three ordinary patches and one extraordinary patch with topology identical to the parent (Fig. 4.5). This process may be repeated iteratively (Fig. 4.5). Therefore, excluding the origin $\mathbf{t} = (0, 0)$ (which



(a) AX **(b)** $\bar{A}AX$ **(c)** $P_1\bar{A}AX$

Figure 4.5: Geometric Loop Subdivision. Take an extraordinary patch where $N = 7$, to be evaluated at $\mathbf{t} = (0.1, 0.2)$. The number of required subdivisions $n = 2$ and the index of the child patch $k = 1$. The original extraordinary patch is shown in white, and intermediate matrices are shown in red. (a) The original patch is first subdivided using the extended subdivision matrix A. (b) The result is further subdivided using the bigger subdivision matrix $\bar{A}$. (c) From the result, an ordinary patch is extracted containing the parametric point of interest using the picking matrix P_1, the surface position of which may then be evaluated directly.

by convention is placed at the extraordinary vertex), the position at any local patch coordinate may be evaluated with (4.1) by subdividing a sufficient number of times, extracting the vertices of the relevant (ordinary) one-ring, and transforming the local patch coordinate into the subdivided patch. In [139], this concept is formalised in terms of matrix algebra. In particular, the "subdivision matrix" $S \in \mathbb{R}^{(N+1)\times(N+1)}$ is described, which subdivides the extraordinary vertex, yielding a vertex with identical valency; the "extended subdivision matrix" $A \in \mathbb{R}^{(N+6)\times(N+6)}$, which subdivides the patch around the extraordinary vertex, yielding a patch of identical topology to the first; the "bigger subdivision matrix" $\bar{A} \in \mathbb{R}^{(N+12)\times(N+6)}$, which additionally generates the three ordinary child patches; and the "picking matrix" $P_k \in \mathbb{R}^{12\times(N+12)}$, which selects the one-ring around the k^{th} ordinary child patch ($k \in \{0, 1, 2\}$). The precise definitions of these matrices are given in [139], and reproduced in §C.2 for convenience and completeness.

For a given $\mathbf{t}$, n geometric subdivisions are required before the surface point of interest is contained within one of the three ordinary child patches:

$$n = \lfloor -\log_2 (s+t) + 1 \rfloor. \tag{4.2}$$

The index of the ordinary child patch k is given by:

$$k = \begin{cases} 0: & 2^{-n} < s \leq 2^{-n+1}, 0 \leq t \leq 2^{-n+1} - s \\ 1: & 0 \leq s \leq 2^{-n}, 2^{-n} - s \leq t \leq 2^{-n} \\ 2: & 0 \leq s \leq 2^{-n}, 2^{-n} < t \leq 2^{-n+1} - s, \end{cases} \tag{4.3}$$

and the patch coordinate $\mathbf{t}$ may be transformed into the appropriate child patch given n and k according to the function $\hat{\mathbf{t}}_{n,k}(\mathbf{t})$:

$$\hat{\mathbf{t}}_{n,k}(\mathbf{t}) = \begin{cases} k = 0: & (2^n s - 1, 2^n t) \\ k = 1: & (1 - 2^n s, 1 - 2^n t) \\ k = 2: & (2^n s, 2^n t - 1). \end{cases} \tag{4.4}$$

Note that the partial derivative of $\hat{\mathbf{t}}_{n,k}(\mathbf{t})$ with respect to either s or t is equal to 2^n for $k \in 0, 2$ and -2^n for $k = 1$[4].

Given these definitions, the surface position for patch j and frame f at $\mathbf{t} \neq \mathbf{0}$ is given by:

$$\chi(\mathbf{t}, X_{f,j}) = X_{f,j} \left(P_k \bar{A} A^{n-1} \right)^\top \mathbf{b}\left(\hat{\mathbf{t}}_{\mathbf{n},\mathbf{k}}(\mathbf{t}) \right). \tag{4.5}$$

Note that the powers of A can be calculated efficiently through eigendecomposition ($A^n = V_A \Lambda_A^n V_A^{-1}$, where V_A is a matrix of eigenvectors and Λ_A is a diagonal matrix of eigenvalues). Note that a subset of eigenvalues of A have multiplicity two, such that the eigendecomposition by naive numerical methods is not guaranteed to give real eigenvectors. In §C.3, a method for computing the eigenstructure of A is given which is guaranteed to be real.

Importantly, because the partial derivatives of $\hat{\mathbf{t}}$ are known and $\mathbf{b}(\mathbf{t})$ is a polynomial in s and t, the partial derivatives of $\chi(\mathbf{t}, X_{f,j})$ are straightforward to specify via the chain rule (though not necessarily straightforward to evaluate).

[4]Strictly speaking, $\hat{\mathbf{t}}_{n,k}(\mathbf{t})$ is more appropriately thought of as a tuple of functions, one of which transforms s, the other of which transforms t. Moreover, the term "partial derivative" has been here abused to denote the derivative of the relevant *component* of $\hat{\mathbf{t}}_{n,k}(\mathbf{t})$, rather than the tuple itself, returning a scalar rather than a tuple.

At the patch origin ($\mathbf{t} = \mathbf{0}$), this equation cannot be used as the power of A approaches infinity. However, as shown in [104], the surface position at the origin can be evaluated by $\chi(\mathbf{0}, X_{f,j}) = X\tilde{v}_1$, where $\tilde{v}_1$ is the normalised, left subdominant eigenvector of A.

4.3.3.2 Optimisation

Levenberg-Marquardt least squares optimisation [120] is used to register the model surface mesh to the boundary candidates. The parameters $\Delta X \in \mathbb{R}^{3\times(C\times K)}$ of the optimisation are Cartesian displacements to the vertices of all model surface meshes. Three surface points $\mathbf{u}_{f,j,\mathbf{t}}$ per patch were sampled across the model surfaces, spaced equally in terms of parametric coordinates ($\mathbf{t} \in \{(0.25, 0.25), (0.25, 0.75), (0.75, 0.75)\}$). At each step in the optimisation, for each of these points, the nearest boundary candidate $\phi(\mathbf{u}_{f,j,\mathbf{t}})$ was calculated, where $\phi : \mathbb{R}^3 \to \mathbb{R}^3$. This was computed efficiently by representing the boundary candidate point set at each frame as a K_d tree. The Cartesian components of the distance between the surface point and nearest boundary candidate were the residuals of E_{cf}, the first term of the cost function,

$$E_{cf} = \sum_{f,j,\mathbf{t}} \|\mathbf{u}_{f,j,\mathbf{t}} - \phi(\mathbf{u}_{f,j,\mathbf{t}})\|^2. \tag{4.6}$$

Additionally, three regularizers were included to enforce physical constraints of anatomical deformation and ensure high mesh quality: control point acceleration, subdivision patch thin-plate energy, and triangle aspect ratio. This differs from the cost function formulation by [104], where the regularising terms were control point velocity and thin-plate energy.

In the cost function, control point acceleration is the only means by which information is shared between frames (that is, the only residual which is dependent upon parameters from more than one frame). At a minimum, regularising against control point velocity as in [104] is necessary to maintain anatomical consistency (the assumption that, for fixed j and $\mathbf{t}$, $\mathbf{u}_{f,j,\mathbf{t}}$ corresponds to the same material point $\forall f$). By regularising against acceleration rather than velocity, smooth, biologically plausible motion is encouraged. The control point acceleration regularizer E_{ac} was

defined as the Cartesian components of the second differences between corresponding vertices $\mathbf{x}_{f,c}$ in three adjacent frames, where $\mathbf{x}_{f,c}$ is the $(f \times C) + c^{\text{th}}$column of X.

$$E_{ac} = \sum_{f,c} \left\| \begin{bmatrix} 1 & -2 & 1 \end{bmatrix} \begin{bmatrix} \mathbf{x}_{(f+2) \bmod K,c}^{\top} \\ \mathbf{x}_{(f+1) \bmod K,c}^{\top} \\ \mathbf{x}_{f,c}^{\top} \end{bmatrix} \right\|^2 \tag{4.7}$$

The thin-plate energy for patch j in frame f is the surface integral over the sum of the partial second derivatives with respect to $\sigma = s + \frac{1}{2}t$ and $\tau = \frac{\sqrt{3}}{2}t$ (the transformation yields an orthogonal coordinate system, which is a necessary condition for isotropic thin-plate energy) [138].

$$E_{tp} = \sum_{f,j} \int_{\mathbf{t} \in \triangle} \left\| \frac{\partial^2 \chi}{\partial \sigma^2} \right\|^2 + 2 \left\| \frac{\partial^2 \chi}{\partial \sigma \partial \tau} \right\|^2 + \left\| \frac{\partial^2 \chi}{\partial \tau^2} \right\|^2 \mathrm{d}\mathbf{t} \tag{4.8}$$

Unfortunately, this integral is not straightforward to evaluate for an extraordinary patch. However, it is possible to define a matrix $B \in \mathbb{R}^{15 \times (N+6)}$ in terms of the position function χ and its first derivatives, evaluated at a discrete number of points, which replaces a Loop subdivision patch $X_{f,j}$ of any valency with an approximate quartic triangle Bézier patch $\hat{X}_{f,j}$ [104]. For an ordinary Loop subdivision patch, the Bézier representation is equivalent, and for an extraordinary patch, the error is negligible in practice (the error may become relevant for extremely high valency patches, which were not encountered in this work).

$$\hat{X}_{f,j} = B X_{f,j} \tag{4.9}$$

The matrix B is defined precisely in §D.

The surface position on the Bézier patch may then be evaluated as a barycentric combination of the 15 relevant control points, where $\hat{\mathbf{b}}(\mathbf{t})$ is a vector of quartic polynomials [139].

$$\hat{\chi}\left(\mathbf{t}, \hat{X}_{f,j}\right) = \hat{X}_{f,j} \hat{\mathbf{b}}(\mathbf{t}) \tag{4.10}$$

The thin plate energy of a Bézier patch can be calculated exactly, regardless of the valency of the Loop subdivision patch which it approximates. In this work, quantities pertaining to the Bézier approximation are indicated with a superposed chevron (ˆ).

$$E_{\hat{tp}} = \sum_{f,j} \int_{\mathbf{t}\in\triangle} \left\| \frac{\partial^2 \hat{\chi}}{\partial \sigma^2} \right\|^2 + 2 \left\| \frac{\partial^2 \hat{\chi}}{\partial \sigma \partial \tau} \right\|^2 + \left\| \frac{\partial^2 \hat{\chi}}{\partial \tau^2} \right\|^2 \mathrm{d}\mathbf{t} \tag{4.11}$$

Though thin plate energy is useful for limiting excessive bending, it is only sensitive to deformations which affect the second derivative of the surface positions with respect to the parametric coordinates, and does not penalise affine transformations. Therefore, thin plate energy regularisation allows long, thin patches to "bunch" along a ridge, resulting in biologically implausible compression. In order to counteract this, the mesh triangle aspect ratio was penalised.

$$E_{ar} = \sum_{f,j} \frac{\|\triangle_{\max}\|}{\|\triangle_{\min}\|} \tag{4.12}$$

Here $\triangle_{\max}$ and $\triangle_{\min}$ denote the longest and shortest edges of the innermost triangle in patch j, respectively.

The overall optimisation problem may then be written in terms of Equations 4.6, 4.7, 4.11, and 4.12 and corresponding scaling factors. Scaling factors ρ_{cf}, ρ_{ac}, $\rho_{\hat{tp}}$, and ρ_{ar} were set empirically to prevent any single term from dominating the optimisation, and are reported in Table 4.1.

$$E = \min \left(\rho_{cf} E_{cf} + \rho_{ac} E_{ac} + \rho_{\hat{tp}} E_{\hat{tp}} + \rho_{ar} E_{ar} \right) \tag{4.13}$$

Two points relating to computational efficiency are worth noting. First, the Jacobians of Equations 4.6, 4.7, 4.11, and 4.12 can all be calculated analytically. By providing explicit Jacobians, the need for numeric derivatives, which would slow computation precipitously, is avoided. For a given set of correspondences between surface positions and boundary candidates, the Jacobians of Equations 4.6, 4.7, and 4.11 are linear with respect to the Cartesian displacements of the control points and therefore trivial to calculate. Equation 4.12 is the ratio of two Euclidean distances. Its Jacobian, therefore, can be calculated with the quotient rule and the knowledge that the partial derivative of Euclidean distance $\|\mathbf{w}\|$ with respect to a particular component w_d is $w_d/\|\mathbf{w}\|$, while noting that whether a particular control point contributes to the numerator, denominator, or neither must be determined

with each iteration. Second, each individual residual depends upon a very small number of parameters. Specifically, the individual terms comprising E_{cf} and $E_{\hat{tp}}$ depend on $3 \times (N + 6)$ parameters, and those comprising E_{ac} and E_{ar} depend on 3×3 parameters. This sparsity is exploited during the optimisation to limit the number of components of the Jacobian which must be evaluated, further reducing computational cost.

4.3.3.3 Multiresolution Approach

Multiresolution techniques frequently have the effect of speeding convergence and avoiding local minima; both of these benefits are expected to apply in this application. Recalling §4.3.2, the template mesh model was decimated to ~ 100 faces. This target was chosen empirically as the minimum number of faces beyond which large discrepancies were observed between the end diastolic boundary candidate mesh and the template mesh. This model is subdivided once prior to registration to ensure that no triangle has more than one extraordinary vertex; therefore, the input to the registration algorithm consists of $\sim 100 \times 4$ faces. The output of the first pass is subdivided and used to initialise a second pass, such that the final mesh model contains $\sim 100 \times 4^2$ faces. In principle, one may perform as many passes as necessary, within the constraints of random access memory. In practice, two passes are sufficient to reflect the endocardial geometry with negligible error.

4.3.4 Cardiac Function

Following registration, the end diastolic mesh is subdivided until visually smooth (5 subdivisions are typically adequate) and the subdivided mesh is segmented according to the 16-segment American Heart Association (AHA) model based on standard clinical planes [14]. The patches in all other frames are assigned to an AHA segment based on the assignment of the corresponding patch in the end diastolic mesh. The surface area of each AHA segment of the subdivided mesh is calculated, and SQUEEZ, $Q(f)$, is calculated for a given frame f as a function of the current and end diastolic areas A_f and A_{ed}, respectively [17], namely,

Parameter	Value
Function Tolerance	10^{-2}
Parameter Tolerance	10^{-2}
Linear Solver Type	`SPARSE_NORMAL_CHOLESKY`
Minimizer Type	`TRUST_REGION`
ρ_{cf}	1.0
ρ_{ac}	0.75
ρ_{tp}	0.4
ρ_{ar}	10.0

Table 4.1: Hyperparameters of the Loop Subdivision Surface Optimization.

$$Q(f) = \sqrt{\frac{A_f}{A_{ed}}}. \tag{4.14}$$

4.3.5 Statistics

Normally distributed variables are reported as mean ± standard deviation. Non-normally distributed variables are reported as median [interquartile range, IQR]. Linear relationships are assessed with Pearson's correlation, where $0.7 < |R| \leq 1.0$ is interpreted as a strong correlation, $0.5 < |R| \leq 0.7$ a moderate correlation, $0.3 < |R| \leq 0.5$ a weak correlation, and $|R| \leq 0.3$ no correlation.

4.4 Implementation Details

Evaluation of Loop subdivision surfaces at arbitrary parameter values was implemented according to [139] in the `C++` programming language. The core classes have been packaged as an external module for the Insight Toolkit (ITK) library [124, 125]. Visualisation and user interaction was implemented using the Visualisation Toolkit (VTK) library [143]. Levenberg Marquardt least squares optimisation was performed using the Ceres Solver [126], configured with OpenBLAS [127]. Experiments were run on an Ubuntu 14.04 desktop computer with eight Intel Xenon 3.50GHz quad-core processors and 16GB RAM. Hyperparameters of the optimisation are listed in Table 4.1.

4.5 Experiments

The algorithm was applied to CCT images obtained from a canine infarct model, and the results compared to those obtained for the CPD algorithm (the details of the CPD algorithm are given in §1.5.3.3). The details of the animal model, imaging parameters, and validation are as follows.

4.5.1 Canine Infarct Model

The images used in this work were obtained from a study at the United States National Institutes of Health of thirteen adult male mongrel canine subjects who had undergone surgical ligation of the left anterior descending (LAD) coronary artery for 90 minutes to simulate myocardial infarction, followed by reperfusion. Subjects were scanned between six and eight weeks following surgery.

4.5.2 Image Acquisition

Images were acquired using the SOMATOM Force scanner (Siemens, Erlangen, Germany). For the cardiac functional analysis test scan, a 30mL bolus of 20% iopamidol 370 (I-370) contrast was used at 2.5mL/s, followed by a 10mL saline chaser. For the final scan, a 30mL bolus of 80% I-370 contrast was used at 2.5mL/s, followed by a 10mL saline chaser. Images were reconstructed over a single heart beat. The gantry rotation time was 250ms; the tube current was 1152-1688mA; the tube voltage was 90kV; and the collimation was 96 rows (full detector). The matrix size: 512 x 512 (slice thickness: 0.5mm; pixel size: 0.3mm x 0.3mm). Twenty cardiac phases were reconstructed over the R-R interval using the Br36d convolution kernel.

4.5.3 Validation

The original SQUEEZ implementation [18] relies upon coherent point drift (CPD). The dataset was analysed with this implementation and the results were compared with those from the subdivision algorithm proposed here. The relationship between whole-heart and segmental peak SQUEEZ values measured by the two methods

was assessed quantitatively by paired Student's t-test and Pearson's correlation, and visually by Bland-Altman plots and linear regression.

4.6 Results

The two optimisation passes combined took under 5 minutes per subject (295.8s, IQR = [242.1s, 378.1s]). The first pass contributed very little to the total compared with the second pass (17.9s, IQR = [17.2s, 359.5s] vs 276.4s, IQR = [220.9s, 359.5s]).

Qualitatively, the registered mesh models (Fig. 4.6) were of high quality, closely tracked the endocardium, and reflected the physiologically observed myocardial contraction throughout the cardiac cycle (Fig. 4.7).

Peak segmental SQUEEZ is presented as a polar projection in Fig. 4.8. The observed peak SQUEEZ values are within a physiologically reasonable range and are consistent with values previously reported in the literature [18]. Representative curves (segmental and global) as calculated by the proposed pipeline as well as the CPD algorithm are shown in Fig. 4.9. Note that the timing of contraction is very consistent between the two methods. Moreover, SQUEEZ curves calculated by the CPD method are slightly noisy, which could be problematic for the calculation of strain rate without smoothing. SQUEEZ curves calculated by the proposed method by contrast are smooth as a result of regularising against control point acceleration, and could be used to calculate strain rate directly.

Correlation between global left ventricular SQUEEZ as measured by the subdivision method versus the CPD method was strong ($R = 0.93$, $p < 0.0001$). A positive bias noted visually on Bland-Altman plot was statistically significant (0.838 ± 0.042 vs 0.823 ± 0.041, $p < 0.01$), though very small in absolute terms and unlikely to be clinically relevant (Fig. 4.10).

Segmentally, correlation was moderate ($R = 0.40$, $p < 0.0001$). A statistically significant positive bias was noted (0.827 ± 0.087 vs 0.810 ± 0.055, $p < 0.01$), though again the difference was small in absolute terms (Fig. 4.11).

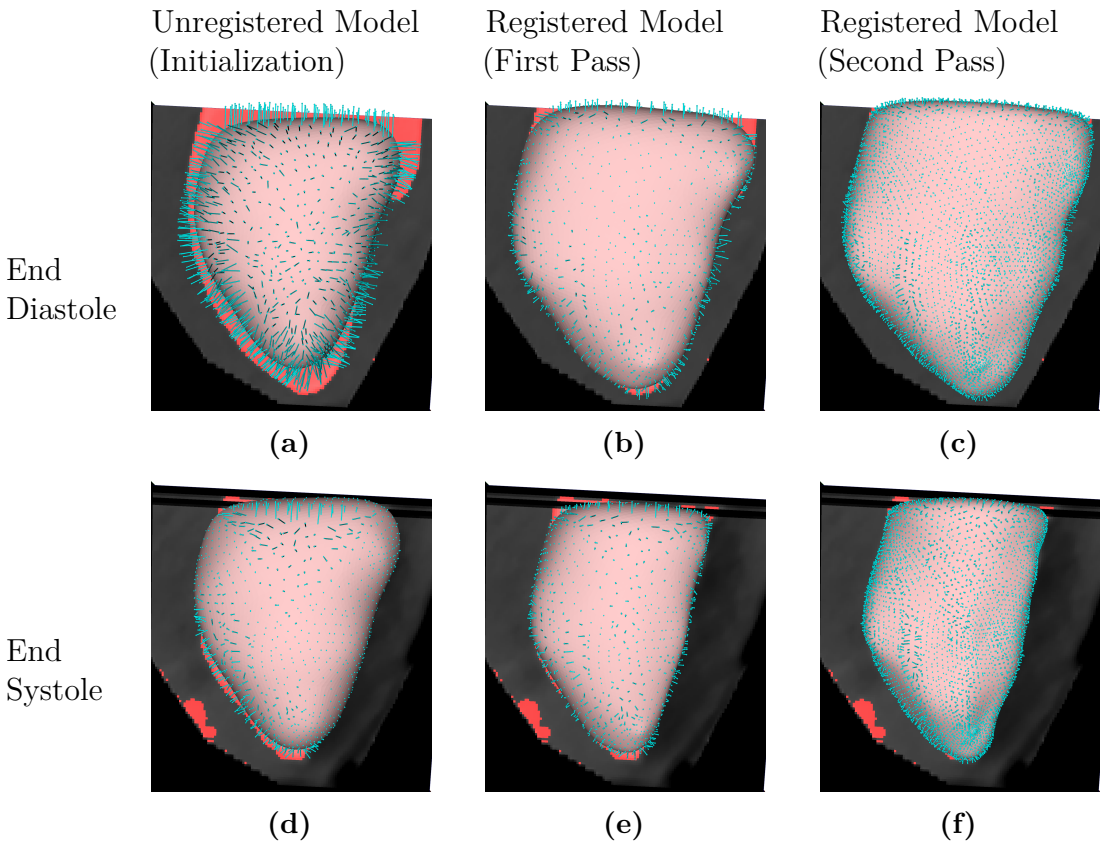


Figure 4.6: Residual Error at Each Registration Stage. Residual error for the end diastolic (top) and end systolic (bottom) frames at various stages of the pipeline, overlayed on a long axis view of the heart. The pink meshes represent the subdivision surface of the model; the blue bars represent the primary residuals of the cost function, pointing from a point on the subdivision surface to the nearest boundary candidate. (a, d) The initial, unregistered model. (b, e) The registered model after the first pass. (c, f) The registered model after the second pass.

4.7 Conclusions

In this chapter, an end-to-end pipeline for quantifying cardiac function from a 3-D+Time CCT image sequence has been described. The method inherits a number of desirable features from the prior state-of-the-art method [104] that have been adapted and extended. Loop subdivision surfaces are useful structures for modelling cardiac anatomy. First, they allow smooth, detailed structures to be represented implicitly with a coarse mesh. Second, they impose minimal modelling requirements on the mesh (only that it be triangular, and avoid pathological topologies such as self-intersection). Third, each control point in the coarse mesh influences only

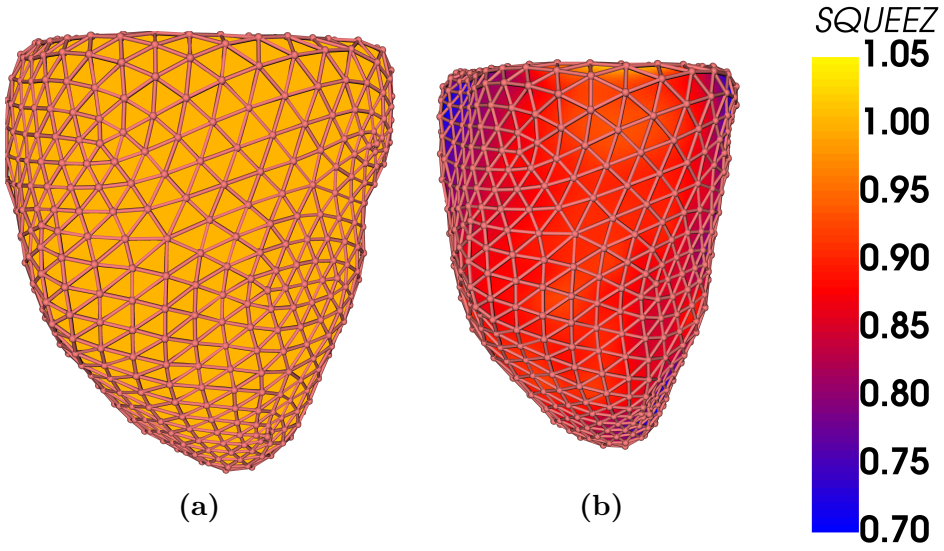


Figure 4.7: Calculation of SQUEEZ from Registered Subdivision Surfaces. Subdivision surfaces at end diastole (left) and end systole (right) are shown. Note that shading has been turned off for the subdivision surface to avoid any ambiguity in interpreting the colormap.

a small portion of the underlying surface, leading to sparse dependence between parameters and residuals during the optimisation and consequent computational gains. Besides making use of subdivision surfaces, the cost function formulation performs the optimisation across all frames simultaneously, which has the effect of avoiding track-to-last errors which typically plague heart tracking algorithms.

The contributions of this chapter include a number of modifications which improve upon the method proposed by [104]. By generating the template mesh directly from the blood pool of the left ventricle, the broad variability in cardiac anatomy is accounted for, providing an excellent initialisation for mesh registration, and minimising the required human intervention. Additionally, two notable changes are made to the cost function. First, control point acceleration (as opposed to velocity) is regularised, encouraging smooth, biologically plausible motion. Second, high mesh quality is explicitly encouraged by penalising mesh faces with high aspect ratio, with the added benefit of discouraging physically unreasonable SQUEEZ

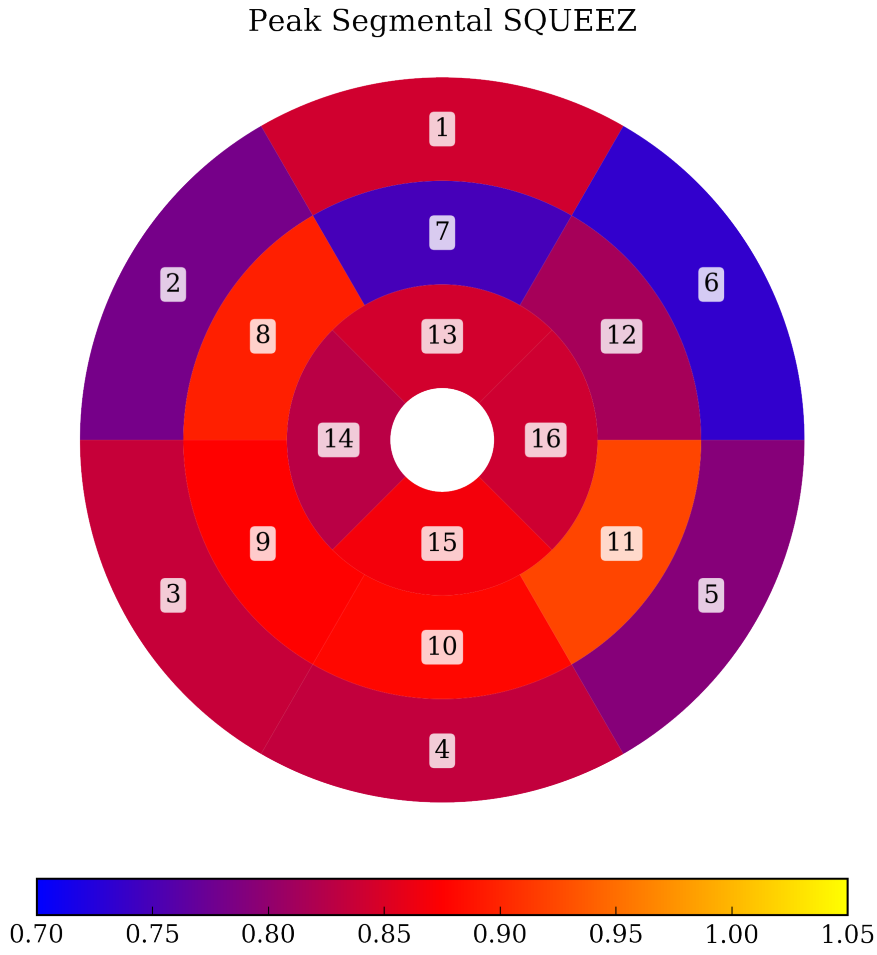


Figure 4.8: Average Peak SQUEEZ. Values are plotted segmentally according to the 16-segment AHA model [14].

values. A multiresolution approach is employed for mesh registration, which has the dual advantages of avoiding local minima and increasing computational efficiency. Finally, [104] stopped short of calculating metrics of regional function. Their template mesh, defined by 40 faces initially and 40×4 faces after subdivision, would likely have been insufficiently detailed to adequately capture regional function. In contrast, it has here been shown that SQUEEZ calculated by the proposed pipeline correlates globally with SQUEEZ calculated with an independent methodology [17], providing further confidence in the reported results beyond visual inspection.

Although there was excellent correspondence between our method and the coherent point drift method in terms of *global* SQUEEZ, segmental agreement was

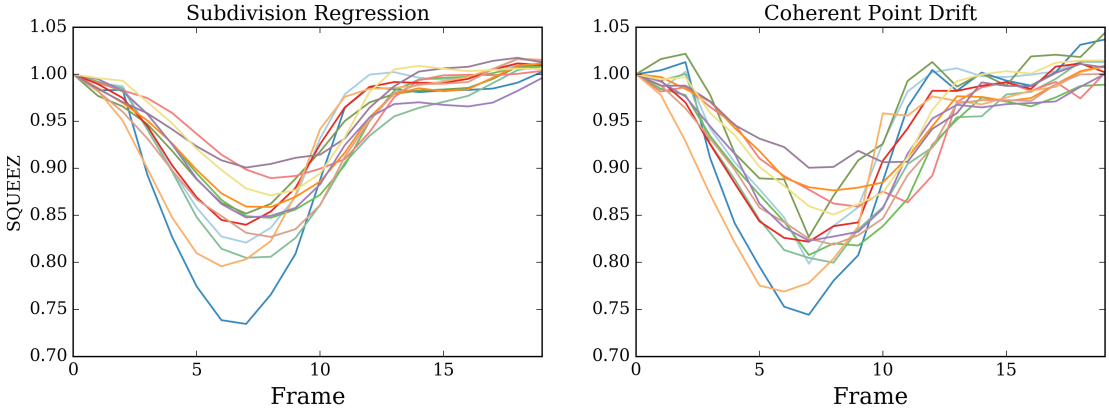


Figure 4.9: Global SQUEEZ Curves: Subdivision vs CPD Methods. Global SQUEEZ curves for all thirteen canine subjects studied as measured by the subdivision regression method (left) and the coherent point drift method (right). Corresponding colors in the two plots indicate the same subject. SQUEEZ is by definition equal to one at the end diastolic frame, indicating no contraction.

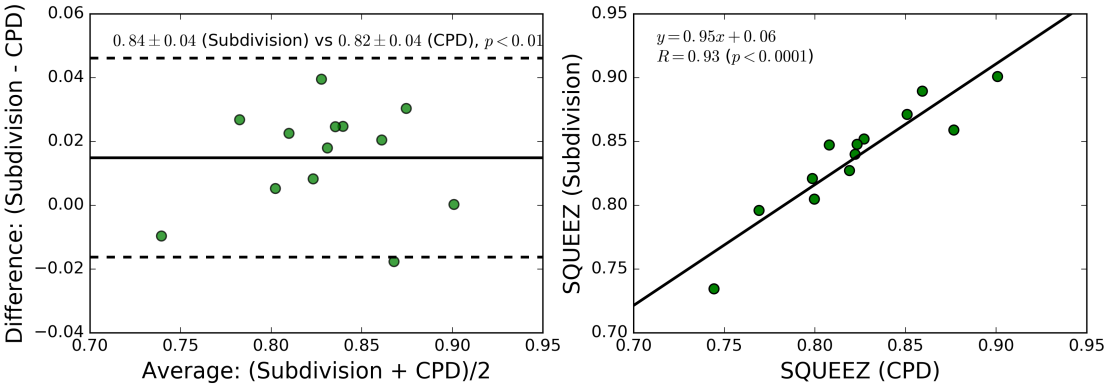


Figure 4.10: Peak Global SQUEEZ: Subdivision vs CPD Methods. Bland-Altman (top) and regression (bottom) comparing whole-heart, peak SQUEEZ as measured by our proposed method (Subdivision) versus the original SQUEEZ implementation (Coherent Point Drift, CPD). In the Bland-Altman, the solid line represents the mean difference, and the dashed lines represent ±1.96 standard deviations. In the regression, the solid line represents the least-squares best fit.

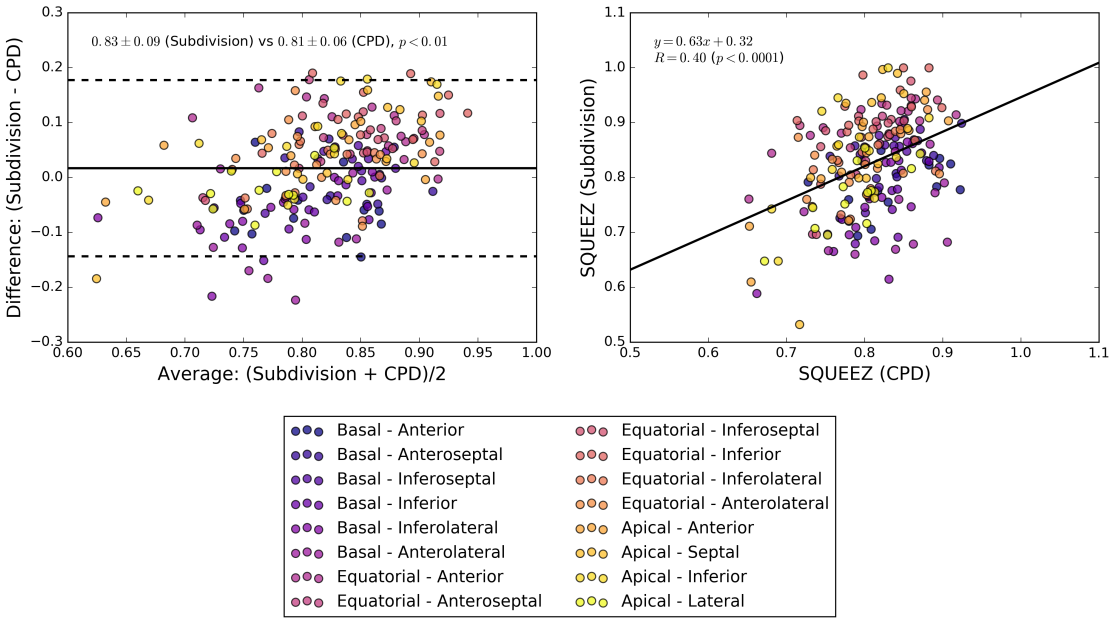


Figure 4.11: Peak Segmental SQUEEZ: Subdivison vs CPD Methods. Bland-Altman (top) and regression (bottom) comparing segmental, peak SQUEEZ as measured by the proposed method (subdivision surface registration) versus the original SQUEEZ implementation (Coherent Point Drift, CPD). In the Bland-Altman, the solid line represents the mean difference, and the dashed lines represent ±1.96 standard deviations. In the regression, the solid line represents the least-squares best fit.

only moderate. This may be attributed to the relative lack of trabeculation of the canine endocardium as compared with humans. Therefore, it is hypothesised that human studies planned for the future will demonstrate higher segmental correlation. Additionally, although the CPD method has itself been validated against HARP, it would be beneficial in the future to validate the subdivision registration method directly against HARP, and to assess the relative accuracy of the two methods. In terms of computational efficiency, this study focused on exploiting sparsity and maximising algorithmic efficiency, and spent relatively less time exploring parallelism beyond what was available by configuring Ceres with OpenBLAS and OpenMP. In the future, it may be possible to further improve the algorithm by adapting the implementation to run on a graphics processing unit (GPU). Although the image acquisition procedure was not optimised for right ventricular contrast, it should be noted that in an appropriate dataset the procedure presented here may be extended to other cardiac chambers with little or no modification. The

contributions made in this work are expected to translate to problems outside the heart, such as foetal neurosonography, where a closely related subdivision surface method has been successfully applied [144]. Finally, although contrast between the myocardium and the left ventricular blood pool is high, it was nonetheless necessary to manually prune the right ventricle in some cases. In future work, our algorithm may benefit from a fully automated segmentation procedure based on a machine learning approach such as a convolutional neural network.

5 Conclusions and Future Directions

Contents

5.1 Summary and Advancements in Knowledge 122
5.2 Limitations and Future Directions 126
5.3 Implications for Specialised Image Sequences 127
5.3.1 Contributions 127
5.3.2 Cine Watermark Imaging 127

5.1 Summary and Advancements in Knowledge

Despite four decades of investigation, robust and automated techniques for the noninvasive quantification of regional cardiac function remain illusive. The difficulty of acquiring specialized image sequences combined with the need for extensive manual intervention in image analysis has limited reproducibility and hampered clinical adoption. With these challenges in mind, the goal of this thesis was to develop a set of algorithms capable of robust and automatic regional cardiac functional analysis. Algorithms were designed to analyse 2-D+Time balanced steady state free precession (SSFP) cardiac magnetic resonance (CMR) sequences, which are routinely acquired in clinical practice, and 3-D+Time contrast-enhanced cardiac computed tomography (CCT) functional studies, which can be acquired in a single

heart beat and are achieving rapid clinical adoption.

In §2, a commercially-implemented cardiac magnetic resonance (CMR) feature tracking algorithm [42] was evaluated, which identifies points of interest and uses block-matching to determine displacements between frames. The algorithm was evaluated in two patient populations: one with hypertrophic cardiomyopathy (HCM), and one with arrhythmogenic right ventricular cardiomyopathy (ARVC) §2. Although manual contouring and adjustment limited both the intraobserver and interobserver reproducibility of cardiac strain measured with this technique, it was nonetheless possible to identify cardiac segments which differed in their strain parameters between healthy and disease patients at a population level. The most significant advancements in knowledge from these studies were:

- Hypertrophic Cardiomyopathy (HCM)
  - circumferential Transmural Strain Difference (cTSD), a novel functional parameter, was defined as the difference between epicardial and endocardial circumferential strain ($\text{cTSD} = \varepsilon_{cc}^{epi} - \varepsilon_{cc}^{endo}$).
  - compared with healthy control subjects, equatorial cTSD is higher in patients with sarcomere mutation regardless of whether they express overt clinical disease.
- Arrhythmogenic Right Ventricular Cardiomyopathy (ARVC)
  - RV longitudinal strain (ε_{ll}) measured in the 4C view is superior to that measured in the axial view (the current clinical standard for qualitative analysis in ARVC) in discriminating between overt disease and healthy control subjects.
  - Subtricuspid RV ε_{ll} measured in the 4C view is superior to qualitative wall motion scoring in discriminating between subjects with and without mutations.

Limitations identified in this commercial implementation (moderate reproducibility, manual contouring, manual contour correction, poor tracking at the termini of open-ended contours) were then used to guide development of an automated algorithm for the same purpose, making use of fully convolutional neural networks (CNN) for segmentation and quadratic basis spline registration across all frame simultaneously for tracking §3. While CNN segmentation of CMR images has been reported previously [112, 115–117, 145], the method presented here is notable for the following features:

- Three clinical planes–short axis (SA), horizontal long axis, (4C), and vertical long axis (2C)–were segmented in a single network. All prior work focused on segmenting a single cardiac plane, typically the SA view.
- Three foreground classes (LV bloodpool, RV bloodpool, and LV myocardium) were segmented. With the exception of Lieman-Sifry, et al [117], who segmented the same three foreground classes and whose work was published simultaneously with ours [146] at FIMH 2017, all prior work segmented at most two foreground classes.
- Prior work did not use CNN segmentation in conjunction with feature tracking.

Moreover, the quadratic basis spline registration method, originally developed in the context of 2-D echocardiography, and chosen because it allows contours to be fitted across all frames simultaneously, itself offers a number of advances over its original implementation [104]:

- The spline registration technique was applied to SSFP CMR, demonstrating the algorithm's the applicability to multiple modalities.
- Control point acceleration was penalized in the optimization, as opposed to control point velocity in the original implementation, with the effect of encouraging smooth, biologically plausible motion.

- A multiresolution version of the technique was implemented, where a coarse spline is registered, and the subdivided output used to initialise a subsequent pass. This has benefits over registering a highly subdivided spline directly in terms of computational efficiency as well as avoiding local minima.

- The registered splines were used to calculate ε_{cc}, while prior work stopped short of calculating functional cardiac parameters.

In §4, a technique was developed for quantification of regional function from 3-D+Time functional CCT studies. The technique is the logical extension of §3 and [104] to 3-D in that Loop subdivision surfaces (one possible extension of basis splines to 3-D) are used in place of quadratic basis splines, and are registered to the data in a single optimization across all frames simultaneously. Compared to previous work [104], the algorithm presented here offers a number of advances in knowledge:

- The Loop registration technique was applied to 3-D+Time CCT studies, on which relatively little work has been done in regional functional analysis.

- Control point acceleration was penalised rather than control point velocity.

- The technique was implemented as a multiresolution framework in which registered meshes were subdivided and used to initialise a subsequent pass, aiding in computational efficiency and avoiding local minima.

- High triangle aspect ratio was penalised to avoid low-quality meshes.

- The registered meshes were used to calculate Stretch Quantifier for Endocardial Engraved Zones (SQUEEZ), while prior work [104] stopped short of calculating functional parameters.

- The initial subdivision surface was generated directly from the image data, avoiding any need to define and initialize a model of the structure of interest as in [17, 104].

5.2 Limitations and Future Directions

Considering the ultimate goal of fully automated, whole-heart analysis, a number of future directions for this research suggest themselves. For example, although atrial structure and function have been shown to be important early indicators of cardiovascular disease [147], this thesis has concerned itself exclusively with ventricular function. Annotation of the atria in the HCM segmentation dataset developed in §3 and retraining the network to predict the five foreground classes (LV, RV, LA, and RA bloodpools and LV myocardium) is a natural first step in rectifying this deficiency. The subdivision surface registration algorithm §4, which currently relies on manual pruning of Hounsfield-unit-based bloodpool segmentations, could be further automated using CNN segmentation based on the Volume-Net [148], a 3-D extension of the U-Net architecture.

The quadratic basis spline tracking algorithm is expected to work similarly in the atria without modification. However, the limitation remains that only edge features from the segmentation are used in tracking, which may result in the contour "sliding" along the tracked boundary. Work done in landmark correspondence in natural images using CNNs [149] suggests that the feature vectors produced by the segmentation network immediately prior to class prediction may be incorporated into the loss function to produce more robust tracking.

In both the CMR §3 and CCT §4 pipelines, *global* functional analysis (global strain and SQUEEZ, respectively) may be performed following segmentation without intervention from the clinician. However, due to the highly variable orientation of the anatomy in the input images, input CMR and CCT images must be rotated into a cannonical orientation prior to segmental analysis. While a network could possibly be trained to predict these parameters separately and inform the segmental analysis, a more elegant solution would be to prepend an affine spatial transformer network (STN) [133] to the existing architecture in order to transform the input into a cannonical orientation. In addition to simplifying downstream functional analysis, this transformation may also simplify the task of the segmentation module and improve performance.

5.3 Implications for Specialised Image Sequences

5.3.1 Contributions

[1] Ronald J. Beyers, Davis M. Vigneault, Dean Schwartz, Nouha Salibi, David A. Bluemke and Thomas Denney. 'Preliminary Results: Cardiac Cine "Watermark" MRI provides both Anatomical Function via Magnitude Cine and 2D Myocardial Strain via Spatially Modulated Phase'. In: *ISMRM*. Singapore, 2016.

[2] Davis M. Vigneault, Ronald J. Beyers, Chia-Ying Liu, J. Alison Noble, Thomas S. Denney and David A. Bluemke. 'Motion tracking in cardiac MRI: Cine Watermark tracking of myocardial strain'. In: *ISMRM*. Hololulu, Hawaii, 2017.

[3] Ronald J. Beyers, Davis M. Vigneault, Nouha Salibi, David A. Bluemke and Thomas S. Denney. 'Accelerated Cardiac Cine "Watermark" MRI provides Cardiac Function via Magnitude Cine and 2D Myocardial Strain via Spatially Modulated Phase'. In: *ISMRM*. Honolulu, Hawaii, 2017.

5.3.2 Cine Watermark Imaging

This work has focused very deliberately on images which are readily acquired clinically, as it is felt that robust analysis of these images is necessary for the widespread clinical adoption of regional functional analysis. However, the information available in these images is fundamentally limited in comparison to more specialised image sequences such as spatial modulation of magnetization (SPAMM) tagged CMR, especially in the LV midwall. For this reason, the author recognizes that specialized acquisitions will remain important in, for example, targeted research in cardiac mechanics where the LV midwall is of particular interest. However, even in the case of specialized image acquisitions, the work presented here may be useful in suggesting more robust and automated analysis.

Take, for example, the "cine-watermarking" CMR image sequence, developed in collaboration with researchers at Auburn Medical Center (Auburn, Alabama) [150, 151].[1] This is a modified CSPAMM acquisition and reconstruction technique §1.5.1.1 where the radiofrequency (RF) prepulse has a flip angle of $\pi/4$ and SPAMM and CSPAMM images are acquired in an interlieved fashion. From the resulting four complex image sequences (frequency encoding SPAMM, f_0; frequency encoding CSPAMM, f_π; phase encoding SPAMM, p_0; and phase encoding CSPAMM, p_π), a

[1] The author wishes to acknowledge Dr. Ronald Beyers for designing the cine watermarking reconstruction technique, and for acquiring the images.

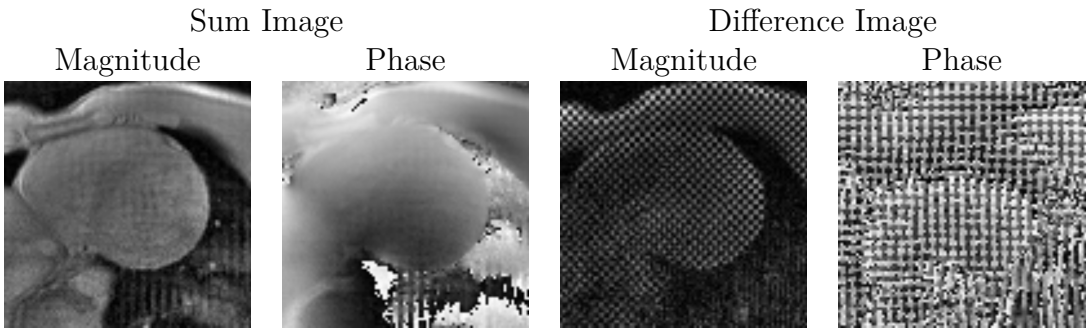


Figure 5.1: Representative Cine Watermarking Images. The sum image (left) is the (complex) sum of four images: the two phase encoding (SPAMM and CSPAMM) images and the two frequency encoding (SPAMM and CSPAMM) images. The difference image (right) is the (complex) difference between the two phase encoding images, subtracted from the difference between the two frequency encoding images, plus π.

normal $T1$-weighted image without tags (the "sum" image, I_s) and an image tagged both in the magnitude *and phase* (the "difference" image, I_d) may be reconstructed (Fig. 5.1). The sum image is the (complex) sum of all four images,

$$I_s = f_0 + f_\pi + p_0 + p_\pi, \tag{5.1}$$

whereas the difference image is a (complex) difference of differences,

$$I_d = (f_0 - f_\pi) - (p_0 - p_\pi) + \pi. \tag{5.2}$$

Traditionally, these images would be analysed using harmonic phase (HARP) analysis, which is subject to the limitations discussed previously §1.5.1.2. Given an appropriate ground truth displacement field, it would be reasonable to train a CNN regression network which would take a four-channel input (the magnitude and phase of the fixed and moving images) and return a two-channel output (either Cartesian or polar components of a 2-D displacement). A schematic of one possible network is shown in Fig. 5.2.[2]

An immediate obstacle is the lack of dense ground truth displacement fields, which it would be infeasible to annotate manually in a dataset large enough to train such a network. However, it may be possible to *simulate* such a dataset from SSFP

[2]The author would like to acknowledge Weidi Xie for aiding in the design of this architecture.

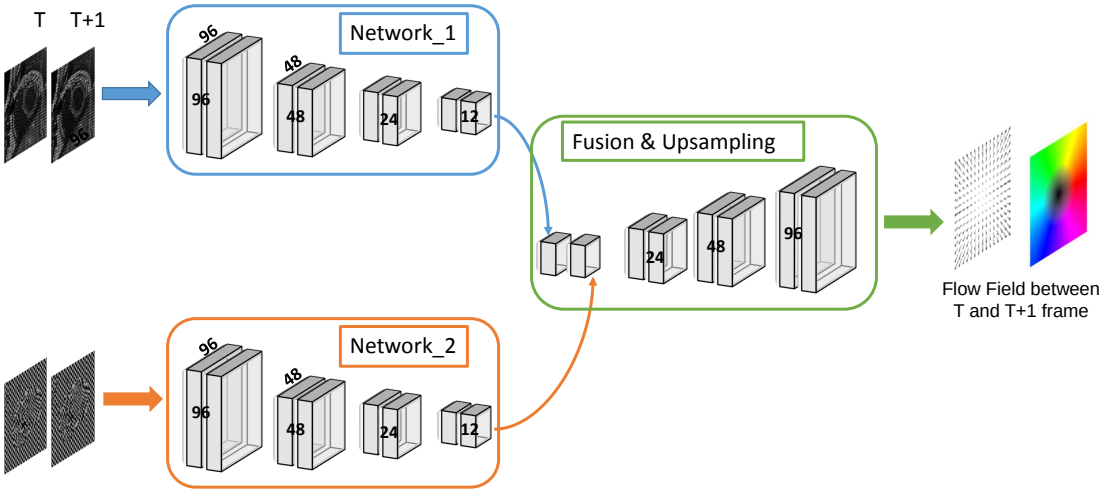
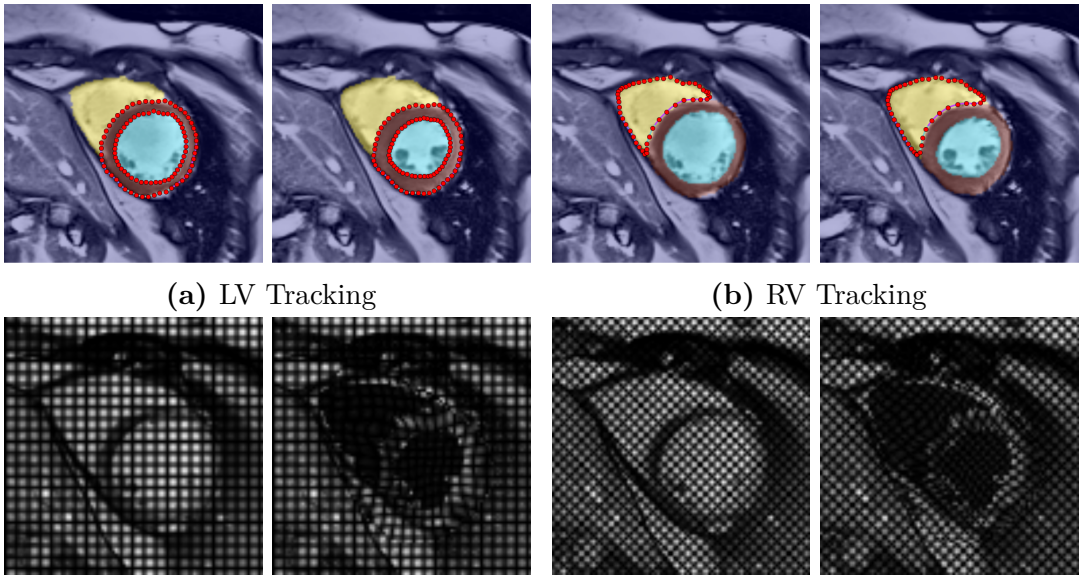


Figure 5.2: Cine Watermarking CNN Architecture. Two separate network branches take as input synthesized magnitude and phase components, respectively, of the fixed (time T) and moving (time $T+1$). The results of these two networks are concatenated, and the result is upsampled.

CMR images from the segmentation and tracking analysis presented in §3. Tag lines are first simulated by multiplying the end diastolic (ED) frame of an SSFP image sequence by the appropriate planar sinusoids. The magnitude of the sinusoid is varied to simulate tag fading, the available ventricular segmentations are used to simulate decay of bloodpool signal, and the cine watermarking images could be reconstructed as prescribed in Eqns. 5.1 and 5.2. A sparse field of displacement vectors may be calculated from the registered splines, and then interpolated to form a dense displacement field. (In order to prevent shifting and warping of the background, zero-valued displacement vectors are spaced at regular intervals throughout the background class, acting as "pins" to constrain the interpolation.) These dense, interpolated deformation fields may then be used to distort the simulated tag images.

A representative simulation is shown in Fig. 5.3. Note that the data may be augmented by generating multiple simulations per patient, using tag spacing, tag line orientation, and bloodpool fading parameters chosen randomly from within a specified range. Compared with using a mathematical model of cardiac contraction such as the Jones model [152], this technique has the benefit of providing a



(a) LV Tracking **(b)** RV Tracking

(c) Simulation A **(d)** Simulation B

Figure 5.3: Simulated Cine Watermarking Images. Bezier tracking results in the LV (a) and RV (b) are used to generate dense displacement fields, which are in turn used to generate simulated cine watermark images. Two possible simulations with different tag parameters for the same image sequence are shown (c, d).

large number of realistic cardiac displacements registered to clinical anatomical images. Additionally, this approach avoids the possibility of the CNN learning the constraints of the model, and failing in the case of nonuniform motion (such as a regional wall motion abnormality).

Preliminary results from a network trained in this way visually agree well with ground truth (Fig. 5.4). Note that, to simplify both training and interpretation, the ground truth displacement field was masked outside the LV myocardium prior to calculating the loss. This prevents the network from focusing on large losses in the highly uncertain blood pool regions. While these results are preliminary, they nonetheless suggest a promising direction for future research.

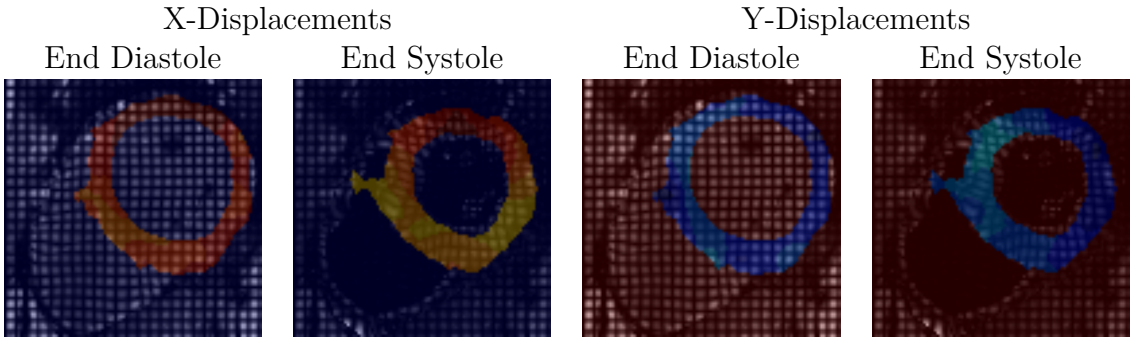


Figure 5.4: Predicted Displacement Fields in Simulated Cine Watermark Images. X- and Y- displacement fields are shown at end diastole (ED) and end systole (ES). The network learns to predict visually appropriate displacements and to ignore regions outside the LV myocardium.

Appendices

A

Wall Thickness vs cTSD in HCM

Contents

A.1 Motivation 133
A.2 Proof 134
A.3 Results 135

A.1 Motivation

The primary result of §2.2 is that circumferential Transmural Strain Difference (cTSD), which is defined as the difference between epicardial and endocardial ε_{cc}, is higher in patients with preclinical hypertrophic cardiomyopathy (HCM) compared with control subjects. Although maximal wall thickness (MWT) was similar between the preclinical HCM and control groups (9.5 ± 1.4 vs 9.8 ± 2.2mm, p = NS) the possibility that the higher cTSD might result from mild, statistically insignificant thickening was nonetheless thoroughly examined.

By treating the myocardium in short axis as two concentric circles, cTSD can be predicted entirely in terms of outer end diastolic radius ($r_{out,ed}$), end diastolic wall thickness (wt_{ed}), epicardial strain (ε_{epi}), and a chosen increase in myocardial area (A_{exp}).

Here, measured cTSD values are compared with those predicted by this cylindrical model when A_{exp} is set empirically to biologically plausible values. It is shown that cTSD values predicted by this model follow a similar trend to those which are measured experimentally, but that the control and preclinical groups are statistically different only in terms of measured cTSD, not predicted cTSD.

A.2 Proof

cTSD is defined in terms of endocardial and epicardial circumferential shortening

$$cTSD = \varepsilon_{epi} - \varepsilon_{end}. \tag{A.1}$$

Treating the myocardium in short axis as two concentric circles, cTSD may be rewritten in terms of inner and outer radii at end diastole (ED) and end systole (ES)

$$cTSD = \frac{(r_{out,es} - r_{out,ed})}{r_{out,ed}} - \frac{(r_{in,es} - r_{in,ed})}{r_{in,ed}}. \tag{A.2}$$

Additionally, it is assumed that the area of the myocardium increases by a constant factor A_{exp},

$$0 = A_{exp}\left(r_{out,ed}^2 - r_{in,ed}^2\right) - \left(r_{out,es}^2 - r_{in,es}^2\right), \tag{A.3}$$

and solve this equation for $r_{in,es}$

$$r_{in,es} = \pm\sqrt{A_{exp}\left(r_{in,ed}^2 - r_{out,ed}^2\right) + r_{out,es}^2}. \tag{A.4}$$

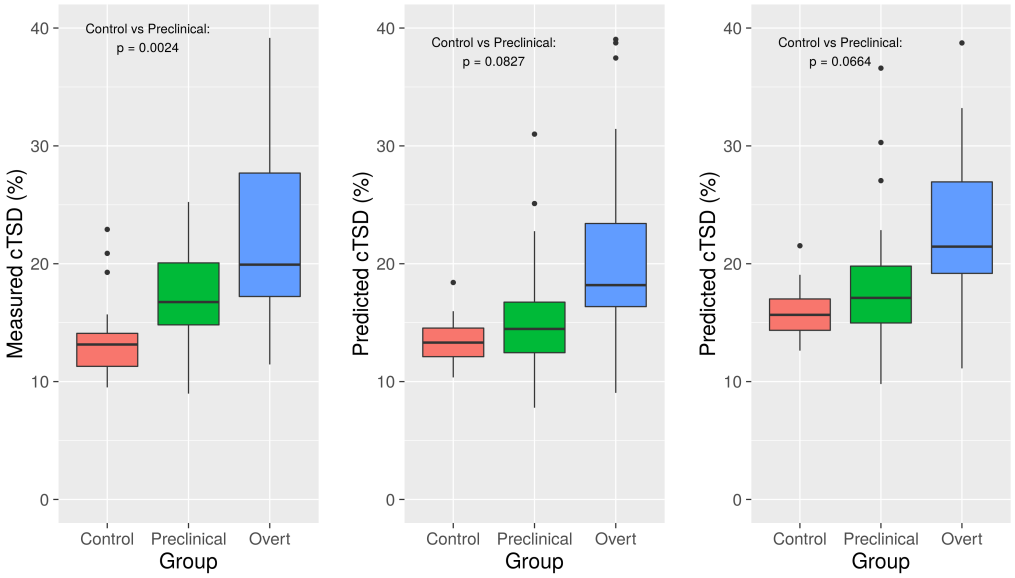
Taking the positive square root of $r_{in,es}$ and writing $r_{out,es}$ and $r_{in,ed}$ in terms of known quantities, cTSD may be written in terms of epicardial strain (ε_{epi}), the outer radius at ED ($r_{out,ed}$), and ED wall thickness (wt_{ed})

$$cTSD = \varepsilon_{epi} - \frac{-r_{out,ed} + wt_{ed} + \sqrt{A_{exp}\left((r_{out,ed} - wt_{ed})^2 - r_{out,ed}^2\right) + (r_{out,ed}\varepsilon_{epi} + r_{out,ed})^2}}{r_{out,ed} - wt_{ed}}. \tag{A.5}$$

A.3 Results

Across all segments and slices, it is reported in [8] that endocardial and epicardial circumferential strain are $32 \pm 4\%$ and $16 \pm 4\%$, or cTSD of $\approx 16\%$. In the HCMNet cohort, cTSD is reported to be 13.6%. To perform the simulation, A_{exp} is set so as to match the mean predicted cTSD in the control group to Moore's and our own measured values ($A_{exp} = 1.23$ and $A_{exp} = 1.17$, respectively).

Measured cTSD values, and predicted cTSD values at the two area factors are shown in Fig. A.1. The measured and predicted cTSD values appear to be broadly correlated. This suggests that our model is reflective of biological contraction, and accounts for some fraction of the observed difference. Moreover, our measured values show that the preclinical group is intermediate between the control and overt groups, and the preclinical group has significantly higher cTSD compared with the control group. Though some difference between control and preclinical values is noted in the simulations, the results do not reach statistical significance. This suggests that some amount of the observed difference in cTSD may be due to mild wall thickening, but equally that there is an additional mechanism independent of simple geometric considerations.



(a) Measured cTSD values. **(b)** Predicted, $A_{exp} = 1.17$. **(c)** Predicted, $A_{exp} = 1.23$.

Figure A.1: Measured vs Predicted cTSD. Measured cTSD values (a), predicted values setting A_{exp} to match predicted and measured means in the control group (b), and predicted values setting A_{exp} to match the normal cTSD value reported in [8] (c).

B
Mesh Decimation

In order to investigate the effect of Gaussian noise applied to a source mesh on the quality of a decimated mesh, three evaluation metrics were chosen: patch area (Figure B.1), patch aspect ratio (Figure B.2), and valency (Figure B.3). For each metric, the histogram and normal probability plot are shown for the unperturbed and perturbed meshes. Histograms provide a generic way of visualizing distributions. Normal probability plots, on the other hand, specifically assess normality by plotting each value against its theoretical quantile for a normally distributed dataset of the same mean and standard deviation; a perfectly normal dataset will lie along a straight line with a coefficient of determination R^2 of one. In the unperturbed case, the histograms have a high standard deviation and significant right skew, with instances of very high triangle area, aspect ratio, and valency. In the perturbed case, the distributions are narrower, with less right skew, indicating greater uniformity. This assessment is confirmed by the normal probability plots, where in each case R^2 is nearer to unity with perturbation than without. (The reader is refered to [142] for a more thorough discussion, including implementation details.)

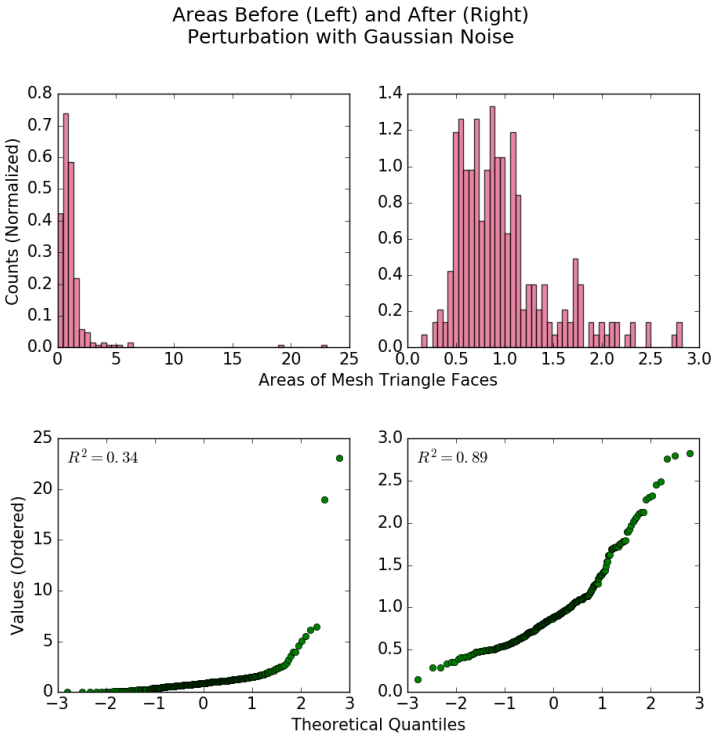


Figure B.1: Distribution of patch areas in the clean and noisy meshes.

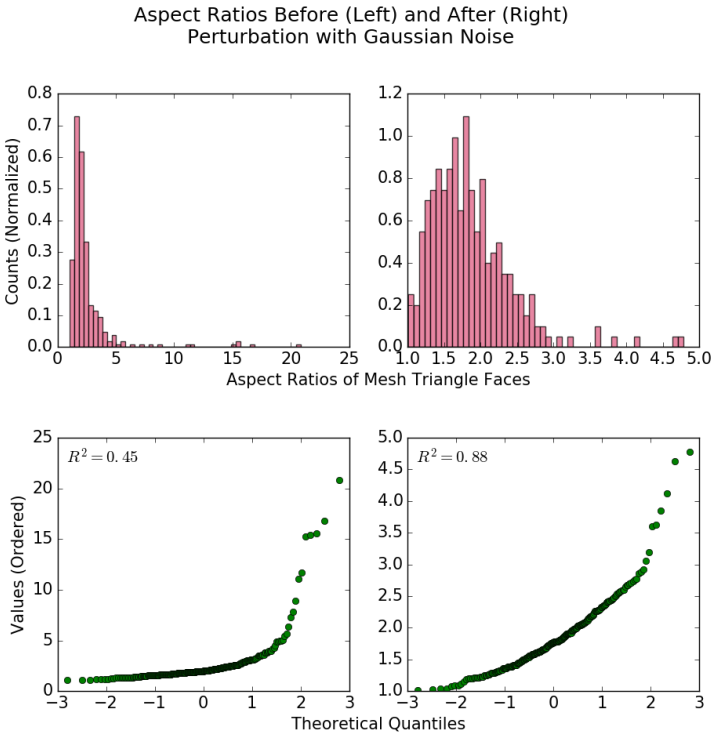


Figure B.2: Distribution of patch aspect ratios in the clean and noisy meshes.

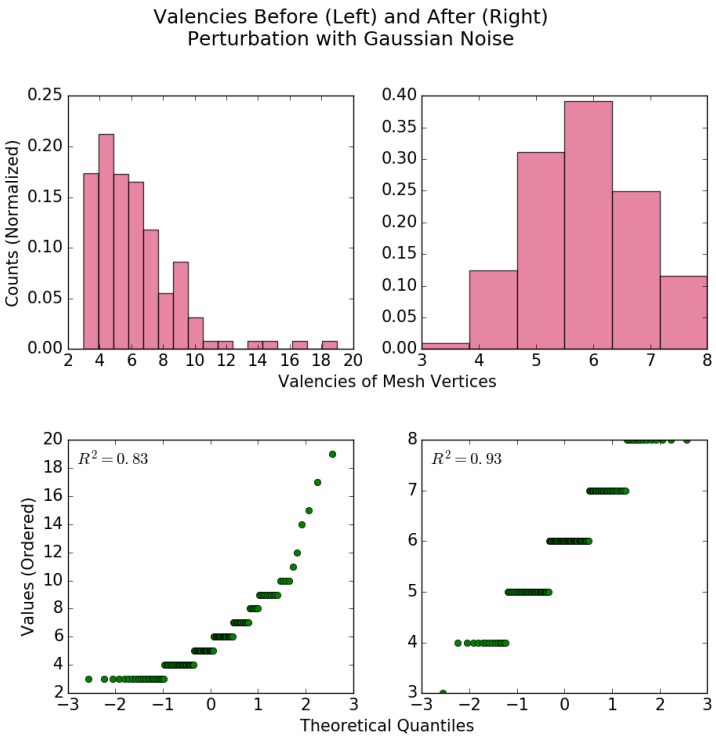


Figure B.3: Distribution of valencies in the clean and noisy meshes.

C

Loop Subdivision Surfaces

Contents

C.1 Barycentric B-Spline Basis Functions 141
C.2 Loop Subdivision Matrices 141
C.2.1 Subdivision Matrix S 141
C.2.2 Extended Subdivision Matrix, A 142
C.2.3 Bigger Subdivision Matrix, $\bar{A}$ 143
C.2.4 Picking Matrix, Pk 143
C.3 Eigenstructure of A 144
C.3.1 Eigenstructure of S 145
C.3.2 Eigenstructure of A 146
C.3.3 Evaluating a Subdivision Patch at the Origin 148

The barycentric B-Spline basis functions for a quartic triangle B-Spline patch and the matrices relevant to Loop subdivision are given in [139] and [104]. Unfortunately, each description suffers from the following shortcomings:

- The subdivision matrix S is not sufficiently explained.
- Details for recovering real eigenvectors for the subdivision matrix S are omitted.
- Details for calculating the lower left block of the eigenvector matrix of A are omitted.

This appendix gives a complete description of the relevant basis functions and matrices, while overcoming these shortcomings.

C.1 Barycentric B-Spline Basis Functions

Given a set of 12 control points $X \in \mathbb{R}^{n\times 12}$ and a local parametric coordinate $\mathbf{t} = (s,t)$, the position on the quadratic triangular basis spline surface is given by $X\mathbf{b}(\mathbf{t})$, where $\mathbf{b}(\mathbf{t}) \in \mathbb{R}^{12}$ is a set of barycentric weights given by

$$\frac{1}{12}\begin{bmatrix} -s^4 - 2s^3t + 8s^3 + 12s^2t - 12s^2 - 2st^3 + 12st^2 - 12st - t^4 + 8t^3 - 12t^2 + 6 \\ -s^4 - 2s^3t - 4s^3 - 6s^2t + 6s^2 + 4st^3 - 12st^2 + 6st + 4s + 2t^4 - 4t^3 + 2t + 1 \\ 2s^4 + 4s^3t - 4s^3 - 2st^3 + 6st^2 - 6st + 2s - t^4 + 2t^3 - 2t + 1 \\ -s^4 - 2s^3t + 2s^3 + 2st^3 - 6st^2 + 6st - 2s + t^4 - 4t^3 + 6t^2 - 4t + 1 \\ s^4 + 2s^3t - 4s^3 - 6s^2t + 6s^2 - 2st^3 + 6st - 4s - t^4 + 2t^3 - 2t + 1 \\ -s^4 - 2s^3t + 2s^3 + 6s^2t + 4st^3 - 6st - 2s + 2t^4 - 4t^3 + 2t + 1 \\ 2s^4 + 4s^3t - 4s^3 - 12s^2t - 2st^3 - 6st^2 + 6st + 2s - t^4 - 4t^3 + 6t^2 + 4t + 1 \\ -s^4 - 2s^3t + 2s^3 + 6s^2t - 2st^3 + 6st^2 - t^4 + 2t^3 \\ s^4 + 2s^3t \\ -s^4 - 2s^3t + 2s^3 \\ 2st^3 + t^4 \\ -2st^3 - t^4 + 2t^3 \end{bmatrix} \tag{C.1}$$

C.2 Loop Subdivision Matrices

C.2.1 Subdivision Matrix S

The subdivision matrix $S \in \mathbb{R}^{(N+1)\times(N+1)}$ encapsulates the logic for subdividing the one-ring surrounding the (possibly extraordinary) *vertex* of interest. The resulting ring has identical topology to the original. S is given by,

$$\begin{bmatrix} a_N & b_N & \cdots & \cdots & \cdots & \cdots & b_N \\ c & c & d & 0 & \cdots & 0 & d \\ \vdots & d & \ddots & \ddots & \ddots & & 0 \\ \vdots & 0 & \ddots & \ddots & \ddots & \ddots & \vdots \\ \vdots & \vdots & \ddots & \ddots & \ddots & \ddots & 0 \\ \vdots & 0 & & \ddots & \ddots & \ddots & d \\ c & d & 0 & \cdots & 0 & d & c \end{bmatrix}, \tag{C.2}$$

where

$$\begin{aligned} a_N &= 1 - \alpha(N), \\ b_N &= \frac{\alpha(N)}{N}, \\ c &= \frac{3}{8}, \\ d &= \frac{1}{8}, \text{ and} \\ \alpha N &= \frac{5}{8} - \frac{(3 + 2\cos(2\pi/N))^2}{64}. \end{aligned} \tag{C.3}$$

Note that the lower right $N \times N$ block of S is a Toeplitz matrix, with c along the diagonal, and d along the subdiagonal, the superdiagonal, and in the upper right and lower left corners.

C.2.2 Extended Subdivision Matrix, A

The extended subdivision matrix $A \in \mathbb{R}^{(N+6)\times(N+6)}$ encapsulates the logic for subdividing the one-ring surrounding the (possibly extraordinary) *patch* of interest. The resulting patch has identical topology to the original. A is a block matrix given by,

$$A = \begin{bmatrix} S & 0 \\ S_{11} & S_{12} \end{bmatrix}, \tag{C.4}$$

where

$$S_{11} = \frac{1}{16} \begin{bmatrix} 2 & 6 & 0 & 0 & \cdots & 0 & 0 & 6 \\ 1 & 10 & 1 & 0 & \cdots & 0 & 0 & 1 \\ 2 & 6 & 6 & 0 & \cdots & 0 & 0 & 0 \\ 1 & 1 & 0 & 0 & \cdots & 0 & 1 & 10 \\ 2 & 0 & 0 & 0 & \cdots & 0 & 6 & 6 \end{bmatrix} \tag{C.5}$$

and

$$S_{12} = \frac{1}{16} \begin{bmatrix} 2 & 0 & 0 & 0 & 0 \\ 1 & 1 & 1 & 0 & 0 \\ 0 & 0 & 2 & 0 & 0 \\ 1 & 0 & 0 & 1 & 1 \\ 0 & 0 & 0 & 0 & 2 \end{bmatrix}. \tag{C.6}$$

C.2.3 Bigger Subdivision Matrix, $\bar{A}$

The bigger subdivision matrix $\bar{A} \in \mathbb{R}^{(N+12)\times(N+6)}$ encapsulates the logic for subdividing the one-ring surounding the patch of interest, and additionally for constructing three ordinary patches. Importantly, the four central patches produced by subdividing X with $\bar{A}$ span the same parametric space as the original patch. $\bar{A}$ is given by,

$$\bar{A} = \begin{bmatrix} S & 0 \\ S_{11} & S_{12} \\ S_{21} & S_{22} \end{bmatrix}, \tag{C.7}$$

where

$$S_{21} = \frac{1}{8}\begin{bmatrix} 0 & 3 & 0 & 0 & \cdots & 0 & 0 & 1 \\ 0 & 3 & 0 & 0 & \cdots & 0 & 0 & 0 \\ 0 & 3 & 1 & 0 & \cdots & 0 & 0 & 0 \\ 0 & 1 & 0 & 0 & \cdots & 0 & 0 & 3 \\ 0 & 0 & 0 & 0 & \cdots & 0 & 0 & 3 \\ 0 & 0 & 0 & 0 & \cdots & 0 & 1 & 3 \end{bmatrix} \tag{C.8}$$

and

$$S_{21} = \frac{1}{8}\begin{bmatrix} 3 & 1 & 0 & 0 & 0 \\ 1 & 3 & 1 & 0 & 0 \\ 0 & 1 & 3 & 0 & 0 \\ 3 & 0 & 0 & 1 & 0 \\ 1 & 0 & 0 & 3 & 1 \\ 0 & 0 & 0 & 1 & 3 \end{bmatrix}. \tag{C.9}$$

C.2.4 Picking Matrix, Pk

The picking matrices $P_k \in \mathbb{R}^{(12\times(N+12)}$ select the one-ring around the k^{th} ordinary child patch ($k \in \{0, 1, 2\}$).

$$P_0 = \begin{bmatrix}
0 & 1 & 0 & 0 & \cdots & 0 & 0 & 0 & 0 & 0 & 0 & 0 & 0 & 0 & 0 & 0 & 0 & 0 & 0 \\
0 & 0 & 0 & 0 & \cdots & 0 & 0 & 0 & 0 & 1 & 0 & 0 & 0 & 0 & 0 & 0 & 0 & 0 & 0 \\
0 & 0 & 0 & 0 & \cdots & 0 & 0 & 0 & 0 & 0 & 1 & 0 & 0 & 0 & 0 & 0 & 0 & 0 & 0 \\
0 & 0 & 1 & 0 & \cdots & 0 & 0 & 0 & 0 & 0 & 0 & 0 & 0 & 0 & 0 & 0 & 0 & 0 & 0 \\
1 & 0 & 0 & 0 & \cdots & 0 & 0 & 0 & 0 & 0 & 0 & 0 & 0 & 0 & 0 & 0 & 0 & 0 & 0 \\
0 & 0 & 0 & 0 & \cdots & 0 & 0 & 1 & 0 & 0 & 0 & 0 & 0 & 0 & 0 & 0 & 0 & 0 & 0 \\
0 & 0 & 0 & 0 & \cdots & 0 & 0 & 0 & 1 & 0 & 0 & 0 & 0 & 0 & 0 & 0 & 0 & 0 & 0 \\
0 & 0 & 0 & 0 & \cdots & 0 & 0 & 0 & 0 & 0 & 0 & 0 & 0 & 1 & 0 & 0 & 0 & 0 & 0 \\
0 & 0 & 0 & 0 & \cdots & 0 & 0 & 0 & 0 & 0 & 0 & 0 & 0 & 0 & 1 & 0 & 0 & 0 & 0 \\
0 & 0 & 0 & 0 & \cdots & 0 & 0 & 0 & 0 & 0 & 0 & 0 & 0 & 0 & 0 & 1 & 0 & 0 & 0 \\
0 & 0 & 0 & 0 & \cdots & 0 & 0 & 0 & 0 & 0 & 0 & 0 & 0 & 0 & 0 & 0 & 1 & 0 & 0 \\
0 & 0 & 0 & 0 & \cdots & 0 & 0 & 0 & 0 & 0 & 0 & 1 & 0 & 0 & 0 & 0 & 0 & 0 & 0
\end{bmatrix} \tag{C.10}$$

$$P_1 = \begin{bmatrix}
0 & 0 & 0 & 0 & \cdots & 0 & 0 & 0 & 1 & 0 & 0 & 0 & 0 & 0 & 0 & 0 & 0 & 0 & 0 \\
0 & 0 & 0 & 0 & \cdots & 0 & 0 & 1 & 0 & 0 & 0 & 0 & 0 & 0 & 0 & 0 & 0 & 0 & 0 \\
0 & 0 & 0 & 0 & \cdots & 0 & 0 & 0 & 0 & 0 & 0 & 1 & 0 & 0 & 0 & 0 & 0 & 0 & 0 \\
0 & 0 & 0 & 0 & \cdots & 0 & 0 & 0 & 0 & 0 & 0 & 0 & 0 & 0 & 0 & 0 & 1 & 0 & 0 \\
0 & 0 & 0 & 0 & \cdots & 0 & 0 & 0 & 0 & 0 & 0 & 0 & 0 & 1 & 0 & 0 & 0 & 0 & 0 \\
0 & 0 & 0 & 0 & \cdots & 0 & 0 & 0 & 0 & 1 & 0 & 0 & 0 & 0 & 0 & 0 & 0 & 0 & 0 \\
0 & 1 & 0 & 0 & \cdots & 0 & 0 & 0 & 0 & 0 & 0 & 0 & 0 & 0 & 0 & 0 & 0 & 0 & 0 \\
1 & 0 & 0 & 0 & \cdots & 0 & 0 & 0 & 0 & 0 & 0 & 0 & 0 & 0 & 0 & 0 & 0 & 0 & 0 \\
0 & 0 & 0 & 0 & \cdots & 0 & 1 & 0 & 0 & 0 & 0 & 0 & 0 & 0 & 0 & 0 & 0 & 0 & 0 \\
0 & 0 & 0 & 0 & \cdots & 0 & 0 & 0 & 0 & 0 & 0 & 1 & 0 & 0 & 0 & 0 & 0 & 0 & 0 \\
0 & 0 & 1 & 0 & \cdots & 0 & 0 & 0 & 0 & 0 & 0 & 0 & 0 & 0 & 0 & 0 & 0 & 0 & 0 \\
0 & 0 & 0 & 0 & \cdots & 0 & 0 & 0 & 0 & 0 & 1 & 0 & 0 & 0 & 0 & 0 & 0 & 0 & 0
\end{bmatrix} \tag{C.11}$$

$$P_2 = \begin{bmatrix}
0 & 0 & 0 & 0 & \cdots & 0 & 0 & 1 & 0 & 0 & 0 & 0 & 0 & 0 & 0 & 0 & 0 & 0 & 0 \\
0 & 0 & 0 & 0 & \cdots & 0 & 0 & 0 & 1 & 0 & 0 & 0 & 0 & 0 & 0 & 0 & 0 & 0 & 0 \\
0 & 1 & 0 & 0 & \cdots & 0 & 0 & 0 & 0 & 0 & 0 & 0 & 0 & 0 & 0 & 0 & 0 & 0 & 0 \\
1 & 0 & 0 & 0 & \cdots & 0 & 0 & 0 & 0 & 0 & 0 & 0 & 0 & 0 & 0 & 0 & 0 & 0 & 0 \\
0 & 0 & 0 & 0 & \cdots & 0 & 1 & 0 & 0 & 0 & 0 & 0 & 0 & 0 & 0 & 0 & 0 & 0 & 0 \\
0 & 0 & 0 & 0 & \cdots & 0 & 0 & 0 & 0 & 0 & 0 & 0 & 1 & 0 & 0 & 0 & 0 & 0 & 0 \\
0 & 0 & 0 & 0 & \cdots & 0 & 0 & 0 & 0 & 0 & 0 & 1 & 0 & 0 & 0 & 0 & 0 & 0 & 0 \\
0 & 0 & 0 & 0 & \cdots & 0 & 0 & 0 & 0 & 0 & 0 & 0 & 0 & 0 & 0 & 0 & 1 & 0 & 0 \\
0 & 0 & 0 & 0 & \cdots & 0 & 0 & 0 & 0 & 0 & 0 & 0 & 1 & 0 & 0 & 0 & 0 & 0 & 0 \\
0 & 0 & 0 & 0 & \cdots & 0 & 0 & 0 & 0 & 1 & 0 & 0 & 0 & 0 & 0 & 0 & 0 & 0 & 0 \\
0 & 0 & 0 & 0 & \cdots & 0 & 0 & 0 & 0 & 0 & 0 & 0 & 0 & 0 & 0 & 0 & 0 & 1 & 0 \\
0 & 0 & 0 & 0 & \cdots & 0 & 0 & 0 & 0 & 0 & 0 & 0 & 0 & 0 & 0 & 0 & 0 & 0 & 1
\end{bmatrix} \tag{C.12}$$

C.3 Eigenstructure of A

The precise eigenstructure of A is required in order to efficiently take powers of A, and to evaluate the surface position and normals at the origin.

C.3.1 Eigenstructure of S

The matrix S has either two or three unique eigenvalues (in the case of even and odd N, respectively). All other eigenvalues are of multiplicity two. For this reason, the eigenvectors are not specified unambiguously, and must be deliberately designed so as to avoid complex values. The complex eigenvectors S are given by the columns of the matrix

$$\Sigma = \begin{bmatrix} 1 & -\frac{8}{3}\alpha_N & 0 & 0 & \cdots & 0 \\ 1 & 1 & 1 & 1 & \cdots & 1 \\ 1 & 1 & E(1) & E(2) & \cdots & E(N-1) \\ 1 & 1 & E(2) & E(2\times 2) & \cdots & E(2\times(N-1) \\ \vdots & \vdots & \vdots & \vdots & \ddots & \vdots \\ 1 & 1 & E(N-1) & E((N-1)\times 2) & \cdots & E((N-1)\times(N-1)) \end{bmatrix}, \tag{C.13}$$

where

$$E(k) = e^{2\pi i k/N}. \tag{C.14}$$

Columns corresponding to equal eigenvalues (e.g., columns 3 and 7 when $N = 6$) have the same real component, and imaginary components of opposite sign. Therefore, the two real-valued eigenvectors can be recovered as $(\sigma_3 + \sigma_7)/2$ and $(\sigma_3 - \sigma_7)/(2i)$, where σ_j is the j^{th} column of Σ and $i = \sqrt{-1}$.

The eigenvalues of S are given by

$$\Lambda = \operatorname{diag}\left(\begin{bmatrix} 1 & \frac{5}{8} - \alpha_N & f(1) & \cdots f(N-1) \end{bmatrix}\right), \tag{C.15}$$

where

$$f(k) = \frac{3}{8} + \frac{2}{8}\cos(2\pi k/N). \tag{C.16}$$

C.3.2 Eigenstructure of A

The eigenvectors of S_{12} are given by

$$\Sigma_{12} = \begin{bmatrix} 0 & -1 & 1 & 0 & 0 \\ 1 & -1 & 1 & 0 & 1 \\ 1 & 0 & 0 & 0 & 0 \\ 0 & 0 & 1 & 1 & 0 \\ 0 & 1 & 0 & 0 & 0 \end{bmatrix}, \tag{C.17}$$

and the eigenvalues are given by

$$\Lambda_{12} = \operatorname{diag}\left(\begin{bmatrix} \frac{1}{8} & \frac{1}{8} & \frac{1}{8} & \frac{1}{16} & \frac{1}{16} \end{bmatrix}.\right) \tag{C.18}$$

In order to complete the eigenanalysis of A, the problem is first represented in block notation,

$$\begin{bmatrix} S & 0 \\ S_{11} & S_{12} \end{bmatrix} \begin{bmatrix} \Sigma & \mathbf{0} \\ \Sigma_{11} & \Sigma_{12} \end{bmatrix} = \begin{bmatrix} \Sigma & \mathbf{0} \\ \Sigma_{11} & \Sigma_{12} \end{bmatrix} \cdot \begin{bmatrix} \Lambda & \mathbf{0} \\ \mathbf{0} & \Lambda_{12} \end{bmatrix} \tag{C.19}$$

Note that the only matrix as yet unspecified is the lower left block Σ_{11} of the eigenvector matrix. Performing the matrix multiplications on both sides, one obtains the relation

$$\begin{bmatrix} S\Sigma & \mathbf{0} \\ S_{11}\Sigma + S_{12}\Sigma_{11} & S_{12}\Sigma_{12} \end{bmatrix} = \begin{bmatrix} \Sigma\Lambda & \mathbf{0} \\ \Sigma_{11}\Lambda & \Sigma_{12}\Lambda_{12} \end{bmatrix}. \tag{C.20}$$

The lower left blocks on either side are equated and rearranged slightly, obtaining

$$S_{11}\Sigma = -S_{12}\Sigma_{11} + \Sigma_{11}\Lambda, \tag{C.21}$$

which is in the form of the Sylvester equation, $Q = AX + XB$, where $Q = S_{11}\Sigma$, $A = -S_{12}$, $B = \Lambda$, and $X = \Sigma$. `LAPACK` contains a subroutine `TRSYL` which solves the Sylvester equation when A and B are real, quasi-upper triangular matrices, which they are not in this case. Begin by expressing A as $URU^\top$ and $B^\top$ as $VSV^\top$ according to the Schur decomposition, where U and V are orthogonal matrices and R and S are quasi-upper triangular matrices. Substituting into the general Sylvester equation, one obtains

$$\begin{aligned} Q &= URU^\top X + X(VSV^\top)^\top \\ &= URU^\top X + XVS^\top V^\top. \end{aligned}$$

Premultiplying by $U^\top$ (and noting that $U^\top U = I$)

$$\begin{aligned} U^\top Q &= U^\top URU^\top X + U^\top XVS^\top V^\top \\ &= RU^\top X + U^\top XVS^\top V^\top \end{aligned},$$

postmultiplying by V (and noting that $V^\top V = I$)

$$\begin{aligned} U^\top QV &= RU^\top XV + U^\top XVS^\top V^\top V \\ &= RU^\top XV + U^\top XVS^\top \end{aligned},$$

and gathering the terms $F = U^\top QV$ and $Y = U^\top XV$, one obtains an equation with the appropriate form to be solved numerically,

$$F = RY = YS^\top \tag{C.22}$$

Having solved for numerically for Y, X may be then be recovered as

$$X = UYV^\top. \tag{C.23}$$

This technique, known as the Bartels-Stewart algorithm [153], can be applied directly to Equation C.21 where $Q = S_{11}\Sigma$, $A = -S_{12}$, $B = \Lambda$, and $X = \Sigma_{11}$.

Having solved for Σ_{11}, the complete right eigenstructure of A is now specified, $AV_A = V_A\Lambda_A$. Two points are worth noting before proceeding further. First, by postmultiplying by V_A^{-1}, one obtains $A = V_A\Lambda_A V_A^{-1}$, which can be trivially extended to show that $A^n = V_A\Lambda_A^n V_A^{-1}$. This equation can be used to efficiently calculate powers of A. Second, by additionally premultiplying by V_A^{-1}, one obtains the left eigenstructure, $V_A^{-1}A = \Lambda_A V_A^{-1}$. Note that the left eigenvectors are given by the *rows* of V_A^{-1}, which is not always intuitive. For this reason, the matrix of columnwise left eigenvectors $\widetilde{V} = (V_A^{-1})^\top$ is defined for convenience, following [104].

C.3.3 Evaluating a Subdivision Patch at the Origin

As $\mathbf{t} \to \mathbf{0}$, the number of required subdivisions $n \to \infty$, and it is therefore not possible to evaluate Equation 4.5 or its derivatives at the origin. However, [104] demonstrates that surface positions and tangents may be evaluated in terms of the left eigenvectors of A. The dominant left eigenvector $\widetilde{v}_1$ and the subdominant eigenvectors $\widetilde{v}_2$ and $\widetilde{v}_3$ are the columns of $\widetilde{V}$ corresponding to the first, second, and third largest eigenvalues, respectively.

Using this notation, evaluation of an extraordinary patch at the origin is given by

$$\chi(\mathbf{0}, X_{f,j}) \approx \widetilde{v}_1^\top X_{f,j}. \tag{C.24}$$

Two vectors specifying the tangent plane at $\mathbf{t} = \mathbf{0}$ are given by $\widetilde{v}_2^\top X_{f,j}$ and $\widetilde{v}_3^\top X_{f,j}$. For detailed proofs of these assertions, the reader is referred to [104].

In addition to $\widetilde{v}_2$ and $\widetilde{v}_3$, [104, 154] define the "tangent masks" $\widetilde{v}_s$ and $\widetilde{v}_t$, which are linear combinations of $\widetilde{v}_2$ and $\widetilde{v}_3$ such that

$$\widetilde{v}_s = \begin{bmatrix} 0 & \cos\left(2\pi\frac{0}{N}\right) & \cos\left(2\pi\frac{1}{N}\right) & \cdots & \cos\left(2\pi\frac{N-1}{N}\right) & 0 & \cdots & 0 \end{bmatrix}^\top \tag{C.25}$$

and

$$\widetilde{v}_t = \begin{bmatrix} 0 & \cos\left(2\pi\frac{1}{N}\right) & \cos\left(2\pi\frac{2}{N}\right) & \cdots & \cos\left(2\pi\frac{N}{N}\right) & 0 & \cdots & 0 \end{bmatrix}^\top. \tag{C.26}$$

Finally, a scale σ is defined as

$$\sigma = \max\left(\left(\widetilde{v}_s^\top v_2\right)^{-1}, \left(\widetilde{v}_s^\top v_3\right)^{-1}\right). \tag{C.27}$$

The maximum term will depend upon whether $\widetilde{v}_s$ is in the direction of v_2 or v_3, which will in turn depend upon the implementation, since the corresponding eigenvalues are equivalent. It is worth noting that the same scale σ is used for both tangent masks.

D

Quartic Triangle Bezier Surfaces

Contents

D.1 Barycentric Bezier Basis Functions 149
D.2 Converting from a B-Spline Surface to a Bezier Surface149

D.1 Barycentric Bezier Basis Functions

D.2 Converting from a B-Spline Surface to a Bezier Surface

The 15 control points $\hat{X} \in \mathbb{R}^{3\times15}$ defining a quartic triangular bezier patch are a function of thirteen components: seven surface positions and six differences of derivatives. These components are summarized in the matrix $D \in \mathbb{R}^{3\times13} =$

$$\begin{bmatrix} \hat{\chi}(0,0)^\top \\ \hat{\chi}(1,0)^\top \\ \hat{\chi}(0,1)^\top \\ \hat{\chi}(\frac{1}{2},0)^\top \\ \hat{\chi}(\frac{1}{2},\frac{1}{2})^\top \\ \hat{\chi}(0,\frac{1}{2})^\top \\ \hat{\chi}(\frac{1}{3},\frac{1}{3})^\top \\ \left(\frac{\partial\hat{\chi}(0,0)}{\partial s} - \frac{\partial\hat{\chi}(0,0)}{\partial r}\right)^\top \\ \left(\frac{\partial\hat{\chi}(0,0)}{\partial t} - \frac{\partial\hat{\chi}(0,0)}{\partial r}\right)^\top \\ \left(\frac{\partial\hat{\chi}(1,0)}{\partial t} - \frac{\partial\hat{\chi}(1,0)}{\partial s}\right)^\top \\ \left(\frac{\partial\hat{\chi}(1,0)}{\partial r} - \frac{\partial\hat{\chi}(1,0)}{\partial s}\right)^\top \\ \left(\frac{\partial\hat{\chi}(0,1)}{\partial r} - \frac{\partial\hat{\chi}(0,1)}{\partial t}\right)^\top \\ \left(\frac{\partial\hat{\chi}(0,1)}{\partial s} - \frac{\partial\hat{\chi}(0,1)}{\partial t}\right)^\top \end{bmatrix}^\top . \tag{D.1}$$

(The dependence of $\hat{\chi}$ on the control points $\hat{X}$ has been omitted for clarity). An additional matrix $W \in \mathbb{R}^{15\times 13}$ is defined, which gives the relative contributions of each column of D to each control point,

$$\frac{1}{12}\begin{bmatrix} 0 & 12 & 0 & 0 & 0 & 0 & 0 & 0 & 0 & 0 & 0 & 0 & 0 \\ 0 & 0 & 12 & 0 & 0 & 0 & 0 & 0 & 0 & 0 & 0 & 0 & 0 \\ 12 & 0 & 0 & 0 & 0 & 0 & 0 & 0 & 0 & 0 & 0 & 0 & 0 \\ 0 & 12 & 0 & 0 & 0 & 0 & 0 & 0 & 0 & 0 & 3 & 0 & 0 \\ 0 & 12 & 0 & 0 & 0 & 0 & 0 & 0 & 0 & 3 & 0 & 0 & 0 \\ 0 & 0 & 12 & 0 & 0 & 0 & 0 & 0 & 0 & 0 & 0 & 0 & 3 \\ 0 & 0 & 12 & 0 & 0 & 0 & 0 & 0 & 0 & 0 & 0 & 3 & 0 \\ 12 & 0 & 0 & 0 & 0 & 0 & 0 & 0 & 3 & 0 & 0 & 0 & 0 \\ 12 & 0 & 0 & 0 & 0 & 0 & 0 & 3 & 0 & 0 & 0 & 0 & 0 \\ 0 & -10 & -10 & 0 & 32 & 0 & 0 & 0 & 0 & -2 & 0 & 0 & -2 \\ -10 & 0 & -10 & 0 & 0 & 32 & 0 & 0 & -2 & 0 & 0 & -2 & 0 \\ -10 & -10 & 0 & 32 & 0 & 0 & 0 & -2 & 0 & 0 & -2 & 0 & 0 \\ -7 & -1 & -7 & 0 & 0 & 0 & 27 & -1 & -1 & 0 & 0 & -1 & -1 \\ -7 & -7 & -1 & 0 & 0 & 0 & 27 & -1 & -1 & -1 & -1 & 0 & 0 \\ -1 & -7 & -7 & 0 & 0 & 0 & 27 & 0 & 0 & -1 & -1 & -1 & -1 \end{bmatrix}, \tag{D.2}$$

such that $\hat{X} = DW^\top$. In its current form, this definition is not useful in discovering the control points defining the Bézier patch, as D is written in terms of $\hat{X}$. However,

the positions and derivatives of the Loop subdivision surface χ and the Bézier surface $\hat{\chi}$ may be set equal to one another at the points of interest (patch corners, patch midpoints, patch centre, and difference of partial derivatives at each patch corner). In this way, a Bézier patch is constructed approximating a Loop subdivision patch. All but the three columns of D involving the origin may be evaluated directly from Equation 4.5 or its partial derivatives. Moreover, the surface position at the origin may be evaluated according to Equation C.24, and the derivative differences along the edges containing the origin may be evaluated using Equations C.25, C.26, and C.27. Therefore, D may be rewritten as $D = X_{f,j}H$, where H is a matrix of well-defined equations describing a (possibly extraordinary) Loop patch,

$$H = \begin{bmatrix} \widetilde{v}_1^\top \\ \left(P_k \bar{A} A^{n-1}\right)^\top \mathbf{b}\left(\hat{\mathbf{t}}_{n,k}(1,0)\right) \\ \left(P_k \bar{A} A^{n-1}\right)^\top \mathbf{b}\left(\hat{\mathbf{t}}_{n,k}(0,1)\right) \\ \left(P_k \bar{A} A^{n-1}\right)^\top \mathbf{b}\left(\hat{\mathbf{t}}_{n,k}(1/2,0)\right) \\ \left(P_k \bar{A} A^{n-1}\right)^\top \mathbf{b}\left(\hat{\mathbf{t}}_{n,k}(1/2,1/2)\right) \\ \left(P_k \bar{A} A^{n-1}\right)^\top \mathbf{b}\left(\hat{\mathbf{t}}_{n,k}(0,1/2)\right) \\ \left(P_k \bar{A} A^{n-1}\right)^\top \mathbf{b}\left(\hat{\mathbf{t}}_{n,k}(1/3,1/3)\right) \\ \widetilde{v}_s^\top/\sigma \\ \widetilde{v}_t^\top/\sigma \\ \left(P_k \bar{A} A^{n-1}\right)^\top \left(\frac{d\mathbf{b}\left(\hat{\mathbf{t}}_{n,k}(1,0)\right)}{dt} - \frac{d\mathbf{b}\left(\hat{\mathbf{t}}_{n,k}(1,0)\right)}{ds}\right) \\ \left(P_k \bar{A} A^{n-1}\right)^\top \left(\frac{d\mathbf{b}\left(\hat{\mathbf{t}}_{n,k}(1,0)\right)}{dr} - \frac{d\mathbf{b}\left(\hat{\mathbf{t}}_{n,k}(1,0)\right)}{ds}\right) \\ \left(P_k \bar{A} A^{n-1}\right)^\top \left(\frac{d\mathbf{b}\left(\hat{\mathbf{t}}_{n,k}(1,0)\right)}{dr} - \frac{d\mathbf{b}\left(\hat{\mathbf{t}}_{n,k}(1,0)\right)}{dt}\right) \\ \left(P_k \bar{A} A^{n-1}\right)^\top \left(\frac{d\mathbf{b}\left(\hat{\mathbf{t}}_{n,k}(1,0)\right)}{ds} - \frac{d\mathbf{b}\left(\hat{\mathbf{t}}_{n,k}(1,0)\right)}{dt}\right) \end{bmatrix}^\top \tag{D.3}$$

It is now possible to convert the control points of an arbitrary Loop subdivision patch those of its Bézier approximation as

$$\begin{aligned} \hat{X}_{f,j} &= X_{f,j} H_N W^\top \\ &= X_{f,j} B_N, \end{aligned} \tag{D.4}$$

where B_N is the Bezier conversion matrix.

References

[1] Nick Townsend, Prachi Bhatnagar, Elizabeth Wilkins, Kremlin Wickramasinghe and Mike Rayner. *Cardiovascular Disease Statistics*. Tech. rep. Oxford, England: British Heart Foundation Centre on Population Approaches for Non-Communicable Disease Prevention. Nuffield Department of Population Health, University of Oxford, 2015 (cit. on p. 2).

[2] *Health, United States, 2015: With Special Feature on Racial and Ethnic Health Disparities*. Tech. rep. Hyattsville, MD: National Center for Health Statistics, 2016 (cit. on p. 2).

[3] *Fact Sheet on Cardiovascular Diseases*. 2016 (cit. on p. 2).

[4] Diane E. Bild, David A. Bluemke, Gregory L. Burke, Robert Detrano, Ana V. Diez Roux, Aaron R. Folsom, Philip Greenland, David R. Jacobs, Richard Kronmal, Kiang Liu, Jennifer C. Nelson, Daniel O'Leary, Mohammed F. Saad, Steven Shea, Moyses Szklo and Russell P. Tracy. 'Multi-Ethnic Study of Atherosclerosis: Objectives and Design'. In: *American Journal of Epidemiology* 156.9 (2002), pp. 871–881 (cit. on p. 2).

[5] Thor Edvardsen, Boaz D. Rosen, Li Pan, Michael Jerosch-Herold, Shenghan Lai, W. Gregory Hundley, Shantanu Sinha, Richard A. Kronmal, David A. Bluemke and João A.C. Lima. 'Regional diastolic dysfunction in individuals with left ventricular hypertrophy measured by tagged magnetic resonance imaging - The Multi-Ethnic Study of Atherosclerosis (MESA)'. In: *American Heart Journal* 151.1 (2005), pp. 109–114 (cit. on p. 2).

[6] Akshay Desai and James C. Fang. 'Heart Failure with Preserved Ejection Fraction: Hypertension, Diabetes, Obesity/Sleep Apnea, and Hypertrophic and Infiltrative Cardiomyopathy'. In: *Heart Failure Clinics* 4.1 (2008), pp. 87–97 (cit. on p. 2).

[7] Michael Tee, J. Alison Noble and David A. Bluemke. 'Imaging techniques for cardiac strain and deformation: comparison of echocardiography, cardiac magnetic resonance and cardiac computed tomography.' In: *Expert Review of Cardiovascular Therapy* 11.2 (Feb. 2013), pp. 221–31 (cit. on pp. 2, 25, 28).

[8] Christopher C. Moore, Carlos H. Lugo-Olivieri, Elliot R. McVeigh and Elias A. Zerhouni. 'Three-dimensional systolic strain patterns in the normal human left ventricle: characterization with tagged MR imaging.' In: *Radiology* 214.2 (Feb. 2000), pp. 453–66 (cit. on pp. 2, 33, 34, 49, 88, 135, 136).

[9] Rainer Hoffmann, Harald Lethen, Thomas Marwick, Mariarosaria Arnese, Paolo Fioretti, Alessandro Pingitore, Eugenio Picano, Thomas Buck, Raimund Erbel, Frank A. Flachskampf and Peter Hanrath. 'Analysis of Interinstitutional Observer Agreement in Interpretation of Dobutamine Stress Echocardiograms'. In: *Journal of the American College of Cardiology* 27.2 (1996), pp. 330–336 (cit. on p. 2).

[10] Hani N. Sabbah, Mario Marzilli and Paul D. Stein. 'The relative role of subendocardium and subepicardium in left ventricular mechanics.' In: *American Journal of Physiology - Heart and Circulatory Physiology* 240.6 (1981), H920–6 (cit. on pp. 3, 12).

[11] Kim P. Gallagher, Genta Osakada, Masunori Matsuzaki, Mark Miller, W. Scott Kemper and John Ross. 'Nonuniformity of inner and outer systolic wall thickening in conscious dogs'. In: *The American Journal of Physiology* 249 (1985), H241–H248 (cit. on pp. 3, 12).

[12] Neil R. Clark, Nathaniel Reichek, Philip Bergey, Eric A. Hoffman, Deanna Brownson, Linda Palmon and Leon Axel. 'Circumferential Myocardial Shortening in the Normal Human Left Ventricle: Assessment by Magnetic Resonance Imaging Using Spatial Modulation of Magnetization'. In: *Circulation* 84.1 (1991), pp. 67–75 (cit. on p. 3).

[13] Mi-Young Jeung, Philippe Germain, Pierre Croisille, Soraya El ghannudi, Catherine Roy and Afshin Gangi. 'Myocardial Tagging with MR Imaging: Overview of Normal and Pathologic Findings'. In: *Radiographics* 32.5 (2012), pp. 1381–98 (cit. on p. 3).

[14] Manuel D. Cerqueira, Neil J. Weissman, Vasken Dilsizian, Alice K. Jacobs, Sanjiv Kaul, Warren K. Laskey, J. Dudley Pennel, John A. Rumberger, Thomas Ryan and Mario S. Verani. 'Standardized Myocardial Segmentation and Nomenclature for Tomographic Imaging of the Heart: A Statement for Healthcare Professionals From the Cardiac Imaging Committee of the Council on Clinical Cardiology of the American Heart Association'. In: *Circulation* 105.4 (Jan. 2002), pp. 539–542 (cit. on pp. 3, 112, 118).

[15] Theodore P. Abraham, Veronica L. Dimaano and Hsin-Yueh Liang. 'Role of Tissue Doppler and Strain Echocardiography in Current Clinical Practice'. In: *Circulation* 116.22 (2007), pp. 2597–2609 (cit. on pp. 10, 24).

[16] Monda L. Shehata, Susan Cheng, Nael F. Osman, David A. Bluemke and João A.C. Lima. 'Myocardial tissue tagging with cardiovascular magnetic resonance.' In: *Journal of Cardiovascular Magnetic Resonance* 11 (Jan. 2009), p. 55 (cit. on p. 10).

[17] Amir Pourmorteza, Karl H. Schuleri, Daniel a. Herzka, Albert C. Lardo and Elliot R. McVeigh. 'A new method for cardiac computed tomography regional function assessment: Stretch quantifier for endocardial engraved zones (SQUEEZ)'. In: *Circulation: Cardiovascular Imaging* 5.2 (2012), pp. 243–250 (cit. on pp. 11, 26, 98, 101, 103, 112, 118, 125).

[18] Amir Pourmorteza, Marcus Y. Chen, Jesper van der Pals, Andrew E. Arai and Elliot R. McVeigh. 'Correlation of CT-based regional cardiac function (SQUEEZ) with myocardial strain calculated from tagged MRI: an experimental study'. In: *International Journal of Cardiovascular Imaging* 32.5 (2015), pp. 1–7 (cit. on pp. 11, 26, 114, 115).

[19] Robert F. Rushmer, Dean L. Franklin and Richard M. Ellis. 'Left Ventricular Dimensions Recorded by Sonocardiometry'. In: *Circulation Research* 4.6 (1956), pp. 684–688 (cit. on p. 12).

[20] Bernell Coleman, Laval N. Cothran, Eleanor L. Ison-Franklin and Edward W. Hawthorne. 'Estimation of Left Ventricular Mass in Conscious Dogs'. In: *American Journal of Physiology* 251 (1986), H1149–H1157 (cit. on p. 12).

[21] Niel B. Ingels, George T. Daughters, Edward B. Stinson and Edwin L. Alderman. 'Measurement of Midwall Myocardial Dynamics in Intact Man by Radiography of Surgically Implanted Markers'. In: *Circulation* 52.5 (1975), pp. 859–867 (cit. on p. 12).

[22] Susan B. Yeon, Nathaniel Reichek, Barbara A. Tallant, João A.C. Lima, Linda P. Calhoun, Neil R. Clark, Eric A. Hoffman, Kalon K.L. Ho and Leon Axel. 'Validation of In Vivo Myocardial Strain Measurement by Magnetic Resonance Tagging with Sonomicrometry'. In: *Journal of the American College of Cardiology* 38.2 (2001), pp. 555–561 (cit. on p. 12).

[23] Stig Urheim, Thor Edvardsen, Hans Torp, Bjørn Angelsen and Otto A. Smiseth. 'Myocardial Strain by Doppler Echocardiography Validation of a New Method to Quantify Regional Myocardial Function'. In: *Circulation* 102.10 (2000), pp. 1158–1164 (cit. on p. 12).

[24] H.Y. Carr. 'Steady-State Free Precession in Nuclear Magnetic Resonance'. In: *Physical Review* 112.5 (1958), pp. 1693–1701 (cit. on p. 12).

[25] Oliver Bieri and Klaus Scheffler. 'Fundamentals of balanced steady state free precession MRI.' In: *Journal of Magnetic Resonance Imaging* 38.1 (July 2013), pp. 2–11 (cit. on p. 12).

[26] Leon Axel and Lawrence Dougherty. 'MR Imaging of Motion with Spatial Modulation of Magnetization'. In: *Radiology* 171 (1989), pp. 841–845 (cit. on p. 12).

[27] Leon Axel and Lawrence Dougherty. 'Heart Wall Motion: Improved Method of Spatial Modulation of Magnetization for MR Imaging'. In: *Radiology* 172.2 (1989), pp. 349–350 (cit. on p. 13).

[28] Darius Dabir, Nicholas Child, Ashwin Kalra, Toby Rogers, Rolf Gebker, Andrew Jabbour, Sven Plein, Chung-Yao Yu, James Otton, Ananth Kidambi, Adam McDiarmid, David Broadbent, David M. Higgins, Bernhard Schnackenburg, Lucy Foote, Ciara Cummins, Eike Nagel and Valentina O. Puntmann. 'Reference values for healthy human myocardium using a T1 mapping methodology: results from the International T1 Multicenter cardiovascular magnetic resonance study.' In: *Journal of Cardiovascular Magnetic Resonance* 16 (2014), p. 69 (cit. on p. 13).

[29] S.E. Fischer, G.C. McKinnon, S.E. Maier and P. Boesiger. 'Improved Myocardial Tagging Contrast'. In: *Magnetic Resonance in Medicine* 30.2 (Aug. 1993), pp. 191–200 (cit. on p. 13).

[30] Moriel NessAiver and Jerry L. Prince. 'Magnitude Image CSPAMM Reconstruction (MICSR)'. In: *Magnetic Resonance in Medicine* 50.2 (2003), pp. 331–342 (cit. on p. 13).

[31] Salome Ryf, Marcus A. Spiegel, Michael Gerber and Peter Boesiger. 'Myocardial Tagging with 3D-CSPAMM'. In: *Journal of Magnetic Resonance Imaging* 16.3 (Sept. 2002), pp. 320–5 (cit. on p. 15).

[32] Nael F. Osman and Jerry L. Prince. 'Direct calculation of 2D components of myocardial strain using sinusoidal MR tagging'. In: *Proc. SPIE Medical Imaging 1998: Physiology and Function from Multidimensional Images*. Vol. 3337. February. 1998, pp. 142–152 (cit. on p. 15).

[33] Nael F. Osman, William S. Kerwin, Elliot R. McVeigh and Jerry L. Prince. 'Cardiac Motion Tracking Using CINE Harmonic Phase (HARP) Magnetic Resonance Imaging.' In: *Magnetic Resonance in Medicine* 42.6 (Dec. 1999), pp. 1048–60 (cit. on pp. 15, 18).

[34] Nael F. Osman, Elliot R. McVeigh and Jerry L. Prince. 'Imaging Heart Motion Using Harmonic Phase MRI'. In: *IEEE Transactions on Medical Imaging* 19.3 (Mar. 2000), pp. 186–202 (cit. on pp. 15, 18).

[35] Smita Sampath, J. Andrew Derbyshire, Ergin Atalar, Nael F. Osman and Jerry L. Prince. 'Real-Time Imaging of Two-Dimensional Cardiac Strain Using a Harmonic Phase Magnetic Resonance Imaging (HARP-MRI) Pulse Sequence'. In: *Magnetic Resonance in Medicine* 50.1 (2003), pp. 154–163 (cit. on p. 18).

[36] Nael F. Osman, Smita Sampath, Ergin Atalar and Jerry L. Prince. 'Imaging Longitudinal Cardiac Strain on Short-Axis Images Using Strain-Encoded MRI'. In: *Magnetic Resonance in Medicine* 46.2 (Aug. 2001), pp. 324–34 (cit. on pp. 18, 19).

[37] Li Pan, Matthias Stuber, Dara L. Kraitchman, Danielle L. Fritzges, Wesley D. Gilson and Nael F. Osman. 'Real-Time Imaging of Regional Myocardial Function Using Fast-SENC'. In: *Magnetic Resonance in Medicine* 55.2 (Feb. 2006), pp. 386–95 (cit. on pp. 20, 28).

[38] Van J. Wedeen. 'Magnetic Resonance Imaging of Myocardial Kinematics - Technique to Detect, Localize, and Quantify the Strain Rates of the Active Human Myocardium'. In: *Magnetic Resonance in Medicine* 27.1 (1992), pp. 52–67 (cit. on p. 20).

[39] Pernilla Selskog, Einar Heiberg, Tino Ebbers, Lars Wigström and Matts Karlsson. 'Kinematics of the Heart: Strain-Rate Imaging From Time-Resolved Three-Dimensional Phase Contrast MRI'. In: *IEEE Transactions on Medical Imaging* 21.9 (2002), pp. 1105–1109 (cit. on p. 20).

[40] Anthony H. Aletras, Shujun Ding, Robert S. Balaban and Han Wen. 'DENSE: displacement encoding with stimulated echoes in cardiac functional MRI.' In: *Journal of Magnetic Resonance* 137.1 (Mar. 1999), pp. 247–52 (cit. on p. 21).

[41] B. S. Spottiswoode, X. Zhong, A. T. Hess, C. M. Kramer, E. M. Meintjes, B. M. Mayosi and Frederick H. Epstein. 'Tracking Myocardial Motion from Cine DENSE Images Using Spatiotemporal Phase Unwrapping and Temporal Fitting'. In: *IEEE Transactions on Medical Imaging* 26.1 (Jan. 2007), pp. 15–30 (cit. on p. 21).

[42] Keitaro Ogawa, Takeshi Hozumi, Kenichi Sugioka, Yoshiki Matsumura, Masahide Nishiura, Ryoichi Kanda, Yasuhiko Abe, Yasuhiko Takemoto, Minoru Yoshiyama and Junichi Yoshikawa. 'Usefulness of automated quantitation of regional left ventricular wall motion by a novel method of two-dimensional echocardiographic tracking.' In: *The American Journal of Cardiology* 98.11 (Dec. 2006), pp. 1531–7 (cit. on pp. 22, 25, 36, 53, 123).

[43] Kan N. Hor, Rolf Baumann, Gianni Pedrizzetti, Gianni Tonti, William M. Gottliebson, Michael Taylor, Woodrow Benson and Wojciech Mazur. 'Magnetic resonance derived myocardial strain assessment using feature tracking.' In: *Journal of Visualized Experiments* 48 (Jan. 2011), pp. 1–6 (cit. on p. 22).

[44] Mimount Bourfiss, Davis M Vigneault, Mounes Aliyari Ghasebeh, Brittney Murray, Cynthia A James, Crystal Tichnell, Firdaus A. Mohamed Hoesein, Stefan L Zimmerman, Ihab R Kamel, Hugh Calkins, Harikrishna Tandri, Birgitta K Velthuis, David A Bluemke and Anneline S J M te Riele. 'Feature tracking CMR reveals abnormal strain in preclinical arrhythmogenic right ventricular dysplasia/ cardiomyopathy: a multisoftware feasibility and clinical implementation study'. In: *Journal of Cardiovascular Magnetic Resonance* 19.1 (Dec. 2017), p. 66 (cit. on p. 22).

[45] Christoph B. Burckhardt. 'Speckle in Ultrasound B -Mode Scans'. In: *IEEE Transactions on Sonics and Ultrasonics* SU-25.1 (1978), pp. 1–6 (cit. on p. 23).

[46] Martino Alessandrini, Brecht Heyde, Sandro Queiros, Szymon Cygan, Maria Zontak, Oudom Somphone, Olivier Bernard, Maxime Sermesant, Herve Delingette, Daniel Barbosa, Mathieu De Craene, Matthew ODonnell and Jan D'hooge. 'Detailed Evaluation of Five 3D Speckle Tracking Algorithms Using Synthetic Echocardiographic Recordings'. In: *IEEE Transactions on Medical Imaging* 35.8 (Aug. 2016), pp. 1915–1926 (cit. on pp. 23, 24).

[47] Paul Viola and Michael J. Jones. 'Robust Real-Time Face Detection'. In: *International Journal of Computer Vision* 57.2 (2004), pp. 137–154. arXiv: `arXiv:1011.1669v3` (cit. on p. 23).

[48] Andrew DiBattista and J. Alison Noble. 'An efficient block matching and spectral shift estimation algorithm with applications to ultrasound elastography.' In: *IEEE Transactions on Ultrasonics, Ferroelectronics, and Frequency Control* 61.3 (Mar. 2014), pp. 407–19 (cit. on p. 24).

[49] Martino Alessandrini, Adrian Basarab, Hervé Liebgott and Olivier Bernard. 'Myocardial motion estimation from medical images using the monogenic signal'. In: *IEEE Transactions on Image Processing* 22.3 (2013), pp. 1084–1095 (cit. on p. 24).

[50] Karl Isaaz, Aubrey Thompson, Gerard Ethevenot, Jean L. Cloez, Beatrice Brembilla and Claude Pernot. 'Doppler Echocardiographic Measurement of Low Velocity Motion of the Left Ventricular Posterior Wall'. In: *The American Journal of Cardiology* 64.1 (1989), pp. 66–75 (cit. on p. 24).

[51] Michael W. Tee, Samuel Won, Fabio S. Raman, Colin Yi, Davis M. Vigneault, Cynthia Davies-Venn, Songtao Liu, Albert C. Lardo, João A. C. Lima, J. Alison Noble, Craig A. Emter and David A. Bluemke. 'Regional Strain Analysis with Multidetector CT in a Swine Cardiomyopathy Model: Relationship to Cardiac MR Tagging and Myocardial Fibrosis'. In: *Radiology* 277.1 (Oct. 2015), pp. 88–94 (cit. on p. 25).

[52] Thomas M. Helle-Valle, Wen-Chung Yu, Verônica R.S. Fernandes, Boaz D. Rosen and João A.C. Lima. 'Usefulness of radial strain mapping by multidetector computer tomography to quantify regional myocardial function in patients with healed myocardial infarction.' In: *The American Journal of Cardiology* 106.4 (Aug. 2010), pp. 483–91 (cit. on p. 25).

[53] Ken C. L. Wong, Michael Tee, Marcus Chen, David A. Bluemke, Ronald M. Summers and Jianhua Yao. 'Regional infarction identification from cardiac CT images: a computer-aided biomechanical approach'. In: *International Journal of Computer Assisted Radiology and Surgery* 11.9 (2016), pp. 1573–1583 (cit. on pp. 25, 69).

[54] H. P. Heinrich, Mark Jenkinson, Michael Brady and Julia A. Schnabel. 'MRF-Based Deformable Registration and Ventilation Estimation of Lung CT'. In: *IEEE Transactions on Medical Imaging* 32.7 (July 2013), pp. 1239–1248 (cit. on p. 25).

[55] Andriy Myronenko and Xubo Song. 'Point Set Registration: Coherent Point Drift'. In: *IEEE Trans Pattern on Pattern Analysis and Machine Intelligence* 32.12 (2010), pp. 2262–2275 (cit. on p. 26).

[56] Jan J. Koenderink and Andrea J. van Doorn. 'Surface shape and curvature scales'. In: *Image and Vision Computing* 10.8 (1992), pp. 557–564 (cit. on p. 26).

[57] Saman Nazarian, Roy Beinart and Henry R. Halperin. 'Magnetic Resonance Imaging and Implantable Devices'. In: *Advances in Arrhythmia and Electrophysiology* 6 (2013), pp. 419–428 (cit. on p. 27).

[58] Bharath Ambale Venkatesh, Chun G. Schiros, Himanshu Gupta, Steven G. Lloyd, Louis Dell'Italia and Thomas S. Denney. 'Three-dimensional plus time biventricular strain from tagged MR images by phase-unwrapped harmonic phase.' In: *Journal of Magnetic Resonance Imaging* 34.4 (Oct. 2011), pp. 799–810 (cit. on pp. 28, 51, 98).

[59] Daniel A. Auger, Xiaodong Zhong, Frederick H. Epstein and Bruce S. Spottiswoode. 'Mapping right ventricular myocardial mechanics using 3D cine DENSE cardiovascular magnetic resonance'. In: *Journal of Cardiovascular Magnetic Resonance* 14.1 (2012), p. 4 (cit. on p. 28).

[60] Geraint Morton, Andreas Schuster, Roy Jogiya, Shelby Kutty, Philipp Beerbaum and Eike Nagel. 'Inter-study reproducibility of cardiovascular magnetic resonance myocardial feature tracking.' In: *Journal of Cardiovascular Magnetic Resonance* 14.1 (Jan. 2012), p. 43 (cit. on p. 28).

[61] Philipp Heermann, Dennis M. Hedderich, Matthias Paul, Christoph Schülke, Jan Robert Kroeger, Bettina Baeßler, Thomas Wichter, David Maintz, Johannes Waltenberger, Walter Heindel and Alexander C. Bunck. 'Biventricular myocardial strain analysis in patients with arrhythmogenic right ventricular cardiomyopathy (ARVC) using cardiovascular magnetic resonance feature tracking'. In: *Journal of Cardiovascular Magnetic Resonance* 16.1 (Oct. 2014), p. 75 (cit. on pp. 28, 49, 64).

[62] Davis M. Vigneault, Anneline S.J.M. te Riele, Cynthia A. James, Stefan L. Zimmerman, Mariana Selwaness, Brittney Murray, Crystal Tichnell, Michael Tee, J. Alison Noble, Hugh Calkins, Harikrishna Tandri and David A. Bluemke. 'Right ventricular strain by MR quantitatively identifies regional dysfunction in patients with arrhythmogenic right ventricular cardiomyopathy'. In: *Journal of Magnetic Resonance Imaging* 43 (2016), pp. 1132–1139 (cit. on pp. 28, 49).

[63] Morgane Evin, Philippe Cluzel, Jerome Lamy, David Rosenbaum, Slawek Kusmia, Carine Defrance, Gilles Soulat, Elie Mousseaux, Charles Roux, Karine Clement, Stephane N. Hatem, Alban Redheuil and Nadjia Kachenoura. 'Assessment of Left Atrial Function by MRI Myocardial Feature Tracking'. In: *Journal of Magnetic Resonance Imaging* 42 (2015), pp. 379–389 (cit. on p. 28).

[64] Anastasia Dick, Björn Schmidt, Guido Michels, Alexander C. Bunck, David Maintz and Bettina Baeßler. 'Left and right atrial feature tracking in acute myocarditis : A feasibility study'. In: *European Journal of Radiology* 89 (2017), pp. 72–80 (cit. on p. 28).

[65] Nasser Moiduddin, Kentaro Asoh, Cameron Slorach, Leland N. Benson and Mark K. Friedberg. 'Effect of Transcatheter Pulmonary Valve Implantation on Short-Term Right Ventricular Function as Determined by Two-Dimensional Speckle Tracking Strain and Strain Rate Imaging'. In: *American Journal of Cardiology* 104.6 (2009), pp. 862–867 (cit. on p. 28).

[66] Ziya Simsek, M. Hakan Tas, Ersin Gunay and Husnu Degirmenci. 'Speckle-tracking echocardiographic imaging of the right ventricular systolic and diastolic parameters in chronic exercise'. In: *International Journal of Cardiovascular Imaging* 29 (2013), pp. 1265–1271 (cit. on p. 28).

[67] Avin Calcutteea, Per Lindqvist, Stefan Soderberg and Michael Y. Henein. 'Global and Regional Right Ventricular Dysfunction in Pulmonary Hypertension'. In: *Echocardiography* 31 (2014), pp. 164–171 (cit. on p. 28).

[68] Rita Vianna-pinton, Carlos A. Moreno, Christy M. Baxter, Kwan S. Lee, Teresa S.M. Tsang and Christopher P. Appleton. 'Two-Dimensional Speckle-Tracking Echocardiography of the Left Atrium: Feasibility and Regional Contraction and Relaxation Differences in Normal Subjects'. In: *Journal of the American Society of Echocardiography* 22.3 (2008), pp. 299–305 (cit. on p. 28).

[69] Matteo Cameli, Matteo Lisi, Marta Focardi, Rosanna Reccia, Benedetta Maria Natali, Stefania Sparla and Sergio Mondillo. 'Left Atrial Deformation Analysis by Speckle Tracking Echocardiography for Prediction of Cardiovascular Outcomes'. In: *American Journal of Cardiology* 110.2 (2012), pp. 264–269 (cit. on p. 28).

[70] Darryl P. Leong, Amy Penhall, Rebecca Perry, Mitra Shirazi, Mikhail Altman, David Chong, Julie Bradley, Majo X. Joseph and Joseph B. Selvanayagam. 'Speckle-tracking strain of the left atrium: a transoesophageal echocardiographic validation study'. In: *European Heart Journal - Cardiovascular Imaging* 14 (2013), pp. 898–905 (cit. on p. 28).

[71] Margherita Padeletti, Matteo Cameli, Matteo Lisi, Valerio Zaca, Charilos Tsioulpas, Sonia Bernazzali, Massimo Maccherini and Sergio Mondillo. 'Right Atrial Speckle Tracking Analysis as a Novel Noninvasive Method for Pulmonary Hemodynamics Assessment in Patients with Chronic Systolic Heart Failure'. In: *Echocardiography* 28 (2011), pp. 658–664 (cit. on p. 28).

[72] Diletta Peluso, Luigi P. Badano, Denisa Muraru, Lucia Dal Bianco, Umberto Cucchini, Gonenc Kocabay, Attila Kovacs, Simona Casablanca and Sabino Iliceto. 'Right atrial size and function assessed with echocardiography in 200 healthy volunteers'. In: *European Heart Journal - Cardiovascular Imaging* 14 (2013), pp. 1106–1114 (cit. on p. 28).

[73] Sherif Moustafa, Hamed Zuhairy, Mostafa A. Youssef, Nanette Alvarez, Michael S. Connelly, Timothy Prieru and Farouk Mookadam. 'Right and Left Atrial Dissimilarities in Normal Subjects Explored by Speckle Tracking Echocardiography'. In: *Echocardiography* 32 (2015), pp. 1392–1399 (cit. on p. 28).

[74] Radwa A. Noureldin, Songtao Liu, Marcelo S. Nacif, Daniel P. Judge, Marc K. Halushka, Theodore P. Abraham, Carolyn Ho and David A. Bluemke. 'The diagnosis of hypertrophic cardiomyopathy by cardiovascular magnetic resonance.' In: *Journal of Cardiovascular Magnetic Resonance* 14.1 (Jan. 2012), p. 17 (cit. on p. 33).

[75] W. J. McKenna, P. Spirito, M. Desnos, O. Dubourg and M. Komadja. 'Experience of clinical genetics in hypertrophic cardiomyopathy: proposal for new diagnostic criteria in adults members of affected families.' In: *Heart* 77 (1997), pp. 130–132 (cit. on p. 33).

[76] C. Y. Ho. 'Assessment of Diastolic Function With Doppler Tissue Imaging to Predict Genotype in Preclinical Hypertrophic Cardiomyopathy'. In: *Circulation* 105.25 (June 2002), pp. 2992–2997 (cit. on pp. 33, 48).

[77] Carolyn Y Ho, Christian Carlsen, Jens Jakob Thune, Ole Havndrup, Henning Bundgaard, Faranak Farrohi, Jose Rivero, Allison L Cirino, Paal Skytt Andersen, Michael Christiansen, Barry J Maron, E John Orav and Lars Køber. 'Echocardiographic strain imaging to assess early and late consequences of sarcomere mutations in hypertrophic cardiomyopathy.' In: *Circulation - Cardiovascular Genetics* 2.4 (Aug. 2009), pp. 314–21 (cit. on pp. 33, 36, 48, 96).

[78] Ertunc Altiok, Mirja Neizel, Sonja Tiemann, Vitali Krass, Kathrin Kuhr, Michael Becker, Christian Zwicker, Ralf Koos, Walter Lehmacher, Malte Kelm, Nikolaus Marx and Rainer Hoffmann. 'Quantitative analysis of endocardial and epicardial left ventricular myocardial deformation-comparison of strain-encoded cardiac magnetic resonance imaging with two-dimensional speckle-tracking echocardiography.' In: *Journal of the American Society of Echocardiography* 25.11 (Nov. 2012), pp. 1179–88 (cit. on pp. 33, 88).

[79] S.A. Chang, H.K. Kim, D.H. Kim, J.C. Kim, Y.J. Kim, H.C. Kim, D.W. Sohn, B.H. Oh and Y.B. Park. 'Left ventricular twist mechanics in patients with apical hypertrophic cardiomyopathy: assessment with 2D speckle tracking echocardiography.' In: *Heart* 96.1 (2010), pp. 49–55 (cit. on p. 34).

[80] Makoto Saito, Hideki Okayama, Toyofumi Yoshii, Go Hiasa, Takumi Sumimoto, Shinji Inaba, Kazuhisa Nishimura, Katsuji Inoue, Akiyoshi Ogimoto, Tomoaki Ohtsuka, Jun-ichi Funada, Yuji Shigematsu and Jitsuo Higaki. 'The differences in left ventricular torsional behavior between patients with hypertrophic cardiomyopathy and hypertensive heart disease'. In: *International Journal of Cardiology* 150.3 (2011), pp. 301–306 (cit. on p. 34).

[81] Alistair A. Young, Christopher M. Kramer, Victor A. Ferrari, Leon Axel and Nathaniel Reichek. 'Three-Dimensional Left Ventricular Deformation in Hypertrophic Cardiomyopathy.' In: *Circulation* 90.2 (1994), pp. 854–867 (cit. on p. 34).

[82] Iris K. Rüssel, Wessel P. Brouwer, Tjeerd Germans, Paul Knaapen, Tim J. Marcus, Jolanda Van Der Velden, Marco J.W. Götte and Albert C. van Rossum. 'Increased left ventricular torsion in hypertrophic cardiomyopathy mutation carriers with normal wall thickness'. In: *Journal of Cardiovascular Magnetic Resonance* 13.1 (2011), p. 3 (cit. on p. 34).

[83] Carolyn Y. Ho, Sharlene M. Day, Steven D. Colan, Mark W. Russell, Jeffrey A. Towbin, Mark V. Sherrid, Charles E. Canter, John L. Jefferies, Anne M. Murphy, Allison L. Cirino, Theodore P. Abraham, Matthew Taylor, Luisa Mestroni, David A. Bluemke, Petr Jarolim, Ling Shi, Lynn A. Sleeper, Christine E. Seidman and E. John Orav. 'The Burden of Early Phenotypes and the Influence of Wall Thickness in Hypertrophic Cardiomyopathy Mutation Carriers'. In: *JAMA Cardiology* 2.4 (Apr. 2017), pp. 419–428 (cit. on pp. 35, 48).

[84] Gabriella Captur, Luis R Lopes, Vimal Patel, Chunming Li, Paul Bassett, Petros Syrris, Daniel M Sado, Viviana Maestrini, Timothy J Mohun, William J McKenna, Vivek Muthurangu, Perry M Elliott and James C Moon. 'Abnormal cardiac formation in hypertrophic cardiomyopathy: fractal analysis of trabeculae and preclinical gene expression.' In: *Circulation - Cardiovascular Genetics* 7.3 (June 2014), pp. 241–8 (cit. on p. 48).

[85] Gaby Captur, Timothy J. Mohun, Gherardo Finocchiaro, Robert Wilson, Jonathan Levine, Lauren Conner, Luis Lopes, Vimal Patel, Daniel Sado, Chunming Li, Paul Bassett, Anna S. Herrey, Maite T. Tome Esteban, William J. McKenna, Christine E. Seidman, Vivek Muthurangu, David A. Bluemke, Carolyn Y. Ho, Perry M. Elliott and James Moon. 'Advanced assessment of cardiac morphology and prediction of gene carriage by CMR in hypertrophic cardiomyopathy - the HCMNet/UCL collaboration'. In: *Journal of Cardiovascular Magnetic Resonance* 16.Suppl 1 (2014), O30 (cit. on p. 48).

[86] Carolyn Y. Ho. 'Hypertrophic cardiomyopathy: preclinical and early phenotype.' In: *Journal of Cardiovascular Translational Research* 2.4 (Dec. 2009), pp. 462–70 (cit. on p. 48).

[87] Doroteia Silva, Hugo Madeira, Augusto Almeida and Dulce Brito. 'Tissue Doppler imaging and plasma N-terminal probrain natriuretic peptide for the identification of hypertrophic cardiomyopathy mutation carriers.' In: *The American journal of cardiology* 112.7 (Oct. 2013), pp. 996–1004 (cit. on p. 48).

[88] Mohamed F A Aly, Wessel P Brouwer, Sebastiaan A Kleijn, Albert C van Rossum and Otto Kamp. 'Three-dimensional speckle tracking echocardiography for the preclinical diagnosis of hypertrophic cardiomyopathy.' In: *The International Journal of Cardiovascular Imaging* 30.3 (Mar. 2014), pp. 523–33 (cit. on p. 48).

[89] Kai Hang Yiu, Douwe E. Atsma, Victoria Delgado, Arnold C.T. Ng, Tomasz G. Witkowski, See Hooi Ewe, Dominique Auger, Eduard R. Holman, Anneke M. van Mil, Martijn H. Breuning, Hung Fat Tse, Jeroen J. Bax, Martin J. Schalij and Nina Ajmone Marsan. 'Myocardial Structural Alteration and Systolic Dysfunction in Preclinical Hypertrophic Cardiomyopathy Mutation Carriers'. In: *PLOS ONE* 7.5 (Jan. 2012) (cit. on p. 48).

[90] Harikrishna Tandri, Hugh Calkins, Khurram Nasir, Chandra Bomma, Ernesto Castillo, Julie Rutberg, Crystal Tichnell, João A.C. Lima and David A. Bluemke. 'Magnetic resonance imaging findings in patients meeting task force criteria for arrhythmogenic right ventricular dysplasia.' In: *Journal of Cardiovascular Electrophysiology* 14.5 (May 2003), pp. 476–82 (cit. on p. 51).

[91] Darshan Dalal, Khurram Nasir, Chandra Bomma, Kalpana Prakasa, Harikrishna Tandri, Jonathan Piccini, Ariel Roguin, Crystal Tichnell, Cynthia James, Stuart D. Russell, Daniel P. Judge, Theodore Abraham, Philip J. Spevak, David A. Bluemke and Hugh Calkins. 'Arrhythmogenic Right Ventricular Dysplasia: A United States Experience'. In: *Circulation* 112.25 (Dec. 2005), pp. 3823–32 (cit. on p. 51).

[92] Judith A. Groeneweg, Aditya Bhonsale, Cynthia A. James, Anneline S.J.M. te Riele, Dennis Dooijes, Crystal Tichnell, Brittney Murray, Ans C.P. Wiesfeld, Abhishek C. Sawant, Bina Kassamali, Douwe E. Atsma, Paul G. Volders, Natasja M. de Groot, Karin de Boer, Stefan L. Zimmerman, Ihab R. Kamel, Jeroen F. van der Heijden, Stuart D. Russell, Maarten Jan Cramer, Ryan J. Tedford, Pieter A. Doevendans, Toon A. van Veen, Harikrishna Tandri, Arthur A. Wilde, Daniel P. Judge, J. Peter van Tintelen, Richard N. Hauer and Hugh Calkins. 'Clinical Presentation, Long-Term Follow-Up, and Outcomes of 1001 Arrhythmogenic Right Ventricular Dysplasia/Cardiomyopathy Patients and Family Members.' In: *Circulation - Cardiovascular Genetics* 8.3 (2015), pp. 437–46 (cit. on p. 51).

[93] Frank I. Marcus, Guy H. Fontaine, Gerard Guiraudon, Robert Frank, Jean L. Laurenceau, Christine Malergue and Yves Grosgogeat. 'Right Ventricular Dysplasia: A Report of 24 Adult Cases'. In: *Circulation* 65.4 (1982), pp. 384–98 (cit. on p. 51).

[94] Frank I. Marcus, William J. McKenna, Duane Sherrill, Cristina Basso, Barbara Bauce, David A. Bluemke, Hugh Calkins, Domenico Corrado, Moniek G.P.J. Cox, James P. Daubert, Guy Fontaine, Kathleen Gear, Richard Hauer, Andrea Nava, Michael H. Picard, Nikos Protonotarios, Jeffrey E. Saffitz, Danita M. Yoerger Sanborn, Jonathan S. Steinberg, Harikrishna Tandri, Gaetano Thiene, Jeffrey A. Towbin, Adalena Tsatsopoulou, Thomas Wichter and Wojciech Zareba. 'Diagnosis of Arrhythmogenic Right Ventricular Cardiomyopathy/Dysplasia: Proposed Modification of the Task Force Criteria'. In: *Circulation* 121.13 (Apr. 2010), pp. 1533–41 (cit. on pp. 51, 52).

[95] Chandra Bomma, Julie Rutberg, Harikrishna Tandri, Khurram Nasir, Ariel Roguin, Crystal Tichnell, Rene Rodriguez, Cynthia James, Edward Kasper, Philip Spevak, David A. Bluemke and Hugh Calkins. 'Misdiagnosis of arrhythmogenic right ventricular dysplasia/cardiomyopathy.' In: *Journal of Cardiovascular Electrophysiology* 15.3 (Mar. 2004), pp. 300–6 (cit. on pp. 51, 64).

[96] Frank I. Marcus, Wojciech Zareba, Hugh Calkins, Jeffrey A. Towbin, Cristina Basso, David A. Bluemke, N.A. Mark Estes, Michael H. Picard, Danita Sanborn, Gaetano Thiene, Thomas Wichter, David Cannom, David J. Wilber, Melvin Scheinman, Henry Duff, James Daubert, Mario Talajic, Andrew Krahn, Michael Sweeney, Hasan Garan, Scott Sakaguchi, Bruce B. Lerman, Charles Kerr, Jack Kron, Jonathan S. Steinberg, Duane Sherrill,

Kathleen Gear, Mary Brown, Patricia Severski, Slava Polonsky and Scott McNitt. 'Arrhythmogenic right ventricular cardiomyopathy/dysplasia clinical presentation and diagnostic evaluation: results from the North American Multidisciplinary Study.' In: *Heart Rhythm* 6.7 (July 2009), pp. 984–992 (cit. on p. 51).

[97] Meriam Astrom Aneq, Jan Engvall, Lars Brudin and Eva Nylander. 'Evaluation of right and left ventricular function using speckle tracking echocardiography in patients with arrhythmogenic right ventricular cardiomyopathy and their first degree relatives'. In: *Cardiovascular Ultrasound* 10.1 (Jan. 2012), p. 37 (cit. on p. 63).

[98] Massimo Iacoviello, Cinzia Forleo, Agata Puzzovivo, Ilaria Nalin, Pietro Guida, Matteo Anaclerio, Vito Marangelli, Sandro Sorrentino, Francesco Monitillo, Marco Matteo Ciccone and Stefano Favale. 'Altered two-dimensional strain measures of the right ventricle in patients with Brugada syndrome and arrhythmogenic right ventricular dysplasia/cardiomyopathy.' In: *European Journal of Echocardiography* 12.10 (Oct. 2011), pp. 773–81 (cit. on p. 63).

[99] Kalpana R. Prakasa, Jianwen Wang, Harikrishna Tandri, Darshan Dalal, Chandra Bomma, Roman Chojnowski, Cynthia James, Crystal Tichnell, Stuart Russell, Daniel Judge, Mary Corretti, David A. Bluemke, Hugh Calkins and Theodore P. Abraham. 'Utility of Tissue Doppler and Strain Echocardiography in Arrhythmogenic Right Ventricular Dysplasia/Cardiomyopathy'. In: *The American Journal of Cardiology* 100.3 (Aug. 2007), pp. 507–12 (cit. on p. 63).

[100] Arco J. Teske, Moniek G. Cox, Bart W. De Boeck, Pieter A. Doevendans, Richard N. Hauer and Maarten J. Cramer. 'Echocardiographic Tissue Deformation Imaging Quantifies Abnormal Regional Right Ventricular Function in Arrhythmogenic Right Ventricular Dysplasia/Cardiomyopathy'. In: *Journal of the American Society of Echocardiography* 22.8 (Aug. 2009), pp. 920–7 (cit. on p. 63).

[101] Anneline S.J.M. te Riele, Cynthia A. James, Binu Philips, Neda Rastegar, Aditya Bhonsale, Judith A. Groeneweg, Brittney Murray, Crystal Tichnell, Daniel P. Judge, Jeroen F. Van Der Heijden, Maarten J.M. Cramer, Birgitta K. Velthuis, David A. Bluemke, Stefan L. Zimmerman, Ihab R. Kamel, Richard N.W. Hauer, Hugh Calkins and Harikrishna Tandri. 'Mutation-positive arrhythmogenic right ventricular dysplasia/cardiomyopathy: the triangle of dysplasia displaced.' In: *Journal of Cardiovascular Electrophysiology* 24.12 (Dec. 2013), pp. 1311–20 (cit. on p. 64).

[102] Jan Fritz, Meiyappan Solaiyappan, Harikrishna Tandri, Chandra Bomma, Ahmet Genc, Claus D Claussen, João A C Lima and David A Bluemke. 'Right ventricle shape and contraction patterns and relation to magnetic resonance imaging findings.' In: *Journal of computer assisted tomography* 29.6 (2005), pp. 725–733 (cit. on p. 64).

[103] Harikrishna Tandri, Ernesto Castillo, Victor A Ferrari, Khurram Nasir, Darshan Dalal, Chandra Bomma, Hugh Calkins and David A Bluemke. 'Magnetic Resonance Imaging of Arrhythmogenic Right Ventricular Dysplasia. Sensitivity, Specificity, and Observer Variability of Fat Detection Versus Functional Analysis of the Right Ventricle'. In: *Journal of the American College of Cardiology* 48.11 (Dec. 2006), pp. 2277–2284 (cit. on p. 64).

[104] Richard Stebbing. 'Model-Based Segmentation Methods for Analysis of 2D and 3D Ultrasound Images and Sequences'. DPhil. University of Oxford, 2014 (cit. on pp. 69, 74, 98, 100, 102, 103, 105, 109, 110, 116–118, 124, 125, 140, 147, 148).

[105] Alex Krizhevsky, Ilya Sutskever and Geoffrey E. Hinton. 'ImageNet Classification with Deep Convolutional Neural Networks'. In: *NIPS*. 2012 (cit. on pp. 69, 71).

[106] Karen Simonyan and Andrew Zisserman. 'Very Deep Convolutional Networks for Large-Scale Image Recognition'. In: *ICLR*. 2014, pp. 1–14. arXiv: `arXiv:1409.1556v6` (cit. on pp. 69, 71).

[107] Jonathan Long, Evan Shelhamer and Trevor Darrell. 'Fully convolutional networks for semantic segmentation'. In: *CVPR*. Vol. 07-12-June. 2015, pp. 3431–3440. arXiv: `1411.4038` (cit. on pp. 69, 70).

[108] Hyeonwoo Noh, Seunghoon Hong and Bohyung Han. 'Learning Deconvolution Network for Semantic Segmentation'. In: *ICCV*. Vol. 1. 2015. arXiv: `1505.04366` (cit. on p. 69).

[109] Fisher Yu and Vladlen Koltun. 'Multi-Scale Context Aggregation by Dilated Convolutions'. In: *ICLR*. 2016, pp. 1–9. arXiv: `1511.07122` (cit. on pp. 69, 72).

[110] Olaf Ronneberger, Philipp Fischer and Thomas Brox. 'U-Net: Convolutional Networks for Biomedical Image Segmentation'. In: *MICCAI*. 2015, pp. 234–241. arXiv: `1505.04597` (cit. on pp. 69, 70).

[111] Weidi Xie, J. Alison Noble and Andrew Zisserman. 'Microscopy Cell Counting with Fully Convolutional Regression Networks'. In: *MICCAI Workshop*. 2015, pp. 1–10 (cit. on pp. 69, 70).

[112] Li Kuo Tan, Yih Miin Liew, Einly Lim and Robert A Mclaughlin. 'Cardiac Left Ventricle Segmentation using Convolutional Neural Network Regression'. In: *IECBES*. 2016, pp. 490–493 (cit. on pp. 69, 124).

[113] Rudra P.K. Poudel, Pablo Lamata and Giovanni Montana. 'Recurrent Fully Convolutional Neural Networks for Multi-slice MRI Cardiac Segmentation'. In: *HVSMR*. 2016. arXiv: `1608.03974` (cit. on p. 69).

[114] Li Kuo Tan, Yih Miin Liew, Einly Lim and Robert A. McLaughlin. 'Convolutional neural network regression for short-axis left ventricle segmentation in cardiac cine MR sequences'. In: *Medical Image Analysis* 39 (2017), pp. 78–86 (cit. on p. 69).

[115] Gongning Luo, Ran An, Kuanquan Wang, Suyu Dong and Henggui Zhang. 'A Deep Learning Network for Right Ventricle Segmentation in Short-Axis MRI'. In: *Computing in Cardiology* 43 (2016), pp. 485–488 (cit. on pp. 69, 124).

[116] Phi Vu Tran. 'A Fully Convolutional Neural Network for Cardiac Segmentation in Short-Axis MRI'. 2016 (cit. on pp. 69, 124).

[117] Jesse Lieman-Sifry, Matthieu Le, Felix Lau, Sean Sall and Daniel Golden. 'FastVentricle: Cardiac Segmentation with ENet'. In: *FIMH*. 2017. arXiv: `1704.04296` (cit. on pp. 69, 124).

[118] Richard V. Stebbing, Ana I.L. Namburete, Ross Upton, Paul Leeson and J. Alison Noble. 'Data-driven shape parameterization for segmentation of the right ventricle from 3D+t echocardiography'. In: *Medical Image Analysis* 21 (2015), pp. 29–39 (cit. on pp. 69, 98).

[119] Sergey Ioffe and Christian Szegedy. 'Batch Normalization: Accelerating Deep Network Training by Reducing Internal Covariate Shift'. In: *ICML*. Vol. 37. 2015, pp. 81–87. arXiv: `arXiv:1011.1669v3` (cit. on p. 71).

[120] Donald W. Marquardt. 'An Algorithm for Least-Squares Estimation of Nonlinear Parameters'. In: *Journal of the Society of Industrial and Applied Mathematics* 11.2 (1963), pp. 431–441. arXiv: `arXiv:1011.1669v3` (cit. on pp. 73, 109).

[121] Paul A. Yushkevich, Joseph Piven, Heather Cody Hazlett, Rachel Gimpel Smith, Sean Ho, James C. Gee and Guido Gerig. 'User-guided 3D active contour segmentation of anatomical structures : Significantly improved efficiency and reliability'. In: *NeuroImage* 31 (2006), pp. 1116–1128 (cit. on p. 76).

[122] Andrew M. Saxe, James L. McClelland and Surya Ganguli. 'Exact solutions to the nonlinear dynamics of learning in deep linear neural networks'. In: *ICLR*. 2014, pp. 1–22. arXiv: `1312.6120` (cit. on p. 76).

[123] Martin Abadi, Paul Barham, Jianmin Chen, Zhifeng Chen, Andy Davis, Jeffrey Dean, Matthieu Devin, Sanjay Ghemawat, Geoffrey Irving, Michael Isard, Manjunath Kudlur, Josh Levenberg, Rajat Monga, Sherry Moore, Derek G. Murray, Benoit Steiner, Paul Tucker, Vijay Vasudevan, Pete Warden, Martin Wicke, Yuan Yu and Xiaoqiang Zheng. 'TensorFlow: A system for large-scale machine learning'. 2016 (cit. on p. 76).

[124] Hans J. Johnson, Luis Ibanez and Matthew Mccormick. *The ITK Software Guide: Book 1*. 4th ed. 2016 (cit. on pp. 76, 113).

[125] Hans J. Johnson, Luis Ibanez and Matthew Mccormick. *The ITK Software Guide: Book 2*. 2016 (cit. on pp. 76, 113).

[126] Sameer Agarwal and Keir Mierle. *Ceres Solver*. 2010 (cit. on pp. 77, 99, 113).

[127] Qian Wang, Xianyi Zhang, Yunquan Zhang and Qing Yi. 'AUGEM: Automatically Generate High Performance Dense Linear Algebra Kernels on x86 CPUs'. In: *Proceedings of the International Conference on High Performance Computing, Networking, Storage and Analysis* (2013), 25:1–25:12 (cit. on pp. 77, 113).

[128] Karen Simonyan, Andrea Vedaldi and Andrew Zisserman. 'Deep Inside Convolutional Networks: Visualising Image Classification Models and Saliency Maps'. In: *ICLR*. 2014. arXiv: `1312.6034` (cit. on p. 80).

[129] Aravindh Mahendran and Andrea Vedaldi. 'Understanding deep image representations by inverting them'. In: *CVPR*. IEEE, June 2015, pp. 5188–5196 (cit. on p. 86).

[130] Davis M. Vigneault, Eunice Yang, C. Linda Chu, Carolyn Y. Ho and David A. Bluemke. 'Left Ventricular Strain Gradient Is Abnormal in Hypertrophic Cardiomyopathy: Assessment by CMR Feature Tracking'. In: *RSNA*. Chicago, IL, 2014 (cit. on p. 88).

[131] Davis M. Vigneault, Anneline S.J.M. te Riele, Cynthia A. James, Stefan L. Zimmerman, Hugh Calkins, Harikrishna Tandri and David A. Bluemke. 'Abnormal Right Ventricular Strain by Cardiac Magnetic Resonance in Preclinical Arrhythmogenic Right Ventricular Cardiomyopathy'. In: *AHA*. Chicago, IL, 2014 (cit. on p. 91).

[132] Kestutis J. Barkauskas, Prabhakar Rajiah, Ravi Ashwath, Jesse I. Hamilton, Yong Chen, Dan Ma, Katherine L. Wright, Vikas Gulani, Mark A. Griswold and Nicole Seiberlich. 'Quantification of left ventricular functional parameter values using 3D spiral bSSFP and through-time non-Cartesian GRAPPA.' In: *Journal of Cardiovascular Magnetic Resonance* 16.1 (2014), p. 65 (cit. on p. 95).

[133] Max Jaderberg, Karen Simonyan, Andrew Zisserman and Koray Kavukcuoglu. 'Spatial Transformer Networks'. In: *NIPS*. 2015, pp. 1–14. arXiv: `arXiv:1506.02025v1` (cit. on pp. 96, 126).

[134] Alejandro Newell, Kaiyu Yang and Jia Deng. 'Stacked Hourglass Networks for Human Pose Estimation'. In: *ECCV*. 2016. arXiv: `1603.06937` (cit. on p. 96).

[135] Iaroslav Melekhov, Juha Ylioinas, Juho Kannala and Esa Rahtu. 'Image-based Localization using Hourglass Networks'. Oulu, Finland, 2017 (cit. on p. 96).

[136] Chen-Yu Lee, Vijay Badrinarayanan, Tomasz Malisiewicz and Andrew Rabinovich. 'RoomNet: End-to-End Room Layout Estimation'. Plantation, FL, United States, 2017 (cit. on p. 96).

[137] Georgios Pavlakos, Xiaowei Zhou, Aaron Chan, Konstantinos G. Derpanis and Kostas Daniilidis. '6-DoF Object Pose from Semantic Keypoints'. Philadelphia, PA, United States, 2017 (cit. on p. 96).

[138] Thomas J. Cashman and Andrew W. Fitzgibbon. 'What shape are dolphins? Building 3D morphable models from 2D images'. In: *IEEE Transactions on Pattern Analysis and Machine Intelligence* 35.1 (2013), pp. 232–244 (cit. on pp. 99, 110).

[139] Jos Stam. 'Evaluation of Loop subdivision surfaces'. In: *SIGGRAPH*. 1998, pp. 1–15 (cit. on pp. 99, 105, 107, 110, 113, 140).

[140] William E. Lorensen and Harvey E. Cline. 'Marching cubes: A high resolution 3D surface construction algorithm'. In: *ACM SIGGRAPH Computer Graphics* 21.4 (1987), pp. 163–169 (cit. on p. 101).

[141] Michael Garland and Paul S. Heckbert. 'Surface simplification using quadric error metrics'. In: *SIGGRAPH*. 1997, pp. 209–216 (cit. on p. 102).

[142] Davis M. Vigneault. 'Perturbing Mesh Vertices with Additive Gaussian Noise'. In: *Insight Journal* 80.1 (2016), pp. 1–8 (cit. on pp. 104, 137).

[143] Will Schroeder, Ken Martin and Bill Lorensen. *The Visualization Toolkit*. 4th ed. Kitware, 2006, p. 512 (cit. on p. 113).

[144] Ana I.L. Namburete, Richard V. Stebbing, Bryn Kemp, Mohammad Yaqub, Aris T. Papageorghiou and J. Alison Noble. 'Learning-based prediction of gestational age from ultrasound images of the fetal brain'. In: *Medical Image Analysis* 21.1 (2015), pp. 72–86 (cit. on p. 121).

[145] Jelmer M. Wolterink, Tim Leiner, Max A. Viergever and Ivana Isgum. 'Dilated Convolutional Neural Networks for Cardiovascular MR Segmentation in Congenital Heart Disease'. In: *HVSMR*. Ed. by Maria A. Zuluaga, Kanwal Bhatia, Bernhard Kainz, Mehdi H. Moghari and Danielle F. Pace. Lecture Notes in Computer Science. Cham: Springer International Publishing, 2017, pp. 95–102 (cit. on p. 124).

[146] Davis M. Vigneault, Weidi Xie, David A. Bluemke and J. Alison Noble. 'Feature Tracking Cardiac Magnetic Resonance via Deep Learning and Spline Optimization'. In: *FIMH*. Toronto, Canada: Springer, 2017 (cit. on p. 124).

[147] Timothy M. Markman, Mohammadali Habibi, Bharath Ambale Venketash, Mytra Zareian, Colin Wu, Susan R. Heckbert, David A. Bluemke and Joao A.C. Lima. 'Association of left atrial structure and function and incident cardiovascular disease in patients with diabetes mellitus: results from multi-ethnic study of atherosclerosis (MESA)'. In: *European Heart Journal - Cardiovascular Imaging* (2017), pp. 1–7 (cit. on p. 126).

[148] Fausto Milletari, Nassir Navab and Seyed-Ahmad Ahmadi. 'V-Net: Fully Convolutional Neural Networks for Volumetric Medical Image Segmentation'. In: *CVPR*. 2016, pp. 1–11. arXiv: `1606.04797` (cit. on p. 126).

[149] Christopher B. Choy, JunYoung Gwak, Silvio Savarese and Manmohan Chandraker. 'Universal Correspondence Network'. In: *NIPS*. 2016, pp. 1–17. arXiv: `1606.03558v3` (cit. on p. 126).

[150] Ronald J. Beyers, Davis M. Vigneault, Dean Schwartz, Nouha Salibi, David A. Bluemke and Thomas Denney. 'Preliminary Results: Cardiac Cine "Watermark" MRI provides both Anatomical Function via Magnitude Cine and 2D Myocardial Strain via Spatially Modulated Phase'. In: *ISMRM*. Singapore, 2016 (cit. on p. 127).

[151] Ronald J. Beyers, Davis M. Vigneault, Nouha Salibi, David A. Bluemke and Thomas S. Denney. 'Accelerated Cardiac Cine "Watermark" MRI provides Cardiac Function via Magnitude Cine and 2D Myocardial Strain via Spatially Modulated Phase'. In: *ISMRM*. Honolulu, Hawaii, 2017 (cit. on p. 127).

[152] Robert T. Jones. 'Blood Flow'. In: *Annual Review of Fluid Mechanics* 1.1 (Jan. 1969), pp. 223–244 (cit. on p. 129).

[153] R. Bartels and G.W. Stewart. 'Algorithm 432: Solution of the Matrix Equation AX + XB = C'. In: *Communications of the Association of Computing Machinery* 15.9 (1972), pp. 820–826 (cit. on p. 147).

[154] Charles Loop and Scott Schaefer. 'Approximating Catmull-Clark subdivision surfaces with bicubic patches'. In: *ACM Transactions on Graphics* 27.1 (2008), pp. 1–11 (cit. on p. 148).